The effect of stress concentrations on fatigue and fracture of 316L stainless steel micro-scale components

Susanne Amanda Wiersma

Submitted in fulfilment of the requirements for the award of the degree of Doctor in Philosophy to The University of Dublin, Trinity College, March 2004.

Supervisor: Professor David Taylor

The work presented in this thesis was conducted at the Department of Mechanical and Manufacturing Engineering, University of Dublin, Trinity College Dublin, Ireland.

Declaration

I declare that the present work has not been submitted as an exercise for a degree at any other University. This thesis consists entirely of my own work except where references indicate otherwise.

I agree that the library of the University of Dublin, Trinity College, Dublin may lend or copy this thesis upon request.

Susanne Amanda Wiersma

Acknowledgements

I would like to thank the following people for their help and support:

David Taylor; Obviously, without you this work would not have existed. Thank you for your endless support and guidance and providing me with a comfortable working atmosphere. I have really enjoyed these years in Dublin. Also thanks to Niamh for her lovely dinners.

Medtronic AVE Galway and Enterprise Ireland; Thank you for funding this work. A special thanks to Barry Dolan from Medtronic; thank you for all your help sorting out the specimens.

Peter O'Reilly; Your experience with the testing equipment has been extremely helpful to me, especially this last year. I am very grateful to you.

Jan, Danny, Giuseppe and Luca; Guys, thank you for all your help and friendship. I have put you in chronological order, but you are all equally important to me. Jan, without you, I would never have known about this PhD. Danny, you were my 'guru' when I started my PhD and since then you have always given me useful advice whenever I needed it. Giu, thank you for always being able to cheer me up whenever I needed it. Life in Dublin would not have been as much fun without you. And last but certainly not least, Luca; You know how much I have appreciated our talks and our friendship.

Tom, JJ, Gabriel, Sean and Danny; thank you all for the help with manufacturing whatever was required for my work. I really enjoyed my machining days. A special thanks to Tom; I think sometimes you were not so happy to see me (more work). A major thanks to JJ for manufacturing my difficult small specimens. I know how much you loved making them!

Joan and Nicole; where would any of us be without you? Neal Leddy; thank you for your help with the electron microscope. My lunch-buddies; Leandro, Lorea, Lia, Frederik, Jesus, Gabriel and Victor. Lunch was always the best part of the day. My colleagues (past and present); Triona, Linda, Mary, Laoise, Bruce, Richard, John B and G, Kevin, James, Laura and the rest of the department. Thanks for a fun working environment.

And last but not least: family and friends; You know who you are, thanks for all your support.

Summary

The aim of this work was to investigate the fatigue and fracture behaviour of microscopic specimens based on a biomedical component (the cardiovascular stent) and to modify existing theories to take account of the observed effects. A stent is a cylindrical wire mesh that is used to scaffold open stenosed arteries in order to retain a sufficient blood flow. Different 316L stainless steel microscopic specimens were designed and tested, which contained notches representing stent-like features. Typical sizes of stent wires are around 100 μm, giving only about 10 grains along the width and thickness of the wires.

Several fatigue prediction theories were discussed: the Stress Life method, the Smith and Miller method, the Crack Modelling Method, The Theory of Critical Distances and the Resistance-curve method. Two types of correction factors were proposed in order for these methods to be made applicable to microscopic specimens: applying a short crack correction based on El Haddad's short crack parameter a_o, or reducing the long crack threshold.

The different prediction methods in combination with the two types of correction factors were found to give varying results. Often the altered method was capable of predicting test data from some of the specimen geometries, but not all of them. The only method that gave good results for all microscopic experimental fatigue data was the Theory of Critical Distances (especially the Point Method) in combination with a reduced threshold value. The Point Method determines the stress at a distance ahead of the notch and compares it to the critical stress of the material, which is the plain specimen fatigue limit, $\Delta\sigma_o$.

The threshold value of the material is constant for long cracks, but it is has been found to reduce for short cracks. Three different reduced threshold values were proposed: based on the net width of the specimen, based on the average experimentally obtained microscopic threshold value and based on the closure-free effective threshold value of the material. The average threshold value for the microscopic specimens and the closure-free effective threshold gave good Point Method predictions. A reduction in the threshold also results in a reduction of the critical distance.

It was hypothesised that the cause for this reduction in threshold and corresponding critical distance is likely to be one of the following three: non-propagating cracks, plane stress/mode-III shear failure or lack of closure. The argument was made that the critical distance could be related to the non-propagating crack length. An analysis was done to investigate this and the non-propagating crack length was found to reduce for microscopic specimens, therefore, the critical distance and threshold value should also be reduced for microscopic specimens. However, one long notch was tested in a microscopic specimen, which could be predicted with the *reduced* threshold value, while it should have been predicted with the *long crack threshold value*, therefore non-propagating cracks are not the cause for the reduced threshold. The specimens also did not experience plane stress/mode-III shear fracture, because the fracture surfaces were flat, not under an angle of 45 degrees. Therefore, the cause of the reduction in threshold value is most likely the lack of closure in the microscopic specimens; this is why the effective closure-free threshold was capable of predicting data from all the microscopic specimen geometries.

One notched microscopic aluminium specimen was tested to investigate if the same approach could be used for a different material. Some differences were found between the aluminium and stainless steel results, however, for the micro-scale aluminium the threshold was again found to reduce and the Theory of Critical Distances was capable of predicting the fatigue behaviour of this aluminium microscopic specimen. Therefore, it is expected that the method can be applied to microscopic components manufactured from a variety of different materials, provided that either a closure-free threshold or a microscopic threshold value is known. Alternatively, the grain size could be used to determine the reduced value for the threshold.

Not enough tensile tests were carried out to draw conclusions, but the static fracture strength of the microscopic specimens was found to be equally strong if not stronger than the macro material. When the design contained symmetrical notches, notch strengthening due to constraint was found to occur, which increased the strength of the microscopic stainless steel specimens substantially.

Table of Contents

Nomenclature

Symbol	Unit	Definition
a	mm	Crack length
a_o	mm	El Haddad's short crack parameter and the crack length where the plain specimen fatigue limit and the long crack fatigue prediction curves intersect in the Kitagawa/Takahashi diagram
a_{oGROSS}	mm	El Haddad's short crack parameter determined at the gross section
a_{oNET}	mm	El Haddad's short crack parameter determined at the net section
a_1	mm	Transition crack length between the microstructurally short crack regime and the physically short crack regime
a_2	mm	Transition crack length between the long and short crack regimes
a_c	mm	Transition crack length between the long and short crack regimes in the *R-curve* plot
a_{NET}	mm	Maximum crack length at the net section, which is used to calculate ΔK_{th_width}
a_w	mm	Half the crack length of a central crack in an infinite plate, defined by Westergaard
A_1	mm^2	Cross sectional area of the grip end
A_2	mm^2	Cross sectional area of the wire
c_o	mm	Tanaka's characteristic crack length similar to the grain size
c_2	mm	Tanaka's characteristic transition crack length between the short and the long crack regimes
CAD		Computer Aided Design
CCT		Centre Crack Tension specimen
CMM		Crack Modelling Method
d_1	mm	Width of the grip end

d_2	mm	Width of the wire
da/dN	mm/cycle	Crack growth rate
D	mm	Notch depth
$DENT$		Double Edge Notch Tension specimen
E	GPa	Young's Modulus
E_1	GPa	Young's Modulus in the grip end
E_2	GPa	Young's Modulus in the wire
F		Geometrical factor in the stress intensity equation
F_1	N	Load in the grip end
F_2	N	Load in the wire
F_{GROSS}		Geometrical factor corresponding to the gross area
F_{NET}		Geometrical factor corresponding to the net area
FEA		Finite Element Analysis
$gross$	mm^2	Cross sectional area at the gross section
HCF		High Cycle Fatigue
k		Inverse of the slope of the S-N_f curves
K	MPa$\sqrt{m}$	Stress intensity factor
K_C	MPa$\sqrt{m}$	Fracture toughness
K_{IC}	MPa$\sqrt{m}$	Fracture toughness for tension
K_{IIC}	MPa$\sqrt{m}$	Fracture toughness for in-plane shear
K_{IIIC}	MPa$\sqrt{m}$	Fracture toughness for out-of-plane shear
K_{cl}	MPa$\sqrt{m}$	Closure stress intensity factor
K_f		Fatigue notch factor
K_{max}	MPa$\sqrt{m}$	Maximum stress intensity factor
K_{maxth}	MPa$\sqrt{m}$	Maximum stress intensity factor at the threshold
K_{min}	MPa$\sqrt{m}$	Minimum stress intensity factor
K_{op}	MPa$\sqrt{m}$	Opening stress intensity factor
K_{opth}	MPa$\sqrt{m}$	Opening stress intensity factor at the threshold, which reduces with reducing crack length
$K_{opth\omega}$	MPa$\sqrt{m}$	Opening stress intensity factor at the threshold for a long crack
K_t		Theoretical elastic stress concentration factor
K_ε		Strain concentration factor in the Neuber rule

K_σ		Stress concentration factor in the Neuber rule
l_1	mm	Length of the grip end
l_2	mm	Length of the wire
l_{total}	mm	Total length of both sections 1 and 2
L	mm	Critical distance which is based on the material threshold
L_{eff}	mm	Critical distance which is based on the effective threshold
L_{exp}	mm	Critical distance which is based on the microscopic experimental value for the threshold
L_{width}	mm	Critical distance, which is based on ΔK_{th_width}
LEFM		Linear Elastic Fracture Mechanics
MEMS		Micro Electro Mechanical Systems
N_f		Number of cycles to failure
net	mm^2	Cross sectional area at the net section
r	mm	Distance ahead of a crack or a notch
r_c	mm	Critical distance ahead of a crack or a notch
r_n	mm	Characteristic critical length of a material proposed by Neuber
r_p	mm	Characteristic critical distance of a material proposed by Peterson
R-curve		Resistance curve
R-ratio		Load ratio: $\sigma_{min} / \sigma_{max}$
scc		Short crack correction
scc_{EH}		Short crack correction using El Haddad's a_o
scc_w		Short crack correction using Westergaards a_w
S	MPa	Stress in S-N_f curve
SENT		Single Edge Notch Tension specimen
S-N_f curve		Stress vs. number of cycles to failure curve
t	mm	Thickness
TCD		Theory of Critical Distances
UTS	MPa	Ultimate Tensile Strength
w	mm	Width
w_{GROSS}	mm	Width of the specimen at the gross section
w_{NET}	mm	Width of the specimen at the net section

Δc	mm	Total crack extension from a pre-crack
ΔK	MPa$\sqrt{m}$	Stress intensity factor range
ΔK_{eff}	MPa$\sqrt{m}$	Effective stress intensity range
ΔK_{eff}	MPa$\sqrt{m}$	Threshold value for the effective stress intensity range
ΔK_{th}	MPa$\sqrt{m}$	Threshold stress intensity factor range for crack propagation
ΔK_{thEH}	MPa$\sqrt{m}$	El Haddad's threshold value which reduces with crack size
ΔK_{th_exp}	MPa$\sqrt{m}$	Threshold based on micro-scale experimental data
ΔK_{th_width}	MPa$\sqrt{m}$	Threshold value based on the net width of the specimen
Δl_{total}	mm	Change in total length of both sections 1 and 2 together
$\Delta\sigma$	MPa	Stress range
$\Delta\sigma_o$	MPa	Fatigue limit of plain specimens
$\Delta\sigma_{oc}$	MPa	Fatigue limit of cracked specimens
$\Delta\sigma_{on}$	MPa	Fatigue limit of notched specimens
$\Delta\sigma_{on\_pred}$	MPa	Prediction value for the fatigue limit
$\Delta\sigma_{onGROSS}$	MPa	Fatigue limit for a notched specimen determined at the gross section
$\Delta\sigma_{onLEFM}$	MPa	Fatigue limit for a notched specimen based on the long crack *LEFM* relation
$\Delta\sigma_{onNET}$	MPa	Fatigue limit for a notched specimen determined at the net section
$\Delta\sigma_{th}$	MPa	Threshold stress used for alternative TCD approach where critical distance L is based on the grain size
ε		Strain
ε_1		Strain in the grip end
ε_2		Strain in the wire
ε_{total}		Total strain over sections 1 and 2
ρ	mm	Notch root radius
σ	MPa	Stress
σ_o	MPa	Static tensile strength for plain specimens
σ_{on}	MPa	Maximum fatigue limit stress for notched specimens
$\sigma_{onGROSS}$	MPa	Maximum fatigue limit stress for notched specimens

		determined at the gross section
σ_1	MPa	Stress in the grip end
σ_2	MPa	Stress in the wire
σ_a	MPa	Stress amplitude
σ_f	MPa	Stress that causes static failure
σ_{fTRUE}	MPa	True static failure stress using reduced area at failure
σ_{GROSS}	MPa	Nominal stress at the gross section
σ_{max}	MPa	Maximum stress
σ_{min}	MPa	Minimum stress
σ_{NET}	MPa	Nominal stress at the net section
$\sigma_{nominal}$	MPa	Nominal stress
σ_{notch}	MPa	Maximum stress at the notch
σ_y	MPa	Yield stress/strength
σ_w	MPa	Tensile stress applied to a centre crack in an infinite plate used in Westergaard's equation
ω_t	mm	Initial plastic zone size

Chapter 1 Introduction

When the railroads were introduced in the 1840's, components like axles started to experience a new type of failure. This type of failure, which is attributed to repeated cyclic loading, was later named fatigue failure. One of the first to research this new phenomenon was Wöhler (1870). He carried out systematic constant amplitude fatigue tests and showed that the fatigue life of a component, defined as the number of cycles to failure, decreases with an increasing level of stress. The Wöhler curve, or stress versus cycles to failure relation (*S-N_f curve*) is still used today.

Fatigue failure is the predominant type of failure in engineering components. It is therefore important to limit the risk of fatigue failure by understanding the phenomenon and trying to prevent it. This explains why so many papers have been published about fatigue. Originally, fatigue research was aimed at analysing whether a component would or would not break as a result of the applied fatigue cycles, but the development of Fracture Mechanics rerouted the focus to the process of fatigue crack growth. Fracture Mechanics evaluates the effect of stress concentrations (e.g. notches, holes and corners) on the fatigue life of components. The method can only be applied when there is a crack or flaw present in the material. It is therefore crack propagation that is the important parameter in fracture mechanics, as opposed to crack formation. Linear Elastic Fracture Mechanics (LEFM) assumes that the material predominantly behaves in a linear elastic manner.

The importance of short cracks became apparent only in the 1980's. The knowledge of long cracks in *macro-scale* components, e.g. in the automotive industry, could not be applied directly to describe the characteristic behaviour of short cracks. Instead short crack models were developed.

The novelty of the present work is to extend the understanding that exists at present of the small crack mechanism in large components to micro-scale components, where sections are of similar size to micro-structural elements. The limited amount of work that has been

published regarding the micro-scale fatigue regime is mainly about components in the biomechanics industry and micro electro mechanical systems, or, MEMS devices.

In the micro-scale regime the usual assumptions of continuum mechanics no longer apply. Factors such as grain orientation play a much greater role as opposed to large components, where the material behaves as the average behaviour over many grains. For micro-scale components, which contain only a few grains along the width and/or thickness of the component, there are not enough grains to establish a continuum. Therefore, micro-scale components are expected to behave differently from macro-scale ones. More research is necessary to clarify this size effect.

This work focuses on the micro-scale behaviour of a specific 316L stainless steel biomedical component: the stent. The findings of this work should be applicable to a wide range of micro-scale components made from different materials.

1.1 Objectives

The objectives of this research are:

- To obtain experimental data on the fatigue and fracture behaviour of 316L stainless steel. This material is used to manufacture a microscopic biomedical component: the intravascular stent.
    - To carry out fatigue tests on microscopic and macroscopic plain and notched specimens to compare macro- and microscopic material behaviour
    - Microscopic specimen designs should contain typical stent features
- To modify existing theories of fatigue and fracture behaviour to take account of the observed effects and enable prediction of the fatigue and fracture behaviour of micro-scale components, using a combination of Computer Aided Design (CAD) and Finite Element Analysis (FEA) techniques.
- To investigate if continuum mechanics can be used for micro-scale components (where there are not enough grains to establish a continuum) or if single grain behaviour has to be taken into account, e.g. through dislocation theory.

1.2 Atherosclerosis, balloon angioplasty and the intravascular stent

Since fatigue testing was carried out on 316L stainless steel specimens that were based on stents, it is relevant to give some background information on the disease *atherosclerosis* and the initial remedy; *balloon angioplasty*. Both have played an important role in the development of stents.

1.2.1 Atherosclerosis

Atherosclerosis is a disease which results in a severe build-up of fatty deposit, or plaque, inside large and medium sized arteries over a period of many years (Ross, 1999), see Fig. 1.2.1. The plaque formation reduces the effective diameter of the artery through which blood can flow and is referred to as a stenosis. Obstruction of the blood flow from atherosclerosis reduces the amount of blood and oxygen distributed to the tissue downstream from the blockage. This can eventually lead to necrosis; death of tissue. In most cases this disease occurs in the coronary arteries around the heart and can ultimately lead to a heart attack.

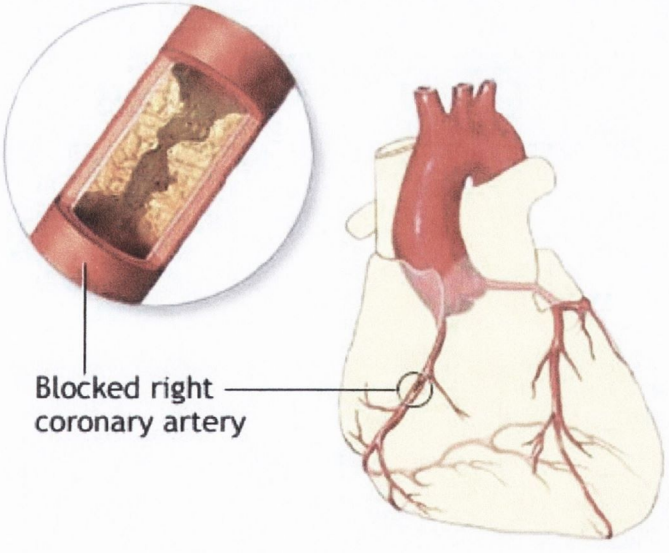

Fig. 1.2.1 Atherosclerosis in the coronary artery around the heart

The risk of a heart attack is not the only adverse effect of atherosclerosis. Plaque can also break away and travel in the bloodstream. If this embolism (clot of foreign material) reaches a small enough vessel, it can get stuck and cause a blockage, which in its turn can also result in tissue necrosis. When this happens in the brain, a person experiences a stroke.

1.2.2 Balloon angioplasty

The first procedure that was developed as a remedy against atherosclerosis was balloon angioplasty (Nobuyoshi et al, 1991). During this procedure a catheter with a balloon is guided through the vascular system to the position of the stenosis. The balloon is inflated within the vessel at the occlusion and the plaque is compressed against the arterial wall. After the procedure, the balloon is deflated and removed, and blood flow is usually restored, see Fig. 1.2.2.

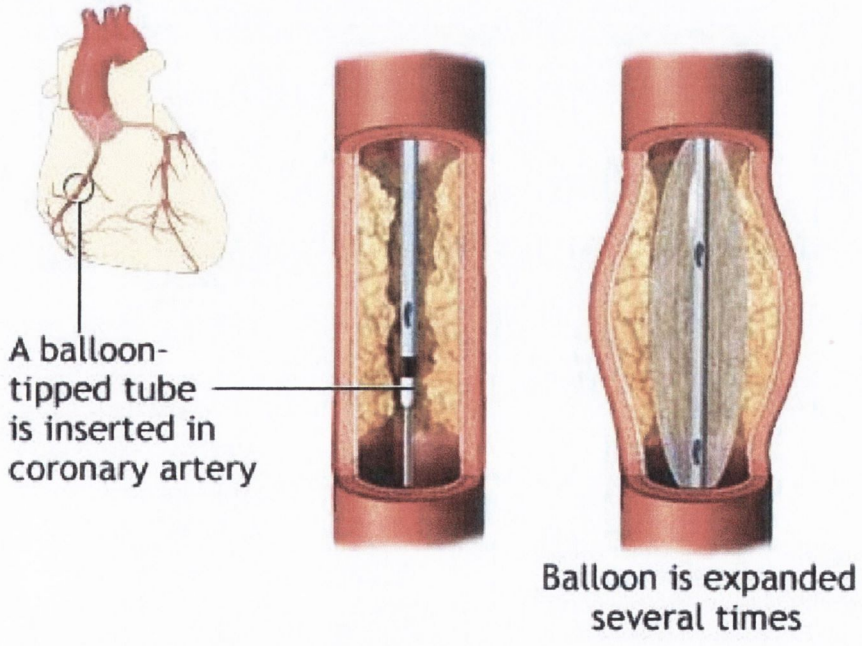

Fig. 1.2.2 Balloon angioplasty

1.2.3 The intravascular stent

The main problem of balloon angioplasty is restenosis; reformation of the occlusion. The intravascular stent was developed to improve the outcome of balloon angioplasty (Sigwart et al, 1987). A stent is a cylindrical wire mesh that remains within the artery as a permanent reinforcement, see Fig. 1.2.3. The stent is navigated to the position of the blockage, where it is deployed using balloon angioplasty thus trapping the plaque between the stent and the arterial wall. The stent material is plastically deformed during the expansion process, which fixes the stent in its expanded form inside the blood vessel.

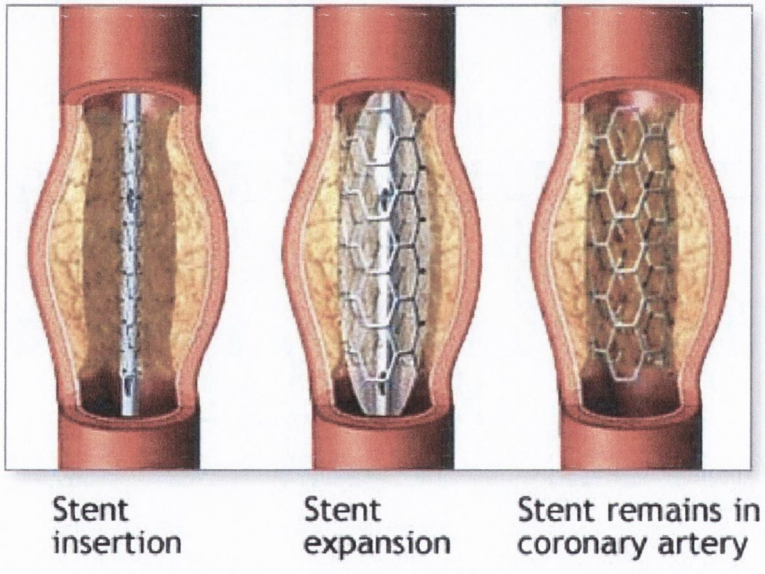

Fig. 1.2.3 Intravascular stenting

Arteries expand and decrease in size as a result of pressure changes and the pulsating nature of the blood flow. It is therefore important to investigate the fatigue properties of the 316L stainless steel, since the stent is cyclically loaded due to the beating of the heart. Stents are normally designed to have a life of 10 years. This corresponds to roughly 395 million cycles at an average heart rate of 75 beats per minute.

1.3 Fatigue prediction method: The Theory of Critical Distances (TCD)

A fatigue prediction method can be a helpful tool in the development of stents and other components that are subjected to fatigue loading. Medtronic AVE Galway, who develop and manufacture cardiovascular balloons and stents, use Computer Aided Design (CAD) and Finite Element Analysis (FEA) as important design and development tools. It would be useful for them to have a fatigue prediction method that can interface with CAD and/or FEA programmes. At present most fatigue prediction methods are developed for *macroscopic* components, e.g. automotive and aerospace components.

Microscopic components are expected to behave in a radically different way from large components, because there are not enough grains to form a continuum material behaviour. The orientation of a single grain becomes more important. The Theory of Critical Distances (TCD) (Taylor, 1999) is a Fracture Mechanics based fatigue prediction method that was also originally developed for large components (Taylor et al, 2000). The approach has been implemented in easy to use software that can interact with CAD and FEA programmes. The aim of the present work was to investigate whether the TCD could be used for microscopic components and whether any modifications were required.

Most conventional Fracture Mechanics fatigue prediction methods can only be used on components that contain a clearly defined crack or flaw. That aspect limits the use of these methods since most components contain stress concentrations of arbitrary geometry. The advantage of the Theory of Critical Distances is that it can predict the fatigue behaviour of these arbitrary stress concentrations.

In publications over the past years, the Theory of Critical Distances (TCD) has been referred to as the Critical Distance Method (CDM). Since the abbreviation CDM could be confused with Continuum Damage Mechanics, the Critical Distance Method has been renamed as: Theory of Critical Distances (TCD).

1.4 Fatigue in microscopic components

Fatigue in micro-scale components, where sizes are in micrometers (μm), is a relatively new area. These last couple of years, most work on micro-scale samples has been done on two types of components and their corresponding materials: micro electro mechanical systems (MEMS devices) and biomedical products. Testing related problems occurred that are normally not encountered with macro-scale specimens, e.g. *handling and gripping* of fragile specimens, *manufacturing processes* and finding/developing *suitable test equipment*. Micro-scale components often have to be able to withstand millions of cycles, in the case of MEMS devices even billions of cycles. Therefore, the test equipment has to be capable of testing at high frequencies with good accuracy and measuring loads in the range of milli-Newtons.

Because of the problems with handling and gripping of the micro-scale specimens in combination with the difficulty of manufacturing samples with good quality and reproducibility, many researchers have chosen to test components instead of specimens. Components are sometimes easier to handle and the manufacturing process already exists, giving good reproducibility. Having to manufacture specimens of a different geometry to the component, can be much more complicated.

Douglas (1998) obtained fatigue data for a digital micro-mirror manufactured by Texas Instruments, a MEMS device. He predicted from macro-scale material properties that the component would not be able to withstand 100 billion cycles, but experimental results suggested otherwise; some components survived even 1 trillion cycles. An explanation given for this effect is that the component is only one grain thick and there is not enough material for dislocations to pile up and initiate fatigue cracks. It is clear that when sizes are in μm, the material behaves differently and macro-scale properties can no longer be used to predict the behaviour of the component.

Even though it might be easier to test components, specimen tests should be carried out to obtain material properties. Hadrboletz and co-workers (Hadrboletz et al, 1999) (Weiss and Hadrboletz, 2002) studied the thickness effect, where they found that the number of grains and the grain size influence the strength vs. thickness relation substantially.

Micro-scale wires are used for biomechanical applications. Matsuda and Yamamoto (1993) have investigated the strength of these wires. Similar to research on MEMS devices, they did not directly test material properties, but looked at the strength of a wire structure that fixes together two broken pieces of bone. Scheiner et al (1991) looked at the strength of different single and multi strand micro-scale wires of different materials.

The micro-scale area in fatigue is still in its infancy and a lot more work needs to be done, especially because the general conclusion is that bulk material properties cannot be used to predict micro-scale fatigue failure. However, no alternative methods for fatigue in micro-scale samples and components have been proposed.

1.5 Overview

This thesis consists of 9 chapters. Chapter 2 gives a short introduction into Fracture Mechanics and discusses several fatigue approaches, most of which are based on Fracture Mechanics. In chapter 3, some of the prediction methods were altered to apply to short cracks and micro-scale components. Experimental details, e.g. test machines used, microscopy and specimen design, are stated in chapter 4.

Tests were carried out on two materials: stainless steel and aluminium. Chapter 5 gives a summary of all the results and chapters 6 and 7 link the theory of chapters 2 and 3 to the experimental results of respectively stainless steel and aluminium. Chapter 8 gives the general discussion followed by the final chapter with the conclusions.

Chapter 2 Review of the Literature: Fatigue and fracture of short cracks and notches

Several methods have been developed over the years in an attempt to predict fatigue failure as a result of stress concentrations (e.g. notches, corners and holes). The problem with many conventional approaches is that they can only be used when a crack is present or when the stress concentration geometry is clearly described by a notch depth, D, and a root radius, ρ. The application of these methods is limited, because most engineering components are of a complex geometry, where no notch depth or root radius can be clearly determined. Finite Element Analysis (FEA) has been a helpful instrument in developing new methods that are capable of making fatigue predictions for components of arbitrary geometry.

This chapter gives an overview of important fracture mechanics parameters. It discusses the influence of cracks and notches on the static tensile and on the fatigue behaviour of specimens and it describes several prediction methods that are applicable to this work.

2.1 A brief introduction to fatigue and fatigue related terms

All engineering components and structures are subjected to some form of external loading. As a result of these external forces, it is likely that a crack starts to grow and may even propagate to failure. It is therefore necessary to look at the physical background: the material cracking behaviour. Fracture Mechanics is an important tool that can be used to describe the material cracking behaviour because of its capability to determine the stress field in the vicinity of a crack or a notch.

2.1.1 Linear Elastic Fracture Mechanics (LEFM)

Before being able to analyse cracks and their propagation behaviour, it is necessary to define several important Fracture Mechanics parameters. When a crack or flaw (e.g. notch) is

present in a component, Linear Elastic Fracture Mechanics (LEFM) can be used to describe the stress field around that crack as a result of the applied external loading. Linear Elastic Fracture Mechanics assumes that the material behaves in a linear elastic manner, therefore, any plasticity present at the crack tip is considered negligible. An important parameter in LEFM is the stress intensity factor, K, which describes the severity of the mathematical singularity at the tip of a crack as a result of an applied stress or an applied stress range:

$$K = F\sigma\sqrt{\pi a} \tag{2-1-1}$$

where F represents the specimen geometry, σ is the nominal stress as a result of the applied external load and a is the crack length. For fatigue loading, equation 2-1-1 is in the form of stress intensity factor range, ΔK, because a stress range, $\Delta\sigma$, is applied during fatigue cycling. Several parameters based on the general equation 2-1-1 can be defined.

Fracture Toughness, K_C :

K increases during crack growth for a constant applied stress range. If the applied stress in combination with the crack length cause the corresponding K value to rise above the critical value, failure will occur. This critical K value is called Fracture Toughness, K_C:

$$K_C = F\sigma_f\sqrt{\pi a} \tag{2-1-2}$$

where σ_f is the stress at which the component fails and a is the corresponding crack length at failure. Dependent on the loading mode, this parameter can be determined for tension, in-plane shear and out-of-plane shear, respectively: K_{IC}, K_{IIC} and K_{IIIC}.

Threshold stress intensity factor range, ΔK_{th}:

An important parameter for fatigue crack propagation is the threshold stress intensity factor range, ΔK_{th}. When the stress intensity range, ΔK, for a certain geometry and loading condition is below the threshold value, no cracks are assumed to grow. In other words, when the stress intensity range is below the threshold value, no failure will occur even when a crack is present. When ΔK rises above the threshold value, a fatigue crack will start to propagate and can potentially cause failure.

Theoretical elastic stress concentration factor, K_t:

The theoretical elastic stress concentration factor K_t gives an indication of the stress gradient of the crack or notch. It is defined as the ratio of the peak stress at the notch over the nominal stress:

$$K_t = \frac{\sigma_{notch}}{\sigma_{nominal}} \qquad (2\text{-}1\text{-}3)$$

where σ_{notch} is the peak stress at the notch or crack tip and $\sigma_{nominal}$ is the nominal stress.

2.1.2 Definitions of fatigue related terms

Initiation and propagation

Long discussions can be held on crack initiation and crack propagation. In this work it is assumed that it is very easy for a crack to *initiate*, therefore, crack *propagation* is the important factor in fatigue life determination. This implies that even at extremely low applied stress ranges, cracks can form and propagate until they get stopped by a microstructural boundary in the material. These initiated cracks are often stopped when they reach the grain boundary.

Fatigue limit/Fatigue strength

Fatigue limit and *Fatigue strength* are commonly used fatigue terms, however, it is not always clear what is meant exactly by these terms. The fatigue life of a component increases when the applied stress range is reduced. For some materials, the fatigue life keeps increasing with decreasing applied stress range, but for some steels, this relation levels off to a safe minimum stress range value (often between 1 and 2 million cycles). The fatigue strength should therefore be related to a certain number of cycles to failure. In this work, unless stated otherwise, the fatigue limit, or fatigue strength is determined at 2 million cycles to failure.

Fatigue life/Cyclic life

The fatigue life, or cyclic life, of a component or specimen is defined at the number of cycles to which the specimen or component is subjected when failure occurs.

Gross vs. net

When a crack or notch is introduced in a component, the cross sectional area at that point is reduced. Normally in *LEFM* studies, K and σ are determined at the larger, *gross*, area, however, in this work these parameters were compared at the *net* area. Where necessary, these will be distinguished, e.g. σ_{NET} and σ_{GROSS}.

2.2 Cracks and their propagation behaviour

Nearly 50 years ago, Irwin proposed a new tool in the prediction of abrupt failures; the stress intensity factor K. This tool could be used to describe the stress field around a crack. He also showed that this stress intensity factor was related to the elastic energy required for the crack extension process; Griffiths energy release rate. This energy release rate was the state of the art method for crack extension in that period.

It took 10 years before the majority of researchers started to believe that the *elastic* parameter K could actually be used in the analysis of fatigue crack growth, where plasticity is a dominant factor. Especially because this new parameter was not based on dislocation theory, which was the general consensus at that time.

Since then many researchers have contributed to the development of Fracture Mechanics. This section discusses experimental data on cracks and their propagation behaviour, followed by Fracture Mechanics based theories that describe these phenomena.

2.2.1 The Smith and Miller diagram

The Smith and Miller diagram (Smith and Miller, 1978) shows the relation of data that were obtained from experimental fatigue tests, see Fig. 2.2.1. The fatigue limits were determined experimentally for a wide variety of notches in the same material. All specimens contained notches of the same depth, but they had different values for the elastic stress concentration factor, K_t. The Smith and Miller diagram can assist in determining the safe and failure regimes in a material containing notches of a constant depth.

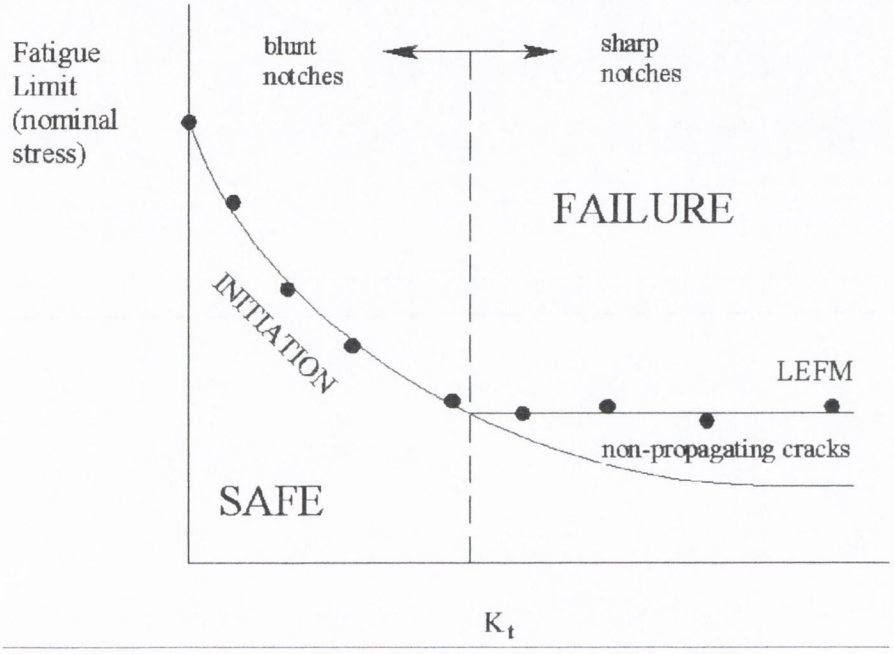

Fig. 2.2.1 Smith and Miller diagram

The Smith and Miller diagram distinguishes two notch regimes: blunt and sharp notches. In the blunt notch regime, where the K_t value is low, the fatigue strength is directly related to K_t. In the sharp notch regime, the notches behave as cracks and Linear Elastic Fracture Mechanics can be used to define failure. The exact value for K_t at the transition between blunt and sharp notches depends on the material.

The last regime to be defined in Fig. 2.2.1 is the non-propagating crack regime. From experimental tests it was found that in some situations an initiated crack could arrest and stop growing before failure occurred. These non-propagating cracks were only found at sharp notches. Frost (1959) confirmed the finding of these non-propagating cracks which were discovered a couple of years earlier by other workers and he did significant work in this area. The Smith and Miller diagram is also known as the Frost diagram.

Section 2.4.1 discusses the Smith and Miller method, which includes equations to describe the fatigue behaviour of blunt and sharp notches in a material.

2.2.2 The Kitagawa/Takahashi curve

The Kitagawa/Takahashi curve (Kitagawa and Takahashi, 1976) shows the experimentally obtained relation between the fatigue stress range and the length of a crack in a component, see Fig. 2.2.2. Three regimes can be found: the long crack regime, the physically short crack regime and the microstructurally short crack regime. The focus of the diagram lies on both short crack regimes, which was the new area in fatigue research at that time.

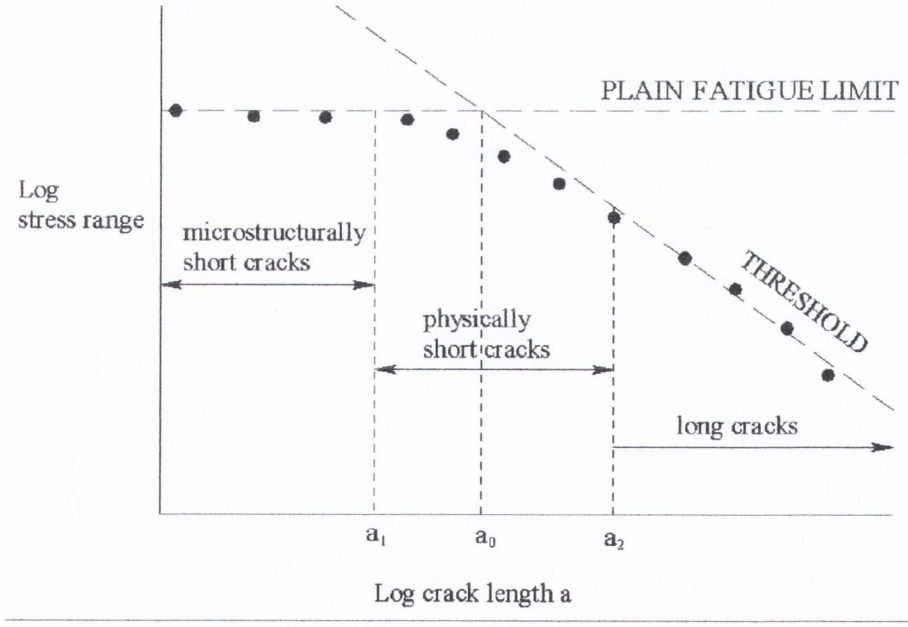

Fig. 2.2.2 The Kitagawa/Takahashi curve

The experimental long crack fatigue data can be described using the *threshold* stress intensity factor, ΔK_{th}:

$$\Delta K_{th} = F\Delta\sigma_{oc}\sqrt{\pi a} \qquad (2\text{-}2\text{-}1)$$

where F is the geometry factor and $\Delta\sigma_{oc}$ is the stress range that causes failure at the fatigue limit for a component with a corresponding crack of size a. The microstructurally short cracks and the physically short cracks do not follow the LEFM threshold relation. Instead, the experimental data bend towards the plain fatigue limit. Crack length a_2, distinguishes the long crack regime from the short crack regime; when a crack is longer than length a_2 it will behave as a long crack.

Crack length a_1 indicates the transition between both types of short cracks, the microstructurally and physically short cracks. Taylor (1989) estimated that for many materials the ratio between a_2 and a_1 is: $a_2 = 10a_1$ where a_1 is roughly the distance to the first microstructural boundary.

The length a_o is the crack length where the plain specimen fatigue limit and the long crack threshold prediction lines intersect. This crack length parameter a_o is known as the El Haddad short crack parameter, which will be discussed further in section 2.6.

2.2.3 The three crack regimes

Fig. 2.2.3 (Smith and Miller, 1978) gives an illustration of the three crack regimes: the long crack regime, the physically short crack regime and the microstructurally short crack regime. In the *physically short crack regime* the crack length a is smaller than roughly ten grains and in the *microstructurally short crack regime* the crack length a is even less, around the distance between two microstructural boundaries, e.g. the diameter of a grain or less.

Smith and Miller consider a crack to belong to the *long crack regime* when its length, a, is larger than roughly a hundred grains. This contradicts with what was said in the previous section, where Taylor estimated that a crack is long when its length is larger than 10 grains

(Taylor, 1989). This demonstrates the complexity of the short crack regime, which is still very much developing.

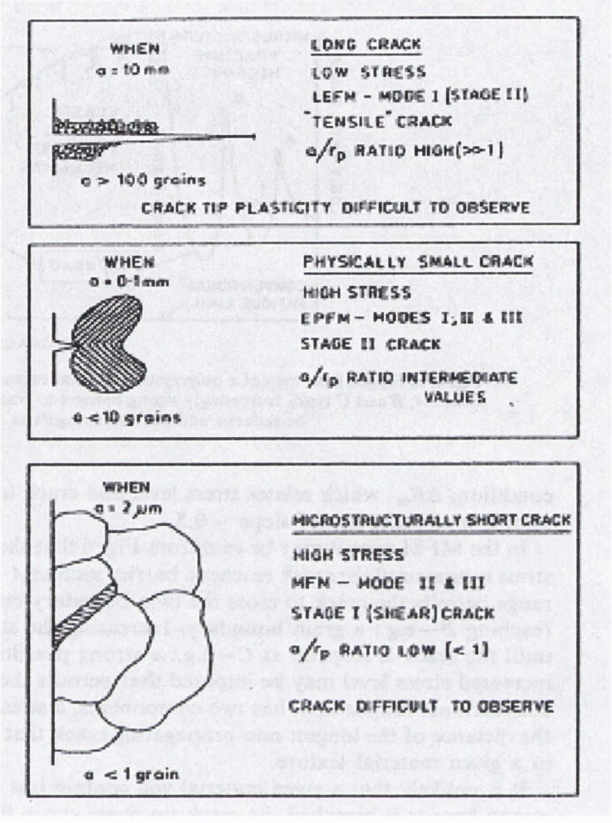

Fig. 2.2.3 The three crack regimes (Smith and Miller, 1978)

One aspect people do agree on is that a *long crack* propagates within a continuum. The long crack experiences average closure behaviour as a result of the negatively stressed wake of the crack. For short cracks this wake has not been (fully) developed and the closure effect increases with crack propagation until it reaches the constant long crack value.

In the *microstructurally short crack* regime, crack growth is dependent on the orientation of one or a few single grains, while in the *physically short crack* regime there are a few more grains, but still not enough to establish the long crack continuum. The physically short crack regime is therefore the transition stage between a continuum and the behaviour of single grains.

When one looks at the growth behaviour of a short crack, it is very different from that of a long crack. Crack growth is defined as the increase in crack length per cycle: *da/dN*. Short cracks grow much faster than long cracks and at lower stress intensity factor values. Therefore, short crack growth data can not be plotted in a single curve, because there is more scatter, as can be seen in Fig. 2.2.4 (Taylor, 2002).

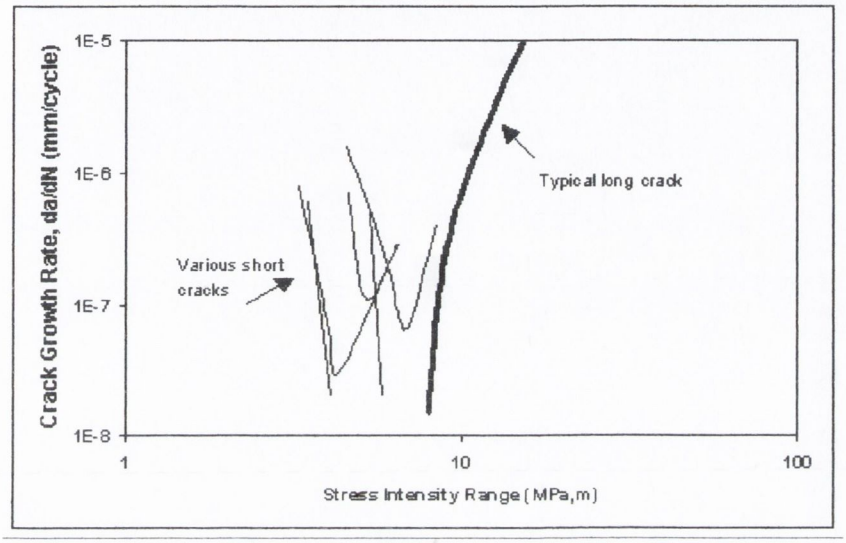

Fig. 2.2.4 Short crack vs. long crack growth behaviour (Taylor, 2002)

2.2.4 Crack Closure

Among researchers, crack closure is believed to be one of the most important causes for the difference in long and short crack growth behaviour. Crack closure is the effect that the crack faces touch prematurely, whilst the applied stress intensity is still larger than zero. The crack faces do not open at K_{min}, but at the higher K_{op}, the opening threshold value. This mechanism results in an effective stress intensity range, ΔK_{eff}, which is smaller than ΔK, see Fig. 2.2.5.

It is assumed that the part of the cycle between K_{min} and K_{op} where the crack is closed, does not contribute to the crack growth and that crack growth can be described by the effective threshold, ΔK_{eff}:

$$\Delta K_{eff} = K_{\max} - K_{op} \qquad (2\text{-}2\text{-}2)$$

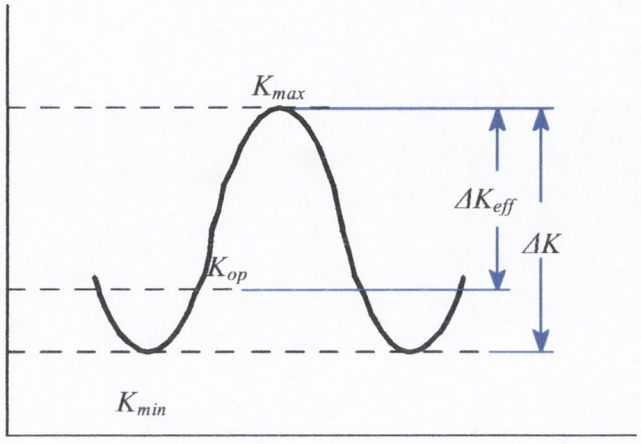

Fig. 2.2.5 Crack closure

Elber's plasticity induced crack closure mechanism assumes that crack closure is caused by the plastic wake of the crack (Elber, 1970). When a crack grows, the plastic zone at the tip moves along with it, leaving a wake behind where residual compressive stresses are found, see Fig. 2.2.6. These compressive stresses cause the crack faces to close prematurely, before the minimum stress intensity factor is reached.

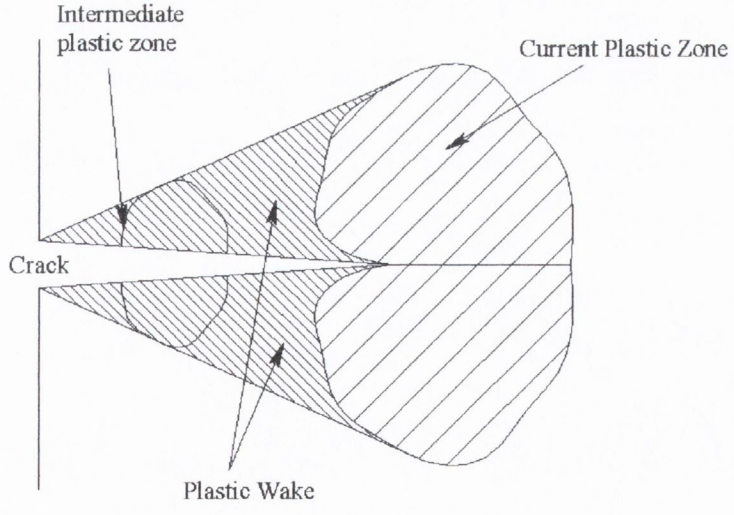

Fig. 2.2.6 The plastic wake of a crack

The reason why short cracks grow faster is simply because the closure effect does not interfere with short crack growth as much as with long crack growth. A crack that has just been initiated will show no crack closure behaviour, because the compressively stressed wake has not yet been developed. Crack closure reduces crack growth rates. The longer the crack becomes, the more closure occurs and the slower the crack grows, until a constant closure value is reached for long crack growth.

Fig. 2.2.7 (Yu et al, 1998) shows how the opening stress, K_{op}, changes with crack length for a loading ratio of –1. Initially, the opening stress is negative, but it increases with increasing crack length until the constant long crack value is reached. σ_a is the stress amplitude, Δc is the total crack extension from a pre-crack and ω_i is the initial plastic zone size.

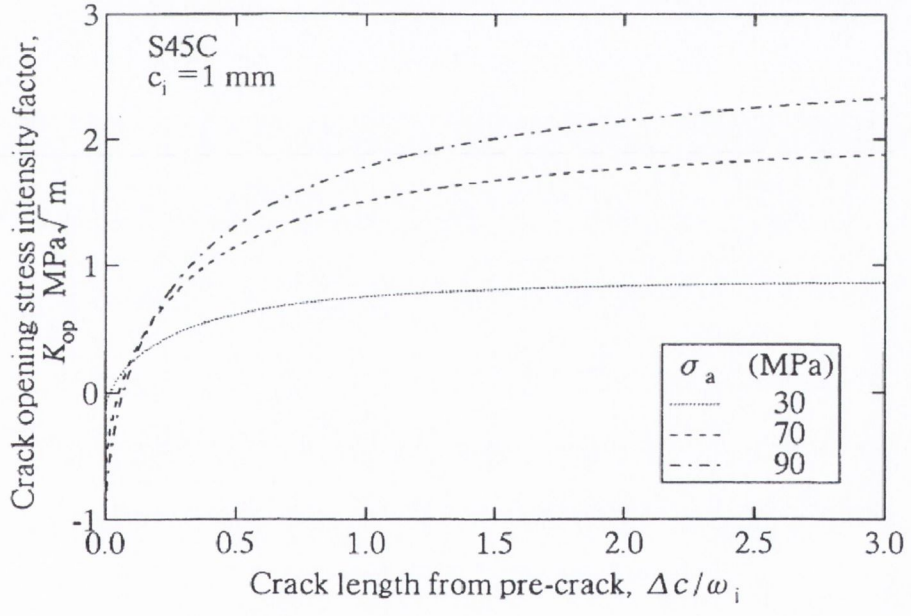

Fig. 2.2.7 Change of K_{op} with crack length (Yu et al, 1998)

Initially it was believed that crack closure only occurred in the compressive part of the loading cycle. Elber (Elber, 1970) argued through his experimental data, that closure also occurs under fully tensile loading ($\sigma_{min}/\sigma_{max} \geq 0$). It is assumed that there is *no* closure when the ratio of the minimum stress over the maximum stress is larger than about 0.6.

Since the publication of Elber's work in 1970, researchers have discovered other crack closure mechanisms, e.g. oxide-induced closure, roughness induced closure, fluid induced closure, crack deflection and crack bridging. Roughness induced closure could also be especially important in the short crack regime, because it might not happen at short crack lengths.

2.2.5 Short cracks in microscopic components

Fatigue research on microscopic components is still in its infancy. There are many difficulties that arise with testing of small specimens and components and not many experimental results are available in this area. This section discusses some of the data that is available on the micro-scale area.

Fig. 2.2.8 shows the influence of nanometre-sized notches on the fatigue results of *single crystal* silicon of the order of micrometers in bending for two applied loads; 50 and 100 mN (Minoshima et al, 2000). The silicon crystal behaves elastically until it finally fails in a brittle manner. The circular data point in the upper left corner does not have a negative notch depth. It is shifted to the left, because otherwise it would coincide with the squared data point. Both data points represent crystals with a notch depth of 0 nm.

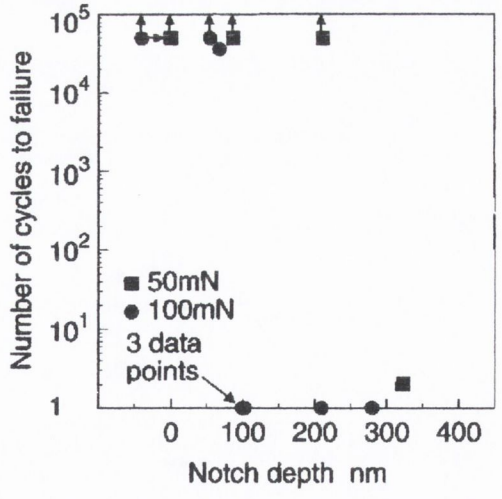

Fig. 2.2.8 Fatigue strength as a function of notch depth (Minoshima et al, 2000)

Until a certain notch depth, the life of the single crystal is longer than 5 x 10^4 cycles, but when the notch depth reaches a threshold value, the fatigue strength decreases dramatically to one cycle to failure; *static* failure. This threshold notch depth decreases with an increasing load. From this data it seems that the single crystal will either not fail at all in the range of 1-5 x 10^4 cycles to failure, or fail in the first cycle, depending on the depth of the notch. This is quite unusual, because normally for fatigue in macroscopic specimens, this change is not as drastic.

Another set of experimental data on specimens of a few μm thick is by Sharpe and Bagdahn (2002). Unlike Minoshima et al (2000), Sharpe and Bagdahn concluded that their polysilicon microscopic material shows a stress-life curve similar to that of metals.

The final example of microscopic fatigue data is that of Hong and Weil (1996). They compared the *microscopic* low cycle fatigue behaviour of thin copper foil to that of the *macroscopic* wrought copper material, see Fig. 2.2.9.

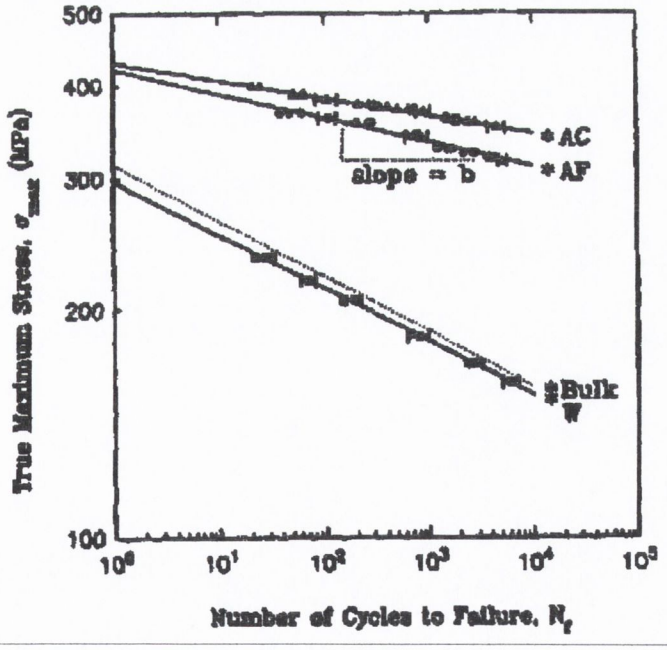

Fig. 2.2.9 Fatigue strength of macro vs. micro copper (Hong and Weil, 1996)

The macroscopic copper material had a larger grain size than the microscopic material, respectively 15 μm and 1 μm. Taking this difference in grain size into account, Hong and Weil stated that the difference between the graph of the bulk copper, *Bulk W*, and the two types of thin foils, *AC* and *AF*, is small. They concluded that the thickness only has a small effect on the fatigue properties under stress control.

It is clear that more work needs to be done in the micro-scale area. Fatigue results are mostly focussed on *MEMS* devices, which are only a few μm thick. This corresponds to a few grains along the net section. The interesting aspect of the present work is therefore, to investigate if continuum mechanics can still be used when there are only a few grains present in a specimen or component. In this work the influence of the separate grains and the mechanisms behind failure will therefore be ignored. These mechanisms can however play an important role and should therefore be investigated further in the future.

2.3 Traditional fatigue failure prediction approaches

Several fracture mechanics based prediction methods were developed to predict the cracking behaviour of the experimental data discussed in the previous section.

2.3.1 The Stress Life Approach

The Stress Life approach determines the fatigue life of a component, by reducing the un-notched, plain specimen fatigue limit by the parameter K_t that expresses the severity of the stress concentration:

$$\Delta\sigma_{on} = \frac{\Delta\sigma_o}{K_t} \qquad (2\text{-}3\text{-}1)$$

where $\Delta\sigma_{on}$ is the prediction for the notched specimen fatigue limit and $\Delta\sigma_o$ is the experimental plain specimen fatigue limit. The value for the theoretical elastic stress intensity factor K_t can be obtained from handbooks (Peterson, 1953; 1974).

Finite Element Analysis (FEA) was not used when the Stress Life method was first developed. Nowadays, FEA is a convenient tool in Fracture Mechanics based analyses. The parameter K_t can be calculated easily through FEA by determining the stress at the root of the notch, σ_{notch}, and dividing it by the nominal stress, $\sigma_{nominal}$:

$$K_t = \frac{\sigma_{notch}}{\sigma_{nominal}} \tag{2-3-2}$$

Since the Stress Life method is based on the theoretical elastic stress concentration factor K_t, it should only be used when there is no considerable plastic deformation present in the material. The method works well for blunt notches, but if a notch becomes sharper, the stress life approach tends to be somewhat conservative, because of the increasing amount of plastic deformation in the material.

2.3.2 The Strain Life Approach

The Stress Life approach works well for blunt notches in the high cycle fatigue regime where there is mostly elastic strain. In the low cycle fatigue region, the influence of plastic strain is large and can no longer be ignored. The Strain Life approach relates the local strain at the root of the notch to that of the un-notched material. Therefore, as well as the un-notched, smooth material strain life behaviour, the stress-strain relation at the root of the notch needs to be determined. The Neuber rule can be used to describe the stress-strain behaviour at the notch root:

$$K_t = \sqrt{K_\sigma K_\varepsilon} \tag{2-3-3}$$

The strain concentration factor, K_ε, is defined as the ratio of the maximum strain at the stress concentration over the nominal strain. When yielding occurs, Hooke's law is no longer valid, and K_ε increases with respect to K_t. The theoretical elastic stress concentration factor for a plastic deformation situation can be approximated as the mean of the strain concentration factor, K_ε, and the stress concentration factor, K_σ, where K_σ is the ratio of the maximum stress at the stress concentration over the nominal stress.

Elastic-plastic Finite Element Analysis could be used to determine the strain concentration factor, however, the results of an elastic-plastic analysis are not always satisfactory. In general, the strain life approach does not work for sharp notches.

2.4 Fracture Mechanics approaches for fatigue failure prediction

2.4.1 The Smith and Miller approach

The Stress Life method works well for blunt notches, but is conservative for cracks and sharp notches. Smith and Miller (1978) avoid this problem by distinguishing two notch regimes, see Fig. 2.2.1: the blunt notch, or, *notch-like* regime and the sharp notch, or, *crack-like* regime. They showed that predictions can be made for both regimes and that the higher of the two results in the good prediction. Since the traditional Stress Life approach discussed in section 2.3.1 works well for blunt notches, Smith and Miller use this method to make a prediction for blunt notches. The prediction method for cracks and sharp notches is based on the assumption that the behaviour of a sharp notch is similar to that of a crack and therefore, fracture mechanics applies:

$$\Delta\sigma_{on} = \frac{\Delta K_{th}}{F\sqrt{\pi D}} \qquad (2\text{-}4\text{-}1)$$

where ΔK_{th} is the threshold stress intensity factor range. This is simply the standard fracture mechanics equation, however, the crack length has been replaced by notch depth D. When the equivalent stress intensity factor range, ΔK, for a component of arbitrary geometry is below the threshold, crack growth is not expected. When the ΔK of a component is above the threshold value, a crack will start to grow and this crack has the potential to cause failure. F is the geometry factor.

The Smith and Miller approach has a limited applicability, because it requires the geometry factor F and a clear notch depth or crack length. Most engineering components are of complex geometry and shape, and have no crack or clearly described notch.

2.4.2 The Crack Modelling Method (CMM)

The limitations of the Smith and Miller method led Taylor and co-workers (Taylor, 1996) (Wang et al, 1999; 2000) to the development of the Crack Modelling Method. This fracture mechanics approach can be used on components without clearly defined notches by modelling the arbitrary stress concentration as a crack. This substitute crack can then be used in conventional fracture mechanics equations.

The Crack Modelling Method (CMM) compares the stress field ahead of an arbitrary stress concentration in a component obtained by Finite Element Analysis (FEA), to a known stress distribution for an ideal centre crack in an infinite plate. The idea is that the fracture mechanics parameters of the ideal centre crack can be used to describe the stress field of the arbitrary stress concentration, because similar stress fields are expected to behave in a similar manner.

A Finite Element model (e.g. ANSYS) is used to obtain a stress-distance curve for a component as a result of an externally applied load. The highest stress generally occurs at the root of the stress concentration and it reduces with the distance ahead of the notch. The path along which the stress distance curve is plotted normally starts at the highest stress and runs perpendicular to the loading direction.

This stress distance curve is then compared to Westergaard's equation (Westergaard, 1939) for the stress distribution ahead of a centre crack of length $2a_w$ in an infinite plate loaded with tensile stress σ_w:

$$\sigma = \frac{\sigma_w}{\sqrt{\left[1-\left(\frac{a_w}{a_w+r}\right)\right]^2}} \qquad (2\text{-}4\text{-}2)$$

where r is the distance ahead of the crack. Parameters a_w and σ_w are varied until a best fit with the *FEA* stress distance curve is obtained.

When both a_w and σ_w are determined, they are put into equation 2-1-1 to obtain a corresponding ΔK value. The assumption is made that the stress field of the component can be described by Westergaard's parameters. Fig. 2.4.1 is a schematisation of the Crack Modelling Method.

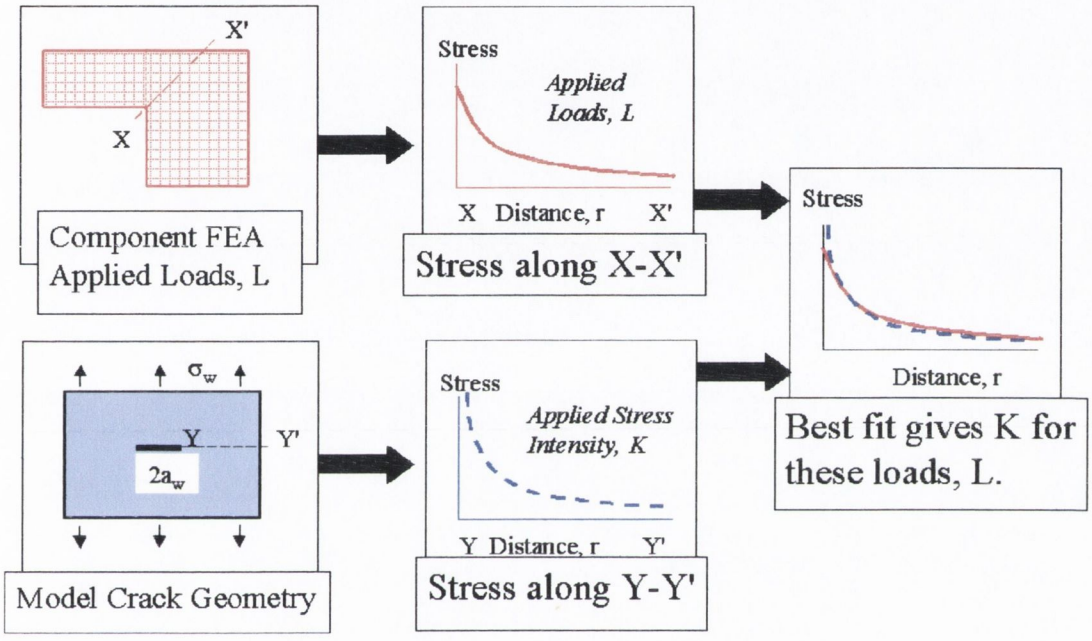

Fig. 2.4.1 Schematic illustration of the CMM

Westergaard's stress intensity factor value is then compared to the threshold value for the material to determine whether failure will occur and what the corresponding fatigue limit for that loading situation will be. The Crack Modelling Method (CMM) is only applicable to cracks or crack-like stress concentrations (i.e. sharp notches). It needs to be used in conjunction with the Stress-Life approach as discussed in section 2.3.1, to cover the blunt notch regime. The highest of the Stress Life and CMM predictions is the actual component prediction.

2.5 Critical Distance approaches for fatigue failure prediction

In some situations, the fatigue life of a component that experiences a very high local stress is not affected as much as would be expected from a traditional Stress Life analysis. The distribution of the stress directly ahead of the stress concentration is of great importance. If there is a very high stress gradient, a high local stress can be reduced within a short distance to a safe level. On the other hand, if the stress gradient is shallow, a lower local stress that is not reduced over a short distance from the stress concentration can be much more dangerous.

With this effect in mind critical volume methods were developed. Instead of using the maximum local stress as an indication of the severity of the notch, the average stress in a specific critical volume surrounding the notch was taken. This average stress may be significantly smaller than the highest stress at the stress concentration.

Simplifications of the critical volume methodology were developed, which consider the average stress over a critical distance or at a critical point close to the stress concentration instead of over a critical volume. The critical volume, distance or point is assumed to be a material property.

2.5.1 The Neuber approach and the Peterson approach

Over the years many researchers have worked on the critical distance theory (Siebel and Stieler, 1955), (Mitchell, 1979) and (Klesnil and Lucas, 1980). The two critical distance approaches that are mostly used in industry because of their simple implementation are Neuber (1958) and Peterson (1959).

The theoretical stress concentration factor K_t is often found to be somewhat conservative in predicting the fatigue strength. Therefore, the fatigue strength reduction factor K_f was introduced. K_f represents the relation between the plain and notched specimen fatigue limits:

$$K_f = \frac{\Delta\sigma_o}{\Delta\sigma_{on}} \tag{2-5-1}$$

The value for K_f as given in equation 2-5-1 can only be determined through experimental data. Neuber and Peterson developed theories to predict the value of K_f. Neuber's relation is given in equation 2-5-2:

$$K_f = 1 + \frac{K_t - 1}{1 + \frac{r_n}{\rho}} \tag{2-5-2}$$

where r_n is an empirically determined characteristic critical length of the material and ρ is the root radius of the notch. A simple description of Neuber's method is that he averages the stress over a critical length ahead of the crack tip and compares it to the critical stress of the material, i.e. to the fatigue limit $\Delta\sigma_o$. However, it is not as simple as that. Neuber's method was developed in the late fifties, where Finite Element analysis was not as common as it is now. Therefore, equation 2-5-2 is an approximation of the stress field at notches and only the root radius and notch depth are required to define the severity of the notch.

Peterson defines his approximation of the K_f relation as follows:

$$K_f = 1 + \frac{K_t - 1}{1 + \frac{r_p}{\rho}} \tag{2-5-3}$$

where r_p is Peterson's empirically determined characteristic critical distance of the material. A simple formulation of Peterson's method is that he determines the stress at a fixed distance ahead of the notch root and compares it to the critical stress of the material. Similar assumptions as for Neuber's method had to be made.

One restriction of these approaches is that the component cannot be of arbitrary geometry, because a root radius is required in equations 2-5-2 and 2-5-3. Another restriction is that, due to the nature of the equations, problems occur when the root radius is equal to zero.

2.5.2 The Theory of Critical Distances (TCD)

The Theory of Critical Distances (Taylor, 1999) is based on general Fracture Mechanics concepts. Taylor pointed out that the critical distance can be determined explicitly for the case of a crack using standard Fracture Mechanics parameters. Assuming that a crack is simply a notch with a root radius equal to zero, this critical distance approach has also been tested on notches, generally resulting in good predictions (Taylor, 2001) (Taylor et al, 2000).

Four different critical distance variations were derived: the Point Method (PM), the Line Method (LM), the Area Method (AM) and the Volume Method (VM). Failure of a component is predicted when the stress at a point (PM), or the average stress over a line (LM), or the average stress over an area (AM), or the average stress over a volume (VM) is greater than the un-notched, plain specimen fatigue limit.

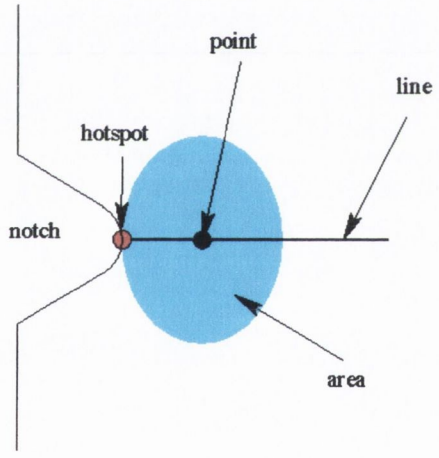

Fig. 2.5.1 Theory of Critical Distances (TCD)

Critical distance, L, was defined as follows:

$$L = \frac{1}{\pi}\left(\frac{\Delta K_{th}}{\Delta \sigma_o}\right)^2 \qquad (2\text{-}5\text{-}4)$$

with the four corresponding critical distance variations, r_c:

Point Method (PM) $$r_c = \frac{1}{2\pi}\left(\frac{\Delta K_{th}}{\Delta\sigma_O}\right)^2 \quad \text{or} \quad \frac{L}{2} \tag{2-5-5}$$

Line Method (LM) $$r_c = \frac{2}{\pi}\left(\frac{\Delta K_{th}}{\Delta\sigma_O}\right)^2 \quad \text{or} \quad 2L \tag{2-5-6}$$

Area Method (AM) $r_c = 1.32L$ (radius) (2-5-7)

Volume Method (AM) $r_c = 1.54L$ (radius) (2-5-8)

The Area Method and Volume Method are not commonly used, because it can be difficult to obtain an average stress over an area or in a volume around the stress concentration. The Point and Line Method are more convenient to use, because a stress-distance plot can easily be obtained from an *FEA* analysis of the component in question. The stress is determined at the critical point or over the critical distance and compared to the fatigue limit. If the stress is below the plain fatigue limit, the design is safe, if it is above, failure will occur.

Tanaka (1983) proposed a similar approach, but did not test his method. Fujimoto and co-workers (Fujimoto et al, 2001) independently presented a reduced version of the TCD approach and named it *The Inherent Damage Zone Model.*

2.6 El Haddad's short crack parameter a_o

Many researchers work with the idea that for the physically short crack regime continuum mechanics should be applicable, provided that a correction is used to take into account the short crack growth behaviour. El Haddad et al (1979) have presented a method to predict short crack behaviour. The focus of their work lies on cracks, so no root radius is required. Good agreement was found between their method and experimental data on steel and aluminium alloys (El Haddad et al, 1980) (El Haddad and Miettinen, 1982).

Short cracks grow faster than long cracks, or, in other words, the short crack behaves as though it is longer than it physically is. The parameter a_o was introduced by El Haddad as an empirical crack length to *extend* the short crack. The stress intensity factor of this effective crack length ($a + a_o$) can be defined as follows:

$$\Delta K = F\Delta\sigma\sqrt{\pi(a+a_o)} \tag{2-6-1}$$

Because the extra crack length a_o is relatively small, it is negligible for long cracks. Equation 2-6-1 will therefore describe both short crack behaviour and long crack behaviour. The assumption was made that it is very easy for a crack to initiate even at low stress ranges. Therefore, at the threshold, above which these initiated cracks or flaws start to propagate, a_o is relatively large in comparison to crack length and the threshold stress intensity factor can be simplified to:

$$\Delta K_{th} = F\Delta\sigma_o\sqrt{\pi a_o} \tag{2-6-2}$$

and rewritten to be:

$$a_o = \frac{1}{\pi}\left(\frac{\Delta K_{th}}{F\Delta\sigma_o}\right)^2 \tag{2-6-3}$$

When geometry factor F is unity, El Haddad's parameter is the same as critical distance L defined by Taylor in equation 2-5-4. El Haddad's method is often found to be somewhat conservative.

The El Haddad short crack parameter can be used in conjunction with long crack fatigue prediction approaches like Smith and Miller's and the Crack Modelling Method (CMM) provided that the component's stress concentration is a clearly defined notch. It was actually Smith (1977) who introduced the idea of a_o, which he called the *intrinsic crack length*, but the concept has become known as the El Haddad short crack parameter a_o.

2.7 Resistance curves

The Resistance-curve method is a Linear Elastic Fracture Mechanics approach, which predicts the fatigue limit at a sharp notch where non-propagating cracks occur. Yates and Brown (1987) based their study of this method on the Kitagawa/Takahashi diagram. Klesnil and Lucas (1972) used a slightly different stress intensity factor for short cracks.

The Resistance-curve describes the stress intensity factor threshold, ΔK_{th}, as a function of crack length a. To determine when and if non-propagating cracks occur and what the corresponding fatigue limit will be, the threshold curve is compared to a ΔK curve. This ΔK curve shows how the stress intensity increases with a as the crack grows from a certain notch geometry for an applied stress range. ΔK_{th} has a constant value for long cracks, but it reduces for short cracks as can be seen in Fig. 2.7.1. Because of the small relative curvature of the threshold line at the point of tangency with the ΔK curve, it is difficult to predict the non-propagating crack length at the fatigue limit with high accuracy.

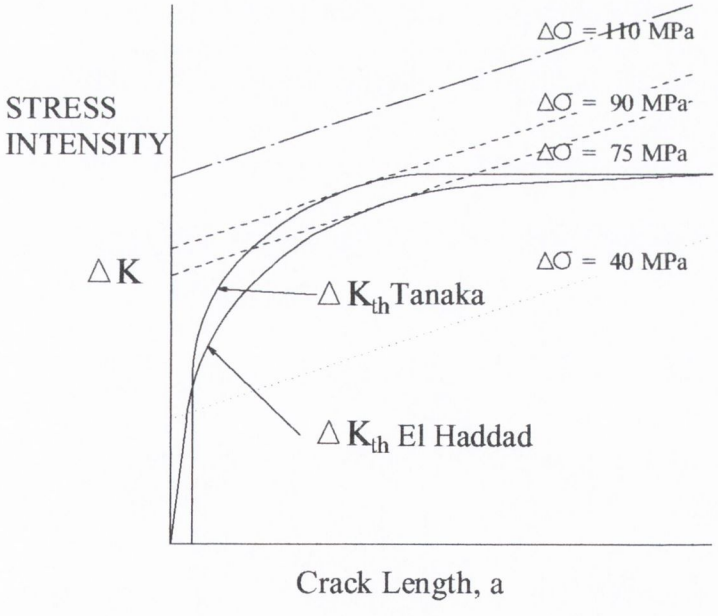

Fig. 2.7.1 El Haddad and Tanaka's Resistance curves

El Haddad's and Tanaka's threshold relations for a fictitious material are shown in Fig. 2.7.1. The dotted, dashed and dash dot lines are ΔK curves for different applied nominal stresses $\Delta\sigma$. Altering the loading conditions for the same specimen geometry shifts the ΔK curve upwards or downwards.

Assuming that a crack will not grow until its applied stress intensity value rises above the threshold value, several situations can occur. When the applied ΔK curve is above the threshold curve, the dash dot line in Fig. 2.7.1 with an applied $\Delta\sigma$ of 110 MPa, a crack will keep on growing until failure occurs. When the applied ΔK line is tangent to the threshold curve, the dashed lines in Fig. 2.7.1, the applied stress for that specific geometry is considered to be the fatigue limit and the corresponding crack length the maximum non-propagating crack length. When the ΔK curve starts above the threshold curve, but crosses over at a certain crack length, the crack will stop growing and becomes non-propagating, the dotted line in Fig. 2.7.1 with an applied stress of 40 MPa. The length at which the ΔK line crosses the threshold curve is the length of the corresponding non-propagating crack for that particular geometry and applied stress range.

2.7.1 El Haddad's Resistance-curve relation

Equation 2-7-1 describes the threshold relation according to El Haddad (El Haddad et al., 1979; 1980), as discussed in section 2.6. This equation corresponds to the threshold curve shown in Fig. 2.7.1:

$$\Delta K_{thEH} = \sqrt{\frac{a}{a + a_o}}\,\Delta K_{th} \qquad (2\text{-}7\text{-}1)$$

where ΔK_{thEH} is El Haddad's threshold value which changes with crack length and ΔK_{th} is the constant threshold value for long cracks.

2.7.2 Tanaka's Resistance-curve equation

Tanaka and co-workers (Tanaka, 1983), (Tanaka and Nakai, 1983; 1984) (Akiniwa et al, 1996) have proposed a model for the threshold curve which is based on the effective stress intensity factor for long cracks, ΔK_{effth}. This approach takes the crack closure effect into account. Tanaka defined 2 characteristic length parameters; c_o and c_2. When a crack is longer than c_2, the crack is a long crack (crack closure is constant) and length c_o is roughly the distance to the first microstructural boundary, see equation 2-7-5. The threshold curve that was shown in Fig. 2.7.1, is a combination of equations 2-7-2, 2-7-3 and 2-7-4:

$$K_{opth} = 98.8\sqrt{a - c_o} \qquad \text{for} \qquad c_o \le a \le c_2 \tag{2-7-2}$$

$$K_{opth} = K_{opth\omega} \qquad \text{for} \qquad c_2 \le a \tag{2-7-3}$$

$$K_{maxth} = K_{opth} + \Delta K_{effth} \tag{2-7-4}$$

where K_{opth} is the stress intensity factor at the point where the crack starts to open, which reduces with reducing crack length. $K_{opth\omega}$ is the constant opening stress intensity factor for long cracks. K_{maxth} is the maximum stress intensity factor at the threshold for the applied load range and ΔK_{effth} is the threshold effective stress intensity range for long cracks, also a constant. The constant 98.8 in equation 2-7-2 is an experimentally determined value for the structural carbon steel JIS S45C that Tanaka used in his work. That constant will therefore change with material.

Equations 2-7-2 and 2-7-3 describe the behaviour of K_{opth}, respectively for the short crack regime and for the long crack regime. Equation 2-7-5 defines length parameter c_o:

$$c_o = \frac{1}{\pi}\left(\frac{\Delta K_{effth}}{1.122\Delta\sigma_o}\right)^2 \tag{2-7-5}$$

where 1.122 is the value for the geometry factor for an edge crack. Length parameter c_o is similar to El Haddad's parameter a_o for an edge crack, but Tanaka uses the effective

threshold, ΔK_{effth}, instead of the long crack threshold, ΔK_{th}. Parameter c_2 represents the length where the long crack threshold takes over, or, where equations 2-7-2 and 2-7-3 are equal.

Tanaka assumes that even at very low stresses, cracks will grow until they are stopped by the first micro structural boundary, e.g. the grain boundary, at a distance of roughly c_o. In other words, there is no substantial resistance against crack growth until the crack reaches the first boundary, i.e. $\Delta K_{th} = 0$, as shown by Tanaka's threshold curve in Fig. 2.7.1.

2.8 A micro-scale approach: The Suo/KK method

The Suo/KK approach was not developed as a fatigue approach, but as a static fracture prediction method for ceramics with notches by Suo (Suo et al., 1993). It was studied further by Keith and Kedward (1997), who emphasized the importance of finite specimen size. This method can therefore be used on micro-scale components. Since both research groups have made important contributions to this method, it will be referred to as the Suo/KK-method.

The prediction for *static* failure at the gross section, $\sigma_{onGROSS}$, is determined by dividing the *static* tensile strength by a term that defines the severity of the notch:

$$\sigma_{onGROSS} = \frac{\sigma_o}{\sqrt{\left(1-\frac{a}{w}\right)^{-2} + \pi a F^2 \left(\frac{\sigma_O}{K_C}\right)^2}} \qquad (2\text{-}8\text{-}1)$$

where σ_o is the static tensile strength for a plain specimen, w is the width of the specimen and K_C is the fracture toughness. Substituting typical static failure parameters by fatigue parameters can make the method applicable to fatigue, see section 3.3.

2.9 The influence of notches on the tensile behaviour of components

This section discusses the influence of notches on the tensile behaviour of a material. When a notch is introduced in the material, the material is expected to be weaker, resulting in a failure stress that is lower than the *UTS* of the material. However, when there is a tri-axial stress state in the material (constraint), the failure stress of the notched specimen can be found to be *higher* than the *UTS*. This effect is known as *notch strengthening*.

Notch strengthening is a theory about the increase of the yield strength. It only occurs for specific notches; usually for a circumferential notch in a cylindrical specimen. The increase of failure stress is due to the constraint caused by the notch, which results in a situation more like plane strain than plane stress in the net section of the specimen. The material at the root of the notch wants to contract when it reaches the yield stress, however, it is constrained by the rest of the material that is still behaving elastically. Because of the tensile stresses in the other two principal directions, the axial stress to initiate plastic deformation is increased. The deeper the notch, the greater the plastic constraint will be (Andrews and Gibson, 2001) (Huang et al, 1996).

2.9.1 Tensile behaviour in microscopic specimens or components

Since fatigue properties have been found to change with specimen size, it is interesting to investigate the tensile properties at the microscopic level.

Hong and Weil (1996) have compared the tensile properties of macro and micro copper foils. Table 2.9.1 gives a summary of the tensile properties of these foils. Two copper micro foils were specified, because they were manufactured in a slightly different manner. The grains in the macro material were 15 times larger than those in the micro material.

Table 2.9.1 Tensile properties of copper foils (Hong and Weil, 1996)

	Micro 1 Grain size: 1 μm	**Micro 2** Grain size: 1 μm	**Macro** Grain size: 15 μm
0.2 % Proof stress [MPa]	262	315	85
True UTS [MPa]	392	426	275
Fracture strain [%]	13	12	30

The micro material has a substantially higher proof strength and *UTS*, but a lower strain to failure than the macro material. Hong and Weil attributed the higher strength of the micro material to *higher dislocation densities*, *twin densities* and *small grains*. Both the micro and the macro material showed necking before failure.

Minoshima et al (2000) have investigated the influence of nanometre sized notches on single crystal silicon microelements. They found that single crystals are sensitive to notches, even to notches in the range of hundreds of nm. The fracture strength decreased as a result of these notches, see Fig. 2.9.1. The un-notched single crystals showed significant scatter as can be seen for a notch depth of 0.

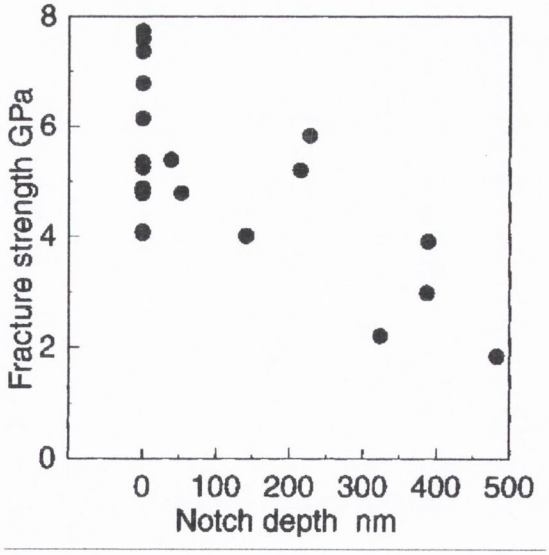

Fig. 2.9.1 Fracture data for silicon single crystals (Minoshima et al, 2000)

2.10 Concluding remarks

One of the aims of this work is to investigate whether continuum mechanics can be applied to situations where there are not enough grains to form a continuum, e.g. microscopic components. Therefore, this chapter has taken the continuum mechanics point of view on crack behaviour and prediction methods. The underlying fracture mechanisms, e.g. dislocation theory, have been ignored in this work, but these mechanisms should be investigated in the future.

Even though some work has been done in the microscopic area, this has not resulted in a variety of prediction theories directly applicable to microscopic components. Chapter 3 will discuss ideas to alter existing prediction methods (based on long cracks in macroscopic components) to apply to short cracks and micro-scale specimens.

Chapter 3 Adapting fatigue methods to apply to short cracks and micro-scale specimens

This chapter discusses several ideas to adapt the existing macro fatigue prediction methods to apply to short cracks and micro-scale components. The proposed short crack and micro-scale corrections can be divided into two groups:

- Applying a correction factor to the long crack prediction value (applicable to *Smith and Miller* and to the *Crack Modelling Method*)
- Reducing the threshold value, ΔK_{th}, which is constant for long cracks (applicable to the *Smith and Miller method* and to the *Theory of Critical Distances*)

The Suo/KK approach, which is a micro-scale static failure method and does therefore not require a short crack correction factor, is made applicable to fatigue in section 3.3.

3.1 Short crack corrections to be applied to the long crack prediction

The first approach to making a short crack correction to micro-scale components is to apply a correction factor to the long crack prediction value.

3.1.1 The El Haddad short crack correction

El Haddad's short crack parameter a_o, which was discussed in section 2.6, can be used to make the *Smith and Miller* and the *CMM* applicable to short cracks (Wang, 1999) (Taylor and Wang, 2000). The short crack correction factor, scc_{EH}, in equation 3-1-1 has to be applied to the conventional prediction value based on the long crack parameters:

$$scc_{EH} = \sqrt{\frac{a}{a + a_o}} \qquad (3\text{-}1\text{-}1)$$

For crack-like notches a is equal to the notch depth.

The problem with this approach, as mentioned before, is that in order to calculate a_o, the notch depth or crack length is required. For most engineering components no clear notch depths can be distinguished and therefore, this short crack correction can only be used in limited situations.

3.1.2 The Westergaard short crack correction

A solution to the problem encountered with the El Haddad short crack correction, that it requires a clearly defined notch depth or crack length, might actually lie within the Crack Modelling Method itself (Wang, 1999) (Taylor and Wang, 2000). The CMM proposes a substitute crack length, a_w, to describe the behaviour of a component of arbitrary geometry with no clear notch depth. One could argue that this a_w could in fact be used as a substitute notch depth or crack length. The short crack correction, scc_w, has to be applied to the long crack prediction value:

$$scc_w = \sqrt{\frac{a_w}{a_w + a_o}} \qquad (3\text{-}1\text{-}2)$$

3.2 Short crack corrections on the basis of a reduced threshold value

A problem with the Theory of Critical Distances (Taylor, 1999), or for that matter any other critical distance approach, is that for micro-scale specimens the critical distance may lie outside the specimen. If that is the case, it is impossible to use the Point Method and the Line Method unless there is a reason to suppose that the critical distance should be reduced in specific situations. Since the critical distance is closely related to the threshold value for the material, this would imply a reduction in the value for ΔK_{th}.

One could make the assumption that the critical distance is related to the non-propagating crack length. The idea behind the Theory of Critical Distances is that by comparing the stress at a critical distance ahead of a stress concentration, one can determine if failure will occur or not. A similar argument can be made for non-propagating cracks. If a crack is longer than the non-propagating crack length, it is assumed to grow until failure occurs, provided that the applied nominal stress remains the same. Therefore, both by looking at the stress at the critical distance and by determining if a crack is non-propagating or not, the decision is made if fatigue failure will occur or not. The next logical step would be to imply that both could be related.

By extension of this logic, it can be argued that the length of a non-propagating crack will be characteristic of the critical distance if it has been shown that the crack has indeed stopped growing. For macro-scale components the non-propagating crack length is constant, but for small specimens the non-propagating crack length reduces, see Tables 3.2.1, 3.2.2 and 3.2.3. This suggests that the critical distance should also be reduced for micro-scale samples.

To obtain more understanding when this reduction of non-propagating crack length occurs, Tanaka's Resistance-curve method, as discussed in section 2.7.2, was studied into more detail. The equations that Tanaka uses to describe the threshold curve (2-7-2, 2-7-3 and 2-7-4) require specific experimental data, therefore, this analysis will be done on the structural carbon steel JIS S45C studied by Tanaka and co-workers (Tanaka and Nakai, 1983; 1984) (Akiniwa et al, 1996). Different combinations of specimen width and notch depth were analysed to understand the influence of the specimen geometry on the non-propagating crack length.

Tanaka defined two important length parameters: c_o and c_2. It is assumed that a crack will always grow until it reaches the first structural boundary of the material, which corresponds to length parameter c_o. Parameter c_2 resembles the crack length where the threshold curve reaches its constant long crack value. El Haddad's Resistance-curve relationship, discussed in section 2.7.1, was also analysed because it only requires standard experimental data and can therefore be used more widely. The difference between El Haddad's and Tanaka's method is that El Haddad's threshold curve is not a material property; it changes with geometry, because a_0 changes with the F factor.

Tables 3.2.1, 3.2.2 and 3.2.3 show the results of an analysis of Tanaka's Resistance curve method to predict the non-propagating crack length as a result of geometry changes: notch depth changes and width changes in respectively a Single Edge Notch Tensile (SENT) specimen, a Centre Crack Tension (CCT) specimen and a Double Edge Notch (DENT) specimen. Each table consists of four sections: section *a)* is a summary of the material properties of Tanaka's material (JIS S45C), section *b)* analyses the change in non-propagating crack length with a changing notch depth at three constant widths, in section *c)* the width is changed for four different constant notch depths and section *d)* analyses geometries that represent micro-scale specimens, i.e. specimens where the width, *w*, is smaller than the long crack non-propagating crack length. Analysing these tables gives an idea of how the non-propagating crack length, and therefore also the critical distance, changes with geometry and size.

Table 3.2.1a) Important material properties required for the JIS S45C material

R	σ_y [MPa]	UTS [MPa]	$\Delta\sigma_o$ [MPa]	c_o [mm]	c_2 [mm]	ΔK_{th} [MPa√m]	ΔK_{eff} [MPa√m]
-1	316	570	446	0.044	0.59	10.52	2.94

Table 3.2.1b) Change in non-propagating crack length with changing notch depth for SENT

Depth D [mm]	**NPC length [mm]**						**Fatigue Limit (net section) [MPa]**					
	El Haddad			Tanaka			El Haddad			Tanaka		
	w=14	w=6	w=1	w=14	w=6	w=1	w=14	w=6	w=1	w=14	w=6	w=1
0.01	0.04	0.035	0.02	c_o	c_o	c_o	360	360	355	435	435	435
0.05	0.08	0.08	0.06	0.05	0.06	0.05	282	284	263	320	320	310
0.1	0.12	0.12	0.07	0.07	0.07	0.06	245	245	210	268	263	235
0.25	0.18	0.17	0.07	0.13	0.13	0.06	192	188	135	200	196	130
0.5	0.24	0.22	0.04	0.31	0.2	0.06	154	145	65	160	148	46
0.75	0.3	0.24	0.02	0.47	0.26	0.06	132	120	25	138	120	14
1	0.32	0.24	N/a	c_2	0.29	N/a	117	102	N/a	123	101	N/a
5	0.29	0.03	N/a	c_2	0.30	N/a	38	8	N/a	38	6	N/a
8	0.15	N/a	N/a	c_2	N/a	N/a	17	N/a	N/a	15	N/a	N/a

Table 3.2.1c) Change in non-propagating crack length with changing width for SENT

Width w [mm]	**NPC length [mm]**								**Fatigue Limit (net section) [MPa]**							
	El Haddad				Tanaka				El Haddad				Tanaka			
	D=2	D=0.75	D=0.5	D=0.1	D=2	D=0.75	D=0.5	D=0.1	D=2	D=0.75	D=0.5	D=0.1	D=2	D=0.75	D=0.5	D=0.1
1	N/a	0.02	0.04	0.07	N/a	0.055	0.06	0.06	N/a	25	65	210	N/a	14	47	235
2	N/a	0.08	0.11	0.09	N/a	0.09	0.09	0.065	N/a	75	112	235	N/a	64	103	260
5	0.12	0.19	0.20	0.12	0.24	0.23	0.18	0.07	50	115	142	242	43	114	144	269
8	0.22	0.24	0.25	0.12	0.46	0.34	0.25	0.07	69	125	150	245	67	128	155	270
14	0.33	0.28	0.26	0.12	c_2	0.48	0.3	0.07	82	130	155	245	87	138	159	270
18	0.40	0.28	0.26	0.12	c_2	0.55	0.32	0.07	86	135	155	245	93	140	160	270
20	0.45	0.28	0.26	0.12	c_2	c_2	0.32	0.07	88	135	155	245	95	142	161	270
25	0.45	0.30	0.26	0.12	c_2	c_2	0.35	0.07	90	135	155	245	98	143	162	270
50	0.50	0.30	0.26	0.12	c_2	c_2	0.35	0.07	92	137	158	245	103	144	162	270

Table 3.2.1d) Change in non-propagating crack for microscopic SENT geometries

Depth D [mm]	**NPC length [mm]**		**Fatigue Limit [MPa]**	
	El Haddad	Tanaka	El Haddad	Tanaka
	w = 0.4	w = 0.4	w = 0.4	w = 0.4
0.05	0.04	c_0	220	245
0.1	0.04	c_0	160	150
0.15	0.03	C_0	118	90

Table 3.2.2a) Important material properties required for the JIS S45C material

R	σ_y [MPa]	UTS [MPa]	$\Delta\sigma_o$ [MPa]	c_o [mm]	c_2 [mm]	ΔK_{th} [MPa$\sqrt{m}$]	ΔK_{eff} [MPa$\sqrt{m}$]
-1	316	570	446	0.044	0.59	10.52	2.94

Table 3.2.2b) Change in non-propagating crack length with changing notch depth for CCT

½ Depth D [mm]	**NPC length [mm]**						**Fatigue Limit (net section) [MPa]**					
	El Haddad			Tanaka			El Haddad			Tanaka		
	w=14	w=6	w=1	w=14	w=6	w=1	w=14	w=6	w=1	w=14	w=6	w=1
0.01	0.04	0.02	0.03	c_o	c_o	c_o	365	370	380	450	450	450
0.05	0.09	0.09	0.07	0.06	0.05	0.06	295	295	290	365	365	350
0.1	0.13	0.14	0.08	0.07	0.07	0.06	258	255	235	300	300	280
0.25	0.20	0.19	0.08	0.15	0.14	0.06	205	205	148	225	222	160
0.5	0.28	0.26	N/a	0.34	0.26	N/a	167	160	N/a	180	174	N/a
0.75	0.34	0.28	N/a	c_2	0.3	N/a	145	137	N/a	159	146	N/a
1	0.40	0.30	N/a	c_2	0.38	N/a	130	117	N/a	144	126	N/a
5	0.26	N/a	N/a	c_2	N/a	N/a	45	N/a	N/a	44	N/a	N/a

Table 3.2.2c) Change in non-propagating crack length with changing width for CCT

Width	**NPC length [mm]**								**Fatigue Limit (net section) [MPa]**							
w	El Haddad				Tanaka				El Haddad				Tanaka			
[mm]	D=2	D=0.75	D=0.5	D=0.1	D=2	D=0.75	D=0.5	D=0.1	D=2	D=0.75	D=0.5	D=0.1	D=2	D=0.75	D=0.5	D=0.1
1	N/a	N/a	N/a	0.09	N/a	N/a	N/a	0.06	N/a	N/a	N/a	235	N/a	N/a	N/a	280
2	N/a	0.08	0.12	0.13	N/a	0.06	0.08	0.06	N/a	78	125	248	N/a	73	130	295
5	0.2	0.26	0.21	0.13	0.12	0.27	0.23	0.07	53	133	168	255	45	141	170	300
8	0.31	0.31	0.29	0.13	0.45	0.41	0.28	0.07	82	142	165	258	85	152	177	300
14	0.48	0.32	0.3	0.13	0.54	c_2	0.36	0.07	95	145	166	258	106	159	180	301
18	0.50	0.32	0.3	0.13	c_2	c_2	0.36	0.07	99	146	167	258	110	160	180	301
20	0.50	0.33	0.3	0.13	c_2	c_2	0.36	0.07	100	146	167	258	112	160	181	301
25	0.50	0.35	0.3	0.13	c_2	c_2	0.39	0.07	101	147	167	258	113	161	181	301
50	0.50	0.35	0.3	0.13	c_2	c_2	0.39	0.07	103	148	167	258	115	162	181	301

Table 3.2.2d) Change in non-propagating crack for microscopic CCT geometries

½ Depth	**NPC length [mm]**		**Fatigue Limit [MPa]**	
D	El Haddad	Tanaka	El Haddad	Tanaka
[mm]	w = 0.4	w = 0.4	w = 0.4	w = 0.4
0.05	0.04	c_o	240	305
0.1	0.04	c_o	175	185
0.15	0.03	c_o	110	55

Table 3.2.3a) Important material properties required for the JIS S45C material

R	σ_y [MPa]	UTS [MPa]	$\Delta\sigma_o$ [MPa]	c_o [mm]	c_2 [mm]	ΔK_{th} [MPa√m]	ΔK_{eff} [MPa√m]
-1	316	570	446	0.044	0.59	10.52	2.94

Table 3.2.3b) Change in non-propagating crack length with changing notch depth for DENT

Depth	**NPC length [mm]**						**Fatigue Limit (net section) [MPa]**					
D	El Haddad			Tanaka			El Haddad			Tanaka		
[mm]	w=14	w=6	w=1	w=14	w=6	w=1	w=14	w=6	w=1	w=14	w=6	w=1
0.05	0.08	0.07	0.09	c_o	0.08	c_o	240	240	240	325	325	325
0.1	0.13	0.13	0.09	0.07	0.07	0.07	210	210	205	267	270	270
0.25	0.19	0.20	0.09	0.15	0.14	0.07	165	165	135	202	202	172
0.5	0.25	0.29	N/a	0.4	0.33	N/a	135	133	N/a	163	162	N/a
0.75	0.32	0.30	N/a	c_2	0.47	N/a	117	116	N/a	145	142	N/a
1	0.38	0.33	N/a	c_2	0.5	N/a	105	102	N/a	133	126	N/a
5	0.38	N/a	N/a	c_2	N/a	N/a	42	N/a	N/a	51	N/a	N/a

Table 3.2.3c) Change in non-propagating crack length with changing width for DENT

Width	**NPC length [mm]**								**Fatigue Limit (net section) [MPa]**							
w	El Haddad				Tanaka				El Haddad				Tanaka			
[mm]	D=2	D=0.75	D=0.5	D=0.1	D=2	D=0.75	D=0.5	D=0.1	D=2	D=0.75	D=0.5	D=0.1	D=2	D=0.75	D=0.5	D=0.1
1	N/a	N/a	N/a	0.09	N/a	N/a	N/a	0.07	N/a	N/a	N/a	205	N/a	N/a	N/a	265
2	N/a	0.09	0.14	0.13	N/a	0.08	0.12	0.07	N/a	76	133	210	N/a	80	139	270
5	0.17	0.28	0.26	0.13	0.18	0.38	0.31	0.07	52	114	134	210	56	140	162	270
8	0.36	0.33	0.26	0.13	0.53	0.38	0.4	0.07	74	117	134	210	91	145	163	270
14	0.50	0.33	0.26	0.13	c_2	c_2	0.4	0.07	80	117	134	210	105	146	163	270
18	0.49	0.33	0.26	0.13	c_2	c_2	0.4	0.07	81	117	134	210	105	146	163	270
20	0.49	0.33	0.26	0.13	c_2	c_2	0.4	0.07	81	117	134	210	105	146	163	270
25	0.5	0.33	0.26	0.13	c_2	c_2	0.4	0.07	82	117	134	210	105	146	163	270
50	0.5	0.33	0.26	0.13	c_2	c_2	0.4	0.07	83	117	134	210	105	146	163	270

Table 3.2.3d) Change in non-propagating crack for microscopic DENT geometries

Depth	**NPC length [mm]**		**Fatigue Limit [MPa]**	
D	El Haddad	Tanaka	El Haddad	Tanaka
[mm]	w = 0.4	w = 0.4	w = 0.4	w = 0.4
0.05	0.05	c_o	225	310
0.1	0.05	c_o	155	210
0.15	0.04	c_o	105	110

The tables do not only show the non-propagating crack length for different geometries, but also the corresponding fatigue limits. The reason is to check whether these fatigue limits make sense or not. It would for instance not be logical if a component gets stronger when a longer notch or crack is introduced. The prediction values found for the geometries that were similar to ones that were analysed by Tanaka and co-workers gave similar predictions as found by Tanaka. It was therefore assumed that the non-propagating crack length analysis would also be realistic.

The root radius of the notch was not taken into account in this analysis, because Tanaka's sharply notched specimens were assumed to be crack-like (ρ=0.04 mm). A brief investigation was done on the influence of the root radius. *FEA* package ANSYS was used to determine the ΔK values at different crack lengths for different root radii. The following range of root radii were investigated: 0.04 - 1 mm. ANSYS gave similar results for the root radius of 0.04

as for the crack-like analysis. Bluntening the root radius to 1 mm only affected the first part of the ΔK curve and this part did not cross with the threshold curve, therefore, the root radius did not affect the results. Obviously, for blunt notches with large root radii, there would be an effect.

The assumption was made that the non-propagating crack length is related to the critical distance. After analysing Tables 3.2.1, 3.2.2 and 3.2.3 it is clear that the non-propagating crack length reduces for certain geometries, e.g. for short notches and for microscopic specimens. Therefore, the critical distance should also be reduced for these geometries. How exactly this should be done still needs to be discussed.

Fig. 3.2.1 shows how one would *expect* the non-propagating crack length to change with geometry size. For instance, the non-propagating crack length would reach the maximum value for macro specimens containing large notches, the right upper part in Fig. 3.2.1. However, for a micro-scale notch in a macro-scale specimen, the non-propagating crack length is expected to be small, the lower right part in Fig. 3.2.1.

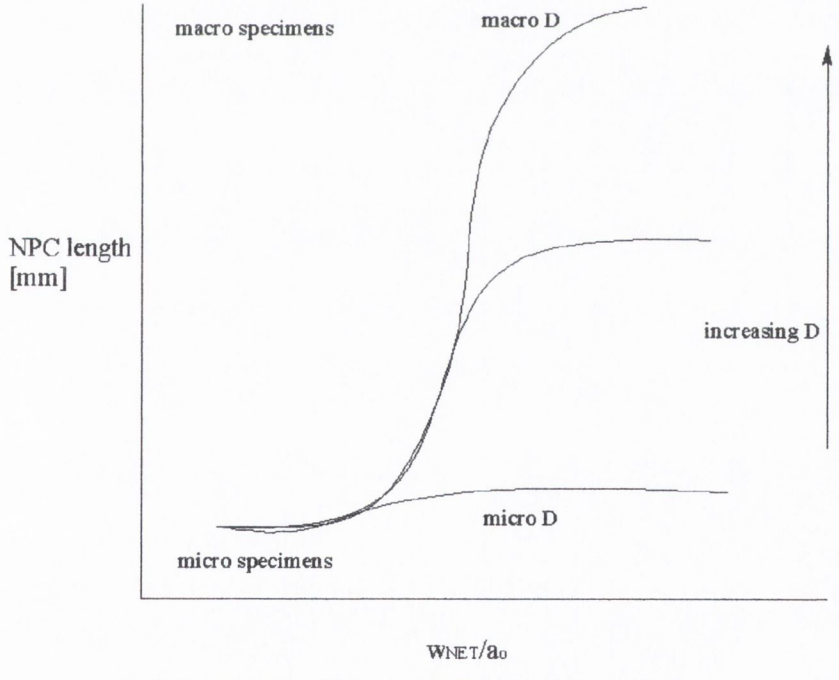

Fig. 3.2.1 Expected relation between specimen size and non-propagating crack length

Fig. 3.2.2 plots the actual data on the effect of the geometry on the non-propagating crack length from Tables 3.2.1, 3.2.2 and 3.2.3. This data should comply with the expected trend that was shown in Fig. 3.2.1. The plots are normalised by dividing the net section width, w_{NET}, by El Haddad's short crack parameter a_o. Parameter c_o is the length of the shortest possible non-propagating crack defined by Tanaka in equation 2-7-5. This minimum non-propagating crack is stopped by the first micro-structural boundary (e.g. grain boundary). Length c_2 is the length of the longest possible non-propagating crack.

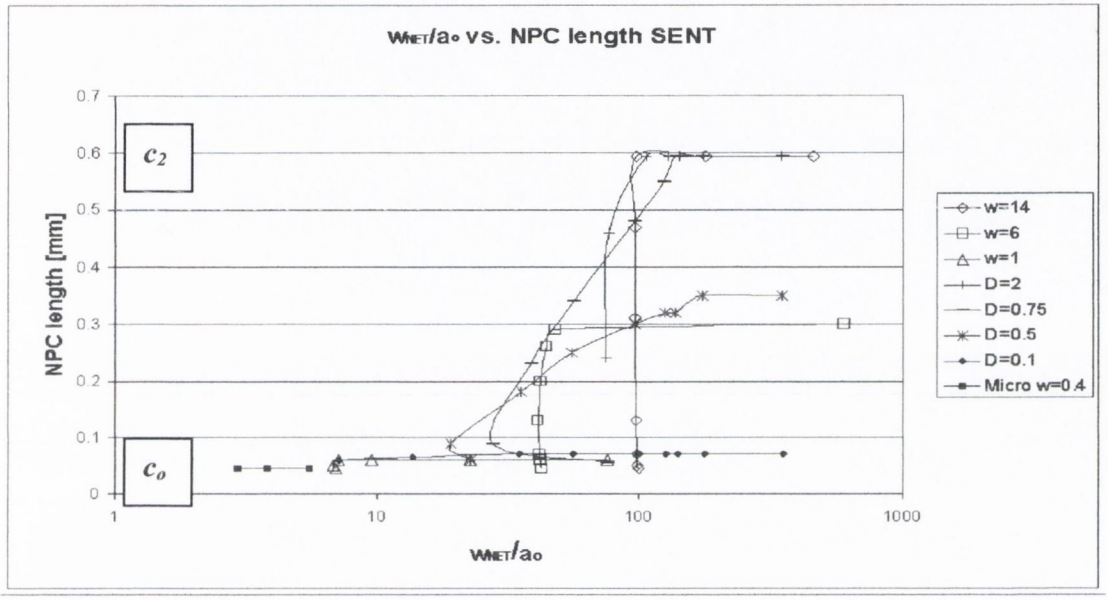

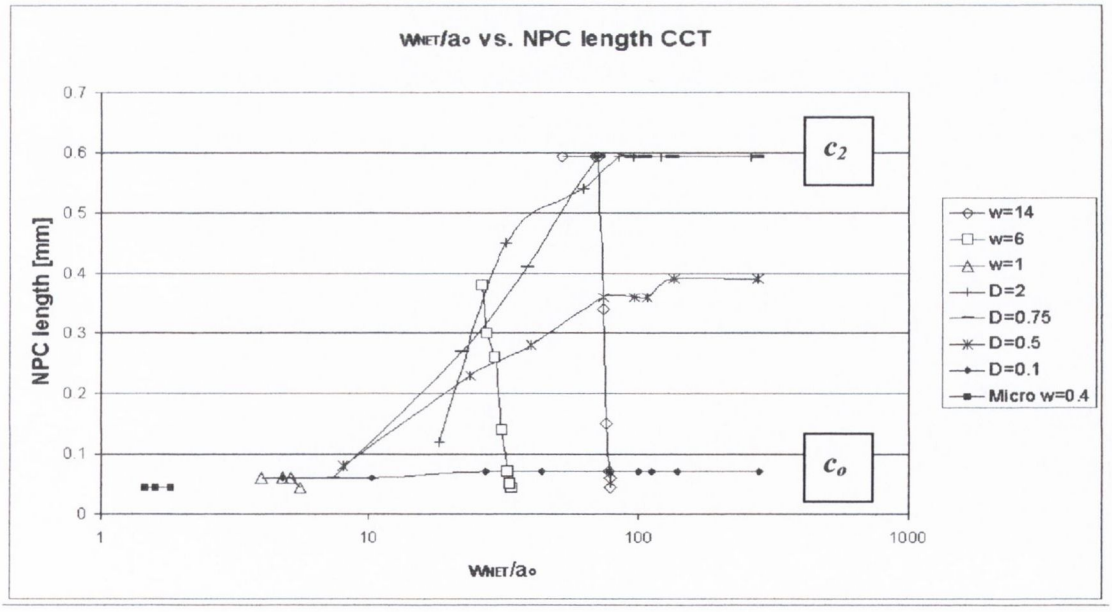

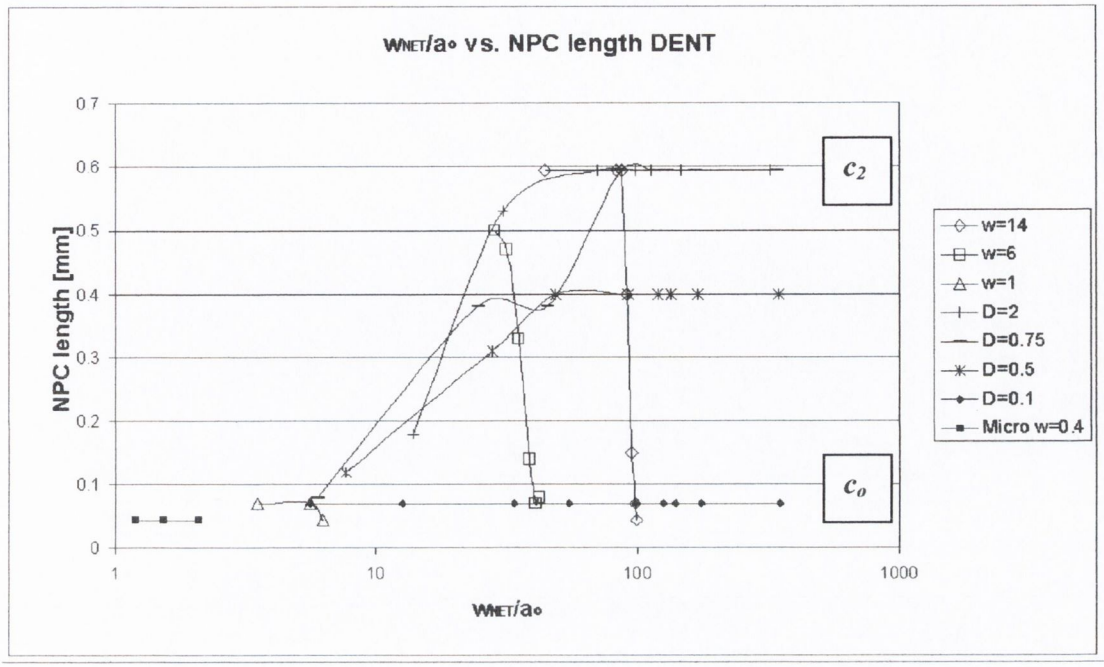

Fig. 3.2.2a) w_{NET}/a_o vs. non-propagating crack length plot for the SENT specimen

b) w_{NET}/a_o vs. non-propagating crack length plot for the CCT specimen

c) $w_{NET}\ a_o$ vs. non-propagating crack length plot for the DENT specimen

Fig. 3.2.2 shows the trend that was expected. The non-propagating crack lengths for most geometries reach either the minimum or maximum values defined by Tanaka: c_o and c_2. Three regimes can be distinguished in the plot. For microscopic specimens and microscopic notches, the corresponding non-propagating crack length is the minimum value c_o. For macroscopic specimens with long cracks, the corresponding non-propagating crack length is the maximum, long crack value c_2. For the remaining geometries, e.g. medium sized notches and medium sized specimens, the corresponding non-propagating crack length will lie in between c_o and c_2.

It is expected that most components will fall either in the regime where the minimum or maximum non-propagating crack length is applicable. The net section widths that were used in this analysis were relatively small, therefore, some in between non-propagating crack lengths were found. The stainless steel micro-scale wire specimens tested in this work, will certainly fall into the regime where the minimum non-propagating crack length c_o is applicable. Assuming that non-propagating crack length and critical distance are related, the

critical distance should also be reduced. In order to calculate critical distance L, the threshold and the plain specimen fatigue limit are required. The plain fatigue limit is a constant, but the threshold is known to reduce with crack length. Therefore, reduced threshold values are expected for the micro-scale specimens.

3.2.1 Reducing the threshold value to fit to the maximum width of the sample

The first proposed approach to reducing the threshold value is by basing it on the width of the sample. Dependent on the length of a crack, it is either long or short. In Fig. 3.2.3 the transition between a long crack and a short crack is defined at length a_c. The net width, w_{NET}, of microscopic components is often smaller than a_c, which means that even if a crack grows to failure, its length is still below critical length a_c. In that situation, it seems strange to use the long crack threshold value, because that value can never be reached. Instead, the reduced threshold value corresponding to the maximum crack length could be used, see Fig. 3.2.3. This reduced threshold parameter will be referred to as: ΔK_{th_width}.

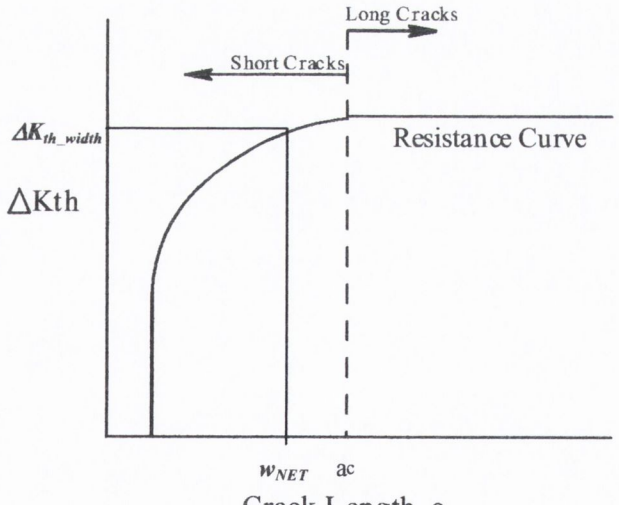

Fig. 3.2.3 Determining the threshold value based on the width of the component

3.2.2 Reducing the threshold value to the value for the effective threshold

The second approach that can be used to reduce the threshold value, is to use the effective threshold of the material. The closure phenomenon does not interfere with short cracks as much as it does for long cracks. The cracks in microscopic specimens are very short, so hardly any closure is expected to occur. The effective threshold value for the material, is the closure-free threshold, ΔK_{effth}.

The effective threshold needs to be determined experimentally. It can be determined by measuring the amount of closure through strain gauges, by measuring changes in electrical potential or by cycling with an R-ratio higher than about 0.6 where no closure is assumed to occur. Tanaka and co-workers state that for most *steels* an initial guess can be made for the effective threshold. It should lie within the range of 2 to 3 MPa$\sqrt{m}$ (Akiniwa et al, 1996).

3.2.3 Reducing the threshold value to the microscopic experimental value

The third proposed reduced threshold value is based on the experimental threshold value for the microscopic specimens, ΔK_{th_exp}. This implies that some data on microscopic specimens is available. It assumes that the threshold is reduced, without implying any particular mechanism for this reduction. Two extreme stress situations need to be tested to be able to calculate ΔK_{th_exp}: a plain specimen (no stress concentration) and a crack-like notched specimen (very severe stress concentration):

$$\Delta K_{th\_exp} = \Delta\sigma_o \sqrt{\pi L_{exp}} \qquad (3\text{-}2\text{-}1)$$

$$\Delta K_{th\_exp} = F\Delta\sigma_{on} \sqrt{\pi(D + L_{exp})} \qquad (3\text{-}2\text{-}2)$$

where L_{exp} is the corresponding critical distance value for the material. The Theory of Critical Distances assumes that the critical distance is a material property, therefore, in equation 3-2-1 for the plain specimen threshold, parameter L is included instead of El Haddad's short crack

parameter a_o. The difference between L and a_o is that no geometry factor is used to calculate L, while a_o is geometry dependent. When micro-scale experimental data is used to calculate the critical distance L, L is effectively the micro-scale critical distance L_{exp}.

The reduced values for the threshold, ΔK_{th_width}, ΔK_{effth} and ΔK_{th_exp}, can be applied to the Smith and Miller method, to the CMM and to the TCD. The R-curve method already uses this reduction in threshold and the Suo/KK method is based on microscopic specimens, therefore, no correction should be used.

3.3 The Suo/KK approach altered for fatigue and compared to Smith and Miller

The Suo/KK method (Suo et al., 1993) (Keith and Kedward, 1997) was originally developed as a static failure approach in ceramics. This method is applicable to microscopic specimens and other specimens where $D<<w$. The approach considers the geometry of the specimen by using the ratio of the crack length to the width of the sample. The method can be altered to apply to fatigue by substituting typical *static* failure parameters by the corresponding *fatigue* parameters.

3.3.1 Adapting the Suo/KK-method to apply to fatigue

Equation 3-3-1 is the original static failure equation for the gross section, as discussed in section 2.8:

$$\sigma_{onGROSS} = \frac{\sigma_o}{\sqrt{\left(1-\frac{a}{w}\right)^{-2} + \pi a F^2 \left(\frac{\sigma_o}{K_c}\right)^2}} \qquad (3\text{-}3\text{-}1)$$

The method was altered to apply to fatigue by substitution of $\sigma_o = \Delta\sigma_o$ and $K_C = \Delta K_{th}$ in equation 3-3-1:

$$\Delta\sigma_{onGROSS} = \frac{\Delta\sigma_o}{\sqrt{\left(1-\frac{a}{w}\right)^{-2} + \pi a F^2 \left(\frac{\Delta\sigma_o}{\Delta K_{th}}\right)^2}} \qquad (3\text{-}3\text{-}2)$$

Combining equation 3-3-2 with the El Haddad threshold equation 2-6-2 ($\Delta K_{th} = F\Delta\sigma_o\sqrt{(\pi a_o)}$) gives the following gross stress fatigue failure prediction:

$$\Delta\sigma_{onGROSS} = \frac{\Delta\sigma_o}{\sqrt{\left(1-\frac{a}{w}\right)^{-2} + \frac{a}{a_o}}} \qquad (3\text{-}3\text{-}3)$$

or, converted to the net section:

$$\Delta\sigma_{onNET} = \frac{\Delta\sigma_o}{\sqrt{1+\frac{a}{a_o}}} \qquad (3\text{-}3\text{-}4)$$

3.3.2 The Suo/KK-method vs. Smith and Miller

When the Smith and Miller method is used in conjunction with the El Haddad short crack correction it is very similar to the Suo/KK approach. Both methods apply a short crack correction; Smith and Miller to the long crack LEFM prediction and Suo/KK to the plain specimen fatigue limit as illustrated in Fig. 3.3.1. Both methods should end up with the same prediction for the notched specimen fatigue limit.

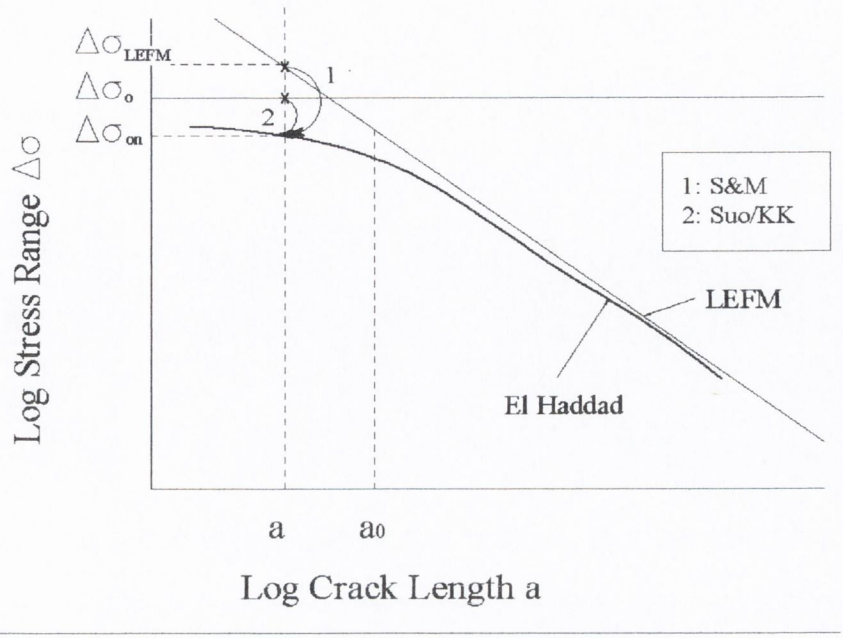

Fig. 3.3.1 Suo/KK vs. Smith and Miller

Assuming that the net stress and the gross stress are equal (macro-scale component, where $a<<w$), the following equations apply to a component with a crack or a crack-like notch:

$$\Delta\sigma_{onLEFM} = \frac{\Delta K_{th}}{F\sqrt{\pi a}} \tag{3-3-5}$$

$$\Delta\sigma_{on} = \frac{\Delta K_{th}}{F\sqrt{\pi(a+a_o)}} \tag{3-3-6}$$

$$\Delta\sigma_{o} = \frac{\Delta K_{th}}{F\sqrt{\pi a_o}} \tag{3-3-7}$$

where $\Delta\sigma_{onLEFM}$ is the long crack prediction value. Equation 3-3-6 is the basis of the Smith and Miller prediction method for short cracks. In some situations it is convenient to rewrite the Smith and Miller short crack equation into the form where the El Haddad short crack correction is applied to the long crack prediction, $\Delta\sigma_{onLEFM}$, similar to short crack correction 1 illustrated in Fig. 3.3.1:

$$\Delta\sigma_{on} = \Delta\sigma_{onLEFM}\sqrt{\frac{a}{a+a_o}} \qquad (3\text{-}3\text{-}8)$$

Suo/KK apply a short crack correction to the plain specimen fatigue limit, instead of to the long crack *LEFM* value. To be able to compare Smith and Miller to Suo/KK, the *LEFM* stress has to be substituted by the plain specimen fatigue limit. Combining equations 3-3-6 and 3-3-9 results in equation 3-3-10, which is illustrated in Fig. 3.3.1 as short crack correction 2:

$$\Delta K_{th} = \Delta\sigma_o\sqrt{\pi a_o} \qquad (3\text{-}3\text{-}9)$$

$$\Delta\sigma_{on} = \Delta\sigma_o\sqrt{\frac{a_o}{a+a_o}} \qquad (3\text{-}3\text{-}10)$$

Equation 3-3-10 is identical to the Suo/KK equation stated in equation 3-3-4. Therefore, when the gross stress is equal to the net stress, the Smith and Miller and the Suo/KK methods are identical. The geometry factor is cancelled out in the substitution process, assuming that it does not change with crack length. This assumption is valid when the crack length is much smaller than the specimen width.

The next step is to analyse the situation where the gross stress is different from the net stress. The different stresses subsequently result in different geometry factors and different a_o values for the gross and the net area:

$$\Delta\sigma_{onGROSS} = \Delta\sigma_o\sqrt{\frac{a_{oGROSS}}{a+a_{oGROSS}}} \qquad (3\text{-}3\text{-}11)$$

$$\Delta\sigma_{onNET} = \Delta\sigma_o\sqrt{\frac{a_{oNET}}{a+a_{oNET}}} \qquad (3\text{-}3\text{-}12)$$

where $\Delta\sigma_{onGROSS}$ is the gross section prediction and $\Delta\sigma_{onNET}$ the net section prediction and

a_{oGROSS} and a_{oNET} are respectively the gross section a_o value and the net section a_o value. Combining equations 3-3-11 and 3-3-12:

$$\frac{\Delta\sigma_{onNET}}{\Delta\sigma_{onGROSS}} = \frac{\sqrt{\frac{a_{oNET}}{a + a_{oNET}}}}{\sqrt{\frac{a_{oGROSS}}{a + a_{oGROSS}}}} \tag{3-3-13}$$

The stress intensity factor at the gross section is equal to that at the net section:

$$F_{NET}\sqrt{a_{oNET}} = F_{GROSS}\sqrt{a_{oGROSS}} \tag{3-3-14}$$

rewriting equation 3-3-14 gives:

$$a_{oGROSS} = a_{oNET}\left(\frac{F_{NET}}{F_{GROSS}}\right)^2 \tag{3-3-15}$$

The combination of equation 3-3-15 with equation 3-3-13 provides the following ratio for net/gross stress predictions:

$$\frac{\Delta\sigma_{onNET}}{\Delta\sigma_{onGROSS}} = \sqrt{\frac{1 + \frac{a}{a_{oNET}\left(\frac{F_{NET}}{F_{GROSS}}\right)^2}}{1 + \frac{a}{a_{oNET}}}} \tag{3-3-16}$$

The difference between the gross prediction and the net prediction can be expressed as the difference in geometry factors. When analysing equation 3-3-16 for a long crack, $a >> a_{oNET}$, the ratio of the conversion is equal to the ratio of the geometry factors as can be seen in Table 3.3.1.

Table 3.3.1 Applicability of equation 3-3-16 to a long crack and a short crack

Equation 3-3-16: $a >> a_{oNET}$	$\frac{\Delta\sigma_{onNET}}{\Delta\sigma_{onGROSS}} = \frac{F_{GROSS}}{F_{NET}}$
Equation 3-3-16: $a = a_{oNET}$	$\frac{\Delta\sigma_{onNET}}{\Delta\sigma_{onGROSS}} = \sqrt{\frac{1+\left(\frac{F_{GROSS}}{F_{NET}}\right)^2}{2}} \langle \frac{F_{GROSS}}{F_{NET}}$

For short cracks, where $a = a_{oNET}$, the conversion is not the same as the ratio of the geometry factors, it is actually smaller. So, for small notches, you get a different prediction, depending on whether you use the net or gross section. The Smith and Miller approach in combination with El Haddad's a_o factor gives the same predictions as Suo/KK provided that the net section stresses are used.

El Haddad's approach has a problem in the situation where the crack length is similar to the width of the specimen. In that situation the solution is not unique, the net stress and gross stress differ from each other, resulting in different geometry factors and a_o values. The Kitagawa/Takahashi diagram in Fig. 3.3.2 illustrates that it is possible that a crack or notch of length a_{oNET} is short using net stresses and long using gross stresses.

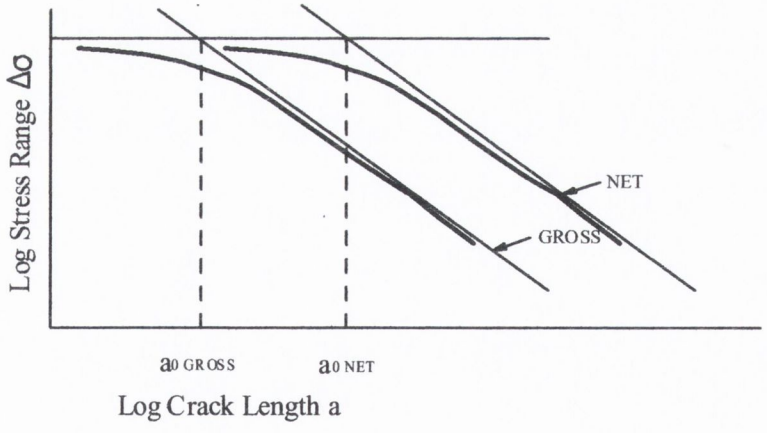

Fig. 3.3.2 Kitagawa/Takahashi plot of a crack that is both long and short

3.4 Concluding remarks

In the previous Chapter 2, several prediction methods were discussed. Most methods will be used to analyse the experimental data on the microscopic specimens. The only methods that will not be used are the Strain Life method and Neuber's and Peterson's critical distance approaches. The Strain Life method will not be used, because it does not work well for sharp notches. Neuber's and Peterson's approaches are approximations, because Finite Element Analysis was not available at that time. Therefore, the Theory of Critical Distances will be used, which is partly based on *FEA*. Table 3.4.1 gives a summary of all the methods that will be used, including the short crack and micro-scale correction factors that were proposed in this chapter.

Table 3.4.1: Prediction methods to be used in this work

METHOD	CORRECTION FACTOR
Stress Life	**none**
Smith and Miller	**- scc a_o (based on El Haddad)** **- scc a_w (based on Westergaard en El Haddad)** **- ΔK_{th_width} (based on the width of the specimen)** **- ΔK_{effth} (based on the closure-free threshold)** **- ΔK_{th_exp} (based on microscopic experimental data)**
CMM	**- scc a_o (based on El Haddad)** **- scc a_w (based on Westergaard en El Haddad)** **- ΔK_{th_width} (based on the width of the specimen)** **- ΔK_{effth} (based on the closure-free threshold)** **- ΔK_{th_exp} (based on microscopic experimental data)**
TCD	**- ΔK_{th_width} (based on the width of the specimen)** **- ΔK_{effth} (based on the closure-free threshold)** **- ΔK_{th_exp} (based on microscopic experimental data)**
Resistance curve method (El Haddad)	**none**
Suo/KK	**none**

Chapter 4 Experimental Details

One of the main objectives of this work was to obtain experimental data on 316L stainless steel microscopic specimens. This is the material from which certain stents are manufactured using a laser process. The laser cuts away excess material from a piece of tubing to create a stent, which consists of a number of repeating units. These repeating units are different for different types of stents. Fig. 4.1.1 shows an example of a stent and a magnification of part of the stent to illustrate the stress concentrations that reduce the fatigue strength of the component. After laser cutting, the stent is annealed to obtain a regular grain structure, followed by an electro polishing process to improve the surface quality of the stent and remove the influence of the laser cutting process on the material.

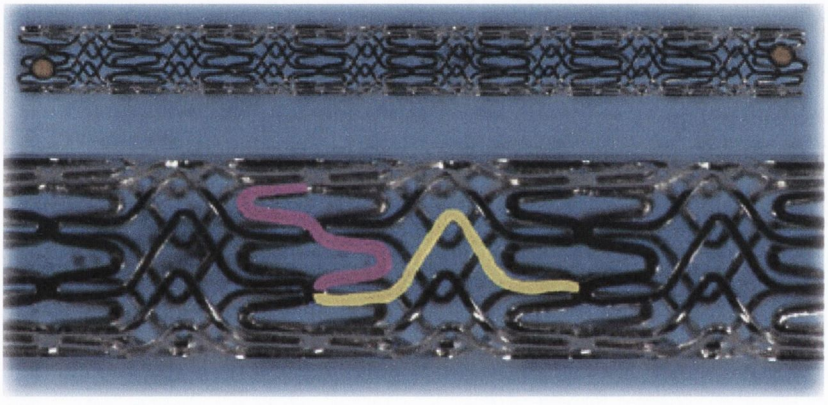

The outer diameter of this stent was 1.7 mm before electro polishing

Fig. 4.1.1 Example of a stent

Tensile and fatigue tests were not carried out on the total stent, but on plain and notched specimens of similar sizes as features found in the stent, e.g. 'flat' wires of roughly 0.1 mm by 0.1 mm. Reference tests were done on macro-scale specimens, but the majority of tests was carried out on micro-scale specimens. Beside the 316L stainless steel tests, some micro-scale and macro-scale tests were carried out on aluminium.

This chapter discusses the equipment, specimen geometry and methods used to assist in the testing and prediction process.

4.1 The MTS Tytron 250: testing of micro-scale tensile and fatigue specimens

The MTS Tytron 250 test machine was used to carry out both tensile and fatigue tests on the microscopic stainless steel and aluminium specimens. This test machine was especially designed to test micro-scale specimens. In combination with the hard to handle micro-scale specimens it provided challenging problems, which would not have occurred in conventional macro-scale tests. The MTS Tytron is able to carry out static and dynamic tests over a wide variety of velocities and frequencies. The horizontally orientated machine is designed for testing at low loads with a range of +/- 250N. The 250N load cell can be used in its 10% range (+/- 25N) and smaller load cells are available to obtain greater accuracy at even lower loads. The accuracy of the system is +/- 0.5% or better. The actuator was used in force control for fatigue tests and in displacement control for tensile tests. The machine's mechanical clamp grips are capable to grip specimens properly up to a load of 250N.

The actuator of the Tytron is powered by a precision electric linear servomotor with static and dynamic force rating. A full stroke linear variable displacement transducer (LVDT) regulates measurement and control of the actuator. This enables the machine to perform both statically and dynamically with high levels of precision. Special air bearings are integrated in the machine to allow the system to operate with virtually no friction, see Fig. 4.1.2.

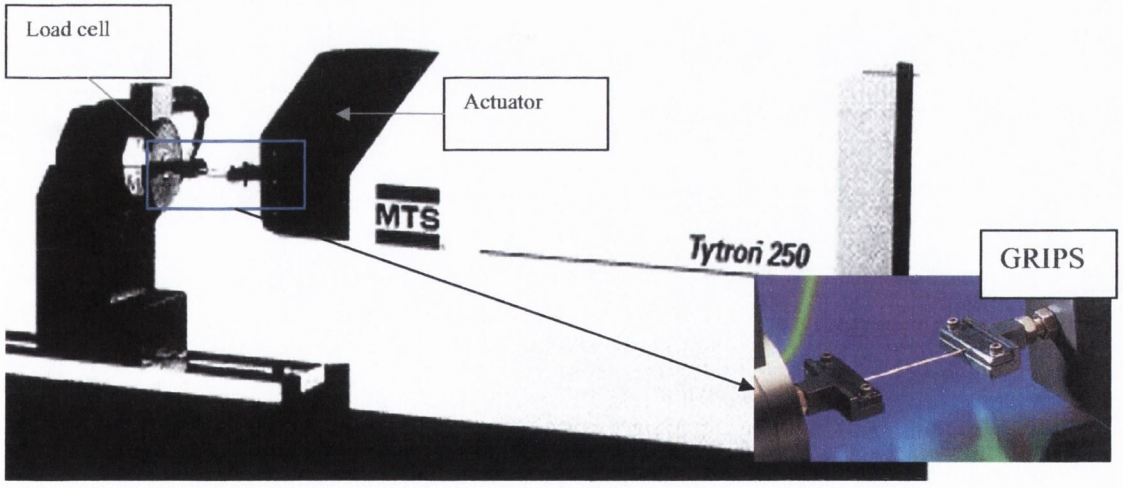

Fig. 4.1.2 The MTS Tytron 250 with its mechanical clamp grips

4.1.1 Tuning

Tuning is an important aspect in the testing process, because the system needs to know what stiffness to expect from the specimen. The tuning process of the Tytron is complicated, because everything has to be set manually. The machine is not capable of automatically fine-tuning during the tests, so the tuning values have to be extremely accurate.

For macro-scale specimens the stiffness of a specimen can be considered constant, but for micro-scale specimens the stiffness changes by introducing a notch or altering the width or the thickness. The micro-scale specimens are only a few grains thick. A slight change in the stiffness of the specimen, even during the test, can result in a bad response from the actuator and can ultimately result in damage to the specimen. Plain and notched specimens of the same material and the same net cross sectional area require a different combination of tuning values for fatigue tests.

The software distinguishes between two sets of tuning values, one set for displacement controlled tests and one set for force controlled tests. In displacement control, the actuator is normally stable using the default tuning settings, in force control the settings are material and geometry dependent.

There are three tuning parameters: *P-gain*, *I-gain* and *D-gain*. The parameters interact, but in general I-gain controls the amplitude of the load signal, P-gain the shape and D-gain the stability. Obtaining the optimum tuning values takes substantial time and many specimens can be lost in the process. Even small changes in tuning values can cause the actuator to move. A macro-scale specimen would not be affected by this (minor) actuator movement, but micro-scale specimens can be fatally damaged. Losing several micro-scale specimens in the tuning process is unfortunate because they are difficult to manufacture and are therefore relatively expensive. Table 4.1.1 contains the tuning values for all the tests that were done on the Tytron. Section 4.7 specifies the different geometries that were tested.

Table 4.1.1 Tuning values for all tests carried out on the MTS Tytron 250

	Displacement Control			**Force Control**			**F** [Hz]	**Tensile speed** [mm/min]
	P-gain	**I-gain**	**D-gain**	**P-gain**	**I-gain**	**D-gain**		
Tensile plain wires	1	0.5	0.025	0.1	50	0.001	N/a	0.2
Fatigue plain wires	1	0.5	0.025	0.5	2328	0.2	50	N/a
Tensile notched wires/tubing	1	0.5	0.01	0.1	50	0.001	N/a	0.2
Fatigue notched wires/tubing	1	0.5	0.01	0.099	1489	0.002	15	N/a
Tensile aluminium wires	1	0.5	0.025	0.1	50	0.001	N/a	0.2
Fatigue aluminium wires	1	0.5	0.025	0.1	1800	0.001	50	N/a

4.1.2 The MPT Test Software

The Multi Purpose Testware (MPT) software provided with the machine enables the user to design a range of testing programs from very simple to extremely complex. The program is a combination of building blocks that describe basic processes such as *RAMP* for tensile testing and *CYCLE* for fatigue testing. Data acquisition process blocks are capable of recording data in many different ways and for different signals, e.g. force, displacement and time. A process block can be activated through a pop up window in which specific details for that process can be specified. Table 4.1.2 describes the process blocks that were used for tensile and fatigue test programs.

Table 4.1.2 MPT tensile and fatigue test programs

Tensile test program
RAMP The basic process *RAMP* uses axial displacement as the main signal. The tensile speed was chosen to be 10 mm of relative displacement in 50 minutes (0.2 mm/min). It is important to use relative displacement. If not, the actuator will move to the absolute position 10 mm in 50 minutes. This results in a different tensile speed.
TIMED DATA ACQUISITION The *Timed Data Acquisition* process was set to take data samples every second (time step is chosen by the programmer) for three signals: time, displacement and force.
Fatigue test program
CYCLE The basic process *CYCLE* uses axial force as the main signal. The absolute minimum and maximum force values have to be stated (all tests were done with $\sigma_{min}/\sigma_{max} = 0.1$). It is important to activate the Active Phase Control function, which compensates for small phase differences between the command signal and the response of the machine.
CYCLIC ACQUISITION The *Cyclic Acquisition* process activates the actual data recording process at set intervals (e.g. every 100,000 cycles) to reduce the size of the output file. The output file would be very large if data was recorded continuously. The actual data recording process used for fatigue tests is *Peak/Valley Data Acquisition*, which takes readings at the peaks and valleys of a loading cycle.

4.1.3 Micro-scale related problems

One of the problems that occurred during micro-scale testing was that the material properties of the specimens changed during the test, resulting in a change in stiffness. The actuator could not compensate, became unstable and damaged the specimen. The solution to this problem is reducing the D-gain in displacement control. However, this makes gripping of the specimen more difficult. The tuning values described above were *stable* tuning values, meaning that the actuator will not move when the specimen is gripped. A stable actuator is a

good match for the specific stiffness of the specimen that is going to be tested. A minor change in material properties during the test can cause the actuator to become unstable. For some materials and specimen geometries the stable actuator settings work fine, in other situations they do not. There is no clear strategy that one can take to determine whether a stable or unstable actuator should be used; this has to be determined for each specimen type.

When stable actuator settings do not work for a particular specimen, one has the option of tuning for a *less stable* actuator. The *less stable* actuator can compensate for larger changes in specimen stiffness during the test. The actuator can be made less stable by changing the D-gain in the default settings in displacement control. These settings should normally not be altered, but in some circumstances it is the only solution. A disadvantage of the less stable actuator emerges when the specimen is gripped. Touching the grip that is connected to the less stable actuator, can cause movement and therefore damage the specimen. Handling of the specimen and the machine becomes even more difficult. Another disadvantage of the less stable actuator is a loss in frequency. The maximum frequency for the stable actuator is 50 Hz, for the less stable actuator it was found to be 15 Hz.

It is important to grip the specimen on the actuator side first, because if gripping causes movement in the actuator, the other side of the specimen is still free and therefore damage is less likely to happen. The grip on the load cell end of the specimen is fixed and cannot move. This end is to be gripped last.

4.2 Testing machine for macro-scale tensile and fatigue specimens: The Instron 8501

The servo-hydraulic fatigue testing machine *Instron 8501* was used for experimental tensile and fatigue tests on macro-scale stainless steel and aluminium specimens. The machine is easy to use and can carry out fatigue tests at a maximum frequency of 100 Hz and a maximum load range of 100 kN, dependent on material and geometry. The load cell has a range of 50 kN.

The Instron can be used in both stress and strain control and an extensometer can be attached to the specimen in order to measure strain. The stiffness related problems that occurred with the micro-scale specimens on the Tytron testing machine should not happen with the Instron 8501. The tuning process is relatively easy. The same tuning parameters are present: P-gain, I-gain and D-gain, but only P-gain needs to be varied until the optimum value for material and corresponding loading condition is reached.

4.3 Hardness measurements: Mitutoyo MVK-H1

The Mitutoyo MVK-H1 was used to measure the hardness of the specimens. A choice has to be made between the Vickers or Knoop indenter; the Vickers indenter will give an indentation in the material that is an even-sided diamond shape, while the Knoop indenter will give a stretched, diamond shaped indentation in the material. Hardness Vickers is more commonly used than Knoop.

After the indentation is made in the specimen, the diameter in the x and in the y direction is measured, after which the machine determines the area of the indentation and gives the corresponding hardness value.

4.4 Microscopy

Two microscopes were used to analyse the specimens. The Mitutoyo 2D microscope has a maximum magnification of 1000X. This microscope is suitable to obtain an initial impression of the quality of the sample. The attached 2 axis coordinate measurement data processors were used to check the geometry of the specimens, e.g. thickness notch depth and root radius.

The Scanning Electron Microscope *Hitachi S-3500N* on the other hand is capable of giving a 3D overview of the samples. In practice, the microscope has a resolution of 1 micrometer. The Scanning Electron Microscope was mainly used to look at fracture surfaces and deformation areas in the failed specimens.

4.5 Annealing, electro-polishing and etching

The 316L stainless steel specimens underwent the same *annealing* and *electro-polishing* process as the stent.

Annealing: All samples were annealed at 925 degrees Celsius for 5 minutes and cooled in a vacuum oven in a N-Ar mix.

Electro-polishing: The microscopic samples were already electro-polished, which resulted in a relatively smooth surface finish.

Etching:

The etching process used to visualise the grains was an electrolytic process. The etching fluid was made by pouring 100 ml of 69% nitric acid into a beaker containing 10 ml of water. Fig. 4.5.1 shows the set up for the etching process.

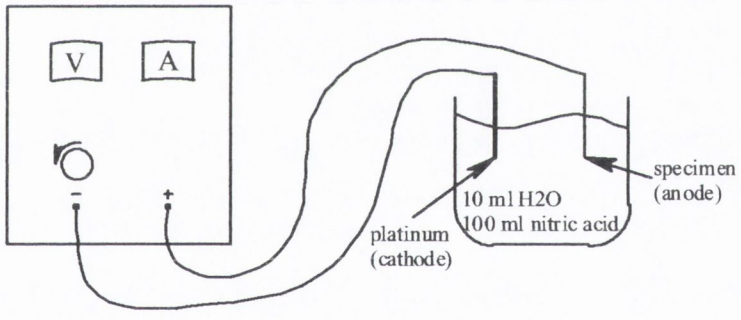

Fig. 4.5.1 Etching set up

Applying 0.8V for 30 seconds was sufficient to visualise the grain structure of the microscopic 316L stainless steel specimens.

Polishing and etching of the macroscopic specimens was done mechanically. The sample was hot-mounted in bakelite resin and ground on the following grit size silicon carbide papers: 500, 1000 and 2500. Afterward the sample was polished using respectively 6 and 1 μm diamond paste. The samples were etched using a solution of 15 ml of Nitric acid, 30 ml of Hydrochloric acid and 45 ml of Ethanol.

4.6 FEA Modelling using commercial package ANSYS

ANSYS is a Finite Element Analysis (FEA) package that is widely used by researchers. ANSYS simulates loading information on a component of a certain material and geometry and calculates the corresponding stresses and strains in the component.

Fig. 4.6.1 illustrates that a Double Edge Notch Tension wire sample contains two symmetry lines. These symmetry lines can be used to simplify the *FEA* model in ANSYS.

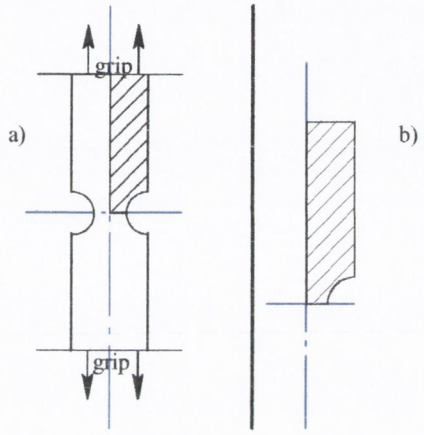

Fig. 4.6.1a) 316L stainless steel wire sample

b) Part of the specimen that is modelled in ANSYS

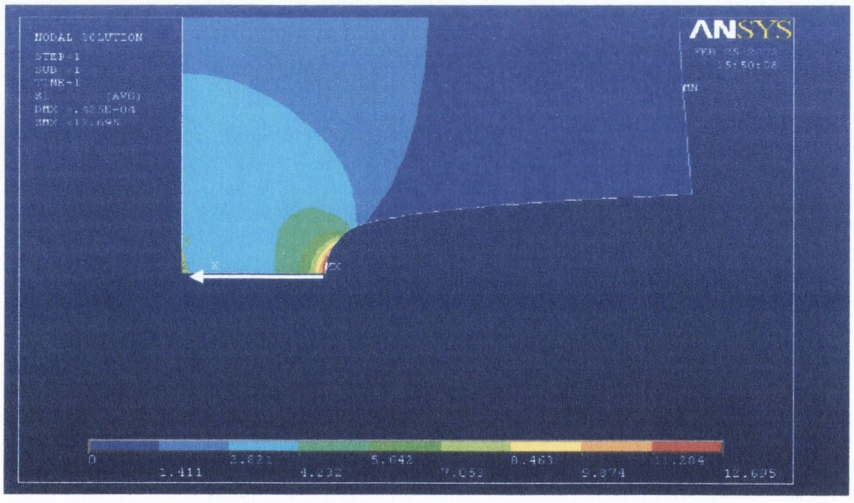

Fig. 4.6.2 FE model of 316L stainless steel DENT wire geometry (units MPa)

ANSYS visualises the stress distribution in different colours, ranging from the highest stress at the root of the notch, which is red in Fig. 4.6.2, to the lowest stress, which is dark blue. The highest local stress value in combination with the nominal stress at the net area was used to determine the theoretical stress concentration factor K_t (equation 2-1-2).

ANSYS was also used to provide the stress distance plots required for the Crack Modelling Method (CMM) and the Theory of Critical Distances (TCD). The stress distance path commences at the highest local stress at the notch and normally runs perpendicular to the loading direction, as indicated by the white arrow in Fig. 4.6.2. The stress distance graph obtained by ANSYS, e.g. Fig. 5.1.2, shows a smooth, curved relation for the reduction of stress ahead of the stress concentration. The behaviour plotted in these graphs is average behaviour. Even though this relation in microscopic components might not be as smooth as shown in the graphs, the average relation will still be used, because one of the aims of this work is to investigate whether continuum mechanics can be used to describe micro behaviour. The other approach would be to model each grain separately, which will result in a stress distance relation that is relatively rough.

4.7 Specimen geometry

A variety of specimens were tested, mostly manufactured from 316L stainless steel, but also some tests were carried out on aluminium samples to check the methodology on a different material. Micro-scale and macro-scale tests were carried out to compare the results.

4.7.1 Specimen Geometry: Macro-scale 316L Stainless Steel bar

The geometries of the plain and notched macro-scale bar samples are given in Fig. 4.7.1. The bars had a circular cross section; notched specimens contained a 1 mm-deep circumferential v-shaped notch with a root radius of 0.075 mm.

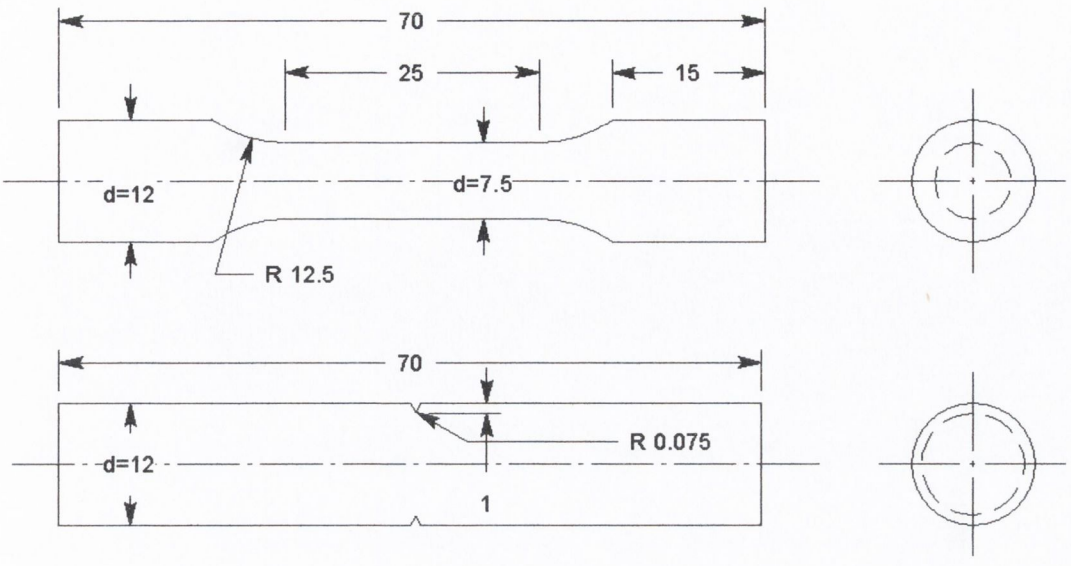

All Dimensions in mm

Fig. 4.7.1a) 316L macro-scale plain bar specimen geometry

b) 316L macro-scale notched bar specimen geometry

4.7.2 Specimen Geometry: Micro-scale 316L Stainless Steel Wires and Tubing

The microscopic stainless steel specimen wires were designed to contain stent-like features. They were manufactured by Medtronic Ltd, Galway, using the same procedures as normally used to manufacture stents. The specimens were laser cut from pieces of tubing. The tubing in combination with two reinforcement struts was used to prevent the wires from being damaged during transportation, see Fig. 4.7.2a. The struts were to be cut in the testing machine before commencing the tests. Plain specimens were manufactured and notched specimens with three different notch depths. The specimens were designed as Double Edge Notch Tension (DENT) specimens to eliminate bending.

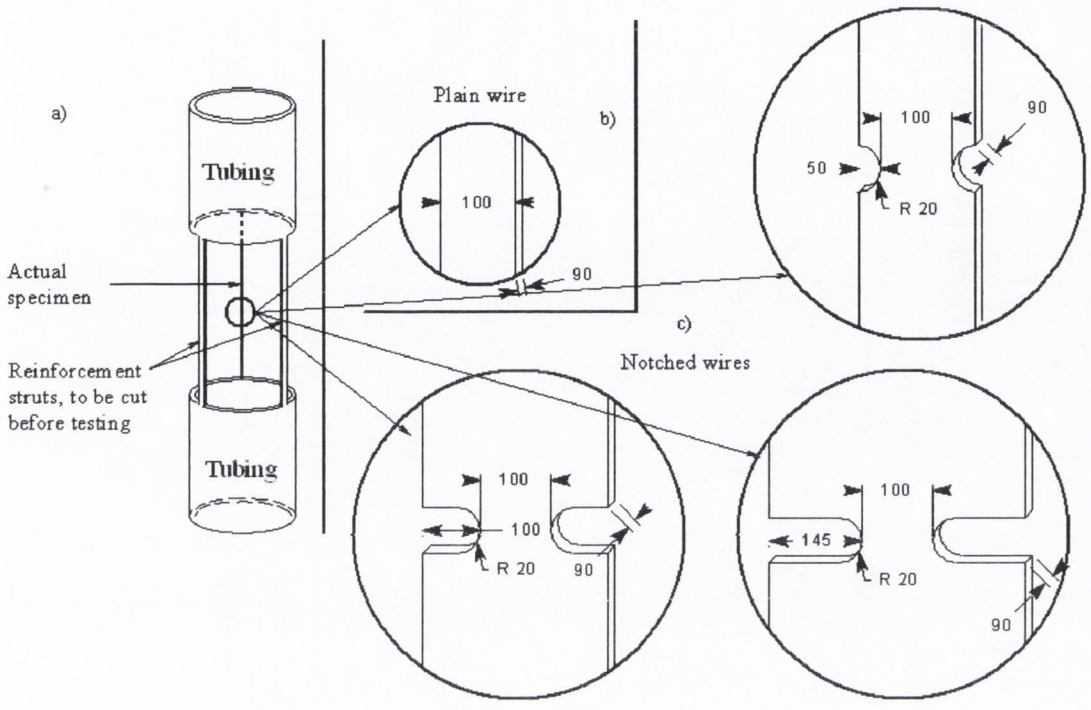

All Dimensions in µm

Fig. 4.7.2a) Wire specimen within the tubing containing reinforcement struts

b) Plain specimen geometry

c) Notched specimen geometry (50,100,150 notch)

The width of the plain wires was designed to be 100 µm, similar to sizes occurring in stents. The distance between the two notches of the DENT specimens was the same 100 µm, in order to compare the net section stresses. Three different notch depths were designed: 50, 100 and 150 µm. The specimen length was 5 mm for all samples and the thickness was 90 µm. The notch root radius was limited by the capability of the laser. Measurements after the electro polishing process gave average root radii of 20 µm.

The wires themselves were so small that gripping was expected to be a problem. Loose wires are difficult to handle and are likely to get damaged during transport. The initial idea was to create a specimen using the tubing from which it is manufactured. The geometry included 2 struts to protect the wire during transport, see Fig. 4.7.2a. The specimen including the struts was to be gripped in the machine at the tubing ends, preventing the wire itself from being

damaged before commencing the test. Once gripped in the machine, the struts could be cut and the wire could be tested.

The Tytron proved to be incapable of testing this specimen geometry. Gripping the strutted specimen could be done quite easily, but problems occurred when the struts were cut. Unlike for macro-scale specimens, cutting a strut seriously reduces the stiffness of the total micro-scale specimen. The initial tuning values were suited for the stiffness of the strutted sample, but the reduction of stiffness as a result of cutting the struts was so large that the machine could not compensate, not even when the tuning values were set for a *less stable* actuator. An altered specimen geometry was proposed: loose wires to be cut from a strutted piece of tubing. The protection struts and notched wire geometries are not shown in Fig. 4.7.3, because they are similar to Fig. 4.7.2.

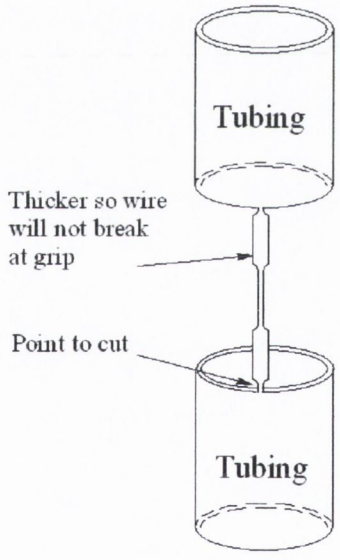

Fig. 4.7.3 Altered specimen geometry

The basic geometry with protection struts was kept the same for transport. The wire itself was changed into a conventional dog-bone shaped test specimen. At the ends of the wire that

are attached to the tubing, the width was reduced to make it easier to cut the wire from the tubing. The width of the wire was design to be the same: 100 μm, but after measuring the samples, all net widths consistently turned out to be 110 μm, both for the plain and the notched samples. The measured thickness was roughly 90 μm.

The best way to cut out the specimens was by using an EDM (Electro Discharge Machining) machine, which is capable of contact-free cutting. The first end of the wire had to be cut in this way, whilst the other end could be cut using snips.

The final microscopic 316L stainless steel wire geometry was the same 50-notch wire as discussed above, but with a sharpened root radius, the *FIB50* specimen. The idea behind this specimen geometry was to check whether a sharpened root radius actually reduces the fatigue strength of the original 50-notch wire specimen or not. It is assumed that the increased stresses as a result of the sharper root radius will have dissipated at the critical distance. In other words; the same fatigue limits are expected for both the original 50-notch wire specimen and the FIB50 specimen.

Ten of the already manufactured, annealed and electro-polished 50-notched wire samples were sent to Princeton, America, to sharpen one of the two notches, see Fig. 4.7.4. The initial root radius after the electro-polishing process was roughly 20 μm. The Focussed Ion Beam (FIB) process was capable of manufacturing a notch with a root radius of 1 μm. This notch was added to the root of the already existing 20 μm notch. The width of the FIB50 samples between the notches was 109 μm and the corresponding thickness 90 μm.

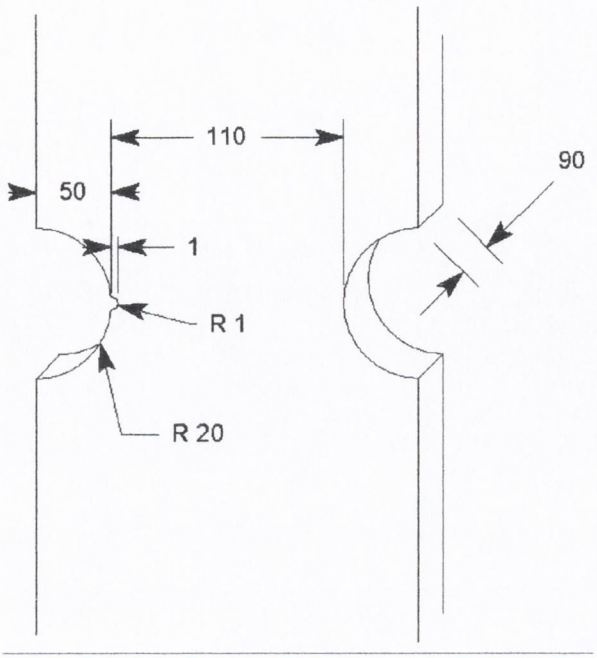

All Dimensions in μm

Fig. 4.7.4 FIB50 sharpened 316L stainless steel wire specimen

Beside microscopic wire samples containing stent like features, fatigue tests were also carried out on 3 types of notched tubing pieces, identical to the tubing from which stents are manufactured. These specimens were designed to contain three different crack lengths, a short crack, a long crack and an in between crack length. The wall thickness of the tubing was 90 μm, similar to the wire specimens. The three geometries that were tested were: a double holed sample with a diameter of 60 μm, a double 400 μm slotted sample and a double 1500 μm slotted sample, as illustrated in Fig. 4.7.5. Annealing and electro-polishing were used to obtain a regular grain size and a smooth surface quality, similar to that of stents. Excess material was placed inside the tubing ends during testing to prevent them from collapsing in the grips.

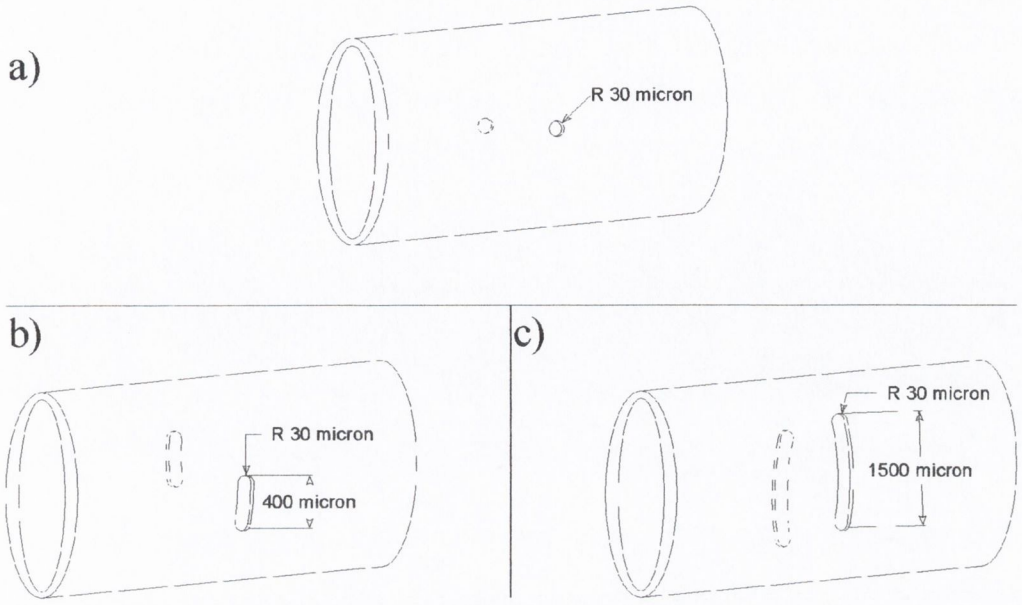

Fig. 4.7.5a) Double holed 60 micron tubing geometry

b) Double 400 micron slotted geometry

c) Double 1500 micron slotted geometry

4.7.3 Specimen Geometry: Macro-scale Aluminium plates

Macro-scale tests were carried out on plain and SENT 99.5% pure aluminium plate specimens of 0.5 mm thickness to obtain bulk material properties, see Fig. 4.7.6. The notched geometry was designed and tested by Bellett (Bellett, 2002).

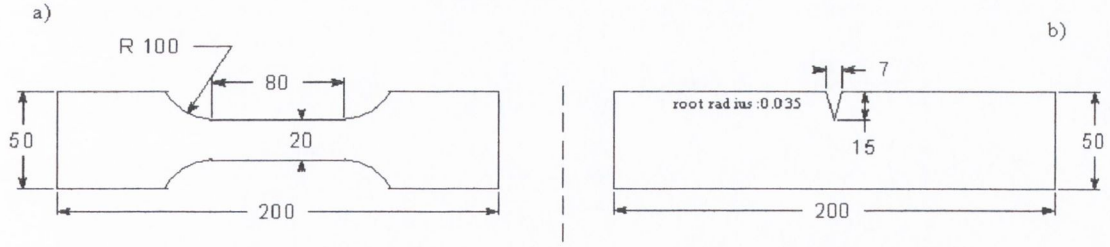

All Dimensions in mm

Fig. 4.7.6a) Aluminium macro-scale plain specimen geometry

b) Aluminium macro-scale notched specimen geometry

4.7.4 Specimen Geometry: Micro-scale Aluminium plates

The plain and notched 0.5 mm thick micro-scale aluminium specimens were designed to have a net section width of a similar size as the critical distance of the material to make sure that the specimens were actually microscopic. Aluminium was chosen because it has a relatively large critical distance, therefore making machining slightly easier. The critical distance of the aluminium could not be determined exactly, because not enough material properties were known. The critical distance was estimated to be around 1 mm. The smallest net section that could be manufactured was 1.5 mm, as demonstrated in Fig. 4.7.7.

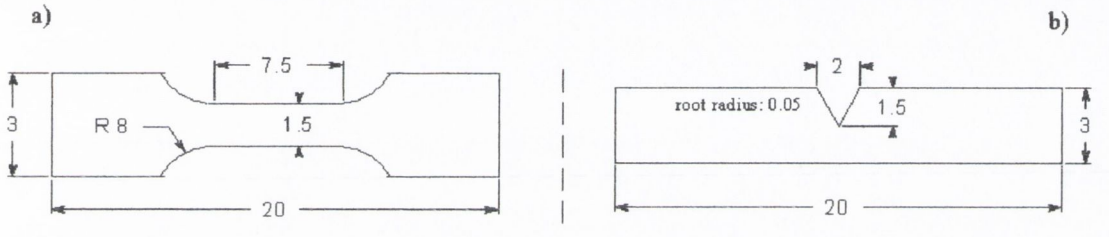

Fig. 4.7.7a) Aluminium micro-scale plain specimen geometry
b) Aluminium micro-scale notched specimen geometry

4.8 Summary of tests done on all stainless steel and aluminium specimens

Tensile and fatigue tests were carried out on macro and micro stainless steel and aluminium specimens. The ramp rate for all tensile tests was 0.2 mm/min and the frequencies for the fatigue tests varied between 15 and 50 Hz. All macro and micro fatigue tests were carried out with a loading ratio of 0.1. An extra series of fatigue tests was carried out on the macroscopic notched stainless steel bar at a loading ratio of 0.8 to determine the closure-free effective threshold of the material.

Generally in this work failure was defined as total failure; the breaking of the specimen into two or more pieces. For the plain and notched stainless steel bar fatigue tests, failure was defined when the Instron test machine detected a displacement larger than 2 mm. The stainless steel material is very ductile and during fatigue cycling the material strains substantially. At that point, the specimens were cracked substantially, therefore not many more cycles were required for failure to occur into two or more separate pieces and this point was used instead.

Chapter 5 Results

This chapter summarises the results of the analyses and tests that were carried out on the different types of specimens and materials. Several batches of macro-scale and micro-scale specimens were tested to analyse the effect of component size. In this work the choice was made to analyse stresses at the net section, so where necessary there will be distinguished between net and gross, e.g. σ_{NET} and σ_{GROSS}. Analysing stresses at the net section implies that the geometry factor has to be converted to the net section as well. F_{NET} can be derived from F_{GROSS} using the following equation:

$$F_{GROSS}\sigma_{GROSS}\sqrt{\pi a} = F_{NET}\sigma_{NET}\sqrt{\pi a} \qquad (5\text{-}1\text{-}1)$$

where F_{GROSS}, F_{NET}, σ_{GROSS} and σ_{NET} are respectively the geometry factors and stresses at the gross and net section. For specimens where the thickness is the same at the gross and net sections, σ_{GROSS} and σ_{NET} are related as follows:

$$\sigma_{NET} = \frac{w_{GROSS}}{w_{NET}}\sigma_{GROSS} \qquad (5\text{-}1\text{-}2)$$

where w_{GROSS} and w_{NET} are the widths at the gross and the net sections. Combining equations 5-1-1 and 5-1-2 results in the relation between the gross and net geometry factor:

$$F_{NET} = \frac{w_{GROSS}}{w_{NET}}F_{GROSS} \qquad (5\text{-}1\text{-}3)$$

The equation for F_{GROSS} can be obtained from handbooks (Murakami et al, 1987).

5.1 Finite Element Analysis results

Finite Element Models (ANSYS) were used to obtain the stress distance curves for all the specimen geometries that were tested. Stress distance curves are an essential step in obtaining fatigue predictions for the Crack Modelling Method and the Theory of Critical Distances. ANSYS is also used to determine theoretical elastic stress concentration factor K_t.

5.1.1 ANSYS results of 316L stainless steel macro-scale bars

The 316L macro-scale notched bar was modelled in 3D using element solid 92. A ¼ model was created making use of the symmetry of the bar geometry that was described in section 4.7.1. The white arrow in Fig. 5.1.1 illustrates along which path the stress distance curve was taken. Fig. 5.1.2 shows the corresponding stress distance curve that was obtained.

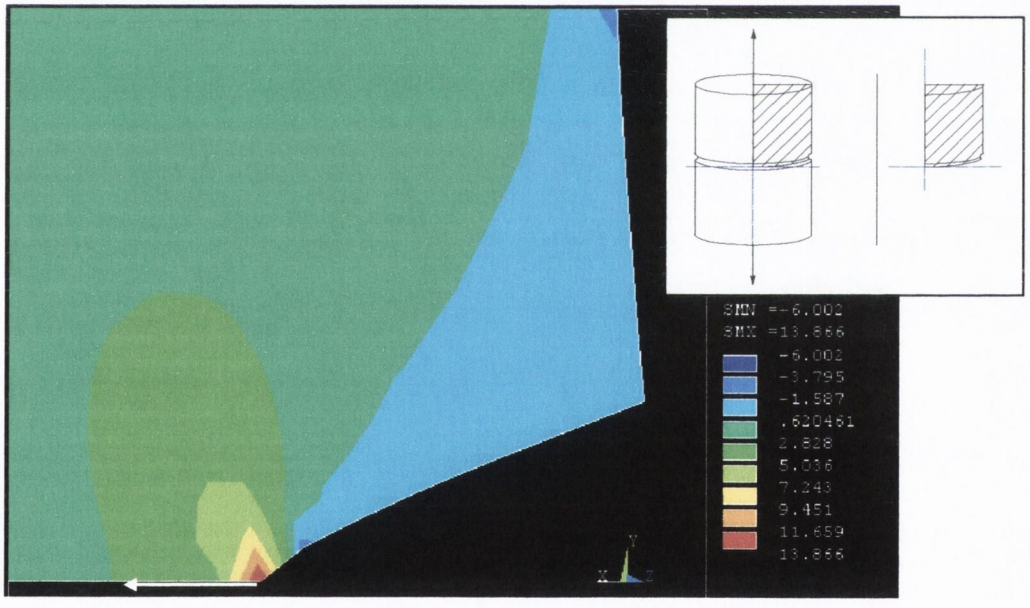

Fig. 5.1.1 FE model of 316L stainless steel macro-scale bar sample (units MPa)

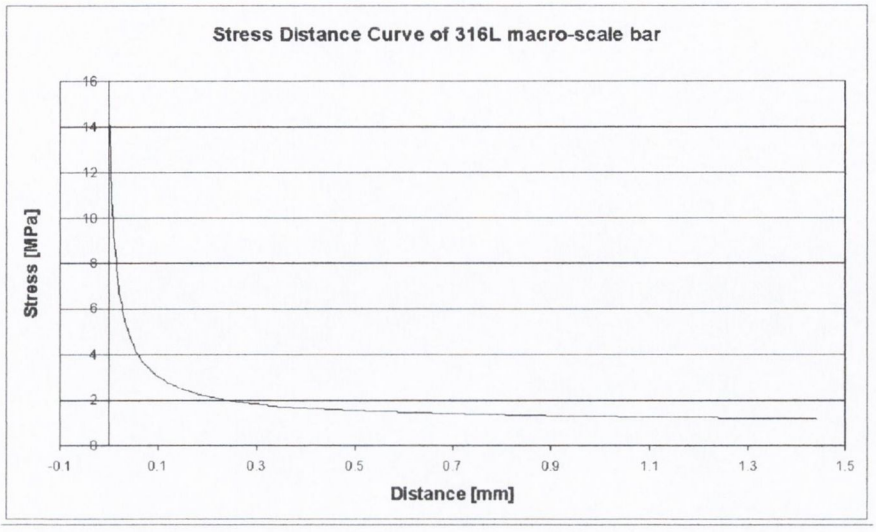

Fig. 5.1.2 Stress distance curve of 316L macro-scale bar sample

The stress distance curve shown in Fig. 5.1.2 is the result of an applied tensile stress of 1 MPa at the gross section.

Table 5.1.1 Summary of important FEA parameters for 316L stainless steel bar samples

	w_{GROSS} [mm]	w_{NET} [mm]	σ_{notch} [MPa]	σ_{NET} [MPa]	K_t
316L notched bar	12	10	11.21	1.2	9.34

where σ_{NET} is the nominal stress at the net section.

5.1.2 ANSYS results of 316L stainless steel micro-scale wires

The geometries of the 50-, 100- and 150-notch wires and the FIB50 wire were discussed in section 4.7.2. All samples were measured before testing and the 150 micron notches were consistently measured to have a depth of 145 μm, not 150. This notch will therefore from now on be referred to as the 145 notch.

Due to symmetry, it was possible to reduce the model in ANSYS to a ¼ of the actual specimen size. The model of a 50-notch wire is shown in Fig. 5.1.3, where the white arrow illustrates along which path the stress distance curves in Fig. 5.1.4 were taken.

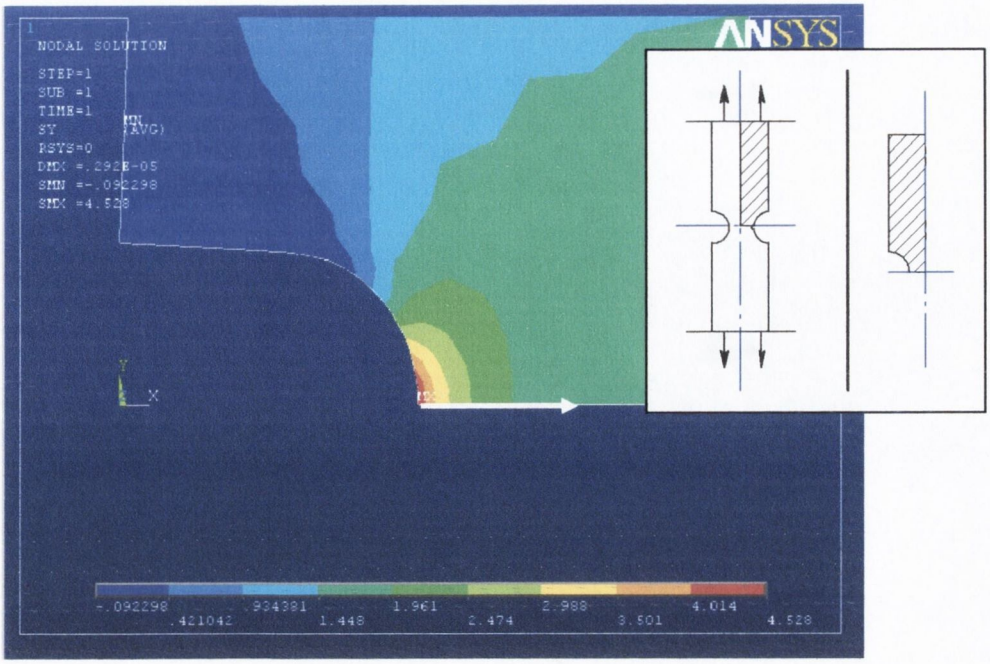

Fig. 5.1.3 FE model of 316L stainless steel DENT wire geometry (units MPa)

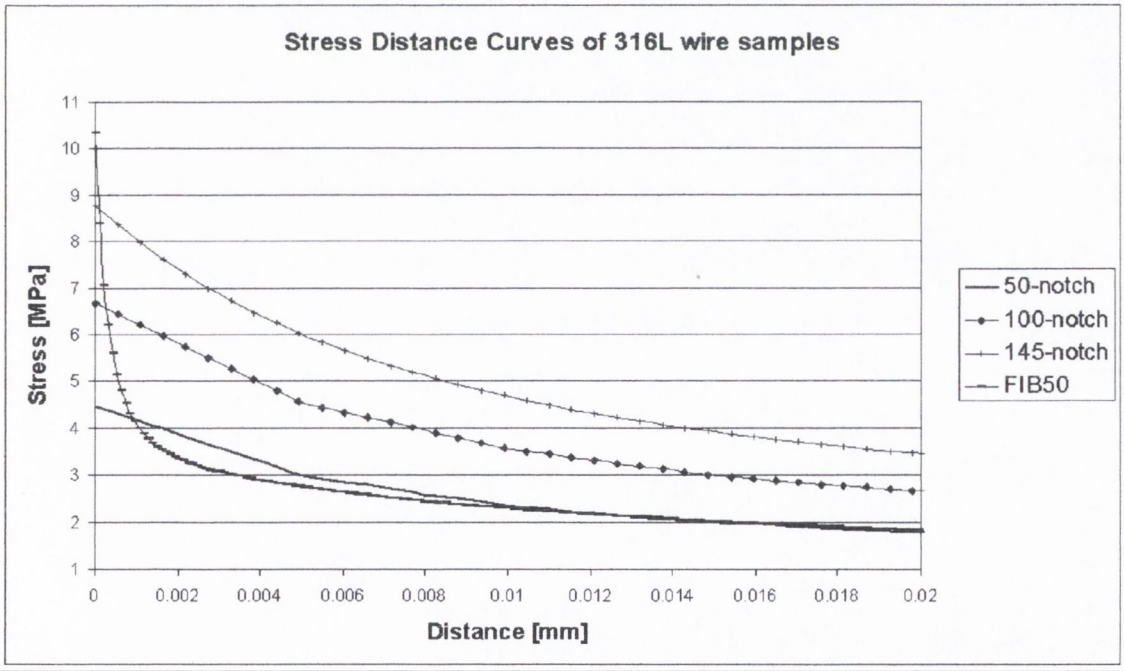

Fig. 5.1.4 Stress distance curves of the four types of DENT wires

The stress distance curves in Fig. 5.1.4 are a result of a 1 MPa applied tensile stress at the gross area.

Table 5.1.2 Summary of important FEA parameters for wire the samples

	w_{GROSS} [mm]	w_{NET} [mm]	σ_{notch} [MPa]	σ_{NET} [MPa]	K_t
50-notch	0.21	0.11	4.52	1.91	2.34
100-notch	0.31	0.11	6.68	2.82	2.4
145-notch	0.4	0.11	8.79	3.64	2.35
FIB50	0.21	0.109	10.34	1.93	5.37

The FIB50 specimen was manufactured from the 50-notch by sharpening the root radius of the notch. This effect can be seen in Table 5.1.2, because the stress at the notch, σ_{notch}, is twice as high for the FIB50 specimen as for the original 50-notch wire. This also results in a higher K_t value for the FIB50 wire.

5.1.3 ANSYS results of 316L stainless steel micro-scale tubing pieces

The geometries of the three types of notched tubing samples were given in section 4.7.2. The choice was made to simplify the model for the tubing samples to a centre hole or notch in a flat plate. Again the ANSYS model was reduced using existing symmetry lines in the samples. Fig 5.1.5 shows the ANSYS model where the white arrow indicates the path along which the stress distance curves in Fig. 5.1.6 were taken.

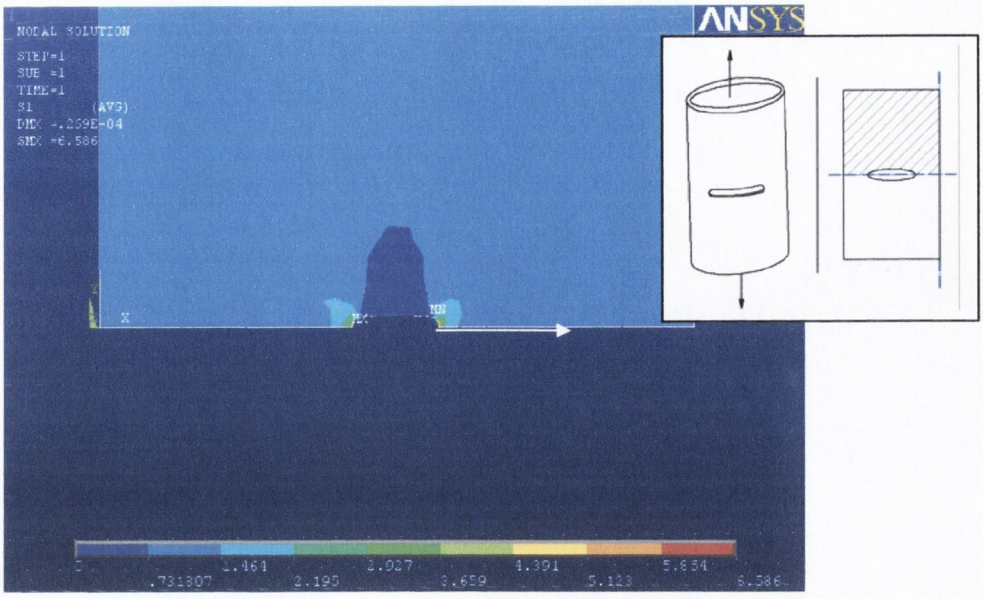

Fig. 5.1.5 FE model of 316L stainless steel tubing geometry (units MPa)

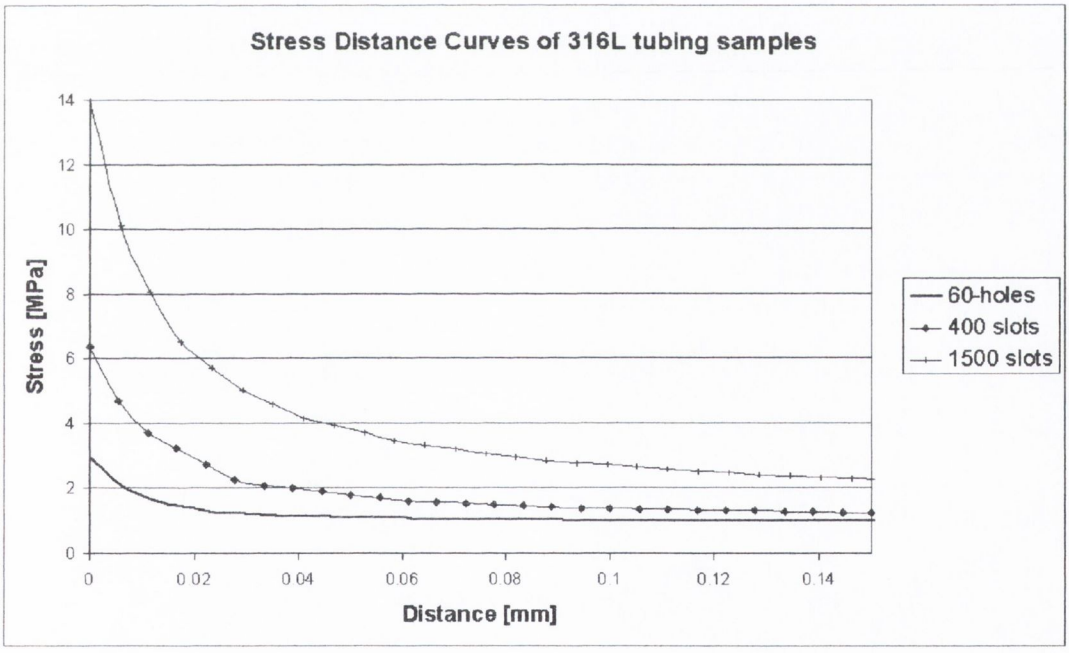

Fig. 5.1.6 Stress distance curves of the three types of tubing pieces

The stress distance curves in Fig. 5.1.6 were the result of a 1 MPa applied tensile stress at the gross section.

Table 5.1.3 Summary of important FEA parameters for tubing samples

	w_{GROSS} [mm]	w_{NET} [mm]	σ_{notch} [MPa]	σ_{NET} [MPa]	K_t
60-holes	2.67	2.61	2.95	1.02	2.88
400-slots	2.67	2.27	6.59	1.18	5.58
1500-slots	2.67	1.17	14.0	2.28	6.13

5.1.4 ANSYS results of 99.5% aluminium alloy macro scale plates

The Single Edge Notch Tension geometry of the macro-scale 99.5% aluminium alloy sample was described in section 4.7.3. The white arrow in the ½ model shown in Fig. 5.1.7 illustrates where the stress distance path in Fig. 5.1.8 was taken.

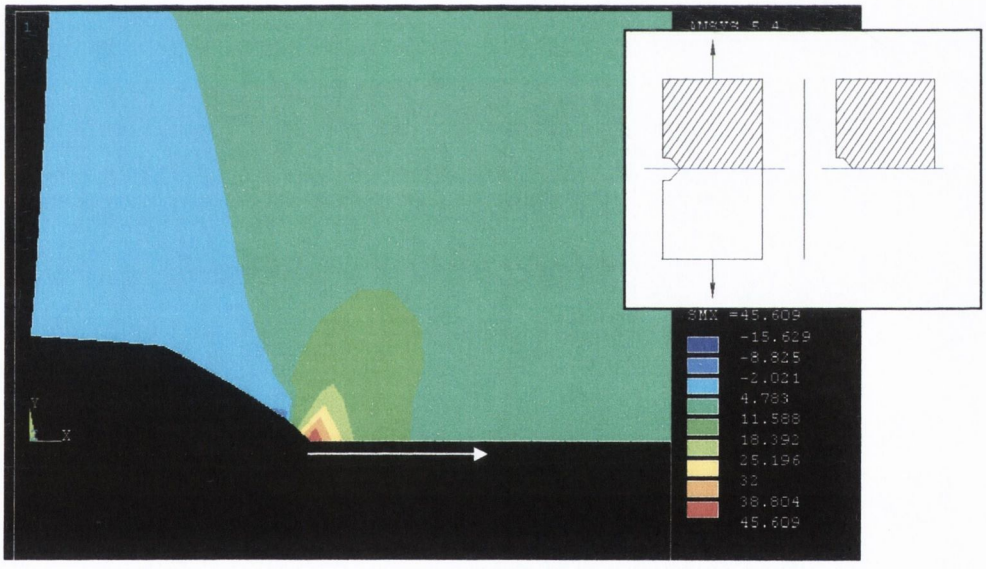

Fig. 5.1.7 FE model of aluminium macro-scale plate sample (units MPa)

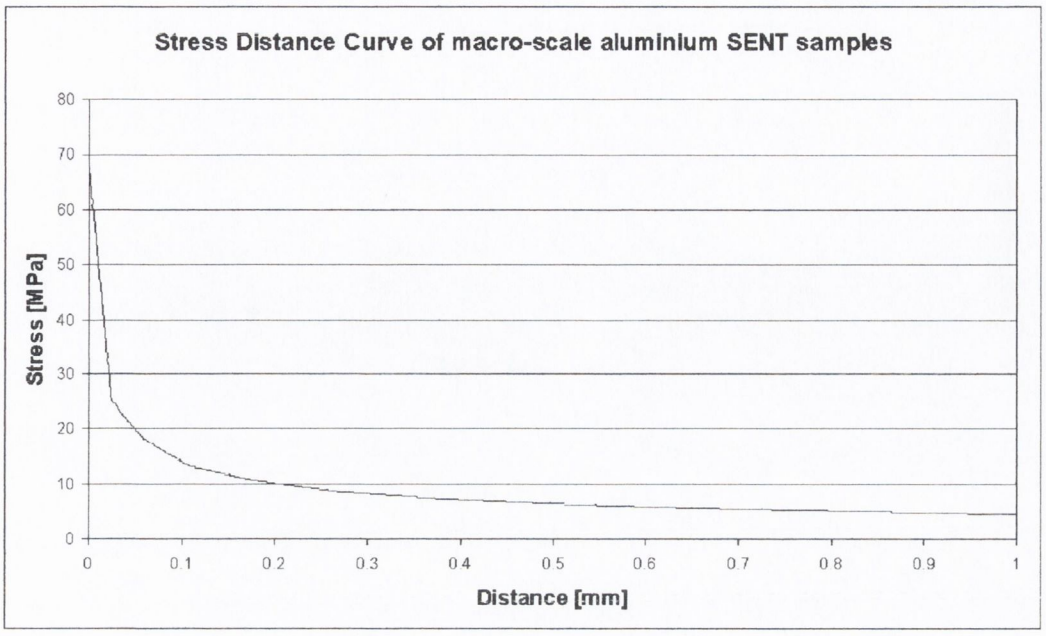

Fig. 5.1.8 Stress distance curve of macro-scale aluminium plate geometry

The stress distance curve shown in Fig. 5.1.8 was the result of an applied tensile stress of 1 MPa at the gross section.

Table 5.1.4 Summary of important FEA parameters for aluminium macro-scale plate samples

	w_{GROSS} [mm]	w_{NET} [mm]	σ_{notch} [MPa]	σ_{NET} [MPa]	K_t
Alu SENT	50	35	68.37	1.429	47.86

5.1.5 ANSYS results of 99.5% aluminium alloy micro-scale plates

A ½ model was made in ANSYS of the Single Edge Notch Tension geometry for the aluminium micro-scale specimens, as described in section 4.7.4. The path of the stress distance curve is indicated by the white arrow in Fig. 5.1.9. The corresponding stress distance curve is given in Fig. 5.1.10.

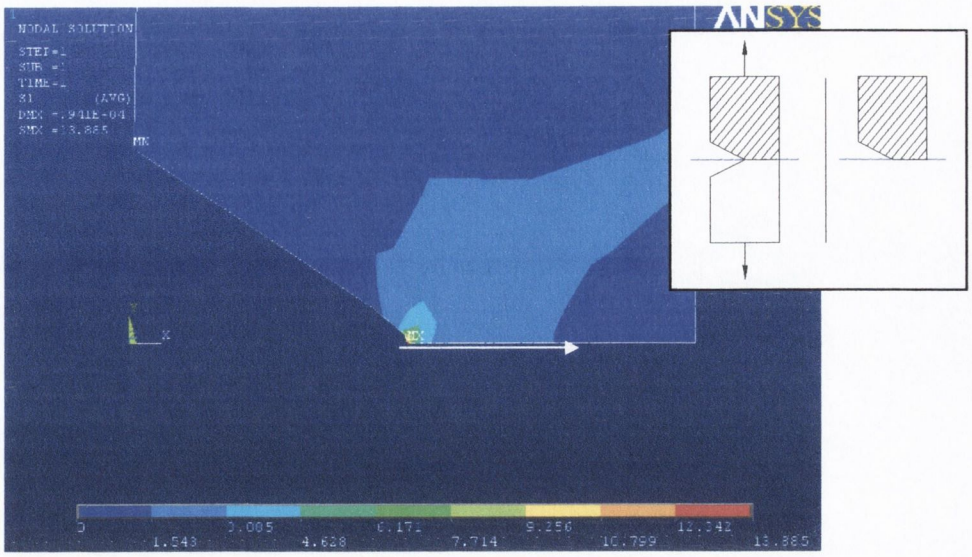

Fig. 5.1.9 FE model of aluminium SENT plate geometry (units MPa)

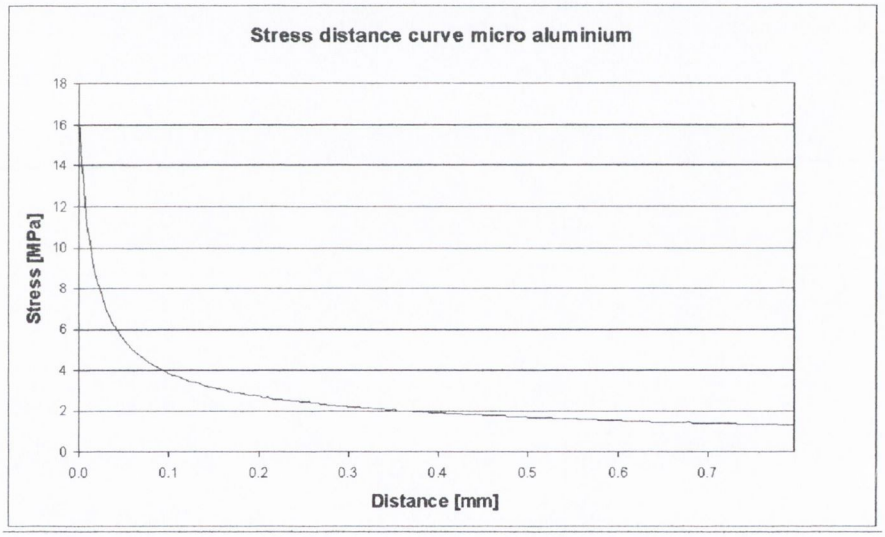

Fig. 5.1.10 Stress distance curve of micro-scale aluminium plate geometry

The stress distance curve shown in Fig. 5.1.10 is the result of an applied tensile stress of 1 MPa at the gross section.

Table 5.1.5 Summary of important FEA parameters for aluminium plate samples

	w_{GROSS} [mm]	w_{NET} [mm]	σ_{notch} [MPa]	σ_{NET} [MPa]	K_t
Micro SENT	3	1.5	28.35	2	14.18

5.2 Tensile Results

Tensile tests were conducted on the same geometries as discussed in section 5.1. Failure is defined as the breaking of the sample into two (or more) separate pieces.

5.2.1 Tensile results of 316L macro-scale bars

Plain and notched macroscopic bar specimens were tested to obtain the macro material properties. The specimen geometry of these macroscopic stainless steel specimens was discussed in section 4.7.1. Fig. 5.2.1 was used to analyze whether the grain size of the macroscopic material is similar to that of the microscopic material. Fig. 5.2.1 shows the grain distribution for a 50-notch wire and for the macroscopic material. Both pictures were taken with a magnification of 200 and can therefore be compared directly. The average grain size was determined by drawing a line and counting the number of grains that were crossed by that line. The length of the line divided by the amount of grains determined the average grain diameter. The values for the average grain diameters for the microscopic and the macroscopic material were similar, respectively 10.53 μm and 11.37 μm.

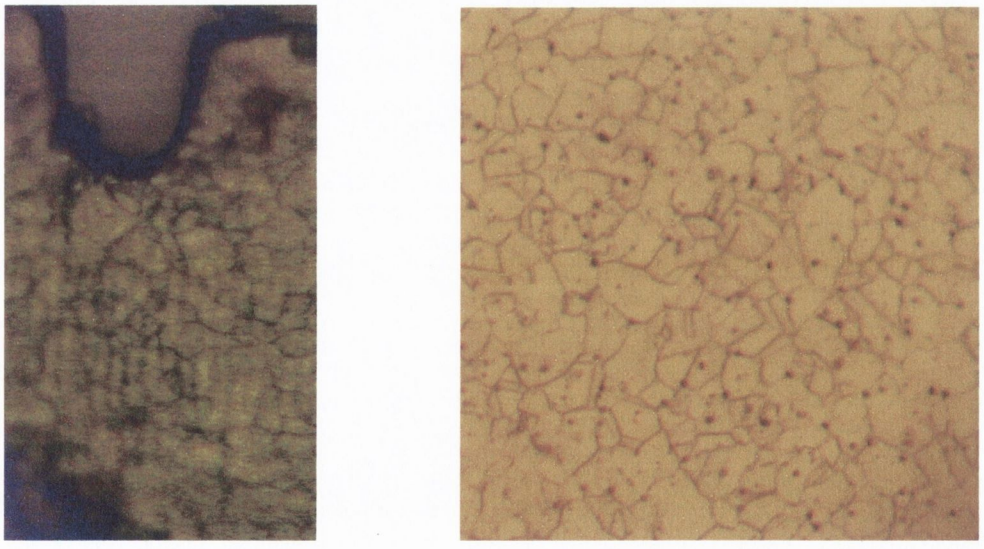

Fig. 5.2.1a) Grain distribution in a 50-notch wire specimen at a magnification of 200
b) Grain distribution in the macro 316L material at a magnification of 200

Plain 316L macro-scale bar tensile results

Fig. 5.2.2 shows the results of the five tensile tests that were carried out on plain 316L stainless steel bars. An extensometer was used to determine the Young's Modulus.

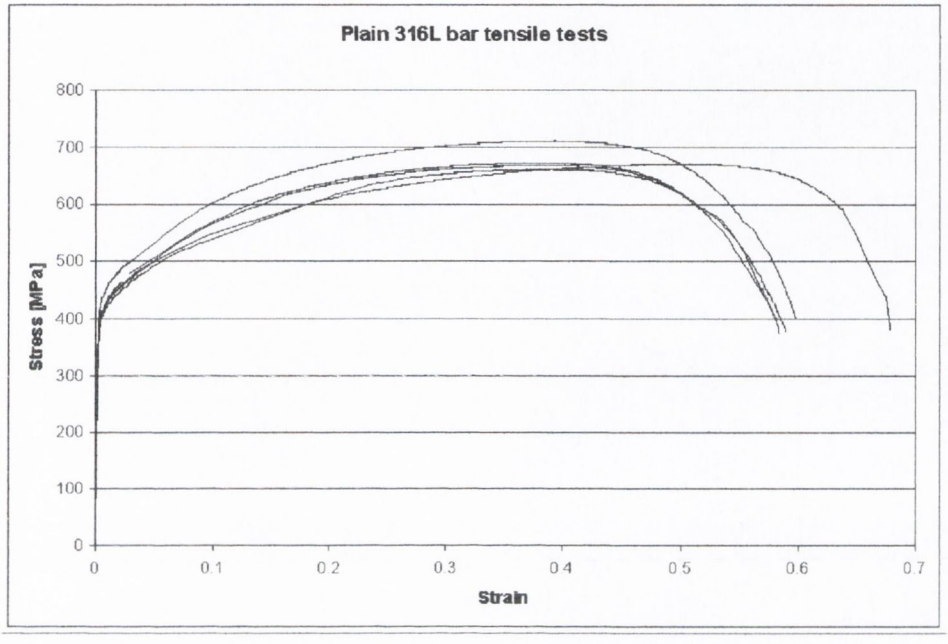

Fig. 5.2.2 Plain macro-scale bar tensile curves

Table 5.2.1 Summary of tensile results of plain 316L macro-scale bars

	0.2% proof stress [MPa]	**Elastic Limit [MPa]**	**UTS [MPa]**	**Young's Modulus [GPa]**	**Strain to failure (extensometer)**
316L macro-scale bar	396	290	754	177	0.61 in 12.5 mm

Notched 316L macro-scale bar tensile results

Fig. 5.2.3 shows the curves resulting from the three tensile tests carried out on 316L stainless steel notched bar specimens. Nominal strain was calculated using the distance between the grips: 22 mm. The 0.2% proof stress could not be calculated from nominal strain, therefore, only the elastic limit was determined.

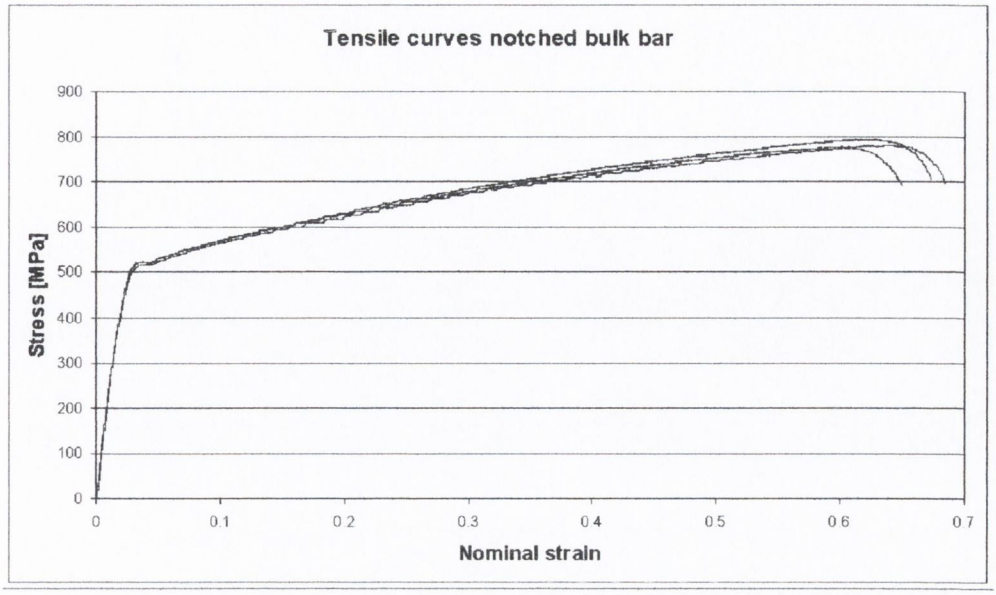

Fig. 5.2.3 Notched macro-scale bar tensile curves

Table 5.2.2 Summary of tensile results of notched 316L macro-scale bars

	Elastic Limit [MPa]	**UTS [MPa]**	**Nominal strain to failure**
316L macro-scale bar	300	780	0.67 in 22 mm

5.2.2 Tensile results of 316L micro-scale wire and tubing samples

The different 316L micro-scale geometries were described in section 4.7.2. Apart from plain specimens, tensile tests were carried out on the three types of Double Edge Notch Tension (DENT) specimens and three types of slotted tubing pieces.

Plain 316L micro-scale wire tensile results

Fig. 5.2.4 shows the results of the five tensile tests carried out on plain microscopic wire specimens. Four of the five specimens were annealed and electro-polished in the same way as stents, the fifth specimen did not undergo the annealing and electro-polishing processes. Strain is calculated for a gauge length of 5 mm. The corresponding distance between the grips was 10 mm.

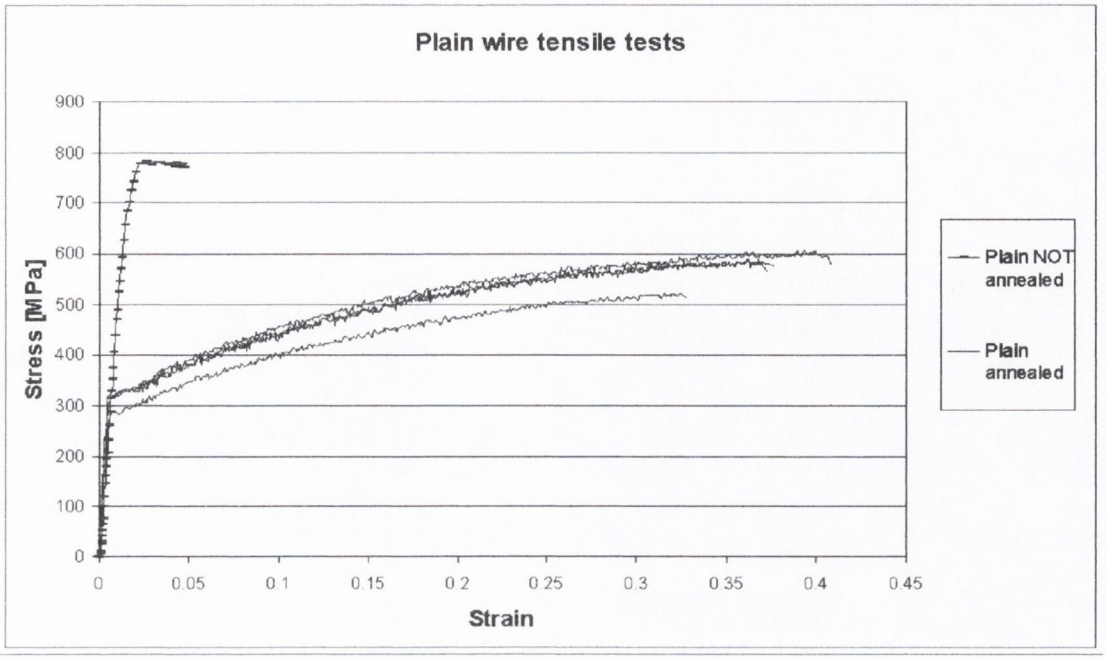

Fig. 5.2.4 Plain wire tensile curves

The sample that did not undergo the annealing and electro-polishing processes has a higher *UTS* and less strain to failure. All four annealed specimen tensile curves are very similar.

Table 5.2.3 Summary of tensile results of plain 316L micro-scale wires

	0.2% proof stress [MPa]	**Elastic Limit [MPa]**	**UTS [MPa]**	**Strain to failure**
Un-annealed sample	680	660	780	0.048 in 5 mm
Annealed samples	315	300	580	0.37 in 5 mm

Notched 316L micro-scale wire tensile results

Fig 5.2.5 shows the tensile curves of the three types of notched wire specimens. Nominal strain was determined using the distance between the grips; 10 mm. No tensile tests were carried out on the FIB50 geometry because there were not enough specimens.

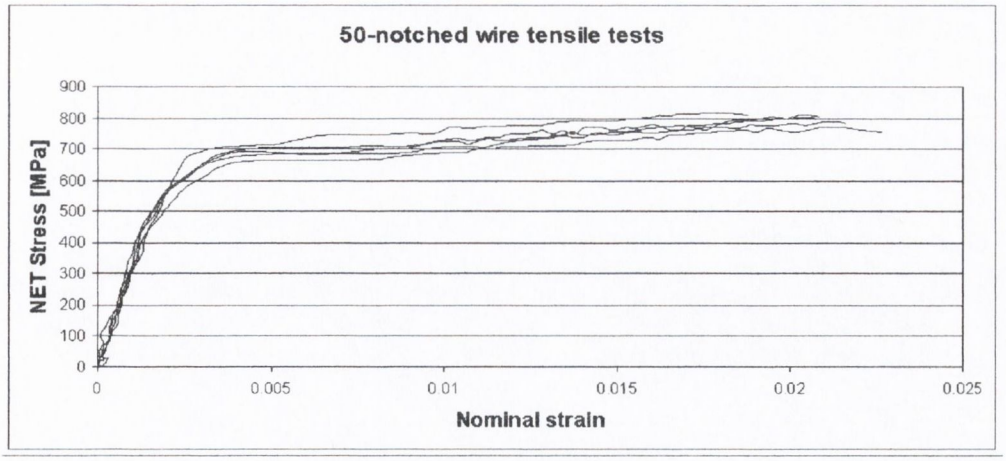

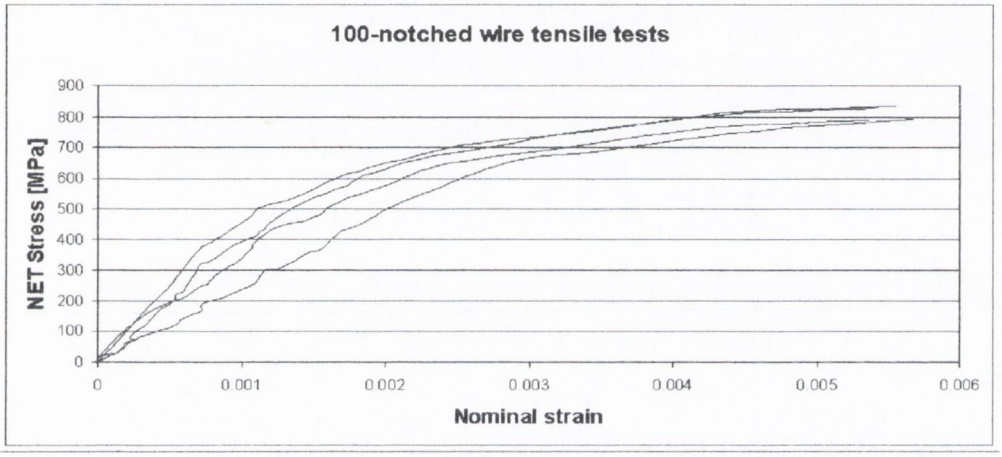

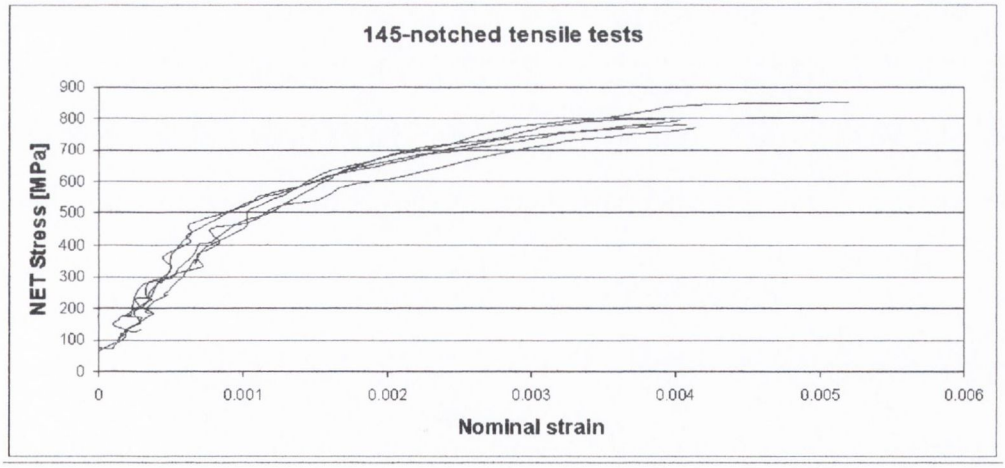

Fig. 5.2.5a) 50-notch wire tensile curves

b) 100-notch wire tensile curves

c) 145-notch wire tensile curves

The tensile strength for all types of wires was around 800 MPa. But the nominal strain to failure changes substantially with the notch depth. The 50-notch experiences a much higher strain to failure than the 100- and the 145-notch samples.

Table 5.2.4 Summary of tensile results of notched 316L micro-scale wires

	Elastic limit [MPa]	***UTS* [MPa]**	**Nominal strain to failure**
50 micron notch	300	790	0.022 in 10 mm
100 micron notch	375	800	0.0055 in 10 mm
145 micron notch	350	800	0.0045 in 10 mm

Determining the elastic limits of the microscopic notched wire specimens was difficult, because the tensile curves are slightly irregular at the beginning.

Notched 316L micro-scale tubing tensile results

The geometries of the three types of notched micro-scale tubing samples were given in detail in section 4.7.2. Fig. 5.2.6 displays the results of the tensile tests done on the tubing specimens. The nominal strain is determined using the distance between the grips; 10 mm. It was not possible to test the 60 holed specimens to failure, because the capacity of the 250N load cell was insufficient.

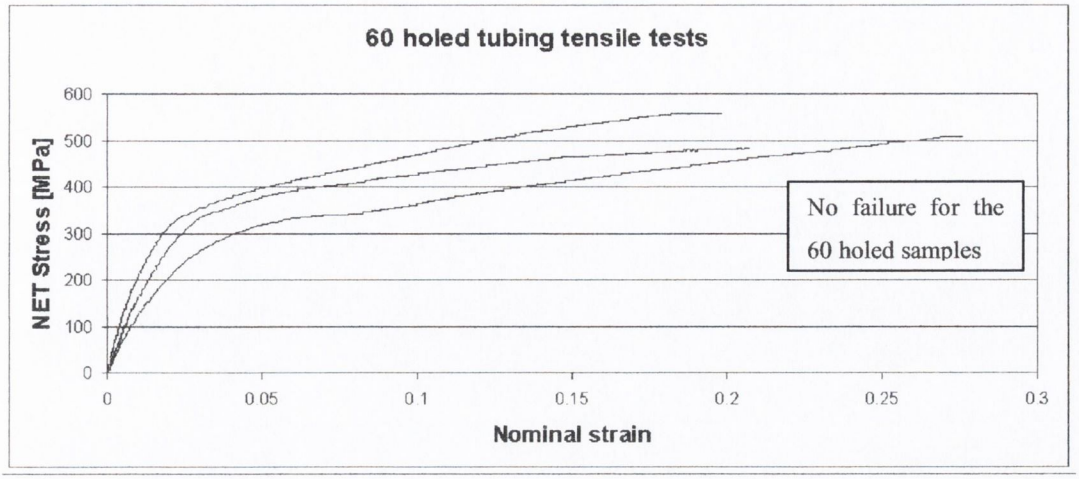

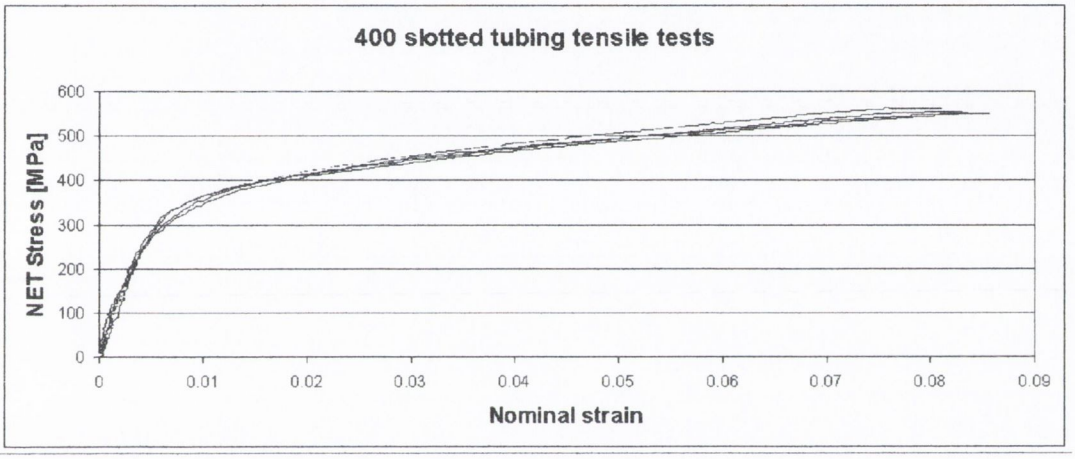

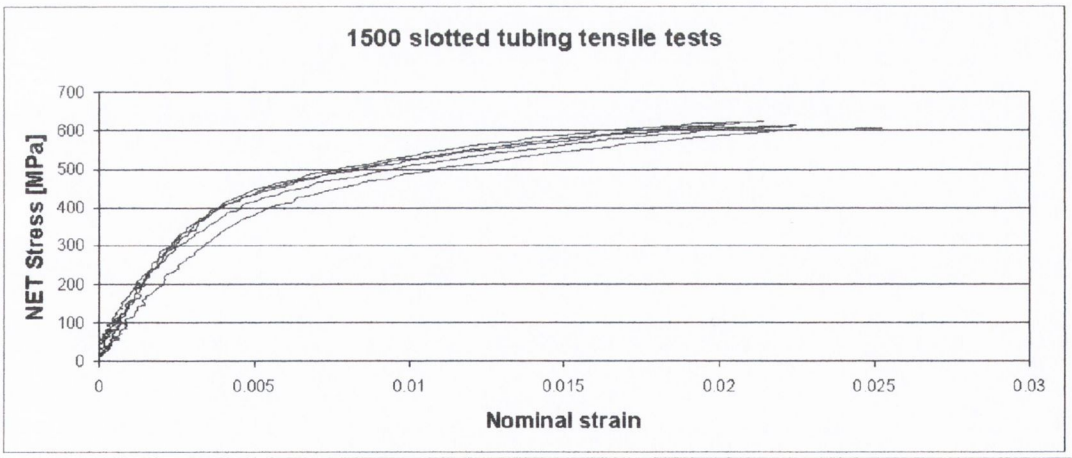

Fig. 5.2.6a) 60-holed tubing tensile curves

b) 400 slotted tubing tensile curves

c) 1500 slotted tubing tensile curves

Table 5.2.5 Summary of tensile results of notched 316L micro-scale tubing pieces

	Elastic limit [MPa]	***UTS* [MPa]**	**Nominal strain to failure**
60 holed notch	180	N/a	N/a
400 slotted notch	290	580	0.08 in 10 mm
1500 slotted notch	330	640	0.0022 in 10 mm

5.2.3 Tensile results of aluminium macro-scale plates

The geometry of the plain 0.5 mm thick macro-scale aluminium plate was given in section 4.7.3. One tensile test was done on a plain aluminium macroscopic plate, however, it was not tested until failure because of an error during the test. Nevertheless, the graph gives a good indication of material properties such as the proof stress and the Young's Modulus. Also the *UTS* was determined, because from Fig. 5.2.7 it is not likely that the stress would have increased if the specimen was tested to failure. An extensometer was used to determine the Young's Modulus.

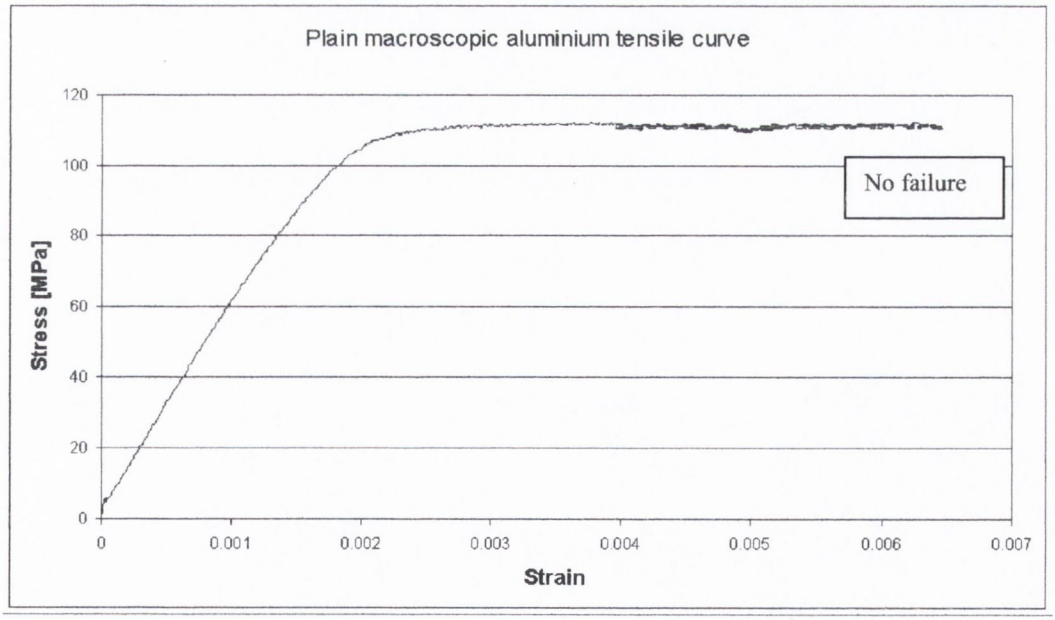

Fig. 5.2.7 Plain macro-scale aluminium tensile results

Table 5.2.6 Summary of tensile results of aluminium macro-scale plate sample

	0.2% proof stress [MPa]	**Elastic limit [MPa]**	***UTS* [MPa]**	**Young's Modulus [GPa]**	**Strain to failure**
Plain	113	113	113	65	N/a

5.2.4 Tensile results of aluminium micro-scale plates

Plain and notched aluminium micro-scale plate tensile results

The geometry of the micro-scale aluminium Single Edge Notch Tension plate specimen was discussed in section 4.7.4. The curves of two plain and one notched tensile tests are given in Fig. 5.2.8. The gauge length of the plain specimens was 7.5 mm and the distance between the grips for the notched specimens was: 20 mm.

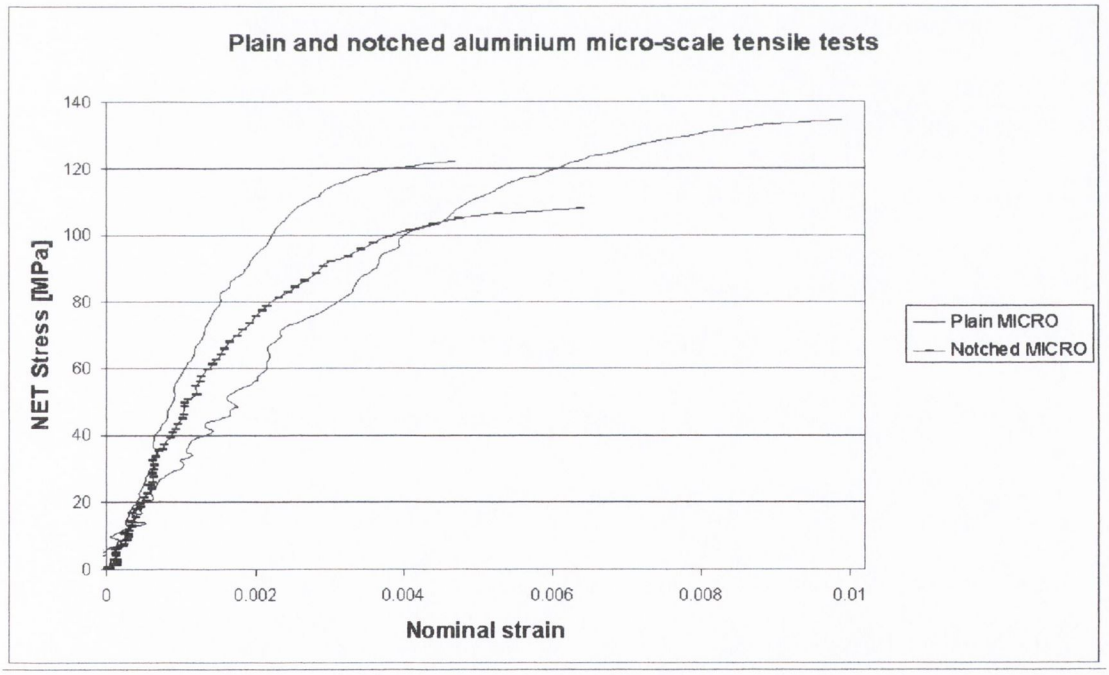

Fig. 5.2.8 SENT aluminium micro-scale tensile results

Table 5.2.7 Summary of tensile results of aluminium micro-scale plate samples

	Elastic limit [MPa]	***UTS* [MPa]**	**Nominal strain to failure**
Plain	60	135	0.0075 in 7.5 mm
Notch	60	108	0.0064 in 20 mm

5.3 Fatigue Results

Fatigue tests were carried out on the same type of specimens as were used for the tensile tests. The experimental fatigue data was plotted in *Stress* vs. *Number of cycles to failure* plots to determine the fatigue limits. Unless stated otherwise, failure was defined as the fracture of the sample into two (or more) separate pieces.

5.3.1 Fatigue results of 316L macro-scale bar samples

The geometries of the plain and circumferentially notched bar specimens were given in section 4.7.1.

Plain 316L macro-scale bar fatigue results

Fig. 5.3.1 shows the fatigue data of the plain 316L macroscopic stainless steel bar cycled at an R-ratio of 0.1.

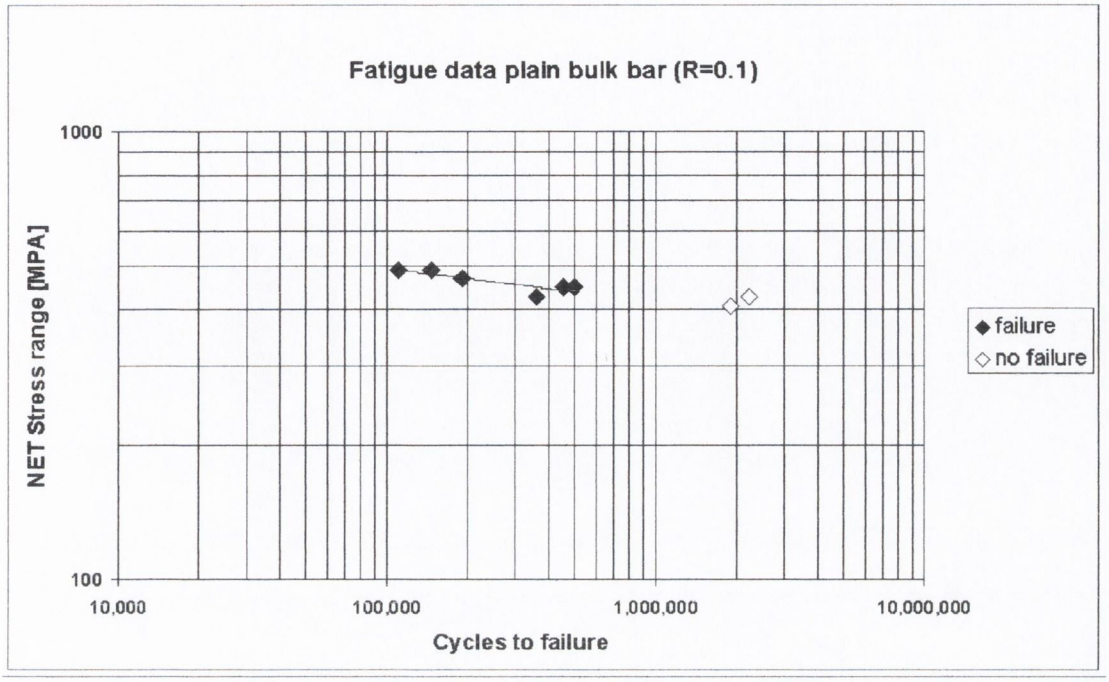

Fig. 5.3.1 Fatigue data for plain 316L bar specimens at R=0.1

The fatigue limit was determined by adding a trendline through the failure points and determining the corresponding fatigue limit at 2 million cycles, provided that the non failure points agreed with that fatigue limit. The plain stainless steel macro-scale specimens showed substantial straining during the test. The Instron test machine was set to stop fatigue cycling at a displacement of 2 mm. The specimens had not broken into two separate pieces at that stage, but were substantially cracked. The choice was made not to cycle to failure into two separate pieces, because that would not have resulted in a significant increase in cycles to failure. The slope of the trendline was determined and the equivalent k value, which is equal to 1/slope.

Table 5.3.1 Fatigue limit of plain 316L stainless steel macro-scale bar samples

	Fatigue limit R=0.1 at net for 2 million cycles	**Slope**	***k*** **(1/slope)**
Plain bar	420 MPa	0.104	9.58

Notched 316L macro-scale bar fatigue results

Fig. 5.3.2 shows the fatigue results of the notched 316L stainless steel bar specimens. Two loading ratios were tested: R=0.1 and R=0.8 The loading ratio of 0.8 was used to determine the closure-free, effective threshold of the material.

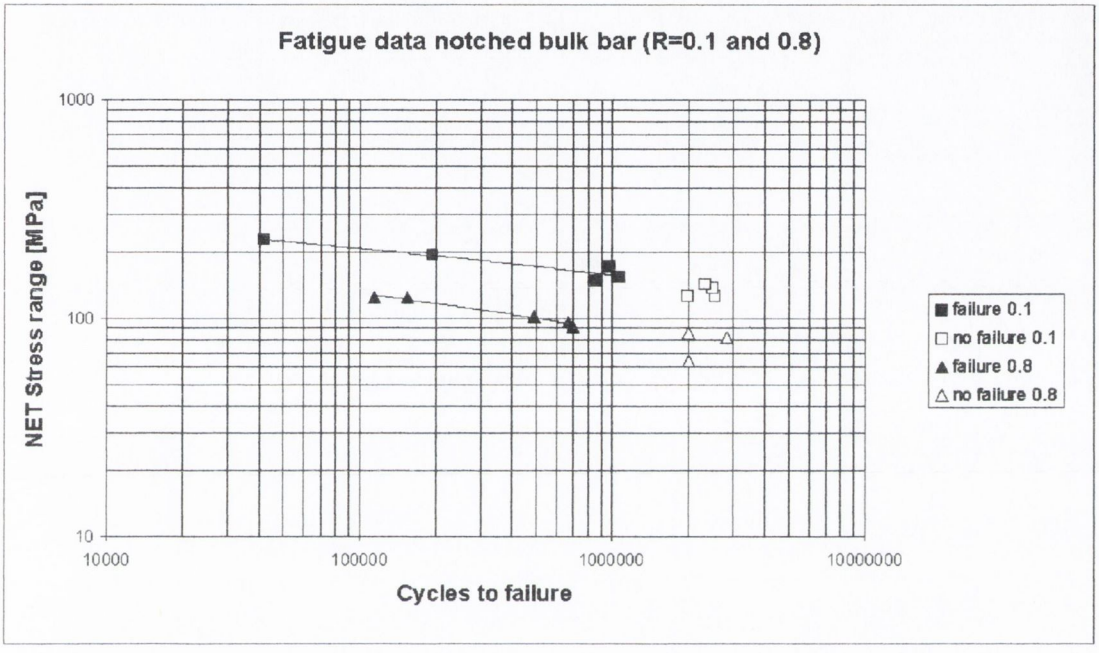

Fig. 5.3.2 Fatigue data for notched 316L bar specimens at R=0.1 and R=0.8

Table 5.3.2 Fatigue limit of notched 316L stainless steel macro-scale bar samples

	Fatigue limit at net for 2 million cycles	**Slope**	***k*** **(1/slope)**
Notched bar R=0.1	150 MPa	0.14	7.13
Notched bar R=0.8	75 MPa	0.23	4.269

5.3.2 Fatigue results of 316L micro-scale wire and tubing samples

The geometries of the plain and notched 316L stainless steel micro-scale wires were given in section 4.7.2. All specimens, which have a thickness of roughly 90 μm, were tested at an R ratio of 0.1.

Plain 316L micro-scale wire fatigue results

The bulk of the plain wire fatigue tests was carried out on specimens that were annealed and electro-polished, similar to stents. However, three plain specimens were tested that did not undergo the annealing and electro-polishing process, see Fig. 5.3.3.

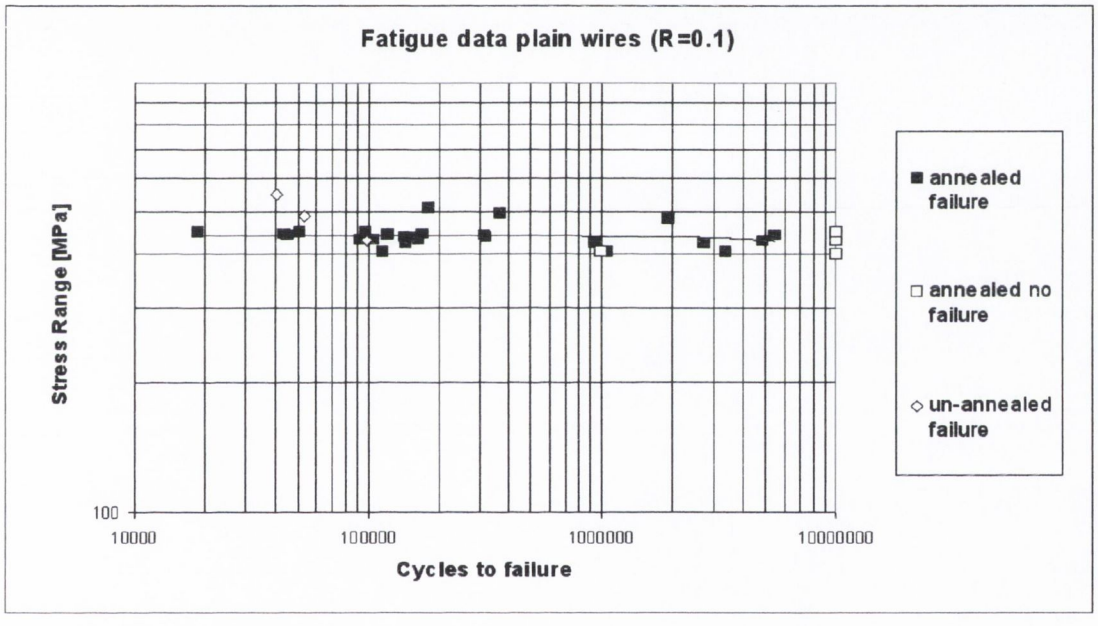

Fig. 5.3.3 Fatigue data for plain wire specimens

The fatigue limit for the annealed specimens, determined at the net section area for 2 million cycles was 420 MPa. There were too few un-annealed specimens to determine a proper fatigue limit. Adding the un-annealed fatigue data to the annealed fatigue data does not change this fatigue limit value, although there is more scatter. Annealing appears to have little effect on the fatigue behaviour.

Table 5.3.3 Fatigue limit of plain 316L stainless steel micro-scale wire samples

	Fatigue limit at net for 2 million cycles	**Slope**	***k*** **(1/slope)**
Plain	420 MPa	0.0058	173

As Table 5.3.3 shows, the line on Fig. 5.3.3 is almost perfectly horizontal.

Notched 316L micro-scale wire fatigue results

Fig. 5.3.4 shows the *notched* specimen fatigue data for the 50-, the 100- and the 145-micron notches and the FIB50 notch. The specimen geometry of these samples was given in section 4.7.2.

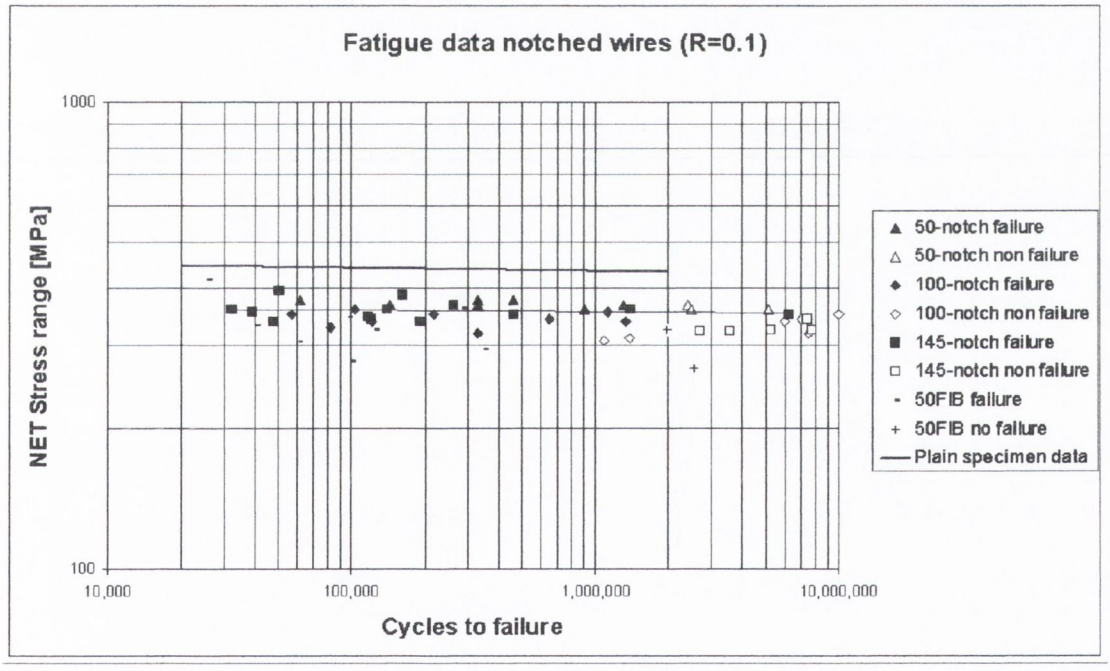

Fig. 5.3.4 Fatigue data for notched specimens

Even though the 50-, 100- and 145-micron notches have different depths, they give similar fatigue limits at 2 million cycles at the net section. The FIB50 notch has a slightly lower fatigue limit; again the slopes of the lines are very low.

Table 5.3.4 Fatigue limits for 316L wire samples

	Fatigue limit at net for 2 million cycles	**Slope**	***k*** **(1/slope)**
50-notch	360 MPa	0.009	111
100-notch	355 MPa	0.0017	586
145-notch	350 MPa	0.0039	259
FIB50	320 MPa	0.067	14.6

Notched 316L micro-scale tubing fatigue results

Fig. 5.3.5 shows the *notched* specimen fatigue data for the 60 holed and the 400 and 1500 slotted tubing samples, which geometry was discussed in section 4.7.2.

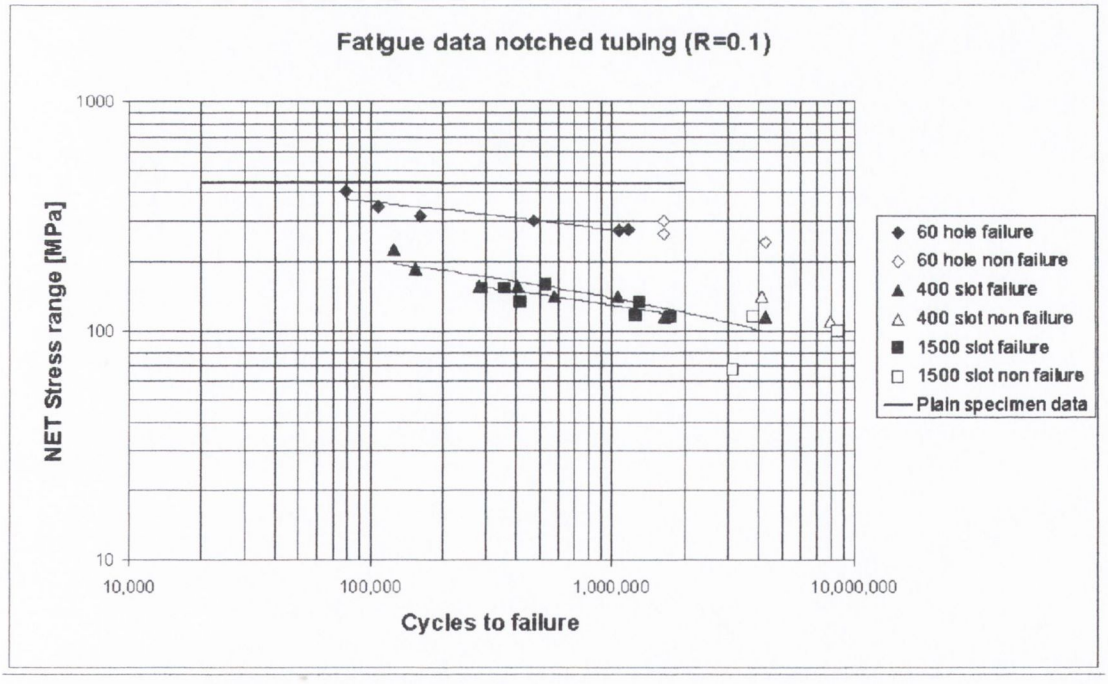

Fig. 5.3.5 Fatigue data for notched tubing specimens

Table 5.3.5 Fatigue limits for 316L tubing samples

	Fatigue limit at net for 2 million cycles	**Slope**	***k*** **(1/slope)**
60 hole	250 MPa	0.127	7.89
400 slot	120 MPa	0.174	5.74
1500 slot	115 MPa	0.15	6.51

The fatigue limits for the 400 and the 1500 slotted specimens are similar. The slopes of the slotted tubing data are larger than the slopes found for the wire specimens.

5.3.3 Fatigue results of aluminium macro-scale plate samples

Fig. 5.3.6 shows the fatigue data of the 0.5 mm thick plain macro-scale aluminium specimens. The fatigue limit of the macro-scale notched aluminium plate was determined by [Bellett, 2002].

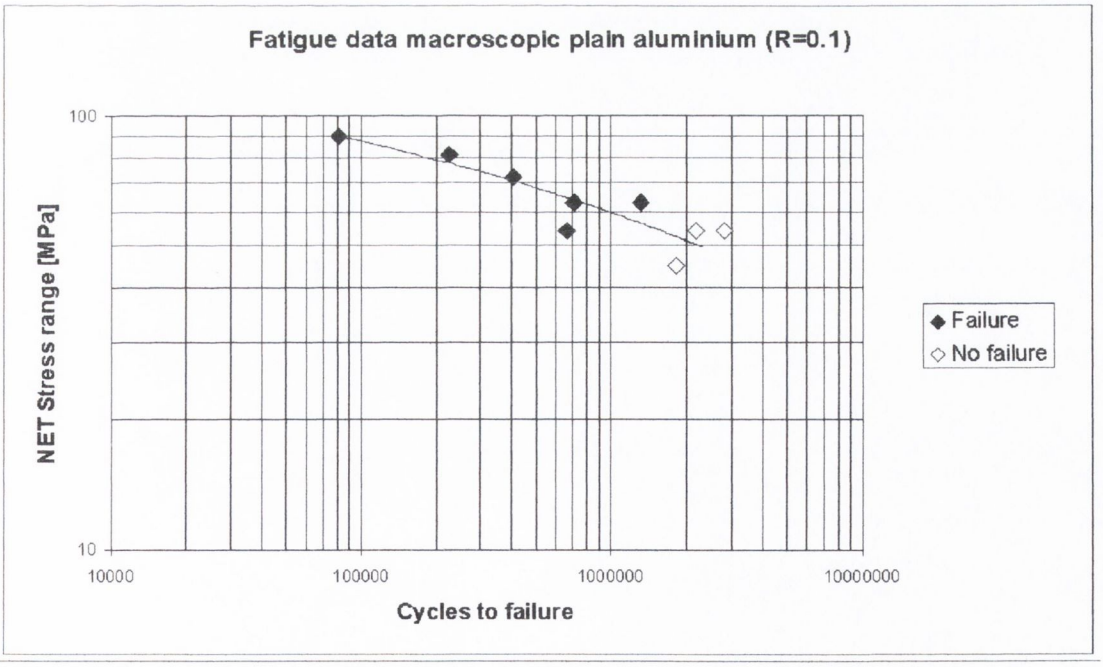

Fig. 5.3.6 Fatigue results of plain macro-scale aluminium specimens

Table 5.3.6 Plain and notched macro-scale aluminium fatigue limits

	Fatigue limit at net for 2 million cycles	**Slope**	***k*** **(1/slope)**
Plain aluminium	55 MPa	0.176	5.67
SENT aluminium	9 MPa [Bellett, 2002]		

5.3.4 Fatigue results of aluminium micro-scale samples

Plain and notched aluminium micro-scale plate fatigue results

Fig. 5.3.7 shows the fatigue data of 0.5 mm thick plain and notched micro-scale aluminium plates, which geometry was described in section 4.7.4. The fatigue limits were determined at the net section at 2 million cycles.

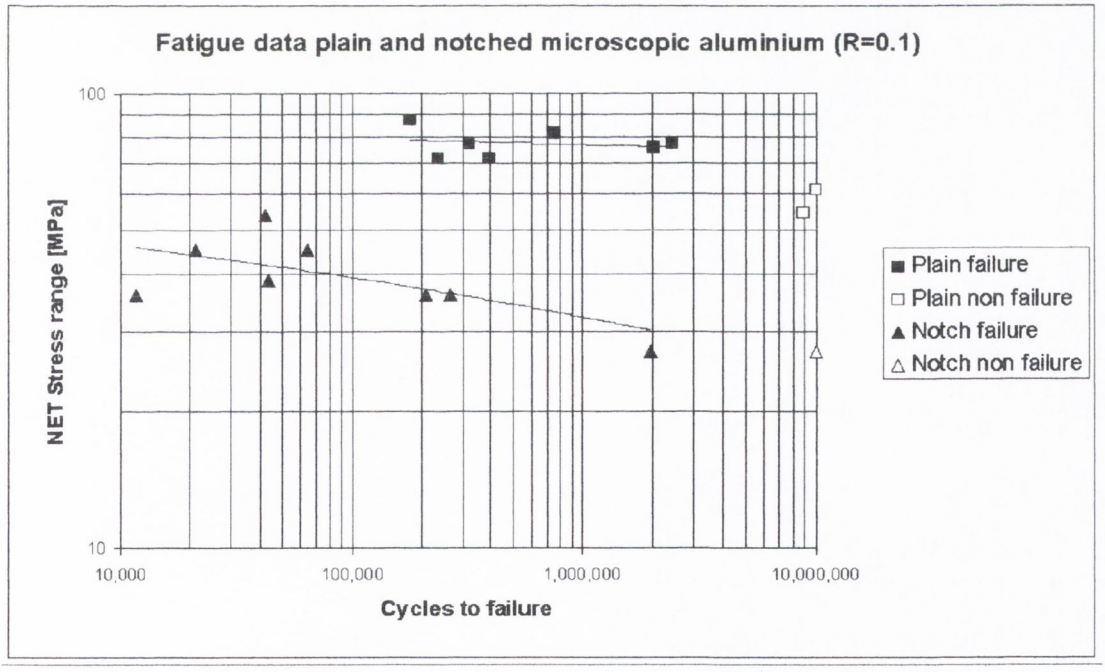

Fig. 5.3.7 Fatigue results of plain and notched micro-scale aluminium specimens

Table 5.3.7 Plain and notched micro-scale aluminium fatigue limits

	Fatigue limit at net for 2 million cycles	**Slope**	***k*** **(1/slope)**
Plain aluminium	75 MPa	0.012	88.57
SENT aluminium	30 MPa	0.081	12.30

For the plain microscopic aluminium specimens, the line shown in Fig. 5.3.7 is nearly horizontal. For the notched samples, the slope is also very low.

5.4 Stress Intensity Factor Threshold and Critical Distance values

From the experimental macroscopic stainless steel and aluminium data, the stress intensity threshold, ΔK_{th}, was calculated. Three approaches could be taken:

- Determining the threshold through the ΔK equation at the fatigue limit *(equation)*
- Determining the threshold via the critical distance through the stress distance curve at the fatigue limit *(FEA)*
- Determining the threshold using the Crack Modelling Method at the fatigue limit *(CMM)*

All three approaches will be discussed in more detail. They should give a similar value for the threshold.

Apart from the macroscopic material threshold, three reduced threshold values were proposed for the microscopic specimens:

- ΔK_{th_width}
- ΔK_{effth}
- ΔK_{th_exp}

The values for these thresholds are calculated respectively in sections 5.4.2, 5.4.3 and 5.4.4.

5.4.1 Determining the macroscopic thresholds and critical distances

The macroscopic thresholds and critical distances were calculated for the experimental fatigue results, using the three approaches mentioned above: Equation, FEA (stress distance curve) and Crack Modelling Method. The equation used to calculate the threshold for the macroscopic specimens assumes that the notch is a crack, following Smith and Miller's idea's:

$$\Delta K_{th} = F_{NET} \Delta \sigma_{on} \sqrt{\pi D} \qquad (5\text{-}4\text{-}1)$$

The required experimental details and the actual value for the threshold calculated through the equation are given in Table 5.4.1.

Table 5.4.1 Results for threshold and critical distance for the macroscopic materials

	$\Delta\sigma_o$ [MPa]	$\Delta\sigma_{on}$ [MPa]	F_{NET}	D [mm]	ΔK_{th} [MPa√m]	L [mm]
Stainless steel	420	150	0.936	1	7.87	0.11
Aluminium	55	12.9	1.16	15	3.25	1.11

Secondly, the threshold was determined through *FEA* (stress distance curve). From the critical distance, one can calculate the corresponding threshold value for the material. The theory behind the critical distance implies that a specimen will fail when the stress at the critical distance is equal to the critical stress of the material; in the case of fatigue that is the plain fatigue limit. Therefore, by applying the fatigue limit stress range of the macroscopic notched component to the ANSYS model, at the critical distance the stress is equal to respectively 420 MPa and 55 MPa for the stainless steel and the aluminium. Since in this exercise the Point Method is used, the critical distance value measured is actually $L/2$.

Fig. 5.4.1 shows the critical distance curves at the notched fatigue limits of both the stainless steel and the aluminium. The minimum value on the y-axis is the plain specimen fatigue limit for that material. Therefore, multiplying the distance where the curve crosses the x-axis by 2, will give the critical distance value L. The corresponding threshold value can then be calculated through equation 5-4-2:

$$\Delta K_{th} = \Delta\sigma_o \sqrt{\pi L} \tag{5-4-2}$$

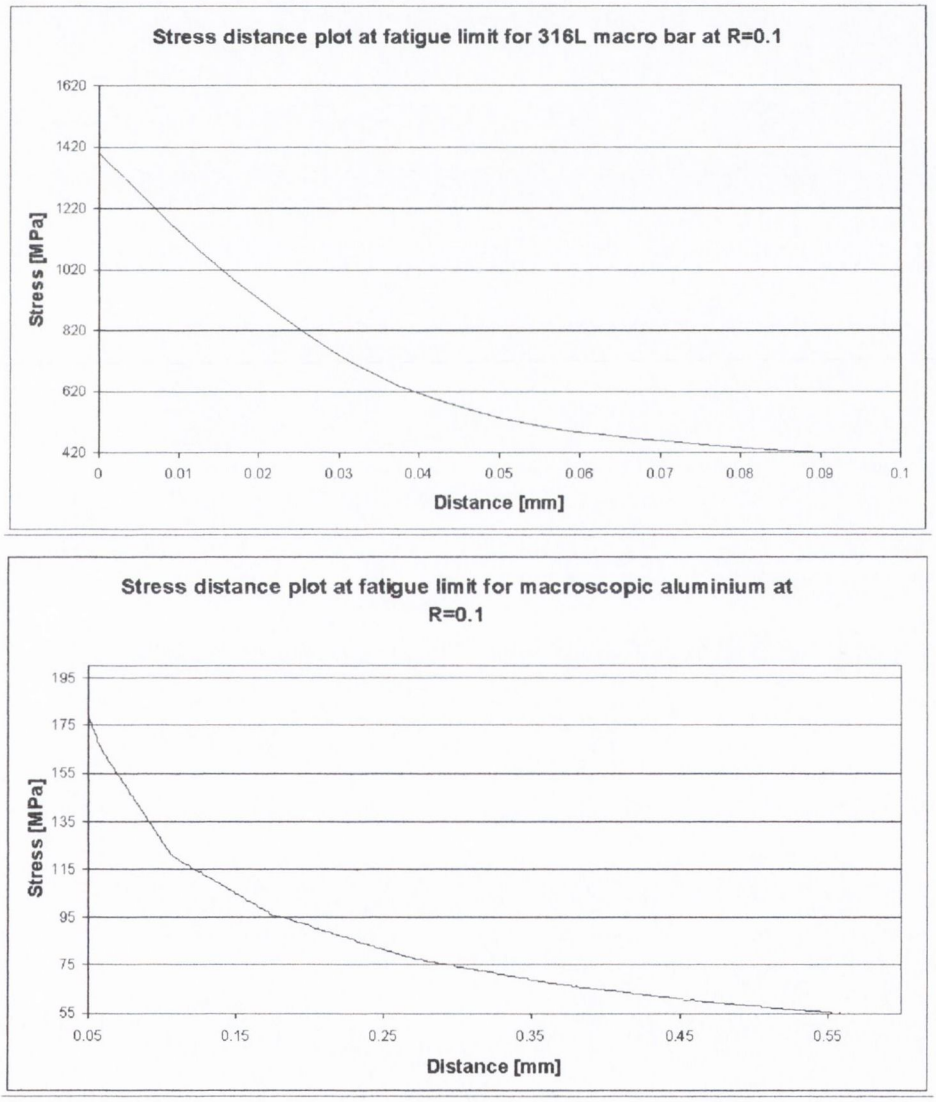

Fig. 5.4.1 Stress distance curves at the fatigue limit for macroscopic specimens

Table 5.4.2 Critical distance values and corresponding thresholds through *FEA* curves

	$\Delta\sigma_o$ [MPa]	$\Delta\sigma_{on}$ [MPa]	F_{NET}	D [mm]	ΔK_{th} [MPa√m]	L [mm]
Stainless steel	420	150	0.936	1	9.71	0.17
Aluminium	55	12.9	1.16	15	3.23	1.10

The third and final method of calculating the material threshold uses the Crack Modelling Method. This method determines a K value from the critical distance curve. When the stress distance curve is plotted at the fatigue limit of the notched specimen, the corresponding K value will therefore be the threshold. This method has been implemented in software and the results are given in Table 5.4.3.

Table 5.4.3 Critical distance values and corresponding thresholds through the *CMM*

	ΔK_{th} [MPa√m]	L [mm]
Stainless steel	8.45	0.13
Aluminium	3.21	1.08

Three different values for the long crack threshold value were calculated. In the case of the aluminium, one extra threshold value can be added, which was determined by Bellett through a *da/dN* plot (Bellett, 2002). Table 5.4.4 summarises the different values for the threshold in the macroscopic stainless steel and aluminium.

Table 5.4.4 Summary of calculated threshold values for the macroscopic materials

	ΔK_{th} Equation [MPa√m]	ΔK_{th} FEA curve [MPa√m]	ΔK_{th} CMM [MPa√m]	ΔK_{th} Bellett [MPa√m]
Stainless steel	7.87	9.71	8.45	N/a
Aluminium	3.25	3.23	3.21	2.8

The three calculated values for the aluminium are very consistent. The reason why the threshold determined by Bellett is slightly lower, is difficult to say. His value of the threshold was determined by decreasing the applied load in steps until the long crack stopped growing. The equation calculates the threshold for the material assuming that the notch is in fact a crack. This normally works well for sharp notches. And it works in this case as well, because the difference between the equation and Bellett's value is not that large.

More scatter is found in the calculations for the stainless steel thresholds. For further calculations, the threshold determined through the equation will be used, since the equation should describe the stress concentration in the specimens. The Point Method predictions are made using *FEA* and since the *FEA* threshold is larger than the equation threshold, an error is expected of around 20%. Table 5.4.5 gives the final values for the thresholds for the macroscopic stainless steel and aluminium and the corresponding critical distance values.

Table 5.4.5 Final values for macroscopic thresholds and critical distances

	ΔK_{th} MPa$\sqrt{m}$]	L [mm]
Stainless steel	**7.87**	**0.11**
Aluminium	**3.25**	**1.11**

5.4.2 Determining ΔK_{th_width} for the microscopic specimens

The threshold value for long cracks is a constant, but it reduces for short cracks. A crack can never grow longer than the net width of a specimen. In the case of microscopic components, the maximum crack length is so small that the constant threshold value can never be reached. ΔK_{th_width} corresponds to the maximum threshold value that can be obtained by this limited maximum crack length. The value for ΔK_{th_width} can be calculated using the resistance curve method (equation 5-4-3) as discussed in section 3.2.1.

$$\Delta K_{th\_width} = \sqrt{\frac{a}{a + a_o}} \Delta K_{th} \qquad (5\text{-}4\text{-}3)$$

where crack length a is the maximum crack length, which is equal to the width of the specimen at the notch, a_o is El Haddad's short crack parameter and ΔK_{th} is the long crack threshold value. The results are given in Table 5.4.6.

Table 5.4.6 Summary of the threshold values based on the net width of the specimens

MICRO specimens	$\Delta\sigma_o$ **[MPa]**	F_{NET}	a (net width) **[mm]**	a_o **[mm]**	ΔK_{th_width} **[MPa√m]**	L **[mm]**
316L stainless steel						
50-wire	420	0.605	0.11	0.305	**4.05**	**0.03**
100-wire	420	0.455	0.11	0.539	**3.238**	**0.019**
145-wire	420	0.385	0.11	0.753	**2.808**	**0.014**
FIB50	420	0.596	0.109	0.314	**3.991**	**0.029**
60-hole	420	0.978	2.61	0.117	**7.696**	**0.107**
400-slot	420	0.862	2.27	0.15	**7.618**	**0.105**
1500-slot	420	0.550	1.17	0.369	**6.858**	**0.085**
Aluminium						
Single edge notch	55	1.414	1.5	0.556	**2.776**	**0.811**

5.4.3 Determining ΔK_{effth}

The effective threshold is the closure-free threshold of the material. This threshold value was determined experimentally for the stainless steel by fatigue cycling at a loading ratio R of 0.8. At that ratio no closure is expected to occur. The only approach to calculate the effective threshold is through equation 5-4-1, because the plain fatigue limit was not determined experimentally at an R ratio of 0.8. The material work hardens substantially and therefore,

the maximum stress required to break the specimens lies above the *UTS*. Table 5.4.7 gives the closure-free threshold value. This value is then used in combination with the plain fatigue limit at an R ratio of 0.1 (420 MPa) to calculate the effective critical distance, L_{eff}.

Table 5.4.7 Results for effective threshold and effective critical distance

	$\Delta\sigma_o$ R=0.1 [MPa]	$\Delta\sigma_{on}$ R=0.8 [MPa]	F_{NET}	D [mm]	ΔK_{eff} [MPa√m]	L_{eff} [mm]
Stainless steel	420	75	0.936	1	**3.93**	**0.0279**

5.4.4 Determining ΔK_{th_exp} for the microscopic specimens

The experimental threshold values for the microscopic material can be determined through the same three approaches as used for the macro-scale material: using the equation, using *FEA* (stress distance curve) and using the *CMM*.

Equations 5-4-4 and 5-4-5 apply to short cracks and are used to calculate the microscopic threshold values and critical distances for the experimental data.

$$\Delta K_{th} = \Delta\sigma_o \sqrt{\pi L} \tag{5-4-4}$$

$$\Delta K_{th} = F\Delta\sigma_{on} \sqrt{\pi (D + L)} \tag{5-4-5}$$

Fig. 5.4.2 shows the stress distance curves for the micro-scale stainless steel and aluminium specimens at the fatigue limit. These curves were used to determine the critical distance value for the materials, which in turn determine the fatigue threshold values for the microscopic specimens.

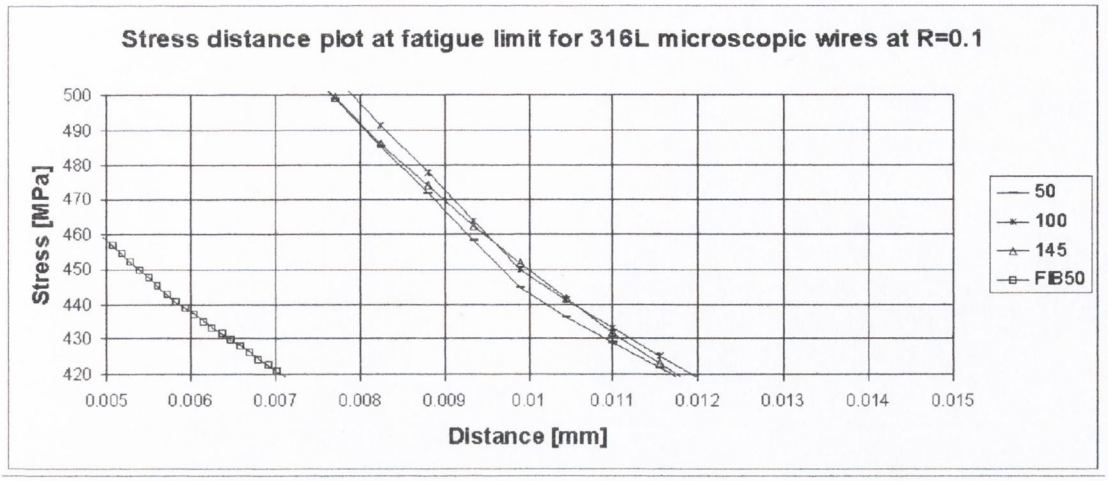

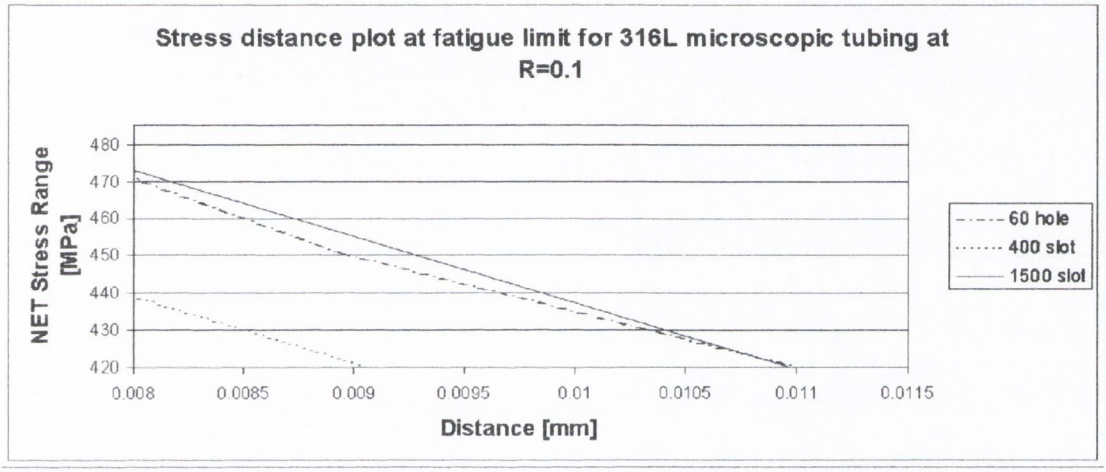

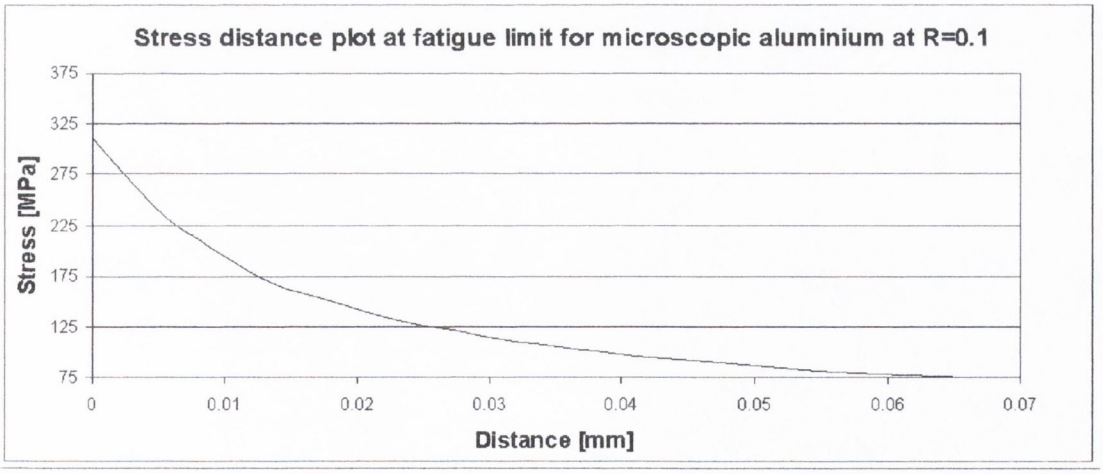

Fig. 5.4.2 Stress distance curves at the fatigue limit for the microscopic specimens

Table 5.4.8 summarises the results for the different micro-scale threshold values. The value for the threshold obtained through the equation will be used in future calculations, therefore for that threshold the corresponding critical distance was calculated. This threshold should give good predictions using the Smith and Miller method, because they use similar equations and they also assume that sharp notches behave like cracks.

Table 5.4.8 Summary of the threshold values and critical distances for micro-scale specimens

MICRO specimens	ΔK_{th} FEA curve [MPa√m]	ΔK_{th} CMM [MPa√m]	ΔK_{th} **Equation [MPa√m]**	L **Equation [mm]**
316L stainless steel				
50-wire	3.59	2.97	2.73	0.018
100-wire	3.63	3.08	2.89	0.017
145-wire	3.60	3.19	2.91	0.017
FIB50	2.79	2.32	2.43	0.013
60-hole	3.49	2.66	2.38	0.015
400-slot	3.16	2.73	2.59	0.013
1500-slot	3.44	3.17	3.07	0.017
Average values stainless steel			**2.71**	**0.0158**
Aluminium				
Single edge notch	1.52	1.76	**3.532**	**0.706**

The stainless steel experimental threshold values based on the equations agree very well: ΔK_{th} and L are obviously constant. For the *FEA* curve, the threshold values are higher than for the equation values and there is more scatter. For the aluminium however, the difference between the *equation* and the *FEA/CMM* is nearly a factor of 2. This difference will be discussed in chapter seven; discussion of the aluminium results.

5.5 Hardness Results

Hardness tests were done on all types of specimens with the Mitutoyo MVK-H1.

Table 5.5.1 Hardness measurements on tested samples

	Hardness H_V
MICRO-SCALE	
316L un-annealed plain wire	312
316L annealed plain wire	170
316L 50-notch wire	154
316L 100-notch wire	157
316L 145-notch wire	162
316L 60 holed tubing	162
316L 400 slotted tubing	156
316L 1500 slotted tubing	159
316L FIB 50-notch	158
Aluminium plain plate	37
Aluminium SENT plate	35

	Hardness H_V
MACRO-SCALE	
316Lannealed plain bar	186
316L annealed notched bar	191
Aluminium plain plate	37
Aluminium SENT plate	40

Chapter 6 Discussion of the 316L stainless steel results

In this chapter the fracture and fatigue results of the 316L stainless steel specimens are discussed and a comparison is made with the prediction methods, which were explained in chapters 2 and 3. The geometries of the tested microscopic specimen are shown in Fig. 6.1.1: 3 types of notched wire specimens, and 3 types of slotted tubing specimens. The last type is a variation on the 50-notched wire, the FIB50-wire, which was sharpened to a root radius of 1 micron using the Focussed Ion Beam (FIB) process. Detailed descriptions of the specimen geometries can be found in section 4.7.

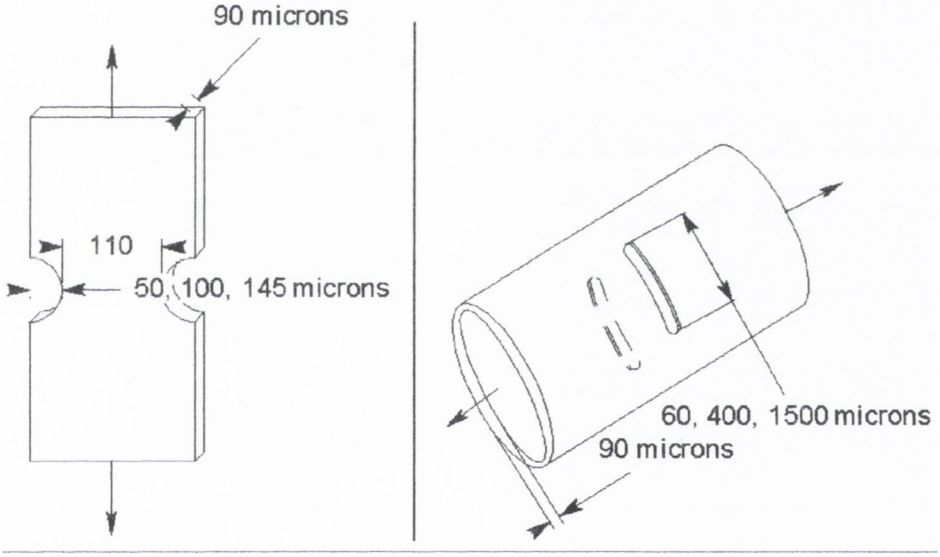

Fig. 6.1.1 Specimen geometries microscopic 316L stainless steel specimens

6.1 Discussion of 316L stainless steel tensile results

The results and graphs of the tensile tests were given in section 5.2, however, it is interesting to have a closer look at them to see if there are unusual things occurring.

6.1.1 Plain annealed and un-annealed wire tensile results

Fig. 6.1.2 shows the tensile curves of the plain specimens. All specimens were annealed, except for one plain un-annealed wire.

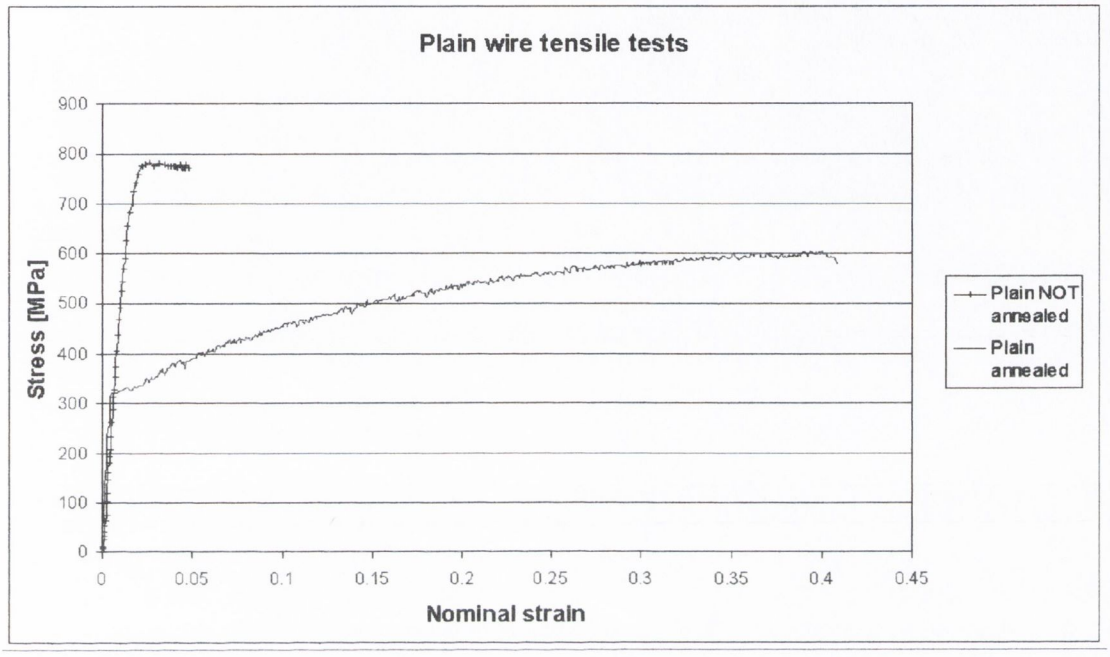

Fig. 6.1.2 Tensile curves for plain wire specimens

The value for the Young's Modulus of these small specimens was also calculated. Determining the value of Young's Modulus was not an aim of this research, but an interesting aspect to investigate. The average Young's Modulus value for the 316L stainless steel measured from *macro-scale* experimental tests was 177 GPa.

The problem with these small specimens is that no extensometer was used to measure the strain, because of the fragility of the specimens. Therefore, the displacement of the actuator had to be used to determine the Young's Modulus. This method is not the most accurate, but nevertheless an attempt was made. The specimens were manufactured as conventional 'dogbone' shaped samples. Two correction factors were used:

- Correction to account for the strain in the testing machine
- Correction to determine strain at net area, eliminating strain at the bigger grip ends

The strain in the testing machine, the MTS Tytron (including grips), can be determined using a dummy specimen. A very large piece of steel is gripped and a tensile test is conducted over the same force range as used for the wire specimens. The dummy specimen is so large and stiff, that all displacement measured is straining of the machine and the grips. Subtracting the dummy displacement values, results in pure straining of the specimen.

The second correction has to be done because the strain at the net section needs to be determined. The gauge length of the wire is 5 mm, but the distance between the grips is 10.5 mm. There is a difference in width between the wire of 5 mm (net section length) and the wider grip heads, see Fig. 6.1.3a. The Tytron can only measure the total displacement between the grips, so the strain in the 5 mm net section of the wire cannot be determined directly. A simplified model, shown in Fig.6.1.3b was made to determine the strain in the wire without grip heads and therefore the Young's Modulus.

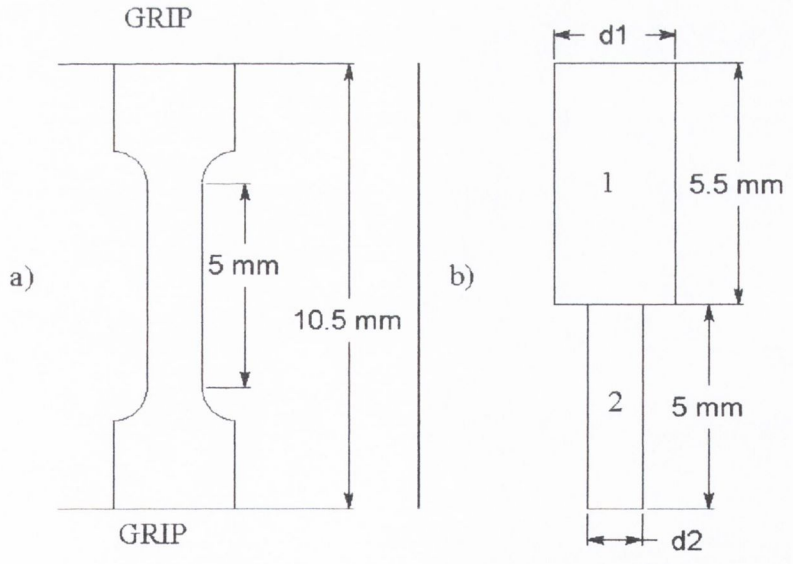

Fig. 6.1.3a) Plain, dogbone shaped, specimen placed between Tytron grips
b) Simplified model to determine strain at the net area

The wire itself has a width of d_2, the wider end has a width of d_1. An equation was derived to calculate the strain, ε, over the 5 mm net section length of the wire. Elasticity is assumed and the fillet radius between d_1 and d_2 is not taken into account. Area 1 in Fig. 6.1.3b correlates with the grip heads, area 2 with the net section of the wire. Subscripts 1 and 2 for will therefore correlate to respectively area 1 and 2 and subscript total to both area 1 and 2. It is important to realise that: $\varepsilon_{total} \neq \varepsilon_1 + \varepsilon_2$. To determine Young's Modulus E, ε_2 has to be calculated.

d_1 = width of the grip end | d_2 = width of the wire | t = thickness

ε_{total} = total strain in both sections | ε_1 = strain in the grip end | ε_2 = strain in the wire

l_{total} = total length of both sections | l_1 = length in grip end | l_2 = length of the wire

Δl_{total} = change in total length of both sections together

E_1 = Young's Modulus of the grip end | E_2 = Young's Modulus of the wire

σ_1 = stress in the grip end | σ_2 = stress in the wire

F_1 = force in the grip end | F_2 = force in the wire

A_1 = area of the grip end | A_2 = area of the wire

$$\varepsilon_{total} = \Delta l_{total}/l_{total} \quad \leftrightarrow \quad \varepsilon_{total} = (\varepsilon_1 l_1 + \varepsilon_2 l_2)/(l_1 + l_2)$$

$$\leftrightarrow \quad \varepsilon_2 = \{\varepsilon_{total}(l_1 + l_2) - \varepsilon_1 l_1\}/l_2 \qquad (6\text{-}1\text{-}1)$$

$$E_1 = E_2 \leftrightarrow \sigma_1/\varepsilon_1 = \sigma_2/\varepsilon_2$$

$$\sigma_1 = F_1/A_1$$

$$F_1 = F_2 \quad \leftrightarrow \quad \varepsilon_1 = \varepsilon_2 A_2/A_1 \qquad (6\text{-}1\text{-}2)$$

$$A_1 = d_1 t \quad \text{and} \quad A_2 = d_2 t \qquad (6\text{-}1\text{-}3)$$

Combining (6-1-1) and (6-1-2) with (6-1-3) gives the following equation for ε_2 (for elastic strain):

$$\varepsilon_2 = \{\varepsilon_{total}(l_1 + l_2)\} / \{l_2 + (l_1 d_2)/d_1\} \qquad (6\text{-}1\text{-}4)$$

Experimental data of two plain annealed wires were analysed, resulting in the following Young's Modulus values:

E_{exp1} = 150 GPa $\qquad$ E_{exp2} = 129 GPa

If these values are compared to the 177 GPa found for the macro-scale stainless steel bar samples, they seem to be quite low. An *FEA* model (ANSYS) was made of the plain wire geometry and it was loaded elastically, using the calculated Young's Modulus as an input. ANSYS gave similar results to the calculated values, the slight differences can be attributed to the fillet radius, which is put into the *FEA* model, but not into the calculations shown above.

Table 6.1.1 summarises the experimental data for the micro and macro material and states the specifications for the material as found on: www.matweb.com.

Table 6.1.1 Macroscopic vs. microscopic material properties

	MACRO	**MICRO**	**Specifications www.matweb.com**
0.2% Proof stress	396 MPa	315 MPa	205 MPa (yield strength)
Elastic Limit	290 MPa	300 MPa	-
Young's Modulus	177 GPa	129 and 150 GPa	193 GPa
UTS	754 MPa	580 MPa	515 MPa
Strain to failure	0.61 in 12.5 mm	0.37 in 5 mm	0.6 in 50 mm

There is an expected difference between the annealed and un-annealed curves. The strength of the un-annealed wire is much higher than the annealed wire and the strain to failure is a lot less. The microscopic wires have a slightly lower 0.2% proof stress than the macroscopic material. This is probably due to the fact that no extensometer was used for the micro material, therefore, the elastic limits were compared. The elastic limit was determined at the point where the curve starts to deviate from the initial linear behaviour and the values for the micro and macro material agree well. There is however a large difference between the proof stresses of the micro and macro material and the specified value of 205 MPa. It is unclear why this difference is observed. The specification gives the value for the yield strength, but even if this value was determined as an elastic limit, it is still roughly 100 MPa lower than the values obtained from the experimental tests.

The Young's modulus of the macro material was also found to deviate from the specification, which might be related to the difference in yield strengths. Still, these values should be the same since it is the same material. There also should not be a difference in Young's Modulus between the micro and the macro material. However, maybe there is a size effect for the Young's Modulus. This was not expected, because in the length direction, there are enough grains to form a continuum and the Young's Modulus should not be affected. But, the difference was found experimentally, so maybe the lack of a continuum in the thickness and width direction causes this change in Young's Modulus, because there are only a few grains at the width and the thickness of the micro wires.

Another difference between the specification and the macro material behaviour was found in the value of the *UTS*. The macro material was found to be stronger than specified, even the micro material was slightly stronger. The corresponding strain to failure for the macro material did agree with the specifications but this value was determined for a different gauge length, which can be significant in the results. The strain to failure in the microscopic specimens is somewhat lower than in the macro material, but again this strain was determined with a different gauge length.

The macro-scale tensile results do not agree well with the specifications. A possible solution might lie in the grain size. Material properties like *proof stress* and *UTS* can change with grain size and the grain size was not stated in the specification. The micro material and the macro material have a similar grain size value, therefore, they should have similar material properties, however, apart from the elastic limit, this was not the case. The difference in Young's Modulus, *UTS* and strain to failure might be caused by the size of the specimens.

To check this assumption, the true stresses at failure were determined. If these are the same for the micro and the macro material, the difference in *UTS* is not due to a size effect. The cross sectional areas at failure were determined; for the macro specimen by measuring the diameter after fracture using Verniers callipers and for the micro specimen by determining the cross sectional area at failure from Fig. 6.1.4 (roughly the area inside the square). The corresponding true stress values at failure, σ_{fTRUE}, are summarised in Table 6.1.2.

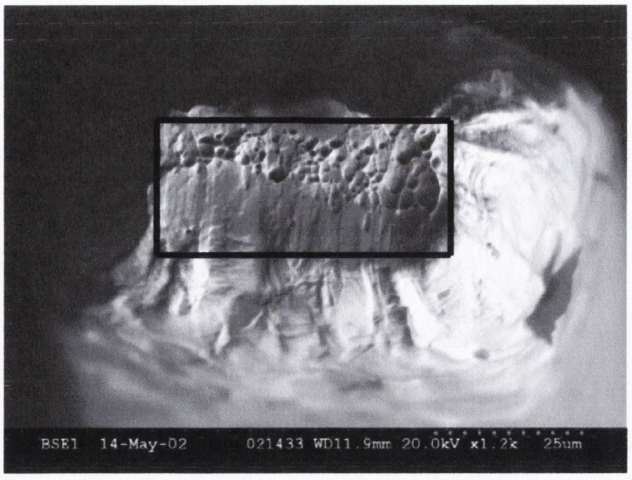

Fig. 6.1.4 Cross sectional area at failure for the micro specimen

Table 6.1.2 Summary of true stresses at failure for the plain material

	Area at failure [mm^2]	**Load at failure** [N]	σ_{fTRUE} [MPa]
MACRO	11.95	16840	1340
MICRO	0.001134	5.96	5255

The micro-scale material necks more before failure than the macro material, thus increasing the true stress at failure substantially. Effectively, when the specimen starts to neck, a situation similar to a circumferential notch is created, thus giving rise to the notch strengthening effect. The exact amount of strengthening depends on the shape and the depth of the notch. Generally an increase in strength of a factor of 3 is said to be the highest possible value, for a deep sharp circumferential notch. Since the micro material necks more than the macro material, more strengthening will occur. However, the true stress at failure of 5255 MPa for the microscopic material is extremely high. More plain wires were analyzed, giving similar values. This is a very interesting result and should be investigated further.

6.1.2 Notched wire tensile results

In section 5.2.2 tensile results on 3 types of microscopic notched wires were shown. For the notched samples no gauge length could be defined, therefore, instead of strain, nominal strain values were determined. No tensile tests were done on the FIB50 geometry, because there

were not enough samples. Comparing the notched tensile results to the plain tensile results suggests that the tensile strength of the notched wires is actually higher than the strength of the material, which is strange. Fig. 6.1.5 shows the plain and notched wire tensile curves, where Fig. 6.1.5b is a magnification at low nominal strain values.

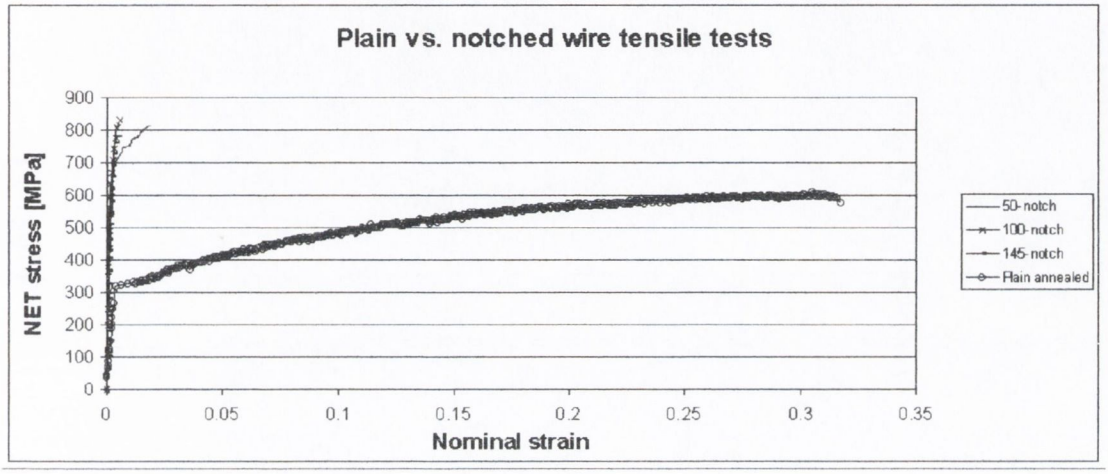

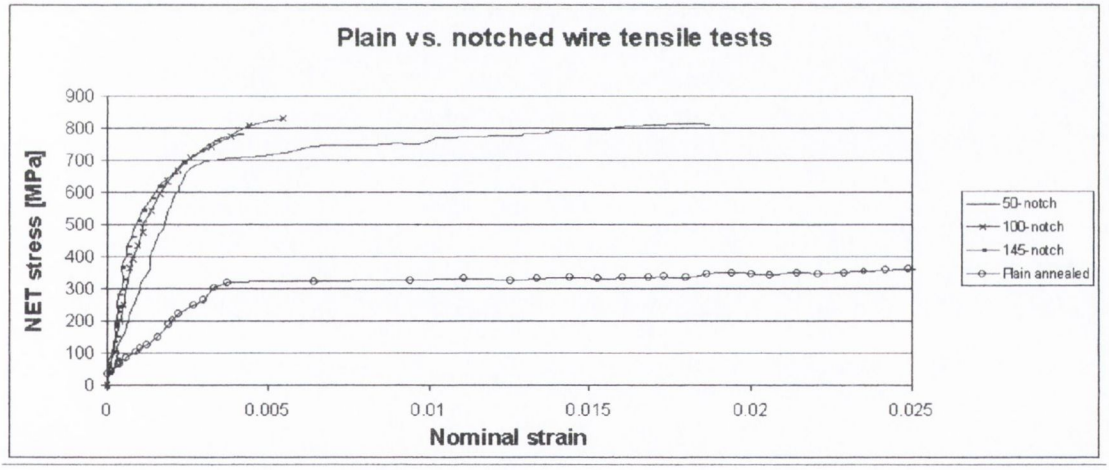

Fig. 6.1.5a) Plain vs. notched wire tensile results

b) Enlargement of the low strain values

The true stresses at failure were also determined for the 50-notch and for the 145-notch to investigate this notch strengthening effect. Fig. 6.1.6 was used to determine the cross sectional areas at failure for these notched wires and the results are given in Table 6.1.3.

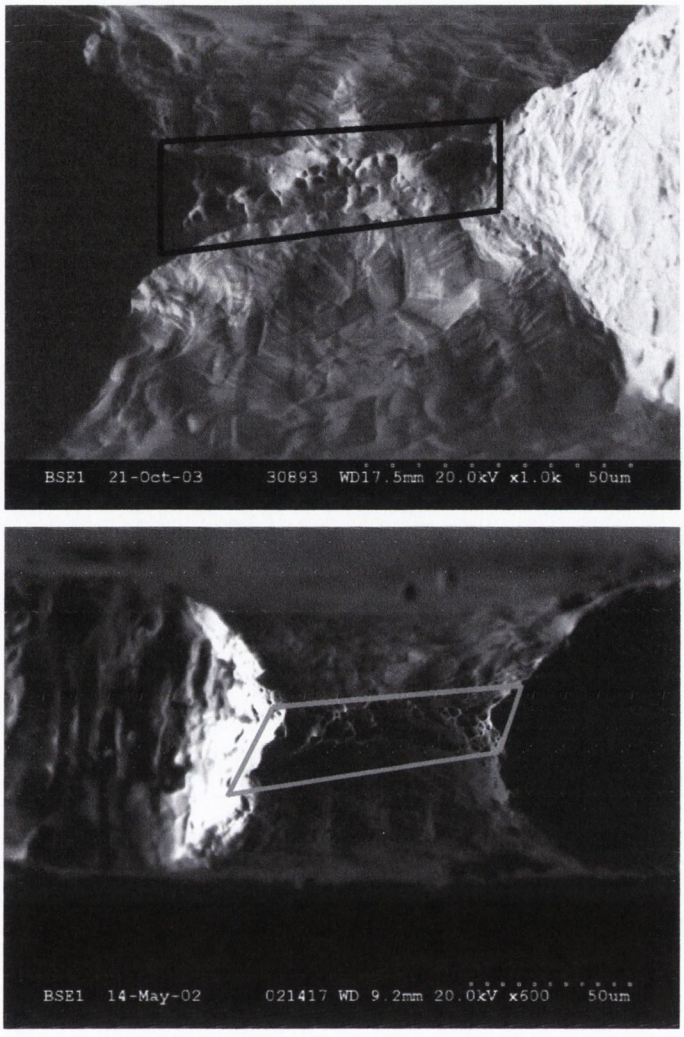

Fig. 6.1.6a) Cross sectional area at failure for the 50-notch wire

b) Cross sectional area at failure for the 145-notch wire

Table 6.1.3 Summary of the true stresses at failure for the notched wires

	Area at failure [mm^2]	**Load at failure** [N]	***UTS* TRUE** [MPa]
50-notch	0.001176	8.27	7036
145-notch	0.0011753	8.06	6860
Plain MICRO			5255
Plain MACRO			1340

The notched wires show even more necking before failure than the plain microscopic material, thus increasing the true stress to failure slightly more. Both notched wires give similar values for the true stress at failure, which is logical, because necking in the thickness direction establishes the circumferential notch, therefore, the notch depth is not that influential.

Tensile testing was not one of the main objectives of this work, therefore, not enough tests were done to draw conclusions. It is however an interesting phenomenon to be investigated further. Especially the high increase in true stress at failure that was found for the microscopic material might be a very interesting phenomenon.

6.1.3 Notched tubing tensile results

Fig. 6.1.7a shows the nominal tensile results of the slotted tubing pieces, Fig. 6.1.7b is an Enlargement of the graph at low nominal strain values. The 60 holed tubing samples could not be tested to failure, because the capacity of the load cell was too low.

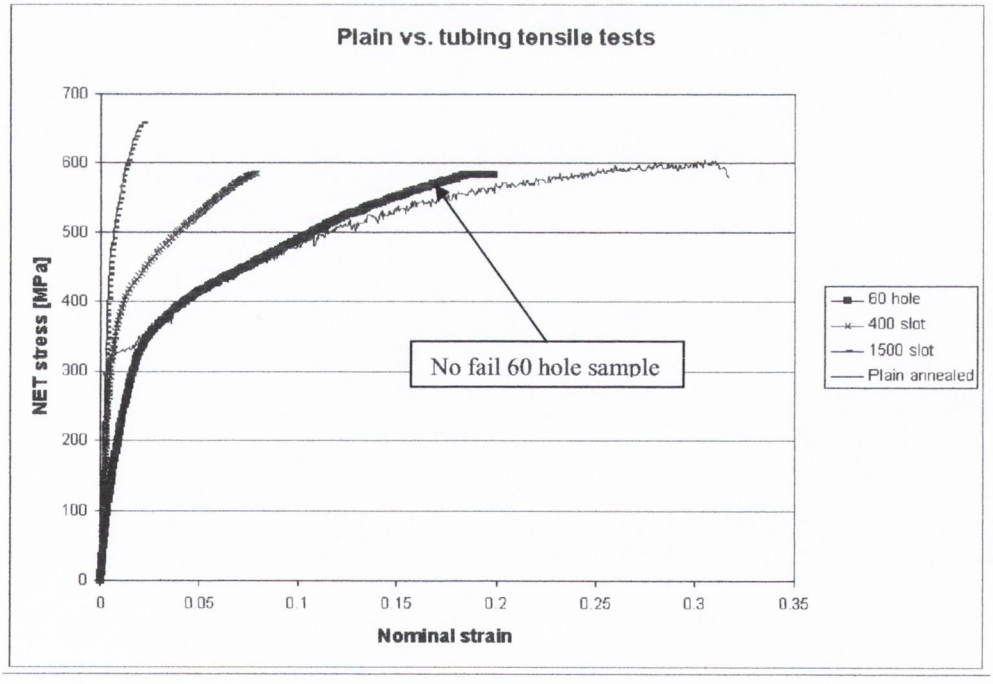

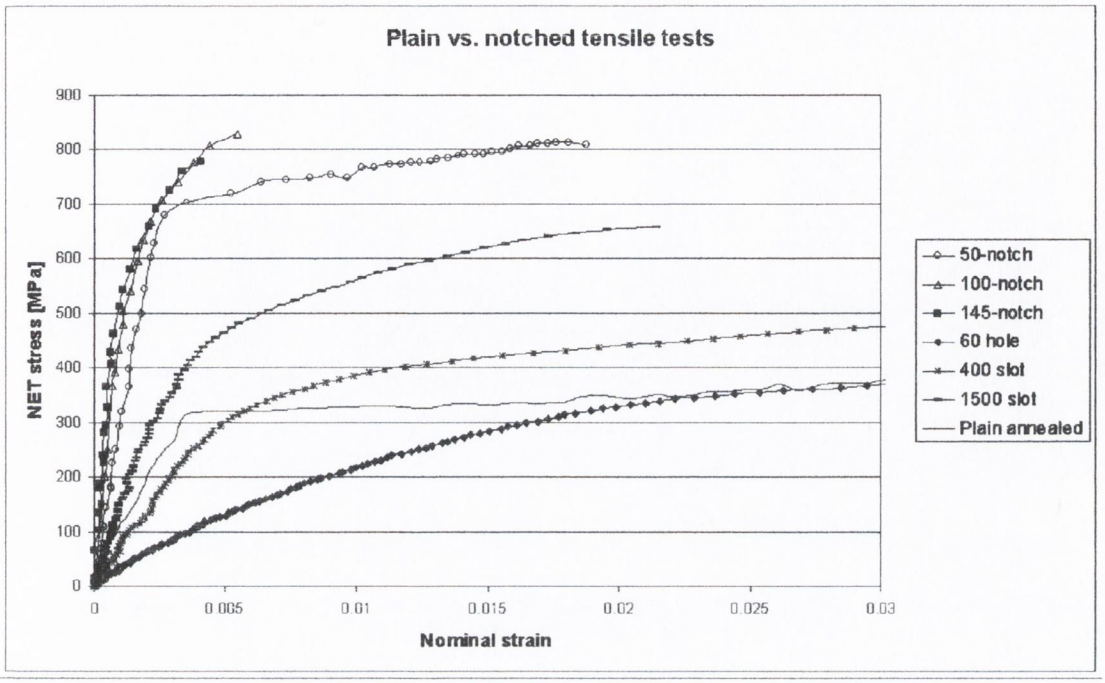

Fig. 6.1.7a) Tensile results on 316L micro-scale wires

b) Enlargement of first part of the graph including wires

The 60 holed sample, which could not be tested to failure, seems to behave more like the plain specimen (apart from the elastic part of the curve) than like the notched wires. The main difference between the notched wires and the slotted tubing pieces is that the tubing pieces have a substantially larger net section width, varying between roughly 2 - 2.5 mm as opposed to the 0.11 mm for the notched wire specimens. This indicates that for the tubing specimens there is continuum behaviour at the net section (not taking into account the thickness of the specimens). Maybe the 60 micron hole is small enough not have that much influence on the strength of the total specimen.

No true stresses at failure were determined for the tubing specimens, because no clear fracture surface area could be found on the SEM pictures. Fracture surfaces will be shown in more detail in section 6.3.

6.1.4 Concluding remarks on the tensile tests

Since fatigue was the main objective of this work, not enough tensile tests were carried out to draw conclusions at this stage. However, from these results it seems that when designing microscopic 316L stainless steel components, one should not be concerned too much about the tensile strength. The results that the microscopic material, expressed in true stress, is stronger than the macro material is very interesting, but should be investigated further.

6.2 Discussion of 316L stainless steel fatigue results

6.2.1 Plain annealed and un-annealed wire fatigue results

Fig. 6.2.1 shows the S-N_f -curve of the plain fatigue data from the microscopic specimens. Many tests were done on annealed plain wires, plus 3 on un-annealed wires. The un-annealed data points do however fit in nicely with the annealed data.

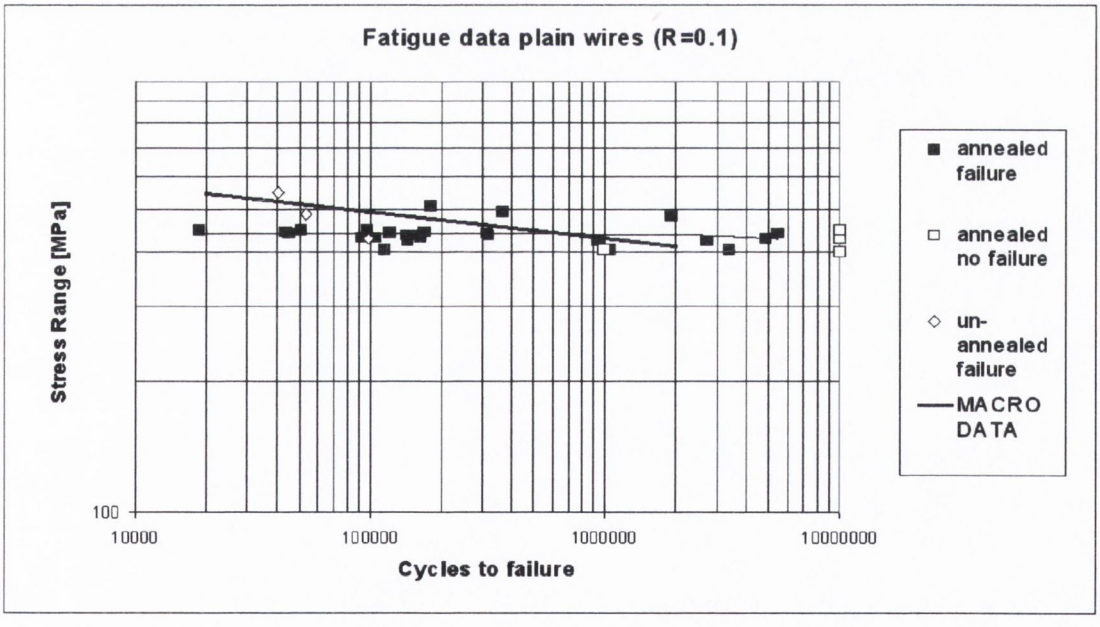

Fig. 6.2.1 Plain fatigue data

The fatigue limit of the material, 420 MPa, is actually above the material's (microscopic) yield strength, which is not usual at an R-ratio of 0.1. In the present work the assumption was made that some plastic deformation and material strengthening will occur in the first few cycles, which will effectively result in an increase of the yield strength, i.e. cyclic hardening. So, for the rest of the test, cycling is assumed to be elastic, below the increased yield strength.

An unexpected result is that the plain specimen fatigue limit for the micro-scale 316L stainless steel seems to be independent of annealing. Of course, only 3 un-annealed samples were fatigue tested, but including these three samples did not alter the annealed fatigue limit. It might be that actually, the annealed samples cyclically harden, while the un-annealed samples cyclically soften, so that eventually they come together, resulting in the same fatigue limit. This is of practical importance, because stents are plastically deformed during deployment, therefore hardening the material. This should not influence the results, because both annealed and un-annealed, hardened specimens resulted in the same fatigue limit value.

Another point of interest is the slope, or actually the lack of a slope of the fitted line to the experimental microscopic data. The difference in slopes for the macro and the micro material was illustrated in Fig. 6.2.1. When plotting fatigue data, the life (N_f) of a component or specimen should reduce with an increase in stress (ΔS). These experimental results imply, similar to the static tensile tests, that microscopic samples might not be affected by notches in fatigue, it might be more of a static problem. The fatigue limit of the material (which was determined to be 420 MPa) can therefore also be determined using a monoparametric analysis, see Table 6.2.1. Since fatigue failure does not seem to depend on the number of cycles to failure in the range of 10,000–10,000,000 cycles to failure, both failure points and run outs were taken into account.

The mean value of the applied stress is 438 MPa. The standard deviation and 2 confidence intervals are given in Table 6.2.1. The 95% confidence interval means that 95 % of the data lie within this interval, the 50% confidence interval means that 50% of the data points fall within that interval. The confidence intervals are very small, the 50% confidence interval for instance states that 50% of the fatigue data points lie within ± 3 MPa of the mean value, which is a very low value, nothing like what is expected for a fatigue situation.

Table 6.2.1 Results of monoparametric analysis of plain wire fatigue data

	Mean value [MPa]	Standard deviation [MPa]	95%-Confidence interval [MPa]	50%-Confidence interval [MPa]
Plain specimen	438	25	9	3

This data is determined within a range of 10,000-10,000,000 cycles to failure; the high cycle fatigue regime. In the low cycle fatigue regime, the slope is expected to increase, because eventually, at 1 cycle to failure, the UTS should be reached; 580 MPa.

6.2.2 Notched wire fatigue results

Fig. 6.2.2 shows the notched wire fatigue data results, no trend lines are added in order to have a clearer picture of the data points. Similar to the plain specimen results, there seems to be no distinct slope and the fatigue limits of the 50-, 100- and 145-micron notches are very similar, respectively 360, 355 and 350 MPa. The FIB50-notch has a fatigue limit of 320 MPa.

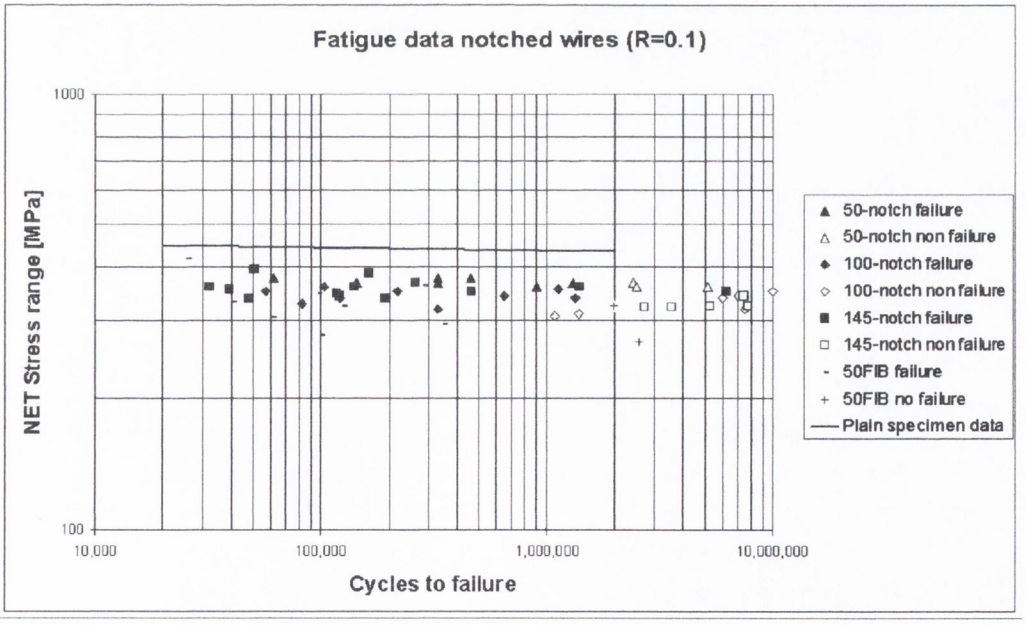

Fig. 6.2.2 Notched wire fatigue data

Again the fatigue limits are above the microscopic yield strength of 315 MPa. For these data a similar monoparametric analysis was done in the range of 20,00-10,000,000 cycles to failure, see Table 6.2.2.

Table 6.2.2 Results of monoparametric analysis of notched wire fatigue data

	Mean value [MPa]	**Standard deviation [MPa]**	**95%-Confidence interval [MPa]**	**50%-Confidence interval [MPa]**
50-notch	369	7	5	2
100-notch	337	16	8	3
145-notch	349	21	10	3
FIB50	326	43	27	9
FIB50 (no outlier)	315	31	20	7

The FIB50 notch shows a lot more scatter than the 3 other notches, but the results are still good. There is one obvious outlier in the FIB50 data, around 26,000 cycles to failure. If this point is excluded from the analysis, and the range is taken between 30,000-10,000,000, the scatter is less, see Table 6.2.2. However, the scatter is not that much less, therefore, it is hardly worth excluding it.

A likely explanation for this scatter is the way this sharp FIB radius was manufactured. A focussed ion beam was used to make a 1μm sharpened root radius at the already existing notch. Since the wires were cut from a piece of tubing, the wires are slightly curved, which gives problems. The sharpened length of the FIB notch is not constant over the thickness of the wires, as illustrated in Fig. 6.2.3. At the surface, there is substantial overshoot, of which the amount varies for the different samples up to 14 μm. Therefore, more scatter is likely to occur, however, the results are still good.

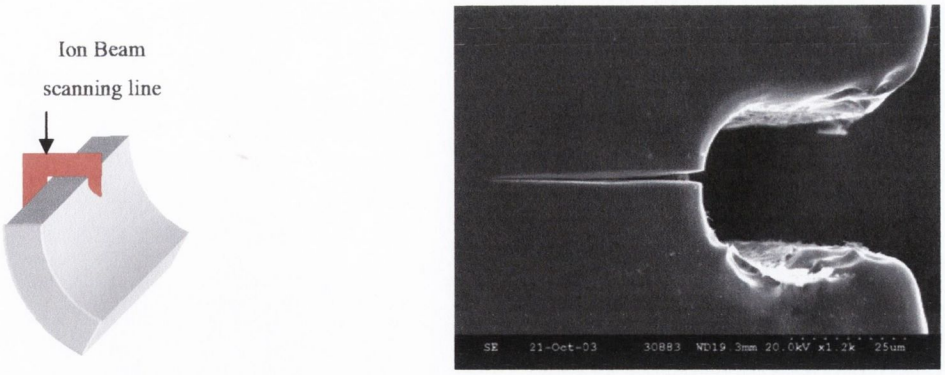

Fig. 6.2.3a) Schematic representation of FIB process
b) Example of a FIB50 specimen

6.2.3 Notched tubing fatigue results

For the plain and notched wire specimens, there was no slope. For the tubing samples there is more sloping visible in Fig. 6.2.4. The fatigue limits for the 60 holed, the 400 slotted and the 1500 slotted geometries are respectively 250 MPa, 120 MPa and 115 MPa.

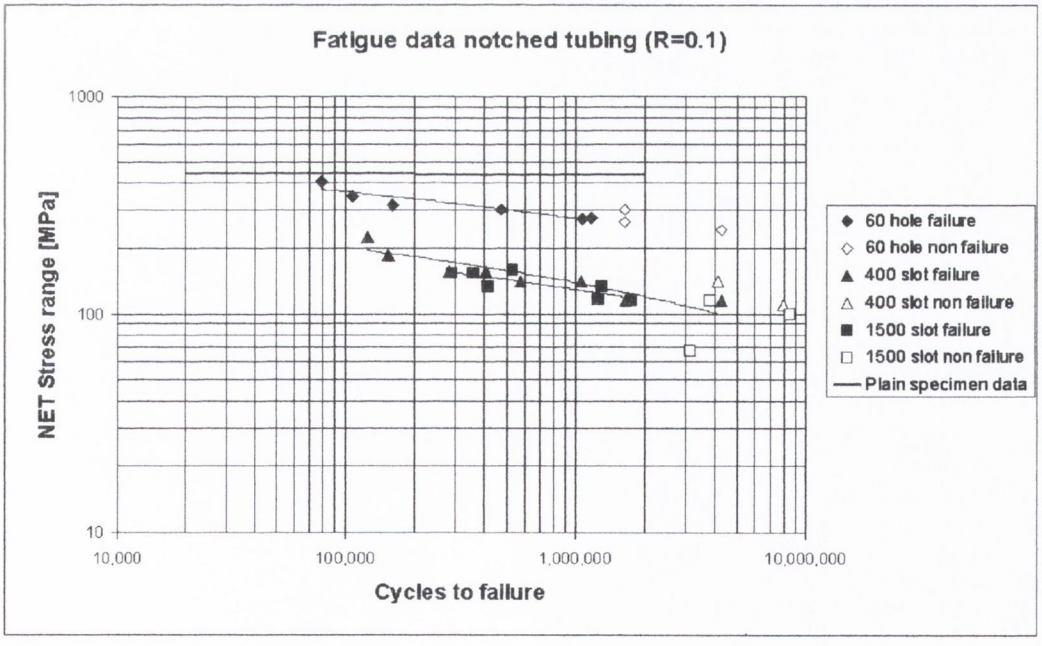

Fig. 6.2.4 Notched tubing fatigue data

Again a monoparametric analysis was done, taking into account the no-failure data. Except for the 60 holed specimen, the fatigue limits are below the yield strength of the material. Comparing the standard deviation values and the confidence intervals to those of the notched wire samples, here the scatter is much larger, which is logical, because there is some sloping for these samples. Yet, for fatigue data, the slope is not large at all.

Table 6.2.3 Results of monoparametric analysis of notched wire fatigue data

	Mean value [MPa]	**Standard deviation** [MPa]	**95%-Confidence interval** [MPa]	**50%-Confidence interval** [MPa]
60-hole	312	55	34	12
400-slot	149	35	25	8
1500-slot	124	28	17	6

The microscopic plain and notched *wire* specimens can fail at any number of cycles in the range of 10,000 – 10,000,000, independent of the applied stress range. In one aspect it is not strange that this happens, because there are only roughly 10 grains at the net section of the wire. The grain distribution is of great importance. When a non-propagating crack forms at a very low applied stress range in the first one (or two) grains, this reduces the net cross sectional area. For the tubing pieces there are more grains along the width, reducing this effect substantially.

For example, the same stress is applied to two microscopic *wires* and a non-propagating crack forms across the first grain. In one of the two wires, the first grain is relatively small and in the other wire the first grain is relatively large, see Fig. 6.2.5. The formation of a non-propagating crack increases the net section stress substantially more for the large grain than for the small grain, because there are only 10 grains along the width. The wire with the large first grain will therefore most likely have a shorter fatigue life than the wire with the smaller first grain. For the tubing specimens, there are more grains at the net section, so even if the first grain is large, the net section stress will be the same as if the first grain were small, resulting in a more sloped S-N_f relation.

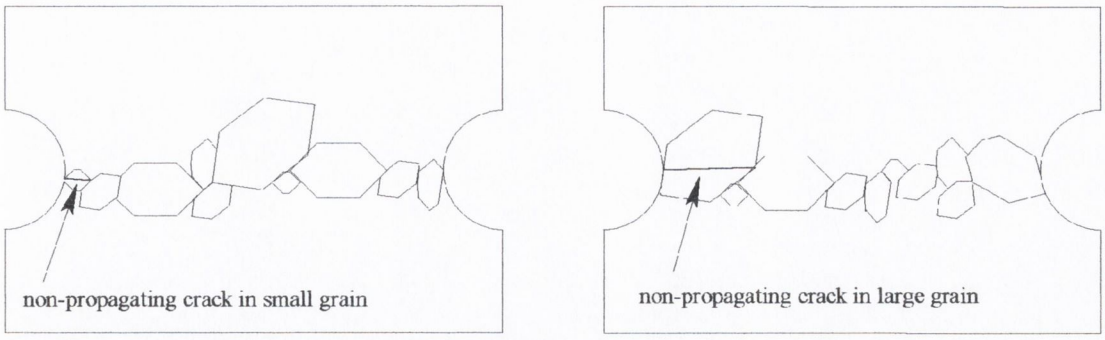

Fig. 6.2.5 Importance of grain distribution for microscopic specimens

The microscopic fatigue data shows very little scatter, which is supported by the narrow scatter bands that were calculated in Tables 6.2.1, 6.2.2 and 6.2.3. More scatter in the fatigue data would affect the tubing specimens more than the wire specimens, because of the sloping in the S-N_f-curves. For example the difference between the fatigue limit from chapter 5 and the fatigue limit from the monoparametric analysis is only 5% or less for the wire specimens, but 25% or less for the tubing specimens. The fatigue results are expected to be repeatable, provided that the testing circumstances and manufacturing processes are similar. However, this can only be said with certainty if the test series would be repeated.

6.3 Microscopy of the microscopic specimens

This section discusses the Scanning Electron Microscope (SEM) pictures that were taken of several fracture surfaces, both tensile and fatigue.

6.3.1 Tensile fracture surfaces

Fig. 6.3.1 shows SEM pictures of the fracture surfaces of a plain and a notched wire.

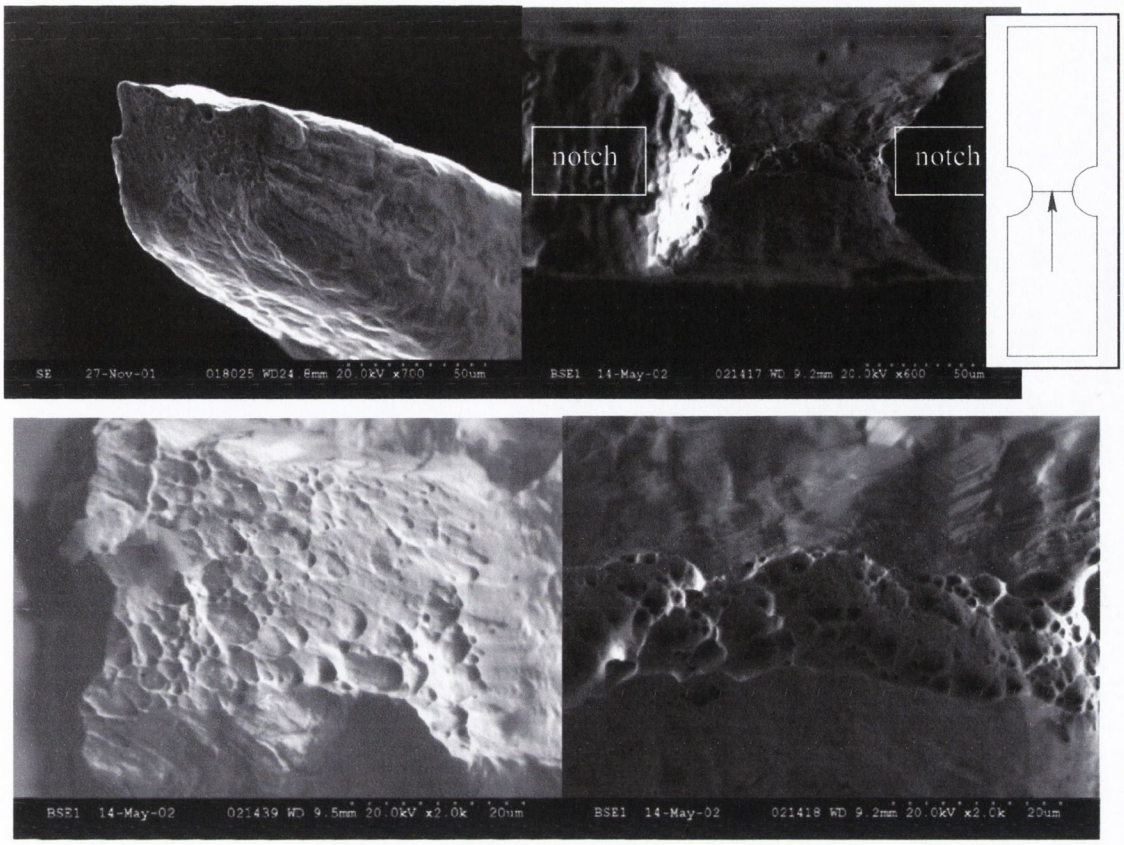

Fig. 6.3.1a) Tensile fracture surface of a plain wire

b) Tensile fracture surface of a 145-notch wire

c) Enlargement of the plain tensile fracture surface

d) Enlargement of the notched tensile fracture surface

The dimples that are visible on the tensile fracture surfaces indicate fast fracture. A closer look, Fig. 6.3.1c and 6.3.1d, suggests that the dimples are slightly sheared, but that is not the case: the fracture surface itself is at an angle. Necking, the reduction of cross sectional area, occurs in both the plain and the notched wire samples. Both the plain wires and the notched wires neck more in the thickness direction than in the width direction as was illustrated in respectively Fig. 6.1.4 and Fig. 6.1.6. In other words, before testing the cross sectional areas were roughly a square and after fracture they were more rectangular.

Fig. 6.3.2 illustrates the tensile fracture surface of a notched tubing piece. The slots are clearly visible in the picture and it looks like some necking occurs at the fracture surface, however, this is difficult to identify. Magnifying the tensile fracture surface, Fig. 6.3.2b and

Fig. 6.3.2c, results in a surface that looks different from the dimpled fast fracture surface that was found for the plain and the notched wire specimens.

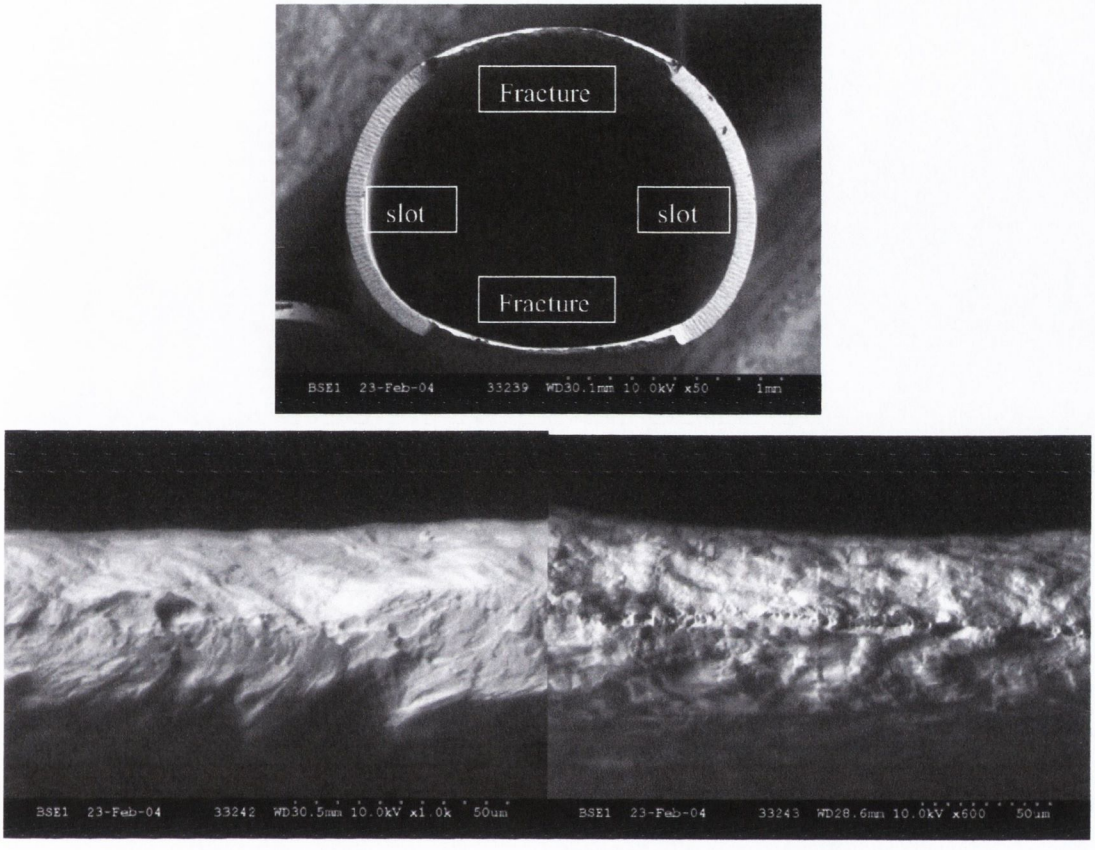

Fig. 6.3.2a) Tensile fracture surface of a tubing specimen

b) Enlargement of the tubing tensile fracture surface

c) Enlargement of the tubing tensile fracture surface

6.3.2 Fatigue fracture surfaces

Fig. 6.3.3 shows typical fatigue fracture surfaces of respectively a plain and a notched wire specimen. The fracture surface can be divided into two regimes. The dimpled fast fracture part, as identified in the previous section and the fatigue part, which is distinguishable by waves or ripples. A magnification of the specific fatigue surface is given in Fig. 6.3.3c.

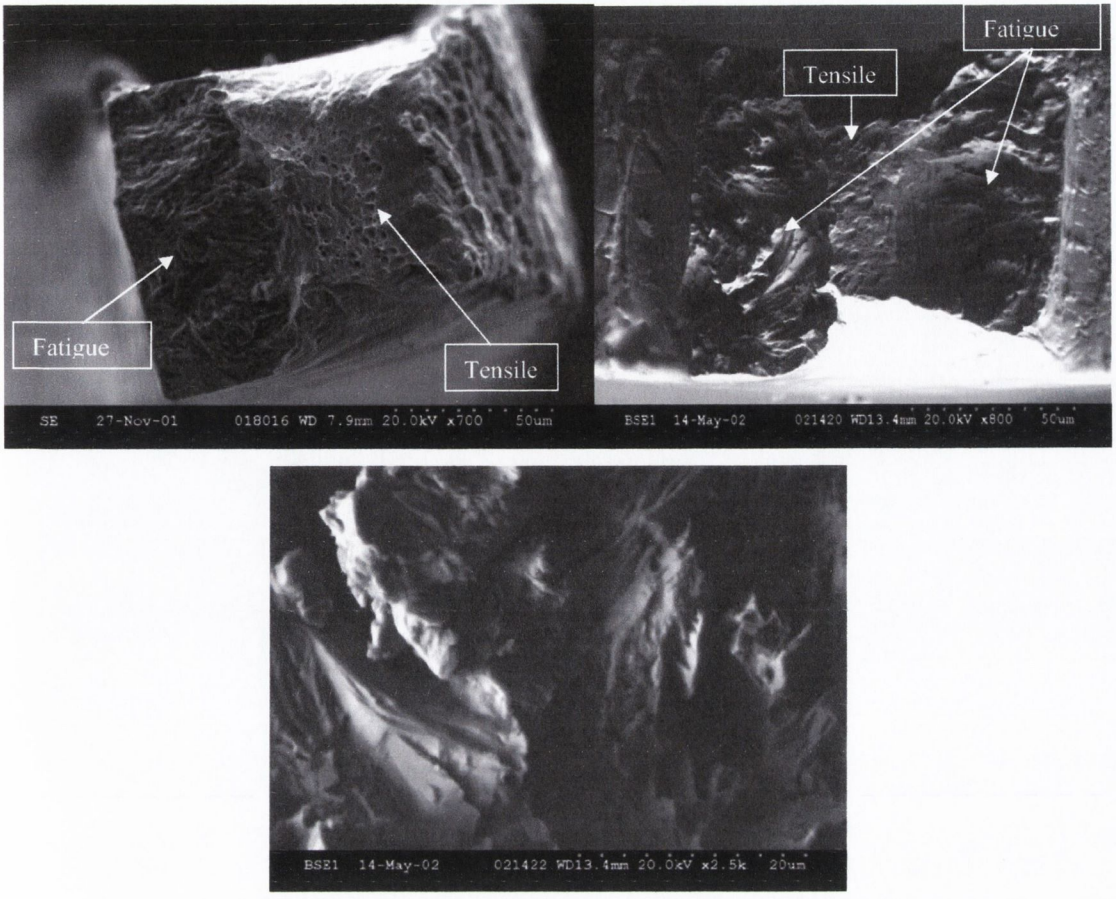

Fig. 6.3.3a) Fatigue fracture surface of a plain wire

b) Fatigue fracture surface of a notched wire

c) Enlargement of the fatigue fracture surface

During fatigue crack growth, hardly any necking occurred. A considerable amount of necking did occur for all specimens at the fast fracture tensile surfaces. In most situations fatigue crack growth started in one notch, but sometimes cracks started to grow simultaneously from both notches, Fig. 6.3.3b.

Fig. 6.3.4 illustrates the fatigue fracture surface of the tubing specimens. At the fatigue surface, hardly any necking occurred, but at the fast fracture part of the fracture surface, necking was found.

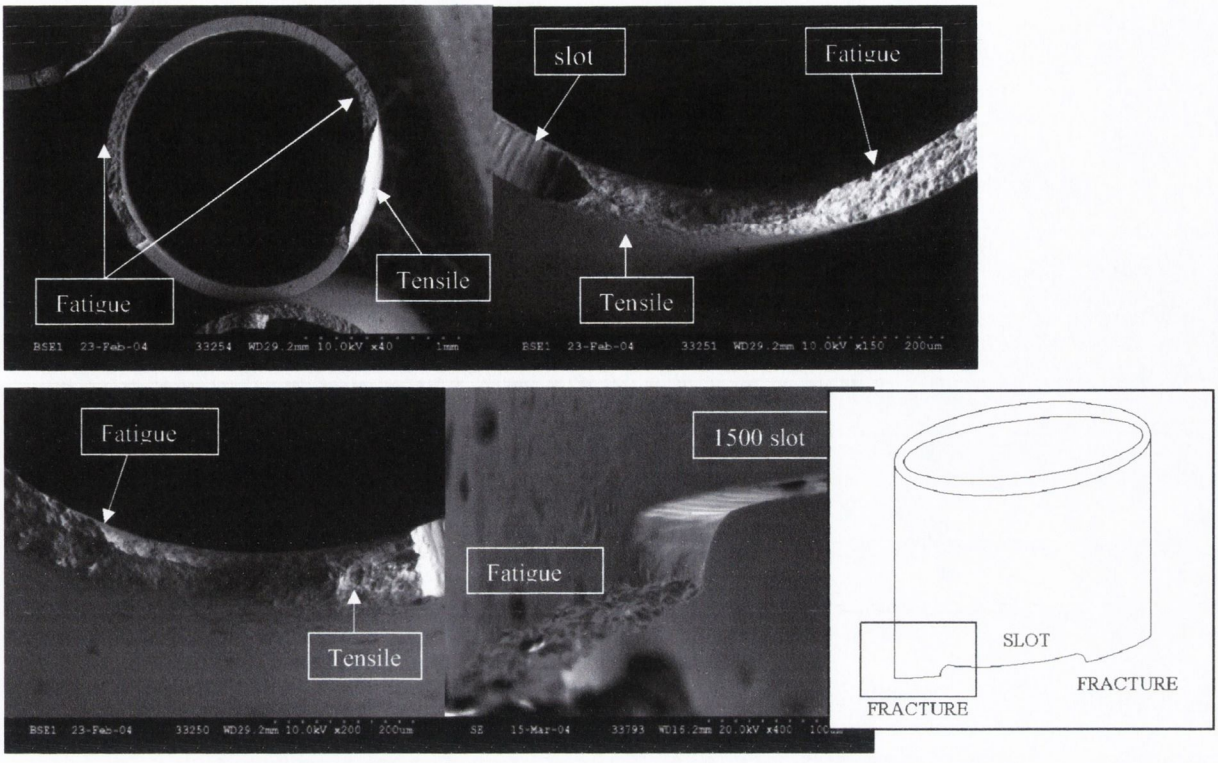

Fig. 6.3.4a) Fatigue fracture surface of a tubing specimen

b) Enlargement of the transition between fatigue and tensile

c) Enlargement of the transition between fatigue and tensile

d) Horizontal fatigue fracture surface

If plane stress/Mode-II shear failure occurred in these samples, the fatigue fracture surface would have been under an angle of 45 degrees (in the thickness direction). Fig. 6.3.4d illustrates that the fatigue fracture surface is horizontal; therefore, no plane stress/Mode-II shear failure occurred. This was also found for all microscopic wire specimens.

6.4 Discussion of prediction methods vs. micro-scale 316L fatigue results

Table 6.4.1 gives a summary of the different fatigue prediction methods that will be used, including proposed short crack and micro-scale corrections. These were discussed in chapters 1 and 2. Abbreviation *scc* stands for short crack correction.

Table 6.4.1: Prediction methods to be used on micro-scale 316L stainless steel specimens

METHOD	COMMENTS
Stress Life	K_t needs to be determined (*FEA*)
Smith and Miller - Long crack prediction **- El Haddad scc a_o** **- El Haddad scc a_w** **- scc using ΔK_{th_width} for width specimen** **- scc using ΔK_{th_effth} from exp. data** **- scc using ΔK_{th_exp} from exp. data**	 D needs to be known a_w needs to be known R-curve needed to determine ΔK_{th_width} at width Exp data needed from macro-scale specimens Exp data needed from micro-scale specimens
CMM - Long crack prediction **- El Haddad scc a_o** **- El Haddad scc a_w** **- scc using ΔK_{th_width} for width specimen** **- scc using ΔK_{th_effth} from exp. data** **- scc using ΔK_{th_exp} from exp. data**	 D needs to be known a_w needs to be known R-curve needed to determine ΔK_{th_width} at width Exp data needed from macro-scale specimens Exp data needed from micro-scale specimens
TCD - Long crack prediction **- Changing L using ΔK_{th_width}** **- Changing L using ΔK_{th_effth}** **- Changing L using ΔK_{th_exp}**	 R-curve needed to determine ΔK_{th_width} at width Exp data needed from macro-scale specimens Exp data needed from micro-scale specimens
Resistance curve method (El Haddad)	Crack length, notch depth, CMM's a_w required
Suo/KK (scc already included)	Notch depth, D, or CMM's a_w required to be able to determine El Haddad's a_o value

Table 6.4.2 summarises several important parameters, which are required to make predictions. These values were given previously in the results chapter. The values for the effective threshold, ΔK_{effth}, and the corresponding critical distance, L_{eff}, are not added in Table 6.4.2 since they are constants. ΔK_{effth} = 3.93 MPa$\sqrt{m}$ and L_{eff} = 0.0279 mm.

Table 6.4.2 Important parameters for fatigue predictions

	$\Delta\sigma_{on}$ [MPa]	K_t	F_{NET}	w_{NET} [mm]	a_w [mm]	D [mm]	ΔK_{th_width} [MPa√m]	L_{width} [mm]	ΔK_{th_exp} [MPa√m]	L_{exp} [mm]
50-notch	360	2.34	0.61	0.11	0.055	0.05	4.05	0.03	2.73	0.018
100-notch	355	2.4	0.46	0.11	0.072	0.1	3.24	0.019	2.89	0.017
145-notch	350	2.35	0.39	0.11	0.082	0.145	2.81	0.014	2.91	0.017
FIB 50	320	5.37	0.59	0.109	0.033	0.051	4.00	0.029	2.43	0.013
60 hole	250	2.88	0.98	2.61	0.038	0.03	7.70	0.107	2.38	0.015
400 slot	120	5.58	0.86	2.27	0.231	0.2	7.62	0.105	2.59	0.013
1500 slot	115	6.13	0.55	1.17	0.772	0.75	6.86	0.085	3.07	0.017
							Average ΔK_{th_exp}		**2.71**	**0.016**

When predictions will be made with the experimental threshold value, the *average* value of 2.71 MPa√m will be used. Since the experimental threshold values for all different microscopic geometries are similar, good predictions are expected.

6.4.1 Discussion of the Stress Life method

The Stress Life method is expected to give bad predictions for these micro-scale specimens, because it does not work well for sharp notches. The results are given in Table 6.4.3. The predicted fatigue limit values were then compared to the experimental fatigue limits to obtain an error value:

$$error = \frac{\Delta\sigma_{on} - \Delta\sigma_{on\_pred}}{\Delta\sigma_{on}} \qquad (6\text{-}4\text{-}1)$$

where $\Delta\sigma_{on}$ is the experimentally determined fatigue limit and $\Delta\sigma_{on\_pred}$ is the prediction value. When the error is positive, the prediction is conservative.

Table 6.4.3 Stress Life predictions of $\Delta\sigma_{on}$ for the 316L micro-scale specimens

	PREDICTION at net for 2 million cycles	
	[MPa]	**error [%]**
50-notch	179	+50.1
100-notch	175	+50.7
145-notch	179	+48.9
FIB50	78.2	+75.5
60-hole	146	+41.7
400-slot	75.3	+37
1500-slot	68.5	+40.4

As expected the Stress Life method gives large conservative predictions.

6.4.2 Discussion of the Smith and Miller method

The Smith and Miller method, discussed in section 2.4.1, was originally developed as a prediction method for long cracks in macro-scale specimens or components. The method assumes that sharp notches behave as cracks and therefore the method can be applied to short cracks in conjunction with El Haddad's short crack correction parameter a_o. Furthermore, the actual notch depth D is not needed if a_w is used which is derived using the Crack Modelling Method. Another way of modifying this method to apply to short cracks and/or microscopic specimens is to use one of the reduced threshold values proposed in chapter 3 and calculated in chapter 5.

Table 6.4.2 summarises all the parameters used to make the Smith and Miller predictions for the micro-scale 316L wire and tubing samples. Length parameter a_w is similar to the actual notch depth D for most geometries. When this is not the case, still a similar prediction was obtained as for the a_o short crack correction, because a_w has to be implemented into the long crack prediction as well. Since the predictions turned out to be similar, only the a_o correction

is stated in Table 6.4.4. No prediction was made using the *average* experimentally determined microscopic threshold value, because that value is based on the same equations as the Smith and Miller method, resulting in perfect predictions. The equations assume sharp notches to behave as cracks, therefore, fracture mechanics equations apply.

Table 6.4.4 Smith and Miller predictions of $\Delta\sigma_{on}$ for the 316L micro-scale specimens

Predictions Smith & Miller	**Using ΔK_{th_long}**		**Using ΔK_{th_long} scc_{ao} and scc_{aw}**		**Using ΔK_{th_width}**		**Using ΔK_{effth}**	
	[MPa]	**error**	**[MPa]**	**error**	**[MPa]**	**error**	**[MPa]**	**error**
50-notch	1038	-188%	389	-8.14%	461	-28.1%	518	-43.9%
100-notch	976	-175%	386	-8.68%	368	-3.76%	487	-37.3%
145-notch	957	-173%	385	-9.88%	321	+8.32%	478	-36.5%
FIB50	1043	-226%	390	-21.8%	464	-44.9%	521	-62.7%
60-hole	829	-232%	375	-49.9%	551	-120%	414	-65.6%
400-slot	364	-203%	275	-129%	241	-101%	182	-51.5%
1500-slot	295	-156%	241	-110%	184	-59.7%	147	-28.1%

As expected, the Smith and Miller method does not give good predictions using the macroscopic long crack threshold value. Both El Haddad short crack corrections (a_o and a_w) are capable of describing the behaviour of the notched wire specimens, but not of the tubing specimens. The main difference between the notched wires and the tubing pieces is the net section area. For the wires, there are only a few of grains along the net section, while for the tubing specimens there are enough grains to establish a continuum.

On the one hand it is surprising that the short crack correction works for the wires, but not for the tubing specimens, because the notched tubing specimens behaves more like a continuum, where El Haddad's correction is normally applied. On the other hand, the short crack correction tends to draw the predictions toward the plain specimen fatigue limit. The wire fatigue limits are closer to the plain fatigue limit value, therefore giving lower errors.

The reduced threshold values, based on the width of the sample and based on the effective closure-free threshold, give bad predictions. This could be expected because these threshold

values were different from the average threshold value based on the microscopic experimental data, as was shown in Table 6.4.2. The microscopic threshold values were calculated using the same equations as the Smith and Miller method uses to make predictions. Therefore, the average experimentally determined threshold value will give good predictions in combination with the Smith and Miller method, because for all microscopic specimens, the experimental threshold was found to be similar. Since the threshold values based on the width of the specimen and on the closure-free threshold are larger than the average experimentally determined threshold values, errors were expected.

In conclusion: the Smith and Miller method does not work in combination with the short crack correction factors, apart from the reduced average value for the experimental threshold which was based on the same equations as the Smith and Miller method. It was shown previously that the Suo/KK method will give the same results as the Smith and Miller method.

6.4.3 Discussion of the Crack Modelling Method (CMM)

The crack-like predictions for the Crack Modelling Method are given in Table 6.4.5. The same short crack corrections and reduced threshold values were used as for Smith and Miller.

Table 6.4.5 CMM predictions of $\Delta\sigma_{on}$ for the 316L micro-scale specimens

Predictions CMM	**Using** ΔK_{th_long}		**Using** ΔK_{th_long} **scc$_{ao}$ and scc$_{aw}$**		**Using** ΔK_{th_width}		**Using** ΔK_{effth}		**Using** ΔK_{th_exp}	
	[MPa]	**error**	**[MPa]**	**error**	**[MPa]**	**error**	**[MPa]**	**error**	**[MPa]**	**error**
50-notch	953	-165%	358	+0.63%	491	-36.28%	476	-32.25%	331	+8.14%
100-notch	907	-156%	377	-6.15%	373	-5.16%	453	-27.61%	333	+6.20%
145-notch	882	-152%	383	-9.52%	315	+10.09%	441	-25.86%	326	+6.83%
FIB50	1083	-238%	356	-11.3%	550	-71.84%	542	-69.22%	335	-4.63%
60-hole	742	-197%	335	-34.1%	726	-190%	371	-48.24%	225	+10.2%
400-slot	345	-187%	260	-117%	334	-178%	172	-43.33%	113	+5.50%
1500-slot	287	-149%	234	-104%	250	-117%	143	-24.52%	112	+2.78%

The FIB50 notch is a sharpened version of the 50-notch wire. It is therefore strange, that the CMM predicts that the sharper notch, the FIB50, is stronger than the 50-notch. This can be explained by redistribution of stress in the material. The stress at the root of the notch is higher for the FIB50 specimen, but the nominal stress at the net section is nearly the same. Therefore, the stress distribution ahead of the FIB50 notch will differ from that of the 50-wire, which in this case results in a lower stress at the critical distance and a higher prediction.

The predictions based on the macroscopic material properties result in large non-conservative errors. Applying the El Haddad short crack correction (both a_o and a_w) gives good results for the wires, but not for the tubing specimens, similar to what was found for the Smith and Miller method. The threshold value based on the width of the specimen only works for the wire specimens, apart from the FIB50 specimens.

The effective threshold does not work well in combination with the CMM, resulting in large non-conservative predictions for all specimen geometries. The average threshold based on the average experimental microscopic results, gives good predictions for all the specimen geometries. This is due to the fact that this average threshold value, which was calculated using the equation, is similar to the threshold determined by the CMM itself, see Table 5.4.8.

6.4.4 Discussion of the Theory of Critical Distances (TCD)

For the Theory of Critical Distances, no short crack corrections should be applied. Therefore only the long crack threshold and the reduced threshold values were used to make predictions. The long crack threshold prediction is given as a reference point. Table 6.4.6 summarises the predictions for the Theory of Critical Distances. The PM looks at a stress at distance $L/2$ ahead of the stress concentration and compares it to the plain specimen fatigue limit, the LM averages the stress over a distance of $2L$.

Table 6.4.6 TCD predictions of $\Delta\sigma_{on}$ for the 316L micro-scale specimens

Predictions TCD	ΔK_{th_long}				ΔK_{th_width}				ΔK_{effth}				ΔK_{th_exp}			
	PM		LM		PM		LM		PM		LM		PM		LM	
	[MPa]	error[%]	[MPa]	error[%]	[MPa]	error[%]	[MPa]	error[%]	[MPa]	error[%]	[MPa]	error[%]	[MPa]	error[%]	[MPa]	error[%]
50-notch	567	-57.5	N/a	N/a	400	-11.0	426	-18.3	388	-7.69	420	-16.6	289	+19.7	337	+6.42
100-notch	687	-65.2	N/a	N/a	323	+8.9	372	-4.79	381	-7.32	420	-18.3	293	+17.5	345	+2.82
145-notch	591	-68.9	N/a	N/a	287	+17.9	338	+3.5	379	-8.37	420	-20	295	+15.8	346	+1.17
FIB50	546	-70.5	N/a	N/a	396	-23.8	423	-32.1	394	-23.0	420	-31.3	298	+6.78	322	-0.47
60-hole	398	-51.9	381	-52.5	396	-58.4	379	-51.7	275	-10.0	298	-19.4	194	+22.6	226	+9.6
400-slot	293	-144	293	-144	282	-154	287	-139	142	-18.7	174	-45.3	108	+10.33	126	-4.75
1500-slot	268	-133	283	-146	234	-103	251	-119	128	-11.5	155	34.8	104	+9.48	127	-10.4

All predictions based on the long crack threshold value are too high. It is however interesting to have a closer look at the wire specimens. The net section width of the wires is 0.11 mm, while the distance over which the Line Method averages the stress is 0.22 mm ($2L$). In other words, the LM requires a distance that is larger than the full width of the specimen, therefore, for the wire specimens the LM prediction could not be made.

The reduced threshold value based on the width of the specimen works for the wire specimens, but not for the tubing specimens. This was also found for the other prediction methods. It is strange that this reduced width threshold does not work for the tubing specimens, because the threshold is similar to that of the macro material and the 400 and 1500 slots are long cracks. Therefore, the thickness has to have an effect on the behaviour of the material. In the future, it would be interesting to investigate the mechanisms of failure.

The Point Method gives good predictions for both the effective threshold and the microscopic threshold based on the equations, apart from the FIB50 specimen, which is slightly above the acceptable 20%. The Line Method gives very good predictions for the average experimental threshold, but using the effective threshold on the tubing specimens causes some problems. This is because the effective threshold is larger than the *FEA* threshold for the tubing specimens. It is not surprising that these threshold values work so well for the wires, because the values are within the range of threshold values that were determined through the *FEA* curves in section 5.4.4.

6.4.5 Discussion of the Resistance-curve method (R-curve)

Table 6.4.7 gives the predictions for the Resistance-curve method. Since Tanaka's relation for the R-curve requires several experimentally determined values, only El Haddad's R-curve relation was analysed.

Table 6.4.7 Resistance curve predictions for the 316L micro-scale specimens

	Fatigue limit		**Non-propagating crack length**
	[MPa]	**error**	**[mm]**
50-notch	250	+30.6%	0.039
100-notch	221	+37.7%	0.053
145-notch	208	+40.6%	0.065
FIB50	250	+21.9%	0.039
60-hole	280	-12%	0.065
400-slot	192	-60%	0.16
1500-slot	144	-25.2%	0.23

The R-curve method gives poor conservative results for the wire specimens. The results for the tubing pieces are better. The 60-hole has a low error value, and for the 1500-slotted pieces the error is only slightly larger than the acceptable 20%. The error for the 400-slotted samples is too large. This might have to do with the fact that the specimen was designed to have a crack length in between a long crack and a short crack. This in between length was based on the R-curve analysis. However, experimental data showed that the 400-slot had a similar fatigue limit than the 1500-slotted piece, therefore, the 400-slot contained a long crack instead of an in between length, thus giving a poor prediction.

6.5 Concluding remarks

The short crack corrections based on El Haddad's short crack parameter only work for the wire specimens, because their fatigue limits lie much closer to the plain material fatigue limit than the fatigue limits of the tubing pieces. Therefore, this correction factor is not capable of describing all the microscopic stainless steel fatigue data.

The reduction of the threshold based on the width of the specimen also only works for the wire specimens, not for the tubing pieces. The effective threshold value gives poor predictions for all methods apart from the TCD, because the value for the effective threshold is much higher than the average value based on the experimental data. This threshold that is based on the equations and the microscopic experimental data is fairly constant for all microscopic geometries, thus giving good predictions for all methods.

The TCD approach gives good predictions for the Point Method using both the effective and the microscopic experimental threshold values. This is very useful, because if no microscopic experimental data is available, reasonable predictions can be made based on the closure-free threshold.

It was expected that the effective threshold and the average microscopic experimental threshold would be similar, because for short cracks, no closure is expected to occur. The effective threshold was higher than the experimentally determined threshold. The TCD is not based on the same equations that were used to determine the threshold value. Instead, stress distance curves (*FEA*) were used to make predictions. These stress distance curves can also be used in combination with the Point Method to determine the threshold value for the microscopic specimens and the *FEA* threshold value should give good Point Method predictions. In section 5.4.4 it was shown that the *FEA* based threshold value for the microscopic specimens was similar to the effective threshold that is why the Point Method with the effective threshold was capable of describing the fatigue data for the microscopic specimens.

Chapter 7 Discussion of the aluminium results

Tensile and fatigue tests were carried out on macroscopic and microscopic aluminium specimens in order to investigate further the size effect already observed in stainless steel. Fig. 7.1.1 shows the geometries of the macroscopic and microscopic 0.5 mm thick aluminium specimens that were discussed in sections 4.7.3 and 4.7.4. The macroscopic notched specimens, Fig. 7.1.1b, were tested by Daniel Bellett (Bellett, 2002).

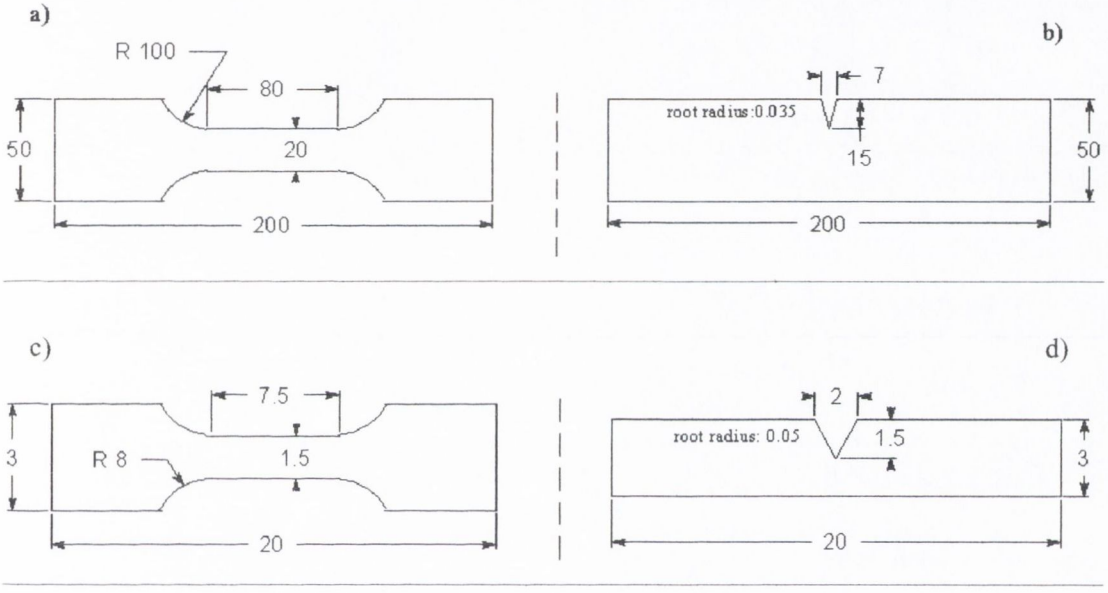

[All dimensions in mm]

Fig. 7.1.1a) Aluminium macro-scale plain specimen geometry

b) Aluminium macro-scale notched specimen geometry

c) Aluminium micro-scale plain specimen geometry

d) Aluminium micro-scale notched specimen geometry

The micro-scale specimens were designed to have a net section width around the size of critical distance size, L, to make sure they would behave as micro-scale samples. The manufacturing process limits the width of the specimen and the minimum value that could be obtained was 1.5 mm. An initial guess for the critical distance value was 1 mm, using a threshold value of 2.8 MP$\sqrt{m}$ (Bellett, 2002) and assuming that the plain specimen fatigue

limit was 50 MPa. After testing, the plain fatigue limit was found to be 55 MPa instead of 50 MPa, therefore the critical distance changed slightly.

7.1 Discussion of tensile results

Fig. 7.1.2 shows the tensile stress/strain curves of the plain microscopic and macroscopic aluminium specimens and the notched microscopic specimen. No notched tensile test was done on the macroscopic material, since this geometry was tested by Daniel Bellett (Bellett, 2002). Only one tensile test could be done on the macroscopic material, but due to an error during the test, it was not tested to failure. Still, the specimen was tested above the yield stress and the *UTS* could also be determined, because judging by the shape of the curve, it was not likely that the stresses would increase before failure.

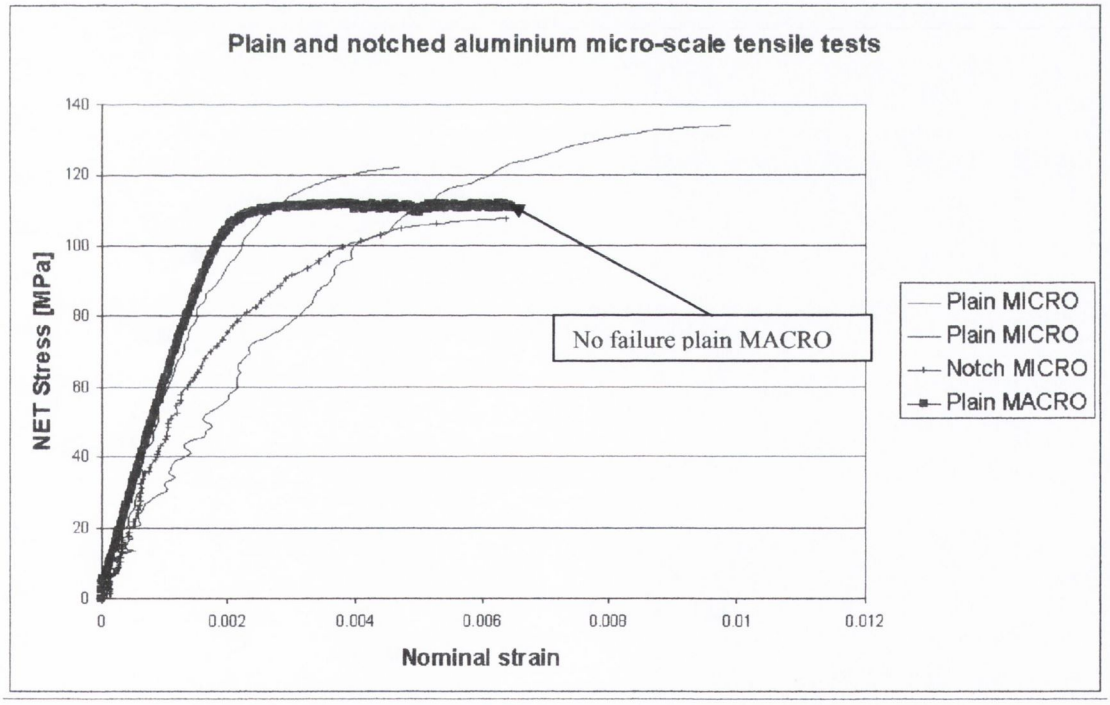

Fig. 7.1.2 Tensile tests on microscopic and macroscopic 0.5 mm thick aluminium

One of the plain microscopic tensile curves was very similar to the macro-scale material, however, the microscopic curve starts to deviate from the macroscopic curve fairly quickly and therefore, the elastic limits differ. The elastic limit was taken at the stress where the curve starts to deviate from the initial linear relation. The second plain microscopic curve's slope and strain to failure is different from the first curve, which is strange. No extensometer was used on the micro-scale material, so the elastic limits will be used to make comparisons between the micro and the macro material. Table 7.1.1 gives a summary of the material properties.

Table 7.1.1 Summary of macroscopic material properties

	Young's Modulus [GPa]	**0.2 % Proof Stress [MPa]**	**Elastic limit [MPa]**	**UTS [MPa]**
MACRO aluminium	65	113	113	113[1]
Plain MICRO aluminium	N/a	N/a	55	130
Notched MICRO aluminium	N/a	N/a	60	108

The specified *UTS* value for this material lies between 100 and 135 MPa (Bellett, 2002), which was the case for all the specimens, although the plain micro-scale specimen had a somewhat higher *UTS* than the notched microscopic material and the plain macroscopic material. The strain to failure of the material, for a gauge length of 50 mm, is specified to be around 4% (Bellett, 2002). No comparison could be made with the macro-scale material having a gauge length of 50 mm, because that specimen did not fail. The micro-scale specimens had much less strain to failure than 4%, but also only $1/10^{th}$ of the specified gauge length.

No value for the yield strength was specified for this material. It is however strange that the microscopic material has a smaller elastic limit than the macro material. This effect was not observed in the stainless steel where the macro-scale elastic limit was 290 MPa and the

[1] This value for the macro UTS is an estimate, since the specimen did not fail. However, looking at Fig. 7.1.2, it is not likely that the stress will increase, therefore, a UTS of 113 MPa seems to be reasonable.

micro-scale elastic limit 300 MPa. The observed Young's Modulus of the 99.5% pure aluminium of 65 GPa is typical of aluminium and aluminium alloys (Ashby and Jones, 1986). The notch in the microscopic specimen does not seem to have much effect on the elastic limit compared to the plain microscopic material and the *UTS* is only reduced slightly by the introduction of the notch.

Fig. 7.1.3 shows SEM pictures of the tensile fracture surfaces of a plain and a notched aluminium micro-scale plate specimen. From these pictures, the true failure stresses were determined, similar as for the stainless steel material in section 6.1.2. No comparison could be made with the true failure stress of the macroscopic material, because it was not tested to failure.

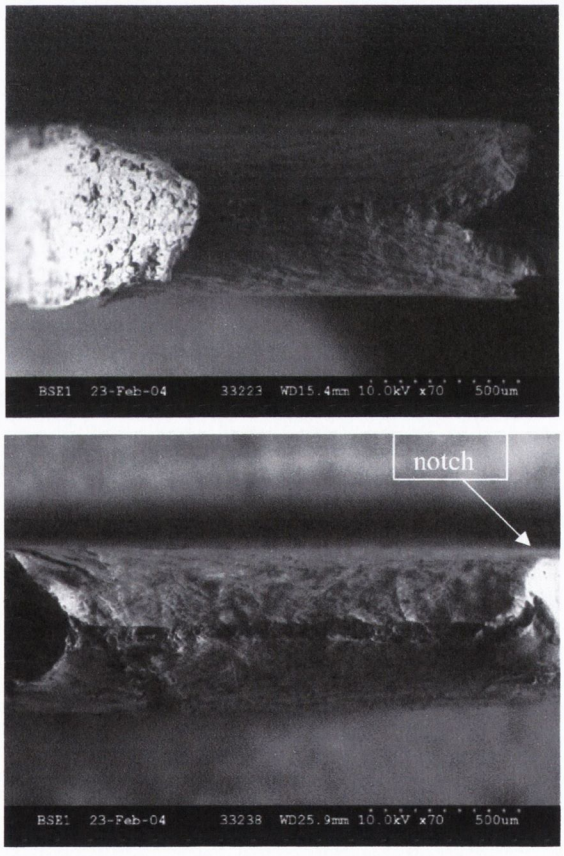

Fig. 7.1.3a) Plain aluminium plate
b) Notched aluminium plate

Table 7.1.2 gives the calculated true stress values for the microscopic aluminium specimen geometries.

Table 7.1.2 Summary of true stresses at failure for the aluminium material

	Area at failure [mm^2]	**Load at failure** [N]	σ_{fTRUE} [MPa]
Micro plain	0.0381	85.59	2247
Micro notch	0.0683	86.14	1260

The *nominal* failure stress for the microscopic aluminium was 130 MPa. The *true* failure stresses are substantially larger, as was also found for the stainless steel microscopic material. However, for the stainless steel, the notched specimens were found to be stronger than the plain material due to constraint as a result of the symmetrical side notches. The aluminium only contained one side notch, therefore no circumferential notch was created and the aluminium notched specimens were found to be weaker than the plain ones.

7.2 Discussion of fatigue results

Fig. 7.2.1 shows that the plain specimen fatigue limits of the macroscopic and the microscopic aluminium are different. In the 316L stainless steel, which was discussed in chapter 6, the plain specimen fatigue limit was the same for micro-scale and macro-scale material. For the aluminium samples, there is an increase in the plain fatigue limit for the microscopic material (75 MPa) compared to the macro-scale plain fatigue limit (55 MPa). It is unclear why this is different from the 316L stainless steel material. The micro-scale specimens were manufactured using the same techniques and the hardness values for the materials were similar, see section 5.5.

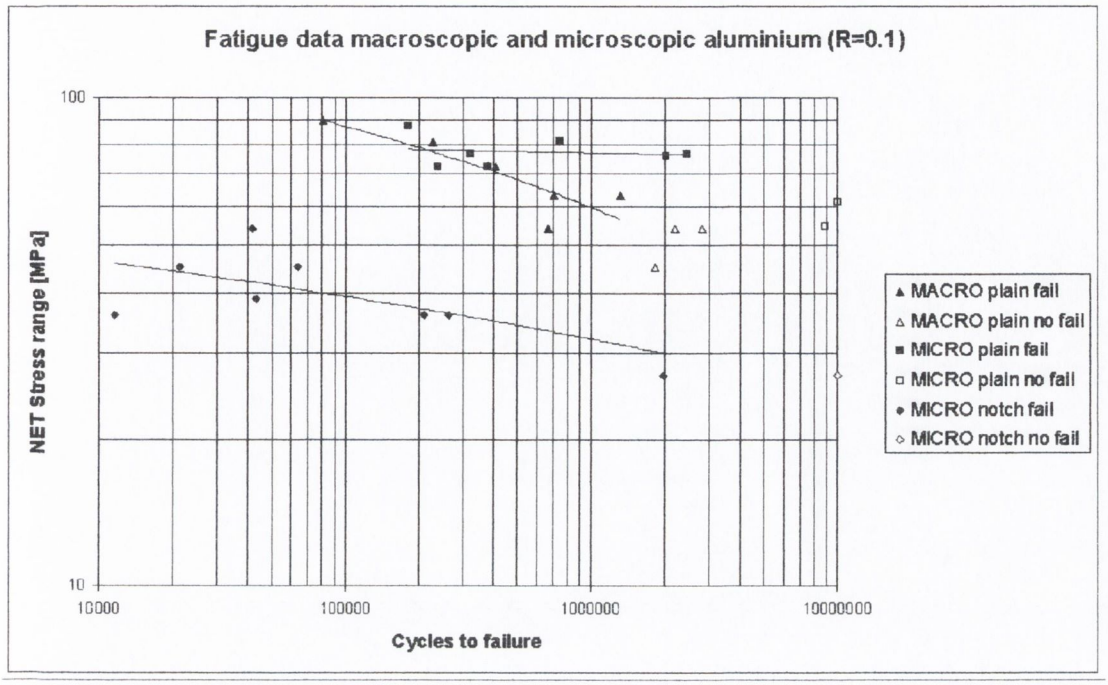

Fig. 7.2.1 Fatigue results of plain and notched aluminium specimens

Another observation for the stainless steel was that the microscopic plain and notched wire specimen fatigue data showed a slope close to zero when plotted on an S-N_f-curve. The same was found for the plain microscopic aluminium fatigue data, see Table 7.2.1. The macroscopic material shows a bigger slope than the microscopic material, which agrees with the stainless steel data. The notched microscopic fatigue data shows sloping similar to what was found for the 316L notched fatigue data.

Table 7.2.1 Summary of slopes of the S-N_f-relation for micro and macro aluminium

	Aluminium slope	
	Slope	**k=1/slope**
Macroscopic plain	0.176	5.67
Microscopic plain	0.0116	86.57
Microscopic notched	0.0813	12.30

7.3 Microscopy of the microscopic specimens

This section discusses the fracture surfaces that were analysed using Scanning Electron Microscopy (SEM).

7.3.1 Tensile fracture surfaces

Fig. 7.3.1a shows the tensile fracture surface of a plain specimen and Fig. 7.3.1b that of a notched specimen. Both microscopic aluminium specimens showed significant necking before failure.

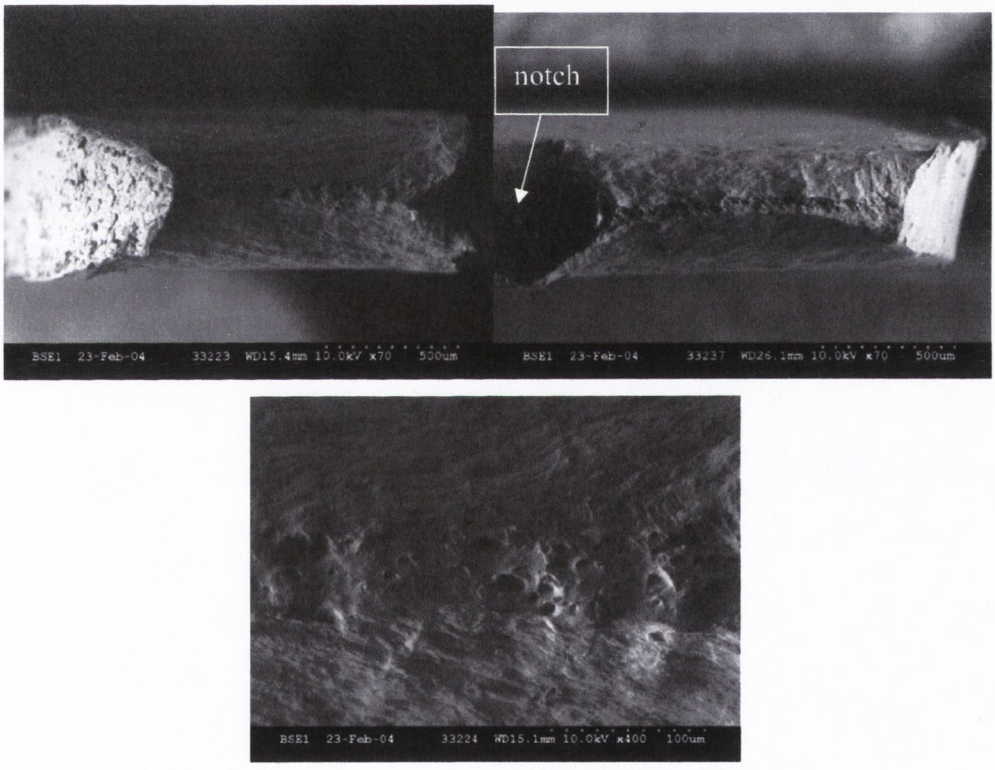

Fig. 7.3.1a) Tensile fracture surface of a plain aluminium plate

b) Tensile fracture surface of a notched aluminium plate

c) Enlargement of the plain tensile fracture surface

The dimples that indicate fast fracture are shown in Fig. 7.3.1c. The aluminium microscopic plates necked more in the thickness direction than in the width direction, similar to that observed in the microscopic stainless steel specimens.

7.3.2 Fatigue fracture surfaces

Fig. 7.3.2 shows typical fatigue fracture surfaces of respectively a plain and a notched aluminium specimen. The fracture surface can be divided into two regimes. The dimpled fast fracture part and the fatigue part, which is distinguishable by waves or ripples. A magnification of the specific fatigue surface is given in Fig. 7.3.2c.

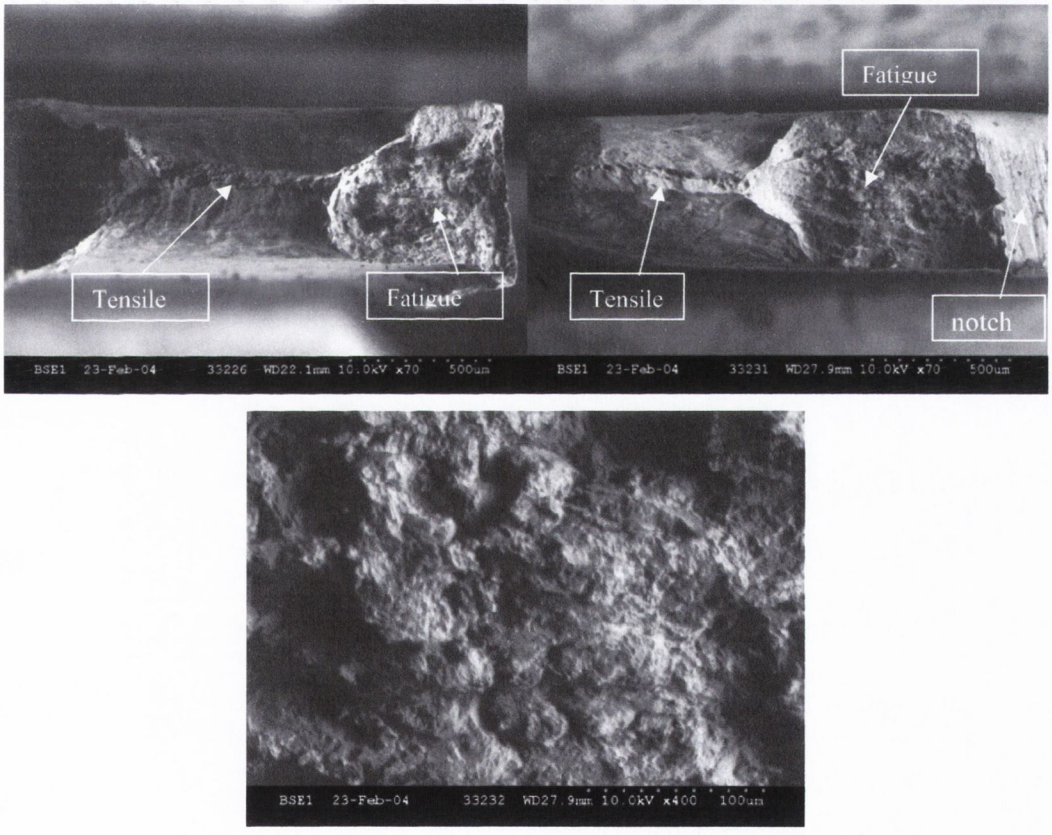

Fig. 7.3.2a) Fatigue fracture surface of a plain aluminium plate

b) Fatigue fracture surface of a notched aluminium plate

c) Enlargement of the fatigue fracture surface

During fatigue crack growth, hardly any necking occurred, but substantial necking did occur in the fast fracture part of the fracture surface that is distinguished by the typical dimples. This was also observed in the micro-scale stainless steel specimens.

7.4 Discussion of prediction methods vs. micro-scale fatigue results

Only one type of notched geometry was fatigue tested for both the macroscopic aluminium and the microscopic aluminium. The experimental data of the macroscopic tests was used to determine the material properties and these material properties were then used to predict the fatigue behaviour of the microscopic specimens. Table 7.4.1 summarises the different fatigue prediction methods that were used. The same short crack and micro-scale corrections were considered as used for the stainless steel. All methods and short crack corrections (scc) were discussed in chapters 2 and 3. The threshold and corresponding critical distance values were calculated in section 5.4.

Table 7.4.1: Prediction methods to be used on micro-scale 316L stainless steel specimens

METHOD	COMMENTS
Stress Life method	K_t needs to be determined through FEA
Smith and Miller - Long crack prediction - El Haddad scc a_o - scc using ΔK_{th_width} for width specimen	 D needs to be known R-curve needed to determine ΔK_{th_width} at width
CMM - Long crack prediction - El Haddad scc a_o - scc using ΔK_{th_width} for width specimen	 D needs to be known R-curve needed to determine ΔK_{th_width} at width
TCD - Long crack prediction - Changing L using ΔK_{th_width}	 R-curve needed to determine ΔK_{th_width} at width
Resistance curve method (El Haddad)	Crack length, notch depth, CMM's a_w required
Suo/KK (scc already included)	Notch depth, D, or CMM's a_w required to be able to determine El Haddad's a_o value

The effective threshold of the macroscopic aluminium material was not determined by testing at a high R ratio. However, information about the effective threshold for a different type of aluminium (2090-T8E41) was found in literature (Taylor and Jianchun, 1993). The material threshold at an R-ratio of 0.1 was 5.5 MPa$\sqrt{m}$ and the corresponding effective threshold was 1.6 MPa$\sqrt{m}$, therefore, a reduction in effective threshold could also be expected for the aluminium tested in this work.

Table 7.4.2 summarises important parameters taken from chapter 5 that are needed to make fatigue predictions for the microscopic aluminium. It makes no sense to predict the fatigue limit of the notched macroscopic specimen, because that fatigue limit was actually used to calculate the material properties, so then a perfect prediction is expected. The microscopic threshold value for the aluminium calculated through the equation was very different from the threshold value through the *FEA* curve, therefore, both thresholds were included in Table 7.4.2 as $MICRO_{eq}$ and $MICRO_{FEA}$.

Table 7.4.2 Important parameters for fatigue predictions

	$\Delta\sigma_o$ [MPa]	$\Delta\sigma_{on}$ [MPa]	K_t [MPa$\sqrt{m}$]	F_{NET}	w_{NET} [mm]	D [mm]	ΔK_{th} [MPa$\sqrt{m}$]	L [mm]	ΔK_{th_width} [MPa$\sqrt{m}$]	L_{width} [mm]
MACRO	55	12.9	47.86	1.16	35	15	3.25	1.11	2.78	0.811
MICRO$_{eq}$	75	30	14.18	1.41	1.5	1.5	3.53	0.706		
MICRO$_{FEA}$							1.52	0.131		

The threshold value calculated using the equation (Murakami et al, 1987) was twice as high as the value calculated using the *FEA* stress-distance curve. This is probably caused by different assumptions made for the flexibility of the grips. The loading situation of the specimen can be modelled in *FEA* in two different ways: allowing rotation at the grip to keep the load constant over the gross section (this should *not* happen if the grips are stiff), or allowing no rotation at the grip. Fig. 7.4.1 illustrates the two loading situations and the corresponding stress distance curves obtained. Coupling is used in FEA to restrict the movement at the grip and prevent bending from occurring.

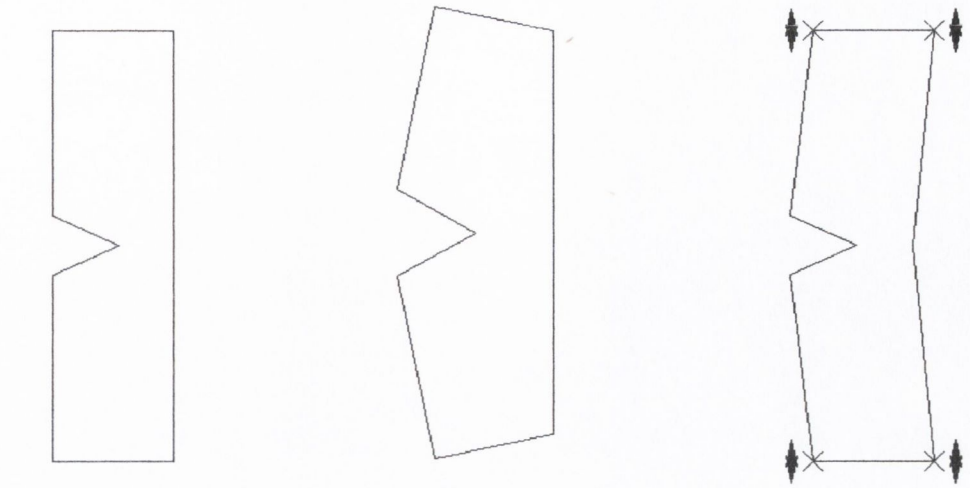

Specimen geometry before testing

NO COUPLING rotation at the grip: EQUATION

WITH COUPLING no rotationat the grip: FEA CURVE

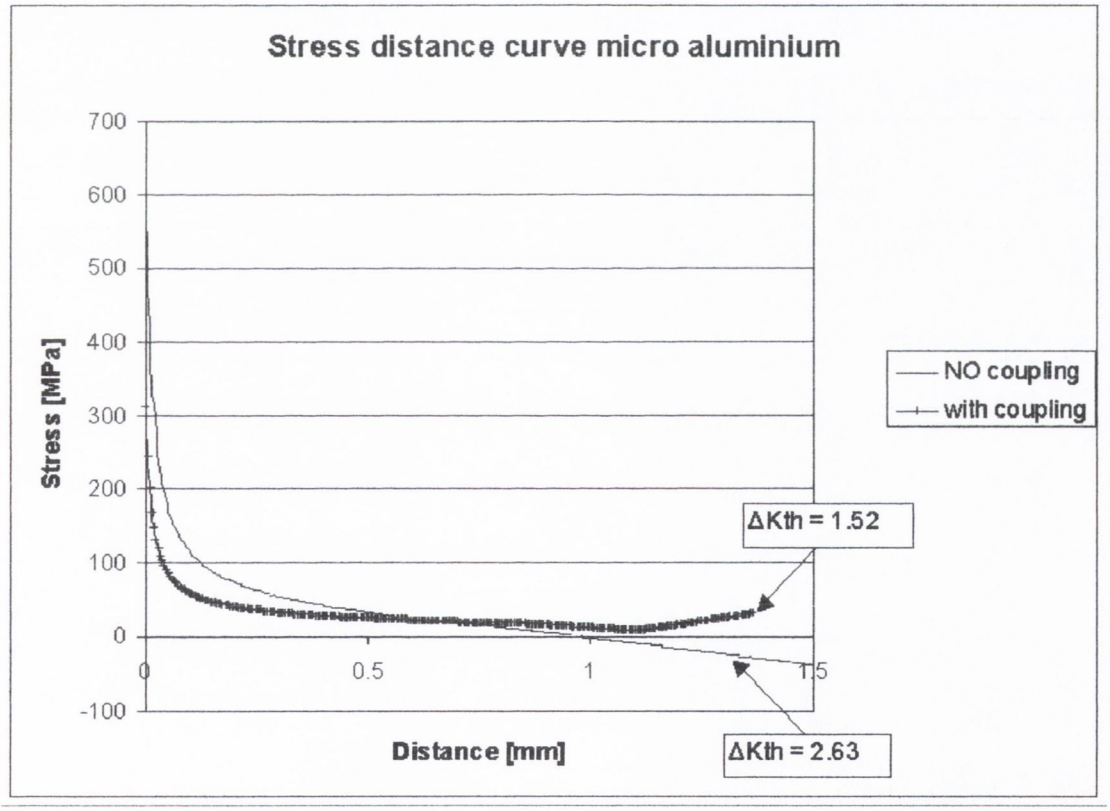

Fig. 7.4.1a) Different ways of modelling the SENT specimen in FEA

b) Corresponding stress-distance curves

The coupling process simulates the actual testing situation, because the grips are stiff and therefore no rotation should occur. Simulating coupling results in bending at the notch, where all stresses at the net section are positive, but the stresses increase again at the far end from the notch. When rotation at the grips was allowed (no coupling), compressive stresses were found at the far end of the net section.

Modelling the specimen in these two different ways, results in two different values for the microscopic threshold of the material. The threshold value based on the model that allows rotation to occur at the grips is more similar to the equation based threshold value given in Table 7.4.2. This suggests that the equations were based on the assumption that rotation can occur at the grips. This is a necessary assumption if the applied stress is to be constant over the gross section at the grips. The *FEA* analysis was done on a small gauge length of 5 mm while the equations assume a finite length of the specimens, which should compensate for the final difference between the equation value and the *FEA* threshold value.

This explains why there was a difference found in the threshold values based on the equation and using *FEA*, the next question is which is the correct value? As mentioned before, from literature the closure-free threshold in a different type of aluminium was found to be lower than the material threshold and a similar reduction in threshold was observed in the stainless steel material. The aluminium specimens in this work are micro-scale specimens and no rotation occurred at the stiff grips. The microscopic threshold value used for the prediction methods will be the lower one, based on *FEA* with coupling, i.e. 1.52 MPa$\sqrt{m}$.

The Smith and Miller and the Suo/KK methods are based on the same equation as was used to determine the higher microscopic threshold value, therefore, using the *FEA* threshold will result in poor predictions for these methods. The CMM and the TCD are based on the *FEA* curve and are thus expected to give good results with this reduced value for the microscopic threshold.

Bending at the notch occurred because of the asymmetry of the specimen and this resulted in a bad fit between the *FEA* curve and the Westergaard function. The best fit for the Westergaard function was a stress close to zero and a corresponding crack length a_w, going to

infinity. Reducing the length of the stress distance curve before implementing it in the CMM software eventually reduces the value of a_w, and a good value for a_w could be obtained at a very short length for the stress distance curve. However, this length can not be predicted, which means that it is more chance than anything else. The a_w short crack correction could therefore not be used.

7.4.1 Discussion of the Stress Life method

The Stress Life method uses the K_t value and the plain specimen fatigue limit to make a prediction. If there are no experimental details for the microscopic material, the macroscopic plain specimen fatigue limit has to be used. As a reference, the second prediction was made using the microscopic plain fatigue limit (for the stainless steel these parameters had the same values). Table 7.4.3 summarises the Stress Life predictions for the aluminium notched specimens. No short crack or micro-scale correction factors are applicable to the Stress Life method.

Table 7.4.3 Stress Life predictions of $\Delta\sigma_{on}$ for the microscopic aluminium specimens

	PREDICTION at net for 2 million cycles using $\Delta\sigma_o$ = 55 MPa		**PREDICTION** at net for 2 million cycles using $\Delta\sigma_o$ = 75 MPa	
	[MPa]	**error [%]**	**[MPa]**	**error [%]**
MICRO aluminium	3.88	+87.07	5.29	+82.37
MACRO aluminium	1.15	+91.06	1.57	+87.81

The predictions in Table 7.4.3 show large conservative errors, as can be expected. The Stress Life method does not work well for sharp notches.

7.4.2 Discussion of the Smith and Miller method

As can be seen in Table 7.4.4, using the macroscopic threshold value to predict the fatigue behaviour of the microscopic specimen gives good predictions. However, the Smith and Miller method is based on the same equation that was found invalid for this aluminium specimen geometry and it should therefore not be used. The reason for the good prediction is that this invalid equation gives a similar threshold value for the microscopic material as was found for the macroscopic material.

Table 7.4.4 Smith and Miller predictions of $\Delta\sigma_{on}$ for the microscopic aluminium specimens

	Fatigue life prediction (2 million cycles, using ΔK_{th} = 3.25)				**Fatigue life prediction (2 million cycles, using ΔK_{th_width} = 2.78)**			
	Using $\Delta\sigma_o$ = 55 MPa		Using $\Delta\sigma_o$ = 75 MPa		Using $\Delta\sigma_o$ = 55 MPa		Using $\Delta\sigma_o$ = 75 MPa	
	[MPa]	**error [%]**	**[MPa]**	**error [%]**	**[MPa]**	**error [%]**	**[MPa]**	**error [%]**
no scc	33.48	-11.61	33.48	-11.61	28.64	4.55	28.64	4.55

It is interesting that it makes no difference whether the macroscopic or the microscopic plain fatigue limit is used. Both give good prediction values. This is not surprising, because the equations used by Smith and Miller do not include the plain fatigue limit.

7.4.3 Discussion of the Crack Modelling Method (CMM)

Table 7.4.5 summarises the CMM predictions for the microscopic aluminium specimens using the macroscopic threshold and the reduced width threshold, ΔK_{th_width}.

Table 7.4.5 CMM predictions of $\Delta\sigma_{on}$ for the microscopic aluminium specimens

	Fatigue life prediction (2 million cycles, using ΔK_{th} = 3.25)				**Fatigue life prediction (2 million cycles, using ΔK_{th_width} = 2.78)**			
	Using $\Delta\sigma_o$ = 55 MPa		Using $\Delta\sigma_o$ = 75 MPa		Using $\Delta\sigma_o$ = 55 MPa		Using $\Delta\sigma_o$ = 75 MPa	
	[MPa]	**error [%]**	**[MPa]**	**error [%]**	**[MPa]**	**error [%]**	**[MPa]**	**error [%]**
no scc	57.55	-91.83	57.55	-91.83	49.23	-64.10	49.23	-64.10
scc_{ao}	49.15	-63.83	52.54	-75.15	N/a	N/a	N/a	N/a

The error values for the CMM are all non-conservative and well above the acceptable 20%. This is not unexpected, because these calculations were done based on the macroscopic threshold value of 3.25 MPa√m and it was shown that the microscopic threshold is 1.52 MPa√m, which is similar to the threshold value that was determined through the CMM itself.

The reduced threshold based on the width of the specimen, ΔK_{th_width}, also gives too large non-conservative errors for the micro-scale predictions. It is clear from Table 7.4.5 that the plain specimen fatigue limit (55 MPa or 75 MPa) does not influence the long crack prediction, but it does influence the short crack correction.

7.4.4 Discussion of the Theory of Critical Distances (TCD)

The Theory of Critical Distances uses the stress distance curve obtained from *FEA* analysis to determine the microscopic fatigue limit of the notched specimen. Therefore, similar errors are expected as found for the Crack Modelling Method. Table 7.4.6 summarises the predictions for the TCD. No Line Method prediction could be made when the plain fatigue limit of 55 MPa was used, because the net width of the specimen was too small.

Table 7.4.6 TCD predictions of $\Delta\sigma_{on}$ for the aluminium specimens

	Fatigue life prediction (2 million cycles, using ΔK_{th} = 3.25)				**Fatigue life prediction (2 million cycles, using ΔK_{th_width} = 2.78)**			
	Using $\Delta\sigma_o$ = 55 MPa		Using $\Delta\sigma_o$ = 75 MPa		Using $\Delta\sigma_o$ = 55 MPa		Using $\Delta\sigma_o$ = 75 MPa	
	[MPa]	**error [%]**	**[MPa]**	**error [%]**	**[MPa]**	**error [%]**	**[MPa]**	**error [%]**
PM	60.41	-101.4	55.19	-83.97	48.85	-62.83	46.05	-53.5
LM	N/a	N/a	60.56	-101.9	N/a	N/a	48.76	-62.53

The reduced threshold based on the net width of the specimen does give better results for the TCD, however, still not good enough. Good predictions should be obtained when the correct threshold value is used: 1.52 MPa√m. This will be discussed in section 7.5.

7.4.5 Discussion of the Resistance-curve method (R-curve)

Table 7.4.7 gives the predictions for the Resistance-curve method. Since Tanaka's relation for the R-curve requires several experimentally determined values, only El Haddad's R-curve relation was analysed.

Table 7.4.7 Resistance curve predictions for the aluminium micro-scale specimen

	Fatigue limit		**Non-propagating crack length**
	[MPa]	**error**	**[mm]**
Micro notch	17	+43.3%	0.25

The Resistance-curve method gives a poor prediction for the microscopic aluminium specimen. This might have to do with the fact that only El Haddad's R-curve relation was used. This relation includes the short crack parameter a_o, which calculation includes the same equation that was found invalid for this asymmetric microscopic geometry.

7.5 Concluding Remarks

Unlike the stainless steel, the aluminium has a different plain specimen fatigue limit for the macro-scale and the micro-scale material. This however does not affect the threshold of the material; for both the macroscopic and the microscopic material, the threshold calculated through the equation was similar. Therefore, it is logical that the Smith and Miller and the Suo/KK methods give good predictions with this value, because they use the same equations.

It is different for the *FEA* based methods: the CMM and the TCD. These methods use stress distance curves from Finite Element Analysis to obtain the predictions. When these curves were used to determine the threshold values, the macroscopic threshold was found to be similar to that calculated through the equations, but the *microscopic* threshold was only half of the corresponding equation value. Since the equation threshold value was used to make the predictions, the results were extremely poor for these *FEA* based methods.

However, it has been demonstrated that the equation assumes that the grip is allowed to rotate, which did not occur in the fatigue tests of the micro-scale aluminium specimens. Therefore, the smaller *FEA* based threshold value is the correct value for the material. This agrees with the reduction in threshold value for the microscopic material that was observed in the stainless steel. Even though the *FEA* threshold is the correct one in order to get good predictions for the Smith and Miller and the Suo/KK methods, the equation threshold value needs to be used, because these methods are based on the same equations.

Under these circumstances, both types of prediction methods should give good predictions. Above it has already been demonstrated that the Smith and Miller and Suo/KK methods work using the microscopic threshold calculated through the equations, Table 7.5.1 shows that the CMM and the TCD give good predictions for the *FEA* threshold value of 1.52 MPa$\sqrt{m}$. The Smith and Miller method gives a poor prediction, but is conservative.

Table 7.5.1 Summary of results using the FEA threshold value

	Fatigue life prediction (2 million cycles, using ΔK_{th} = 1.52)	
	Using $\Delta\sigma_o$ = 75 MPa	
	[MPa]	**error [%]**
Smith & Miller	15.66	47.81
CMM	26.92	10.27
TCD: PM	27.30	+9
TCD: LM	28.94	+3.53

The microscopic plain specimen fatigue limit was used for these predictions, but is was found that the plain specimen fatigue limit does not substantially influence the prediction.

Chapter 8 Discussion

A general discussion is given in this chapter on the stainless steel and aluminium fatigue and fracture results and the corresponding prediction methods that were used. Also recommendations will be given how to apply certain prediction methods to micro-scale components, e.g. the stent.

8.1 Stainless steel vs. aluminium results

Macro and micro fracture and fatigue tests were done on 316L stainless steel and on a 99.5% pure aluminium alloy. Some similarities and some differences were found between the two materials.

8.1.1 Stainless steel vs. aluminium tensile results

Even though a limited number of tensile tests were carried out on the stainless steel and aluminium specimens, some interesting results were found.

Stainless steel

The 0.2% proof stress for the macro material (396 MPa) was found to be higher than for the micro material (315 MPa). Why this is the case is unclear, especially because the elastic limits of the macro and micro material are similar. Probably, there is some sort of size effect that causes this difference. There was also a difference found in the Young's Modulus values; the value found for the micro material was smaller than that for the macro material. This difference was not expected, because even though there are only a few grains in the width and thickness direction, in the length direction, there are enough grains to form a continuum. However, it seems that the influence of the micro sizes in the width and/or thickness

direction do influence the Young's Modulus. How and why can not be explained, more tests should be carried out to investigate this effect. The Young's Modulus for the macro specimens was determined using an extensometer, while for the micro specimens no extensometer was used. Instead an *FEA* model was created, which agreed with the micro results.

All microscopic plain and notched wires and tubing pieces, were found to be stronger than the macro material, expressed in true stresses. This is a very useful result, because it means that when designing stents, one should not be too concerned about the effect of notches on the strength of the material, probably because of the notch strengthening effect; the notched microscopic specimens were much stronger than the plain microscopic specimens. In order for the notch strengthening effect to occur, it is however important to manufacture *symmetrical* features in the stent. A *circumferential* notch is required for the strengthening effect to occur. When the microscopic specimens start to neck, most necking occurs in the thickness direction, therefore side notches are required to obtain a circumferential notch.

Aluminium

For the aluminium material fewer tensile tests were carried out, than for the stainless steel. Also, the one macroscopic tensile test that was carried out could not be tested to failure, due to an error of the test machine. The elastic limit of the macro material was found to be twice as large as for the microscopic material, which is strange, because for the stainless steel, the elastic limit was found to be similar.

Since the macro material was not tested to failure, the true failure stress could not be determined. For the plain and notched microscopic specimens, these true failure stresses were calculated. Because the microscopic notched specimen only contained one edge notch, the strengthening effect did not occur; the plain micro-scale specimen was found to be around 1.75 times as strong as the notched micro specimen, which is the opposite of what was found in the stainless steel material.

Stainless steel vs. aluminium

The aluminium was found to behave differently to the stainless steel with respect to the elastic limit and the true failure stresses. The elastic limit was found to be similar between the macro and microscopic stainless steel, but different for the aluminium. Notch strengthening occurred for the microscopic stainless steel specimens, but not for the aluminium specimens.

There is an important difference between the stainless steel and the aluminium macroscopic specimens; the thickness. For the stainless steel bars, the thickness was macroscopic, however, for the aluminium, the thickness of the macroscopic specimens was smaller than the critical distance value; the thickness for the macro aluminium was microscopic.

Notch strengthening did occur in the stainless steel, but not in the aluminium microscopic specimens. This is probably because the aluminium samples only contained one side notch, therefore, when the specimen started to neck, no real circumferential notch was created. For the stainless steel this did happen, because there were two notches present.

The differences found in the elastic limit values for the macro and microscopic aluminium that were not found in the stainless steel, might be due to the fact that the aluminium specimen was already partly microscopic (thickness). Maybe, the parameters thickness and width have opposite effects on the elastic behaviour, e.g. a microscopic thickness with macroscopic width decreases the elastic limit, while a microscopic width in combination with a microscopic thickness increases the elastic limit again roughly up to the original macro value. Therefore, for the macro and micro-scale stainless steel, the elastic limits were similar, because both thickness and width were macroscopic for the macro tests and microscopic for the micro tests. For the aluminium, both the thickness and the width were microscopic, but the macroscopic specimens were not macroscopic in thickness, thus resulting in different elastic limits.

8.1.2 Stainless steel vs. aluminium fatigue results

Fatigue tests were carried out on several microscopic notched stainless steel geometries and on one aluminium geometry.

Stainless steel

For the stainless steel, the macro and microscopic plain fatigue limits were the same. The threshold values for the micro specimens were found to be smaller than for the macro material. What might cause these reductions will be discussed in section 8.1.3. Fig. 8.1.1 illustrates how the experimental threshold value for the microscopic stainless steel specimens changes with half the notch depth. The thresholds were calculated using the equations.

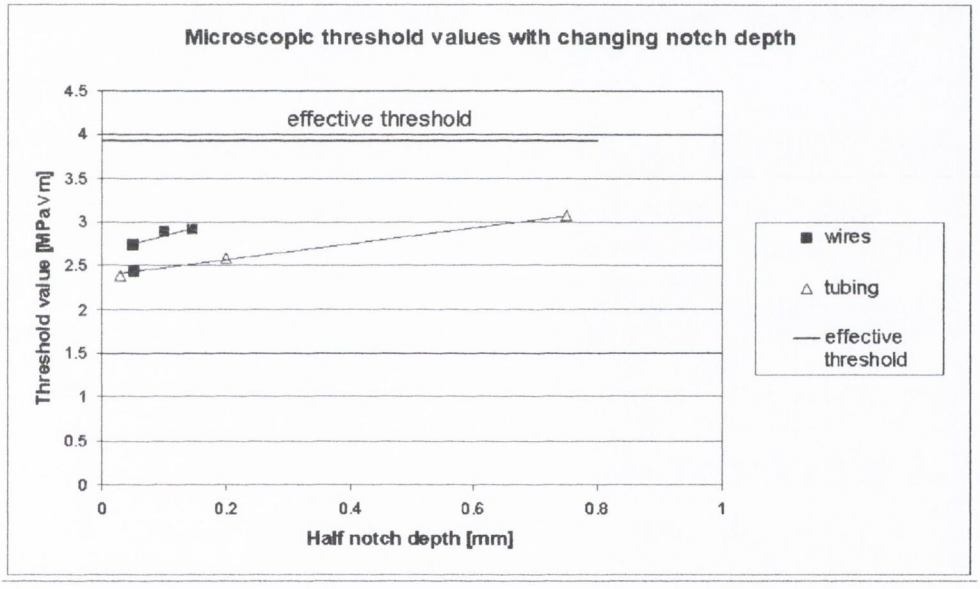

Fig. 8.1.1 Microscopic threshold values with changing notch depths

Since the slots in the tubing pieces were modelled as centre notches, the corresponding crack length is half the notch depth. Considering the microscopic specimens in groups (wires and tubing pieces), Fig. 8.1.1 illustrates that the microscopic threshold increases with increasing notch depth. The FIB50 threshold value was given in the Fig. 8.1.1, however, it is left out of the wire relation, because the FIB50 specimen always behaved somewhat differently from the other wires.

The reduction in threshold value with decreasing crack length is what one would expect. This effect is normally attributed to crack closure. The long crack effective threshold value is also shown in Fig. 8.1.1, but all these microscopic threshold values lie below that closure-free threshold. This probably has to do with the fact that the specimens are microscopic and that the grain distribution or some other effect comes into play as well as crack closure.

Aluminium

For the aluminium material, the macro and microscopic fatigue limits were found to be different. This again might also have to do with the fact that the macro specimens had microscopic dimensions in the thickness direction, thus influencing the fatigue limit of the material. More research should be done in order to investigate this effect.

The same reduction in threshold value was found between the macro and micro material as for the stainless steel, indicating that a similar mechanism seems to be at work. Why these reductions occur will be discussed in the following section.

8.1.3 Why are the threshold values and critical distances smaller for the microscopic specimens?

In chapter three, the fatigue prediction methods were altered to apply to microscopic components on the assumption that the critical distance is related to the maximum non-propagating crack length. An analysis was done, according to Tanaka's R-curve method, and a trend was found that the non-propagating crack length does reduce with component size.

There are two other possible causes for the reduction in threshold and critical distance in micro-scale components. The first is that plane stress/mode-III shear loading occurs. Very thin specimens that are in plane stress fail in mode-III shear; therefore the fatigue fracture surface should have an angle of 45 degrees. The final cause for the reduced values could be the lack of closure in these micro specimens containing very short cracks.

Which of the three possibilities causes this reduction? It can not be the assumption of the non-propagating cracks, because, the 1500-slotted tubing, contains *long cracks*, therefore, *the long crack threshold*, should give a good prediction, not the reduced one, which is not the case for the TCD method. In other words, the thickness has an effect, even on long cracks.

Also, the specimens are not experiencing mode-III shear loading, because the fatigue fracture surfaces are not at 45 degrees (in the thickness direction), as can be seen in Fig. 8.1.2. The fatigue fracture surface is almost parallel to the surface of the slot; therefore, it did not fail from mode-III shear. This effect was found in all geometries. In the background of Fig. 8.1.2, also, a part of the fast fracture surface is visible.

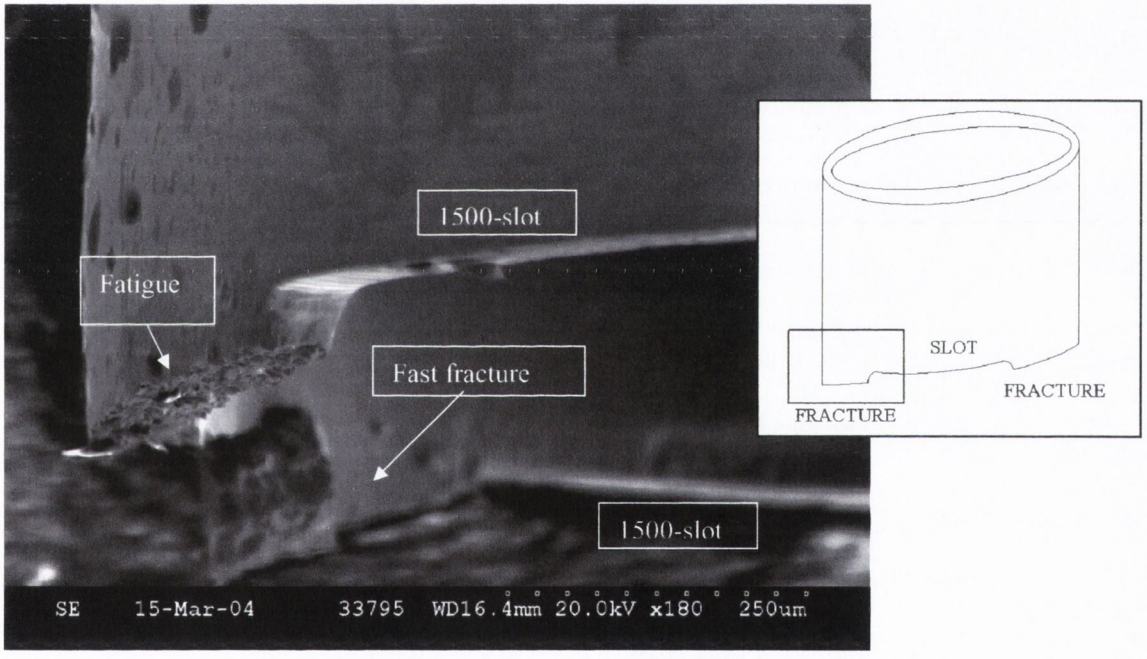

Fig. 8.1.2 Flat fracture surface of a 1500-slotted tubing piece

Therefore, the most likely cause for the reduction in threshold and critical distance is the lack of closure, which is why the effective threshold gives good results for the microscopic stainless steel and aluminium specimens. Maybe the *extra* reduction in threshold for the microscopic notches that was seen in Fig. 8.1.1 is due to the non-propagating crack length.

8.1.4 Concluding remarks

More research needs to be done before conclusions can be drawn about the influence of notches on the tensile strength of microscopic specimens, however, it seems that the microscopic material is equally strong or stronger than the macroscopic material. This effect will be enhanced, if the notches are designed to be symmetrical, thus giving rise to the notch strengthening effect.

There were some differences found between the stainless steel and the aluminium with respect to macro and microscopic material behaviour. This might be caused by the fact that the macro-scale aluminium was in fact microscopic in the thickness direction, which could have influenced the results. Therefore, more work should be done in order to investigate this thickness effect.

It is expected however, that the same reduction in threshold value occurs in other materials as well. Whether the plain specimen fatigue limits will differ between macro and micro-scale components is unclear, but the threshold should reduce for small components as was found for both the stainless steel and the aluminium.

8.2 Discussion of the prediction methods

Several prediction methods were altered and applied to the microscopic specimens. Why some methods worked very well and others did not, will be discussed in this section.

8.2.1 The only prediction method applicable to both the stainless steel and aluminium micro data: the TCD

The altered Theory of Critical Distances was the only method capable of predicting the fatigue failure for all types of microscopic specimens: both in the wires and in the tubing pieces. The *average experimental threshold* value based on the microscopic specimens gave

good predictions. All errors were well below the acceptable 20%, except for the FIB50 specimen, which had an error value of 22.6% for the Point Method. The FIB50 data showed more scatter than the other microscopic fatigue data, partly because of manufacturing problems, see Fig. 6.2.3.

The reason why the average experimental micro-scale threshold gave such good results was because this threshold based on the *equations*, was close enough to the *FEA* threshold value. The TCD approach uses *FEA* based stress-distance curves to make predictions. In Table 8.2.1 it can be seen that the experimental threshold was almost the same for all micro notches, so the average value should give good results for all specimens. This shows that all the tested notches were in fact crack-like, as was assumed.

Table 8.2.1 Summary of the threshold values and critical distances for micro-scale specimens

MICRO specimens	ΔK_{th} FEA curve [MPa√m]	ΔK_{th} CMM [MPa√m]	ΔK_{th} Equation [MPa√m]
316L stainless steel			
50-wire	3.59	2.97	2.73
100-wire	3.63	3.08	2.89
145-wire	3.60	3.19	2.91
FIB50	2.79	2.32	2.43
60-hole	3.49	2.66	2.38
400-slot	3.16	2.73	2.59
1500-slot	3.44	3.17	3.07
Average values	**3.386**	**2.87**	**2.71**
Aluminium			
Single edge notch	1.52	1.76	**3.532**

For the aluminium, there is a large difference between the equation value for the threshold and the *FEA* value for the threshold. This was found to be due to certain assumptions about loading that were made for the equation. These assumptions for the equations were not believed to be correct and therefore, the *FEA* threshold was used instead, which gave good results with the TCD approach for the aluminium specimens.

The effective closure-free threshold in combination with the TCD also gave good results for the stainless steel specimens. The *FEA* threshold is based on the Point Method and because the effective threshold value (3.93 MPa$\sqrt{m}$) is close enough to this value, good results were obtained for the Point Method. The Line Method however, had more difficulty in describing the micro-scale fatigue behaviour. The errors for the wire specimens, apart from the FIB50 are within the acceptable 20%, but higher than for the Point Method. For the 400- and the 1500-slots, the Line Method errors are too large, while the corresponding Point Method values are good. This is strange, but must be the result of the stress distribution ahead of the notch. The Point Method uses the stress at a point, while the Line Method averages the stress over a certain distance. The Line Method is more susceptible to the stress gradient of the stress concentration over a longer distance. Even though these Line Method errors are too large, they are still a lot less than for other prediction methods.

For the aluminium, the effective threshold was not determined experimentally; therefore no predictions could be made. From literature, it was found that also for aluminium, this reduced threshold was found, when cycling at a high, closure-free, R ratio. Therefore, the effective threshold should also work for the microscopic aluminium specimen. In conclusion: the altered TCD is a good approach to predict fatigue failure in microscopic specimens. It is advisable to obtain the threshold using notches in micro-scale specimens, but if this is not possible then the macro-scale effective threshold gives a good approximation.

The Smith and Miller method based on the average microscopic experimental threshold value obviously also works well, because they use the same equations for their predictions as were used to calculate the threshold values.

8.2.2 Why did the other methods not work?

The other prediction methods used throughout this work, did not work for all micro-scale specimen geometries. The Stress Life approach gave large conservative predictions; this is not surprising because this approach does not work for sharp notches. Some of the short crack corrections in combination with the Smith and Miller method worked for the wires, but not for the tubing specimens. This method was not capable of describing the fatigue data for all geometries. The same is valid for Suo/KK, which is the same as the Smith and Miller method.

The Crack Modelling Method also does not work, apart from when using the average experimentally based reduced threshold, because this average threshold value based on the equation was close to the threshold value determined by the CMM itself as can be seen in Table 8.2.1.

The Resistance Curve method does not work well for the stainless steel specimens. This is not surprising, because El Haddad's equations were used, which are generally found to give conservative results. Tanaka's method could not be used, because specific experimental data is required for those equations.

8.3 Recommended procedure for implementation of the altered TCD to microscopic components

For the above specimens, it has been explained how to proceed with the TCD. This section recommends what approach to take when predicting the fatigue strength of microscopic components using the Theory of Critical Distances, with the stent as an example. Fig. 8.3.1 shows an FEA model of a stent (Lally et al, 2002). The stent is a cylindrical wire mesh, consisting of repeating units. The section illustrated in Fig. 8.3.1, which consists of four rings, is the repeating unit of a type of stent that uses two welds around the circumference to connect two rings together. Stents are not always welded, e.g. laser cut stents do not contain welds.

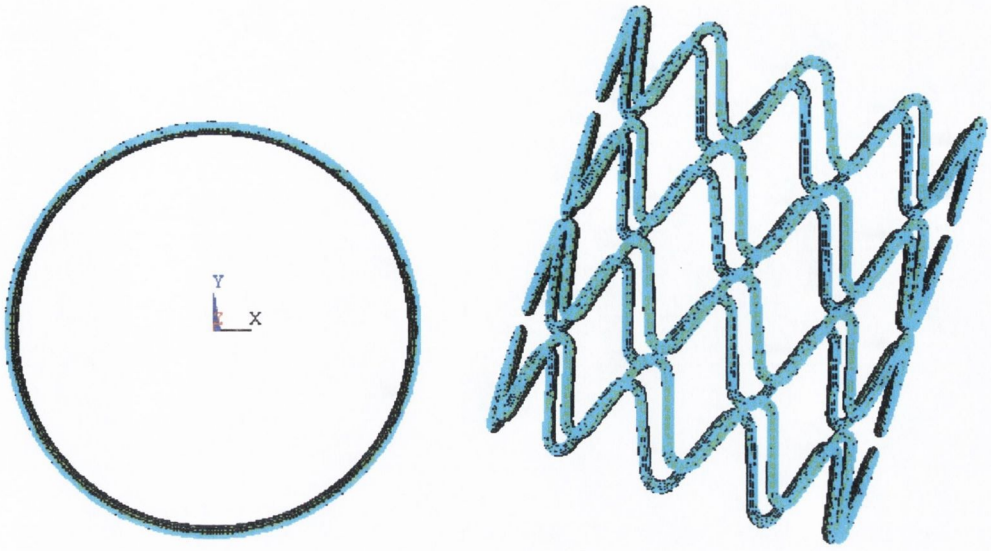

Fig. 8.3.1 FEA model of a stent (Lally et al, 2002)

8.3.1 The stress distance curve

Components contain stress concentrations, which are the weak points where fatigue failure is likely to occur. An *FEA* model of the component with the corresponding loading on that component is used to obtain stress distance curves for these stress concentration points. For the specimens tested in this work, it was clear in what direction to plot the stress distance curve, because of the simple geometry. For a component, it is not always obvious in what direction the path has to be taken (Taylor, 1999).

The weak points in the stent are shown in Fig. 8.3.2: the welds and the bends/curvatures. The path should correspond to the crack propagation path. If this approach is used, the path should be taken along the straight lines shown in Fig. 8.3.2 for situation 1 and 2 (weld and curve). If the weld fails, it will most likely fail across the weld, the curvature will probably fail across the wire itself.

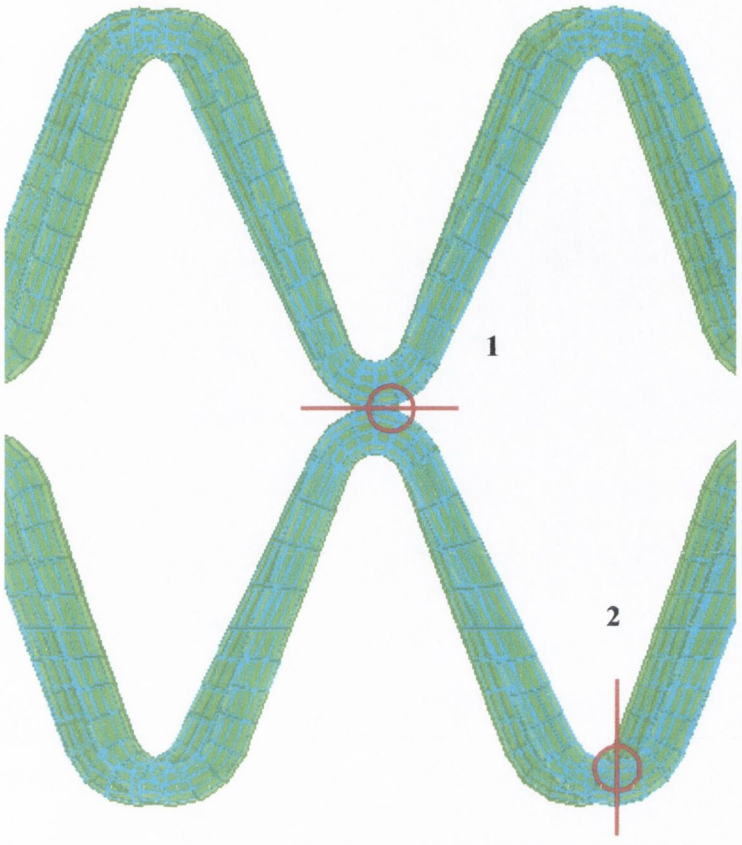

Fig. 8.3.2 Enlargement of the FEA model (Lally et al, 2002)

However, another approach can be taken to make a fatigue prediction. The Point Method gave a more reliable prediction than the Line Method, which is convenient, because the stress at the critical distance for the Point Method can be determined in another way. The idea behind the Point Method is that if the stress at a point ahead of the stress concentration is greater than the critical value (in this case the plain material fatigue limit), the component will fail. Therefore, by drawing a circle with the centre in the point of highest stress and a radius that corresponds to L/2, a prediction can be made, see circles in Fig. 8.3.2. All points on the circle are the points at the critical distance. Therefore, the point on the circle with the highest stress will be the point that will fail first. Or, one could look at all the points located at a distance of $L/2$ from the surface.

8.3.2 The influence of the R-ratio on the critical distance

In order to make predictions, only a few experimental tests need to be carried out to determine the critical distance L; the threshold value of the material and the corresponding plain material fatigue limit. The loading ratio affects these material properties, therefore, it is important to use the same R-ratio as is applicable to the component itself.

If the threshold value and plain fatigue limit are determined using a different loading ratio than that of the component, they have to be converted to the appropriate R-ratio, which can be difficult. However, the conclusion for the microscopic samples was that the effective closure-free threshold should be used, which is very convenient, because it is a material constant and is therefore not dependent on the R-ratio. The plain fatigue limit can be changed to the appropriate value using the Goodman or Gerber relation. Fig. 8.3.3 shows a Haigh diagram, also known as Constant Life diagram, which plots the Goodman and Gerber relations for a material similar to the 316L stainless steel; 316LN (Strizak and Mansur, 2003).

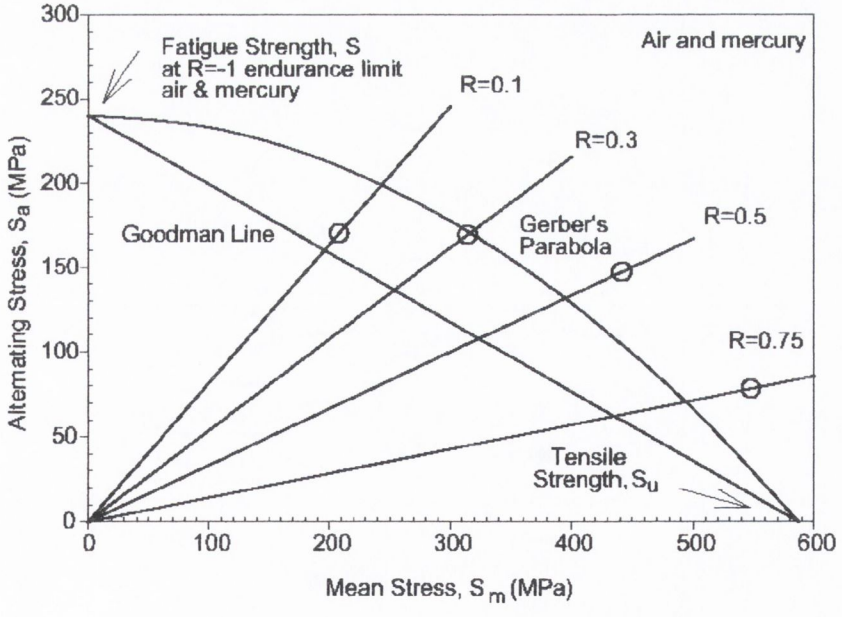

Fig. 8.3.3 Constant life diagram for 316LN stainless steel (Strizak and Mansur, 2003)

When the stent is placed inside the artery, it is expanded using balloon angioplasty. During this expansion process, the stent is plastically deformed, which results in residual stresses. These residual stresses affect the mean stresses of the applied loading and therefore the loading ratio. It is important to be able to account for this phenomenon and the Goodman relation is an easy way to do this, provided that one knows what the effect of the residual stress is on the R-ratio. Again, the R-ratio only affects the plain material fatigue limit in microscopic components, because the effective threshold value is independent of mean stresses.

8.3.3 Making the actual prediction for the stress concentrations

The plain fatigue limit of the stainless steel lies above the yield strength at an R-ratio of 0.1. The material is assumed to cyclically harden in the first cycles after which it should behave elastically, under the increased yield stress. The stents themselves are also plastically deformed by the balloon angioplasty expansion process. Therefore, it is assumed that a linear elastic model can be used to determine the fatigue strength of the weld and the curve features.

Since the stents work-harden during the balloon angioplasty process, it is useful that the un-annealed fatigue data seems to have the same fatigue limit and maybe even a similar threshold value. Obviously more work needs to be done to investigate this, but it seems promising.

The TCD is implemented in easy to use software and in order to make predictions, the threshold value and corresponding plain fatigue limit are required. So, to make predictions for the microscopic specimens, instead of giving the long crack threshold value, the effective threshold value or the experimentally determined threshold value has to be given, resulting in the reduced critical distance value.

8.3.4 Limitations

Even though the results for the TCD, especially the Point Method, were very good for the tested microscopic geometries, the approach should be applied to actual components. The method can be used to determine whether a new design is good or not, it can assist in the design process. When the method predicts no failure, the design can be altered and then tested, thus skipping a step in the development process.

The effective threshold is not known for all materials. However, this value can be obtained quite easily by carrying out macro tests at a high loading ratio. Obtaining the plain material fatigue limit can be difficult, however, since these stents were manufactured using a laser cutter process, it is not that difficult to manufacture specimens to determine the experimental microscopic plain fatigue limit. Only a month, maybe two, are needed to test these two sets of specimens. Then the critical distance is known and the method can be used. The same goes if a different material is used; one to two months of testing is required.

8.4 Why do the microscopic specimens show hardly any slope on the S-N_f curve?

The microscopic *S-N*$_f$-curves showed hardly any sloping, especially the plain and notched stainless steel wires and the aluminium specimens. The stainless steel tubing specimens did show some sloping. There are two possible reasons why this occurs; microscopic specimens are not affected by fatigue, or the distribution of the grains.

8.4.1 No sloping because micro specimens are not affected by fatigue

From the fact that most microscopic Stress-Life curves hardly show sloping, one could conclude that fatigue does not affect these microscopic specimens. A horizontal scatter band can be drawn and it seems that the number of cycles to failure are not related to the applied

stress range, which is unusual. Therefore, the whole High Cycle Fatigue range could be described with a threshold stress. The reason why the tubing specimens do show some sloping, is because the net width is much larger for those specimens, therefore, the width is not microscopic for those geometries.

The tensile results support the idea that microscopic specimens seem to be unaffected, because for the notched specimens a higher true failure stress was found than for the plain material, which also can be attributed to notch strengthening.

Using this logic, one could also argue the existence of non-propagating cracks in these specimens. It seems that the specimen will either fail or not and it is not likely that non-propagating cracks occur.

8.4.2 No sloping because of the distribution of the grains

Another possibility for the lack of sloping is due to the distribution of the grains. Assuming that non-propagating cracks do occur, even at very low loads a non-propagating crack will be formed, which has a length of one or maybe two grains. There are roughly 11 grains along the width of the stainless steel wires. The *average* grain size was determined to be 10 μm, however, grains as small as 1 μm and as large as 20 μm were found.

The size of the first grain, where the non-propagating crack is formed, is therefore important. If the first grain is small, the remaining width is relatively large, while if the first grain is large, the remaining width is much smaller. Therefore, applying the same gross stress range in both situations will result in different values for the nominal net stress, because of the differences in net cross sectional areas. Fig. 8.4.1 illustrates these two extremes.

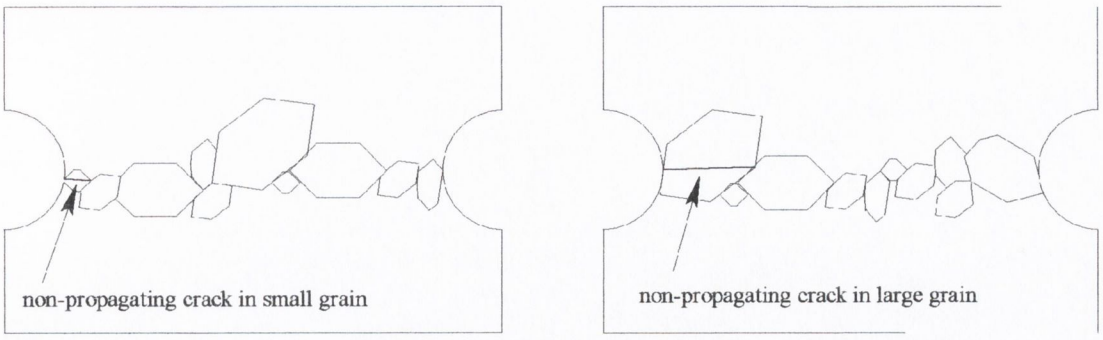

Fig. 8.4.1 Influence of grain distribution on the remaining width of the specimen

If the first grain is small, the nominal net stress will be lower than if the first grain is large. Therefore, the specimen will most likely have a longer fatigue life than when the first grain is large, for the same applied stress range. This can explain why scatter occurred in the microscopic results and why there is hardly any slope on the S-N_f curves.

8.5 A different approach to predicting fatigue failure in microscopic specimens

From the above, one could propose another way to determine the critical distance value for these specimens. The first grain is the most important grain in the microscopic specimens. Therefore, the grain size could be used as the critical distance for the Point Method ($L/2$). This results in a critical distance L of 0.02 mm for the average grain size of 0.01 mm in the 316L stainless steel. To make the fatigue predictions, the stress at that critical distance should be compared to the threshold stress, $\Delta\sigma_{th}$, from the stress life curve, which is the same as the fatigue limit, because there is no sloping in these graphs. Table 8.5.1 gives the prediction for the stainless steel specimens using L = 0.02 mm and a threshold fatigue failure stress, $\Delta\sigma_{th}$, of 420 MPa.

Table 8.5.1 Summary of parameters required for alternative TCD approach

	Prediction alternative TCD approach			
	PM		LM	
	$\Delta\sigma_{on}$ [MPa]	Error [%]	$\Delta\sigma_{on}$ [MPa]	Error [%]
50-wire	341	5.28	382	-6.11
100-wire	333	6.20	379	-6.76
145-wire	332	5.14	379	-8.29
FIB50	353	-10.3	385	-20.3
60-hole	242	3.2	274	-9.6
400-slot	126	-5.0	153	-27.5
1500-slot	111	3.48	135	-17.4

This approach gives excellent results for the Point Method and also good results for the Line Method apart from the 400-slot prediction. For these specimens, the threshold value can be determined through the grain size in combination with the threshold stress range for fatigue failure. The threshold value corresponding to a critical distance of 0.02 mm is 3.33 MPa$\sqrt{m}$, which is lower than the closure-free effective threshold (3.93 MPa$\sqrt{m}$) and since the *FEA* thresholds were lower than the effective threshold, this altered approach will give better predictions than the effective one.

If the threshold stress range, which is equal to the fatigue limit because there is no sloping, is not known, the macro material plain specimen fatigue limit could be used as an initial guess. For the stainless steel, these micro and macro values were the same.

8.6 Concluding remarks

This chapter has discussed several interesting aspects of material behaviour that could be useful to stent manufacturers, or manufacturers of other microscopic components. Especially for biomedical products, it is important to investigate if the material behaviour in air is different from the material behaviour inside the human body. The stainless steel samples in this work were tested in air. Several research groups have investigated ways of improving the 316L material's corrosion resistance. Shih et al (2004) have investigated the effect of several surface improvement techniques on 316L stainless steel wires. They found that these techniques could improve the corrosion resistance of the stainless steel wires, which is useful for the stent manufacturers.

Chapter 9 Conclusions and future work

This chapter summarises the conclusions that can be drawn from this work and gives suggestions for more work that could be done in the future.

9.1 Conclusions

The objectives for this work were to gather data on the fatigue and fracture behaviour of microscopic specimens and to investigate if current *continuum mechanics* prediction theories are capable of describing this behaviour. If not, the methods should be altered and if possible implemented in easy to use software that can interact with CAD and FEA software, which is commonly used by companies. From this work, the following conclusions can be drawn:

1 None of the conventional prediction methods was capable of predicting the microscopic fatigue data without alteration. From the altered methods, the only one capable of describing all the tested microscopic geometries was the Theory of Critical Distances, more specifically the Point Method. The other methods could only predict some of the test data, not all of it.

2 The proposed short crack correction based on El Haddad's short crack parameter a_o, did not work for the full range of specimens. The reduced average experimentally determined threshold value or the effective threshold value, gave good results for all specimen geometries in combination with the Point Method.

3 The threshold values were found to decrease with specimen size for both the stainless steel and the aluminium. The most likely reason for this phenomenon is the lack of closure in microscopic specimens and components. That is why the closure-free effective threshold value was capable of predicting the whole range of specimens, including one long notch that was tested in a microscopic specimen.

4 The Point Method gave good results for both the tested microscopic stainless steel geometries and the microscopic aluminium geometry. It is expected that this method will work for microscopic components for a wide variety of materials.

5 Flat slopes were found in the S-N_f curves for the microscopic specimens. This may be due to the grain distribution.

6 The Theory of Critical Distances has already been implemented in easy to use software. In order to use the altered method, the reduced threshold value (effective or experimental) needs to be given instead of the constant long crack threshold value. Alternatively, the critical distance can be specified as the grain size and the threshold then calculated.

7 Not enough tensile tests were carried out to draw conclusions, but it seems that the micro-scale specimens are not necessarily weaker than the macro-scale material (similar grain size in micro and macro material). If the features in the microscopic components are designed to be symmetrical, notch strengthening can occur, which substantially increases the strength of the micro-scale specimens.

8 For the 316L stainless steel, the un-annealed plain material fatigue limit seems to be similar to the annealed fatigue limit.

9 More tests should be carried out in order to investigate the effect of material and thickness in microscopic components and on the static fracture behaviour.

9.2 Future work

From this work, several conclusion were drawn, but also some interesting areas were discovered that need more investigation:

1 The focus of this work lies on fatigue, therefore, more static tests should be carried out on microscopic specimens to investigate the strengthening effect that was observed in the plain and notched micro-scale tensile tests.

2 More fatigue and static tests should be carried out on plain and notched specimens of a variety of thicknesses to investigate the effect of the thickness on macroscopic and microscopic material.

3 For the stainless steel and the aluminium specimens, the threshold values were found to reduce for microscopic specimens. More materials should be tested for this observed effect.

4 All microscopic specimens were tested at the same R-ratio. It would be interesting to repeat the fatigue tests for different loading ratios.

5 For the 316L stainless steel, the un-annealed/work-hardened material seemed to have the same fatigue limit as the annealed material. More testing should be done to confirm these findings in both the stainless steel and other materials. It would be interesting to see if this effect will be observed in materials which plain fatigue limit is below the yield strength.

6 One of the aims of this work was to investigate if continuum mechanics could be used for microscopic components where there are not enough grains to form a continuum. Therefore, the mechanisms behind failure, e.g. dislocation theory, has been ignored in this work. However, it would be very useful to investigate this in the future.

References

Andrews E.W., and Gibson, L.J., 2001, The influence of cracks, notches and holes on the tensile strength of cellular solids, *Acta Mater 49*, pp. 2975-2979

Akiniwa, Y., Tanaka, K., and Zhang, L., 1996, Prediction of fatigue thresholds of notched components based on Resistance-curve method, *Fatigue '96*, pp. 449-454

Ashby, M.F., and Jones, D.R.H., 1986, *Engineering materials 2: an introduction to microstructures, processing and design*, Pergamon Press, England.

Bellett, D., 2002, The fatigue behaviour of three-dimensional stress concentrations, *PhD thesis*, Trinity College Dublin

Douglass, M.R., 1998, Lifetime estimates and unique failure mechanisms of the Digital Micromirror Device (DMD), *36th Annual International Reliability Physics Symposium*, pp. 9-16

Elber, W., 1970, Fatigue crack closure under cyclic tension, *Engineering Fracture Mechanics*, Vol. 2, pp. 37-45

ElHaddad, M.H., Dowling, N.F., and Topper, T.H., 1979, Fatigue crack propagation of short cracks, *J. Engng. Mater. Techn.*, 101, 42-45

ElHaddad, M.H., Dowling, N.F., Topper, T.H., and Smith, K.N., 1980, J integral applications for short fatigue cracks at notches, *Int. J. Fract.* Vol.16, pp. 15-24

ElHaddad, M.H., and Miettinen, B.I., 1982, Prediction of initiation and early fatigue crack growth in materials, *Fatigue thresholds* (editors: J.Backlund, A.F.Blom and C.J.Beevers), 2, 827

Frost, N.E., 1959, A relation between the critical alternating propagation stress and crack length for mild steel, *Proc. Instn. Mech. Engrs.*, Vol. 173, No. 35, pp. 811-827

Fujimoto, Y., Hamada, K., Shintaku, E., and Pirker, G., 2001, Inherent damage zone model for strength evaluation of small fatigue cracks, *Engineering Fracture Mechanics*, 68, pp. 455-473

Hadrboletz, A., Kathibi, G., Weiss, B., and Stickler, R., 1999, Fatigue crack growth behaviour of thin metallic foils, *Fatigue '99*, pp. 1865-1870

Hong, S., and Weil, R., 1996, Low cycle fatigue of thin copper foils, *Thin solid films*, Vol. 283, pp. 175-181

Huang Z.W., McColl, I.R., and Harris, S.J., 1996, Notched behaviour of a silicon carbide particulate reinforced aluminium alloy matrix composite, *Materials Science and Engineering A215*, pp. 67-72

Keith, W.P., and Kedward, K.T., 1997, Notched strength of ceramic-matrix composites, *Composites Science and Technology*, 57, pp. 631-635

Kitagawa, H., and Takahashi, S., 1976, Applicability of fracture mechanics to very small cracks or the cracks in the early stage, *Proceedings of the Second International Conference on Mechanical Behaviour of Material*, Boston, pp. 627-613

Klesnil, M., and Lucas, P., 1972, Influence of strength and stress history on growth and stabilisation of fatigue cracks, *Engineering Fracture Mechanics*, 4, pp. 77-92

Klesnil, M.K., and Lucas, P.L., 1980, *Fracture of Metallic Materials*, Elsevier, Amsterdam

Lally, C., Prendergast, P.J., Lennon, A.B., Quinn, D., and Dolan, F., 2002, Finite element analysis of tissue prolapse within intravascular stents calculated using a single repeating unit of a stent and a full 3D model of a stent, *In: proceedings of the 13th conference of European society of biomechanics*, pp. 537-538

Matsuda, Y., and Yamamoto, T., 1993, The application of titanium wire for the reattachment of the greater trochanter in total hip arthroplasty, *Clin. Mater.*, 12, pp. 41-47

Minoshima, K., Terada, T., and Komai, K., 2000, Influence of nanometre-sized notch and water on the fracture behaviour of single crystal silicon microelements, *Fatigue Fract. Engng. Mater. Struct.*, Vol 23, pp. 1033-1040

Mitchell, M.R., 1979, *SAE/SP-79/448*, Publ. Society of Automotive Engineers (USA)

Murakami, Y., *et al.*, 1987, *Stress intensity factors handbook*, Oxford, Pergamon

Neuber, H., 1958, Theory of notch stresses, *Publ. Society*, Berlin

Nobuyoshi, M., Kimura, T., Ohsihi, H., Horiuchi, H., Nosaka, H., Hamasaki, N., Yokoi, H., and Kim, K., 1991, Restenosis after percutaneous transluminal coronary angioplasty: Pathologic observations in 20 patients, *Journal of the American College of Cardiology*, 17(2), pp. 433-439

Peterson, R.E., 1953, *Stress Concentration Design Factor*, New York: John Wiley

Peterson, R.E., 1959, Notch sensitivity, In *Metal Fatigue* (Ed. G. Sines & J. L. Waisman) McGraw Hill (New York), pp. 293-306

Peterson, R.E., 1974, *Stress Concentration Factor*, New York: John Wiley

Ross, R., 1999, Atherosclerosis - an inflammatory disease, *The New England Journal of Medicine*, Vol. 340, pp. 115-126

Scheiner, A., Mortimer, J.T., and Kicher, T.P., 1991, A study of the fatigue properties of small diameter wire used in intramuscular electrodes, J. *Biomed. Mater. Res.*, Vol. 25, pp. 589-608

Sharpe, W.N., and Bagdahn, J., 2002, Fatigue of materials used in microelectromechanical systems (MEMS), *Fatigue* 2002, pp. 2197-2212

Shih, C.C., Shih, C.M., Su, Y.Y., Su, L.H.J., Chang, M.S., and Lin, S.J., 2004, Effect of surface oxide properties on corrosion resistance on 316L stainless steel for biomedical applications, *Corrosion Science*, Vol. 46, pp. 427-441

Siebel, E., and Stieler M., 1955, Dissimilar stress distributions and cyclic loading, *Z.Ver.Deutsch.Ing.*, 97, pp. 121-131

Sigwart, U., Puel, J., Mirkovitch, V., Joffre, F., and Kappenberger, L., 1987, Intravascular stents to prevent occlusion and restenosis after transluminal angioplasty, *New England Journal of Medicine*, 316, pp. 701-707

Smith, R.A., 1977, International Journal of Fracture, 13, pp. 717-720

Smith, R.A., and Miller, K.J., 1978, Prediction of fatigue regimes in notched components, *Int. J. Mech. Sci.*, 20, pp. 201-206

Suo, Z., Ho, S., and Gong, X., 1993, Notch ductile-to-brittle transition due to localized inelastic band, *J. Eng. Mater. Technol.*, 115, pp. 319-326

Tanaka, K., 1983, Engineering formulae for fatigue strength reduction due to crack-like notches, *Int. Journal of Fracture*, 22, pp. 39-45

Tanaka, K., and Nakai, Y., 1983, Propagation and non-propagation of short fatigue cracks at a sharp notch, *Fatigue of engineering materials and structures*, Vol 6, No.4, pp. 315-327

Tanaka, K., and Nakai, Y., 1984, Mechanics of growth threshold of small fatigue cracks, *Fatigue crack growth threshold concept*, edited by D. Davidson and S. Suresh, TMS_AIME NY USA

Taylor, D., 1989, *Fatigue Thresholds*, London: Butterworths

Taylor, D., 1996, Crack modelling A technique for the fatigue design of components. *J. Engineering Failure Analysis,* Vol. 3, No. 2, pp. 129-136

Taylor, D., 1999, Geometrical effects in fatigue: a unifying theoretical model, *International Journal of Fatigue*, 21, pp. 413-420

Taylor, D., 2001, A mechanistic approach to critical-distance methods in notch fatigue, *Fatigue Fract. Engng. Mater. Struct.*, 24, pp. 215-224

Taylor, D., 2002, Modelling of fatigue crack growth at the microsctructural level, *Computational Materials Science*, 25, pp. 228-236

Taylor, D., Bologna, P., and Bel Knani, K., 2000, Prediction of fatigue failure location on a component using a critical distance method, *Int. J. Fatigue*, 22, pp. 735-742

Taylor, D., and Carr, A.J., 1999, The crack modelling technique: optimisation of parameters, *Fatigue Fract. Engng. Meter. Struct.*, 22, pp. 41-50

Taylor, D. and Jianchun, L., 1993, *Source book on fatigue crack propagation: thresholds and crack closure*, The chameleon press ltd, London, UK

Taylor, D., and Lawless, S., 1996, Prediction of fatigue behaviour in stress-concentrators of arbitrary geometry. *Eng. Fract. Mechanics*, Vol. 53, pp. 929-939

Taylor, D., Zhou, W., Ciepalowicz, A.J., and Devlukia, J., 1999, Mixed-mode fatigue from stress concentrations: an approach based on equivalent stress intensity, *Int. J. Fatigue*, 21, pp. 173-178

Taylor, D., and Wang, G., 1999, A critical distance theory which unifies the prediction of fatigue limits, small cracks and notches, *Proc.Fatigue'99*, China, publ. Higher Education Press (China) and EMAS (UK), 1, pp. 579-584

Wang, G., 1999, Prediction of fatigue failure in engineering components using the finite element method, *PhD Thesis*, University of Dublin, Trinity College

Wang, G., Taylor, D., Bouquet, B., Ciepalowicz, A., and Devlukia, J., 2000, Prediction of Fatigue Failure in a Camshaft Using the Crack Modelling Method, *Journal of Engineering Failure Analysis*, pp. 189-197

Wang, G, Taylor, D., Ciepalowicz, A., and Devlukia, J., 1999, Prediction of fatigue failure in cast aluminium alloy components using the crack modelling method, *Proc.Fatigue'99*, China, publ. Higher Education Press (China) and EMAS (UK), 2, pp. 735-740

Weiss, B., and Hadrboletz, A., 2002, Fatigue of micromaterials, *Fatigue 2002*, pp. 2233-2244

Westergaaard, H. M., 1939, Bearing pressures and cracks, *J. Appl. Mech.* A, pp. 49-53

Wöhler, A., 1870, Über die Festigkeits-Versuce mit Eisen und Stahl [On strength tests of iron and steel], *Z. Bauwesen,* N. 20, pp. 73-106

Yates, J.R., and Brown, M.W., 1987, Prediction of the length of non-propagating fatigue cracks, *Fatigue Fract. Engng. Meter. Struct.*, 10, 3, pp. 187-201

Yu, H., Tanaka, K. and Akiniwa, Y., 1998, Estimation of torsional fatigue strength of medium carbon steel bars with a circumferential crack by the cyclic resistance-curve method, *Fatigue Fract. Engng Mater. Struct.,* Vol. 21, pp. 1067-1076